Coláiste na Tríonóide, Baile Átha Cliath
Trinity College Dublin
Ollscoil Átha Cliath | The University of Dublin

Individual blade pitch control strategies for spar-type floating offshore wind turbines

Saptarshi Sarkar

A thesis submitted in fulfilment of the requirements for the degree of Doctor of Philosophy

in the

Department of Civil, Structural and Environmental Engineering
Trinity College Dublin

2020

Declaration of Authorship

I declare that this thesis has not been submitted as an exercise for a degree at this or any other university and it is entirely my own work.

I agree to deposit this thesis in the University's open access institutional repository or allow the library to do so on my behalf, subject to Irish Copyright Legislation and Trinity College Library conditions of use and acknowledgement.

Signed: Saptarshi Sarkar

Date: 11/05/2020

Abstract

The aim of this thesis is to study the dynamics of spar-type Floating Offshore Wind Turbines (FOWTs) and investigate the performance of the individual blade pitch control strategies proposed to improve dynamic response of the turbine. The improvement in response is obtained in the form of reduced structural vibrations and improved power production. Wind loads are the largest source of dynamic loads on the wind turbines and it is well known that it is possible to reduce this aerodynamic loads by actively pitching the blades to the inflowing wind. The power output of the wind turbines are also regulated by active pitch control above the rated wind speed. Therefore, it an open problem to design intelligent controller capable of optimizing the performance by reducing the aerodynamic loads and/or improving the power production. In this thesis, three different individual blade pitch control strategies have been proposed and their performance has been evaluated using a high fidelity FOWT model.

First, a dynamic model of the spar-type FOWT is derived using Kane's method. Kane's method of deriving equations of motion of dynamic systems has emerged recently and presents certain advantages over the traditional Euler-Lagrangian energy formulation. Using Kane's method the equations of motion are derived from the kinematics of the system and solved directly by a computer without the need for human intervention. The derived dynamic model is verified again state-of-the-art simulator FAST (Jonkman and Buhl Jr, 2005). This derived model of the wind turbine is then used to investigate the performance of the proposed control strategies.

The first individual blade pitch control strategy proposed in this thesis is designed based on the wavelet-LQR control strategy. The wavelet-LQR control strategy provides a framework for a time-varying controller by assigning frequency band dependent gain suitable for wind turbine applications. In this chapter, the effect of wave-current interaction is also investigated. It has been shown that wave-current interaction does not have a significant effect on the dynamics of the FOWTs. The proposed wavelet-LQR individual pitch controller was excellent in mitigating aerodynamic loads on the turbine and reducing the vibrations of the turbine and the floating platform. Since the design objective of the controller was vibration control, the excellent vibration control was accompanied by small increase in power variability. However, it has been argued that the individual wind turbine power variability will be less important as an offshore

wind turbine will almost certainly be situated in a large wind farm and the total output of the farm will be predominantly dictated by the spatial and temporal variations of the farm rather than the variability of a single turbine. Hence, this increase in individual wind turbine power variability is judged to be acceptable considering the promising reduction in structural loads.

The second individual blade pitch controller proposed in this thesis is a dual objective controller. It is well known from literature that reducing aerodynamic loads and power variability are two competitive objectives and improving one has a deteriorating effect on the other. To address this issue, the control strategy proposed in this chapter intelligently combines a simple PI (proportional-integral) controller with a low-authority LQ (Linear Quadratic) regulator. The results presented in this chapter show that the proposed controller is better than the existing controller in literature in both vibration control and power regulation. However, the benefits obtained by the above controllers comes at a cost of increased pitch actuation.

While vibration control and improved power tracking was achieved with increased pitch actuation, it is also known that one of the largest contributors to turbine downtime is failure of pitch systems. As future turbines are continuously being up-scaled, controllers that increase pitch actuation will only compound this problem, unless, improved and reliable pitch systems are developed. To this end, the final individual pitch control strategy proposed in this thesis is developed under the optimal framework of Non-linear Model Predictive Control (NMPC). The preview of the inflow wind field required by the controller is assumed to be available from LIDAR measurements. The aim of the controller is to minimize blade pitch actuation while maintaining/improving tracking of rated rotor speed and mitigating structural vibrations of the FOWT. The existing baseline controller is designed solely to maintain rated rotor speed and hence pitch actuation is low and scope of further reduction is limited. However, the NMPC offers and optimal control framework and accounts for the future disturbance. This opens up the possibility of further reduction in blade pitch actuation without deteriorating the performance of the FOWT which is investigated in this chapter.

"If you don't go after what you want, you'll never have it. If you don't ask, the answer is always no. If you don't step forward, you're always in the same place."
—Nora Roberts

Acknowledgements

A heartfelt gratitude to Trinity College Dublin and my supervisors, Dr Breiffni Fitzgerald and Professor Biswajit Basu, for supporting my PhD. It is difficult to overstate my gratitude to both Dr Basu and Dr Fitzgerald in the way they supervised my work. I would like to thank them both for all of the knowledge and encouragement they have given me throughout my years working with them. Their advice and support from even before I arrived at the college has been invaluable. I wish to acknowledge the entire faculty, technical and administrative staff of the Department of Civil, Structural and Environmental Engineering at Trinity College Dublin for their help and support.

I would like to thanks all my friends, Giacomo, Lea, Elia, Juan, Alex, Hoa, Matthew, John, Unni, Himangsu, Shreya, Niti, Radson, Rodolfo for the fun times and making my stay in Dublin memorable.

I'm especially grateful to my girlfriend, Riyanka, for always being there; for the patience, support and the motivational talks whenever I needed one.

And most importantly of all, I would like to thank my family for their sacrifice and support. My inspiration of becoming an academic certainly comes from them.

Contents

List of Figures

List of Tables

List of Abbreviations

SS	Low speed shaft-skew angle (rad)
ST	Low speed shaft-tilt angle (rad)
$TwrHt$	Height of the wind turbine tower (meters)
$PreCone$	Blade cone angles (rad)
$BlPit$	Blade pitch angles (rad)
$PtfmCMzt$	Vertical distance from the MSL to the platform CM (meters)
$PtfmRefzt$	Vertical distance from the MSL to the platform reference point (meters)
$NacCMxn$	Downwind distance from the tower-top to the nacelle CM (meters)
$NacCMzn$	Vertical distance from the tower-top to the nacelle CM (meters)
$NacCMyn$	Lateral distance from the tower-top to the nacelle CM (meters)
$Overhang$	Distance from yaw axis to rotor apex [3 blades] (meters)
$Twr2Shft$	Vertical distance from the tower-top to the rotor shaft (meters)
$Yaw2Shft$	Lateral distance from the tower center line to the rotor shaft (meters)
$HubCM$	Distance from rotor apex to hub mass [positive downwind] (meters)
$HubRad$	Hub Radius
$GenDir$	Generator direction
$GBRatio$	Gear Box ratio
$GenIner$	Generator inertia about HSS (kg m^2)
$TFA1$	First fore-aft tower bending-mode
$TFA2$	Second fore-aft tower bending-mode
$TSS1$	First side-to-side tower bending-mode
$TSS2$	Second side-to-side tower bending-mode
$GeAz$	Generator azimuth angle
$DrTr$	Drive-train torsion
$BiF1$	First flapwise bending-mode of i^{th} blade
$BiF2$	Second flapwise bending-mode of i^{th} blade
$BiE1$	First edgewise bending-mode of i^{th} blade
Sg	Platform surge
Sw	Platform sway
Hv	Platform heave

R	Platform roll
P	Platform pitch
Y	Platform yaw
$PtfmRIner$	Platform inertia for roll tilt rotation about the platform CM (kg m^2)
$PtfmYIner$	Platform inertia for yaw rotation about the platform CM (kg m^2)
$PtfmPIner$	Platform inertia for pitch tilt rotation about the platform CM (kg m^2)
YBM	Yaw bearing mass (kg)
$YawSpring$	Nacelle-yaw spring constant (N-m/rad)
$YawDamp$	Nacelle-yaw damping constant (N-m/(rad/s))
$NacYIner$	Nacelle inertia about yaw axis (kg m^2)
$HubIner$	Hub inertia about rotor axis (kg m^2)
$Bldlen$	Flexural length of the blade
HSS	High speed shaft
LSS	Low speed shaft
$DTTorSpr$	Drive-train torsional spring (N-m/rad)
$DTTorDmp$	Drive-train torsional damper (N-m/(rad/s))

List of Symbols

q_{Sg}	Platform surge DOF
q_{Sw}	Platform sway DOF
q_{Hv}	Platform heave DOF
q_{R}	Platform roll DOF
q_{P}	Platform pitch DOF
q_{Y}	Platform yaw DOF
q_{TFA1}	First tower fore-aft bending mode DOF
q_{TFA2}	Second tower fore-aft bending mode DOF
q_{TSS1}	First tower side-to-side bending mode DOF
q_{TSS2}	Second tower side-to-side bending mode DOF
q_{yaw}	Nacelle yaw DOF
q_{GeAz}	Generator azimuth angle DOF
q_{DrTr}	Drive-train torsional flexibility DOF
q_{BiF1}	First flapwise bending mode for i^{th} blade DOF
q_{BiF2}	Second flapwise bending mode for i^{th} blade DOF
q_{BiE1}	First edgewise bending mode for i^{th} blade DOF
q_{TMD}	Tuned mass damper DOF
$\theta_{SS}(h)$	Tower side-to-side rotation (rad)
$\theta_{FA}(h)$	Tower fore-aft rotation (rad)
$\theta_{s}^{Bi}(r)$	Structural pre-twist of blades (rad)
$\theta_{x}^{Bi}(r)$	Blade out-of-plane rotation (rad)
$\theta_{y}^{Bi}(r)$	Blade in-plane rotation (rad)
$\mu^{T}(h)$	Tower mass per unit length (kg/m)
m^{N}	Nacelle mass (kg)
m^{H}	Hub mass (kg)
μ^{Bi}	Blade per unit length of i^{th} blade (kg/m)
σ	Local blade solidity $(N_B c/(2\pi r)$
N_B	No of blades
c	Local cord length (m)
c_l	Lift coefficient

c_d	Drag coefficient
a	Axial induction factor
a'	Tangential induction factor
ϕ	Local inflow angle
ϕ_1^{TFA}	First fore-aft tower mode shape
ϕ_2^{TFA}	Second fore-aft tower mode shape
ϕ_1^{TSS}	First side-to-side tower mode shape
ϕ_2^{TSS}	Second side-to-side tower mode shape
ϕ_1^{BiF}	First flapwise blade i mode shape
ϕ_2^{BiF}	Second flapwise blade i mode shape
ϕ_1^{BiE}	First edgewise blade i mode shape
λ_r	Local tip speed ratio
C_A	Normalized hydrodynamic-added-mass coefficient in Morison's equation
C_M	Normalized mass (inertia) coefficient in Morison's equation
C_D	Normalized viscous-drag coefficient in Morison's equation
h_{TMD}	Vertical distance of TMD center of mass from tower top

Chapter 1

Introduction

Development of offshore wind energy presents great scientific and engineering challenges. It is a broadly multi-disciplinary field that requires expertise of structural, mechanical, electrical, control and environmental engineers for its development and growth. A plethora of aspects such as met-ocean conditions, foundations, structural design, electro-mechanical components, spatial planning, environmental impacts etc., must be considered for the successful growth of this industry. In this chapter, a brief introduction on the development of offshore wind energy is presented followed by a discussion on optimization of offshore wind technology based on the Levelized Cost Of Energy (LCOE). The chapter is concluded with the aims and organisation of the thesis.

1.1 Development of offshore wind energy

The driving force for the development of wind energy is to reduce the emission of greenhouse gases such as CO_2 and provide a cleaner source of energy and hence battle climate change. Offshore wind can provide long term security in the energy sector as it is an sustainable source of energy unlike the depleting resources of fossil fuels. It also has the potential of boosting industrial activities of construction and operations by opening up a new dimension in the energy sector. Many large cities of the world are located close to the sea and offshore wind farms can be build in proximity to them. This can be attractive as the requirement for transmission over long distances can be avoided. Also, building land based power plants close to the cities can be very expensive due to high property value. Offshore wind can provide a cheaper alternative. Offshore wind has greater potential than onshore wind with relatively less negative environmental impacts.

Evidently, there is a need for the development of the offshore wind industry. The market and technology must be mature enough to be able to carry out offshore wind

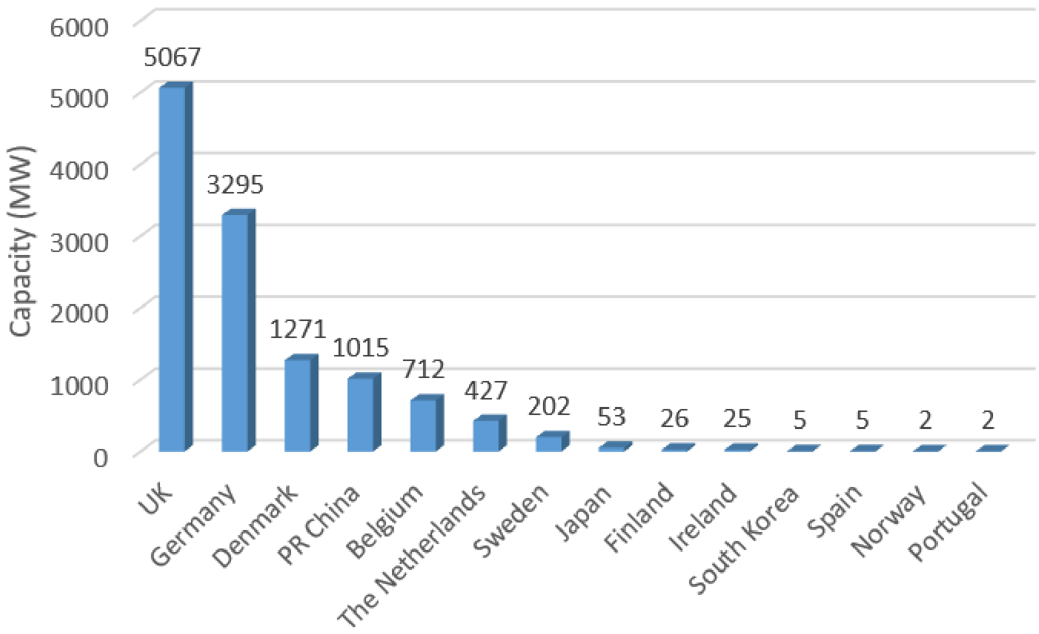

Figure 1.1: Installed offshore wind capacity at the end of 2015. (Source: Anaya-Lara et al., 2018)

farm projects with minimum risk and deliver energy at a competitive cost. A 220 kW turbine was the first offshore wind turbine installed about 250 m from the coast of Nogersund in southern Sweden in 1990 at a water depth of 6 m. In the following year, 1991, the first offshore wind farm was build 1 km from the shore of Lolland in Denmark. The farm consisted of eleven 450 kW turbines installed at a water depth of 2-4 m.

Although these developments might seem small compared to the state of the offshore wind industry today these were mighty steps during this time and pushed the technology further. They showed that offshore wind energy is a viable option and the challenges regarding installation and operation can be overcome. The growth of offshore wind has been slow until the turn of this century when in a period of fifteen years (2000-2015) the size of offshore wind farms grew from a few tens of megawatts to hundreds of megawatts (Anaya-Lara et al., 2018). By the end of 2015, the global offshore wind capacity was 12.1 GW with UK leading the list with 5.1 GW followed by Germany (3.3 GW), Denmark (1.3 GW) and China (1.0 GW). Figure 1.1 summarizes the installed offshore wind capacities of various countries at the end of 2015. Most of these wind farms consisted of bottom fixed offshore wind turbines.

Among the first offshore wind farms projects to deploy floating wind turbines to harness energy from deep offshore were Hywind (Norway, 2.3 MW, 2009), WindFloat (Portugal, 2 MW, 2011) and Fukushima (Japan, 2 MW, 2013). Following these projects

Figure 1.2: The London Array 630 MW offshore wind farm in operation in the outer Thames estuary. (Source: London Array, 2016)

there are tens of new projects on the way to take this technology forward. The Fukushima project was expanded by installing a 5 MW and a 7 MW wind turbine. The Hywind project was expanded by installing six 5 MW turbines in the Scottish waters making it a 30 MW offshore wind farm.

As of September 2018, the 659 MW Walney Extension in the United Kingdom is the largest offshore wind farm in the world. The Hornsea wind farm under construction in the United Kingdom will become the largest when completed at 1,200 MW. The London Array completed in 2013 comprised of 175 3.6 MW turbines resulting in a total capacity of 630 MW. It is located 20 km from the Thames estuary covering an area of 100 km^2 with water depths upto 25 m (see Figure 1.2). In 2015 the farm produced 2.5 TWh which corresponds to a capacity factor of 45%. It is known (Taylor, Ralon, and Ilas, 2016), that offshore wind farms experience more favourable wind conditions than onshore wind farms. For example the global capacity factor for onshore wind farms was 27% in 2015 (Taylor, Ralon, and Ilas, 2016).

Offshore wind farms can reduce CO_2 emissions in the range of 300 to 700 gm per kWh compared to energy produced from natural gas and fossil fuels respectively. However, the actual savings will depend on the operation of the power system along with the wind farm. According to London Array, 2016, the annual average saving is 925,000 tones of CO_2 based on 420 g/kWh and a capacity factor of 39%. This number can be put into perspective by comparing it to the emission of 289,000 passenger cars.

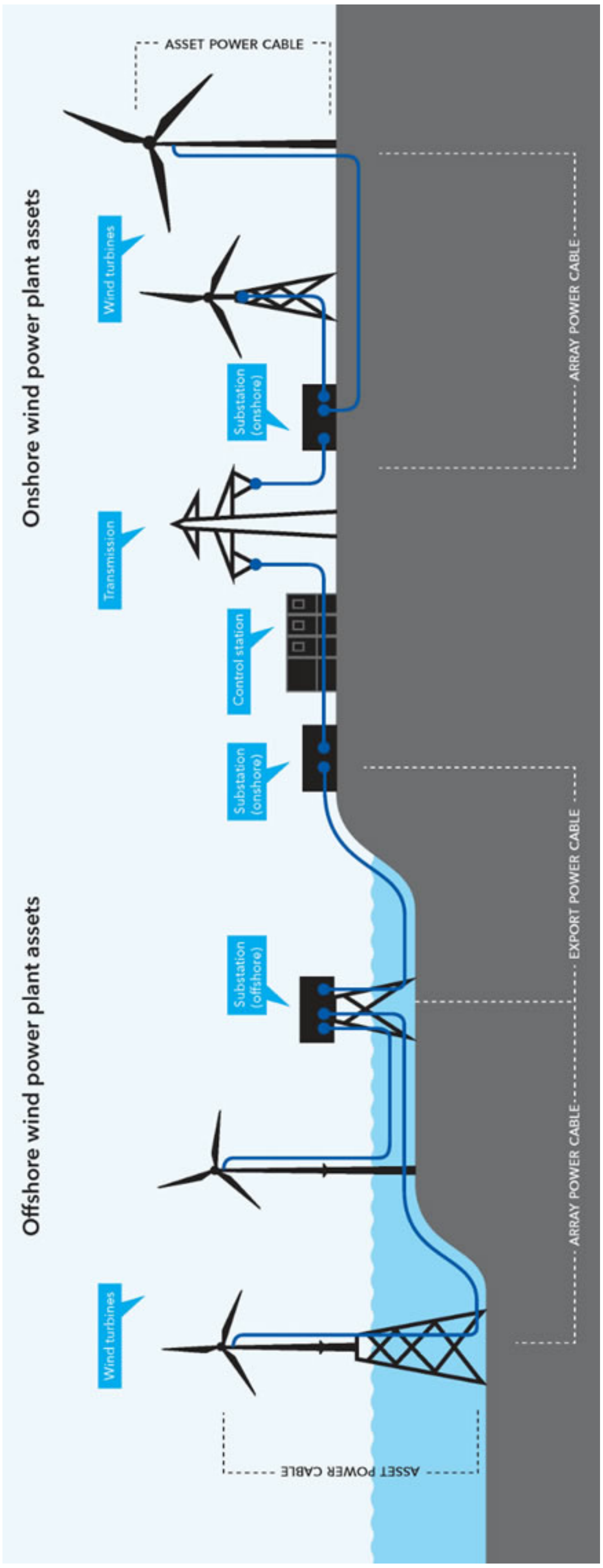

Figure 1.3: Elements of an offshore wind farm. (Source: DNV GL, 2015)

1.2 Offshore wind technology

Offshore wind technology has a few significant elements such as a) the wind turbines themselves, b) the substructure or foundation, c) internal connection grid, d) substation, e) farm layout and design, and, f) transmission to shore (Figure 1.3). Offshore wind turbines are similar to onshore wind turbines but are typically of higher rating. The largest offshore wind turbine till date is the MHI Vestas 9.5 MW turbine with a rated power of 9.5 MW and rotor diameter of 164 m.

Offshore wind turbines can have different types of substructure or foundation (Figure 1.4). For shallow depths, typically up to 40-60 m monopiles or bottom fixed jacket type foundations are used. As we delve deeper, tension leg platforms or semi-submersible foundations are used. At depths >120 m spar type floating wind turbines are used. This thesis focuses on the spar-type floating wind turbines. Located far-shore, these turbines have the advantage of being located in an energy rich deep offshore region but they also must survive the harsh marine conditions. These turbines are typically of higher rating (5-10 MW). Modern turbines are equipped with sophisticated control systems aimed to optimize energy output at all times while ensuring safe operations. Individual turbines have their independent control systems though they might be constrained by the wind farm Supervisory Control And Data Acquisition (SCADA) system.

The transmission of energy from the turbine to shore goes through the internal grid and substation before being delivered to the shore. Typically, a group of turbines are connected to a substation through the internal grid. Depending on the size of the farm there may be one of more substations that are connected to the transmission network. The layout can have different arrangements depending on the size of the farm and the distance to the shore. Internal grids are commonly operated with alternating current at about 33 kV, though, 66 kV solutions are emerging for larger wind farms. The design of the internal grid and substation should be assessed carefully to account for switching transience and high frequency resonance. As an alternative to alternating current internal grids, direct current internal grids have been proposed but not yet implemented in any commercial wind farm. The substation normally has a transformer that brings the voltage up to the transmission level, for example 150 kV. Over short distances and smaller wind farms high voltage alternating current (HVAC) is the normal choice for transmission. For wind farms more than 100 km from shore and above 200 MW in capacity high voltage direct current (HVDC) is the suggested option due to lower losses in transmission. However, this requires HVDC converters to be installed offshore and on land which can considerably increase the cost of the farm. Hence, the industry has

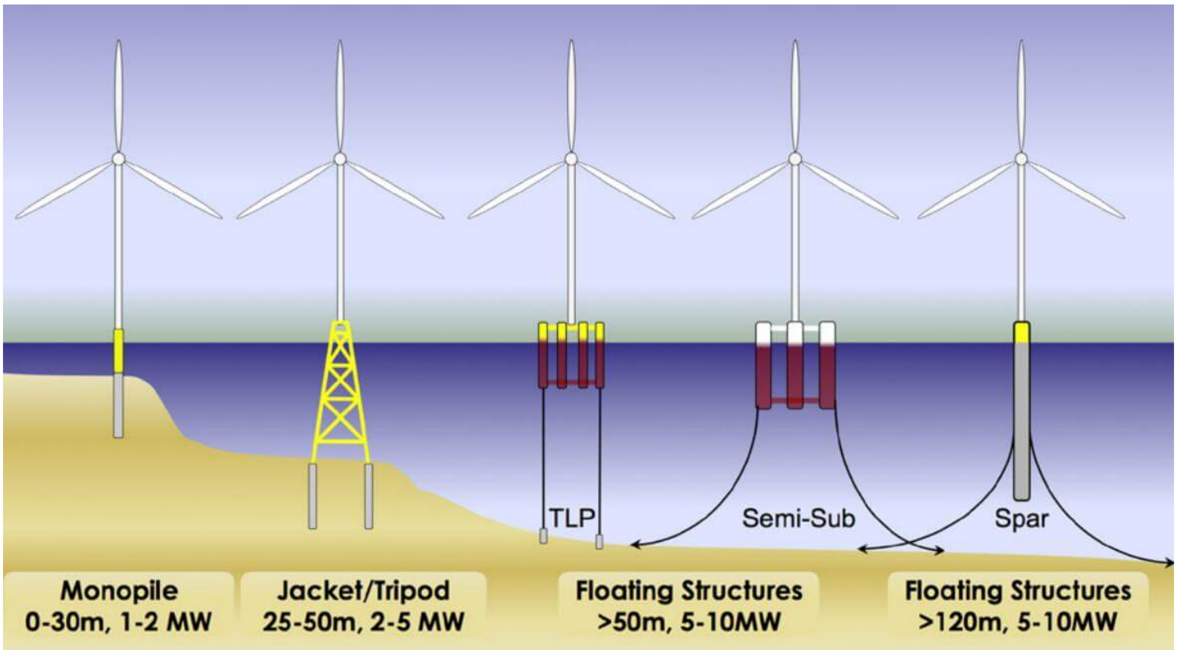

Figure 1.4: Different types of substructure for offshore wind turbines. (Source: (Arapogianni et al., 2013))

also shown interest in using HVAC for long distance transmission.

Operation and maintenance (O&M) of offshore wind farms is significantly more complicated and expensive compared its onshore counterparts. Performing maintenance tasks mean bringing service personnel, equipment and spare parts on the turbines which is not trivial and often expensive. Various cost effective methods have been proposed to secure efficient O&M but it is not straightforward to select one. Ideally, one would want the turbine to fulfil its design life with minimum maintenance. This includes safe operation of its structural, mechanical and electro-magnetic components in the harsh marine conditions which is the main challenge of offshore wind energy.

1.3 Levelized cost of energy

The offshore wind farms must be capable of providing high energy output while ensuring safe and reliable operations and complying with the grid and environmental requirements. The design of an offshore wind farm is optimized by minimizing the cost of energy production per kWh over its entire design life. Therefore it is important to understand the basics of how cost of energy is calculated. As an example, lets assume that it was found that the energy output of a wind farm can be increased by increasing the space between the turbines. But this means more cost in the form of longer cables

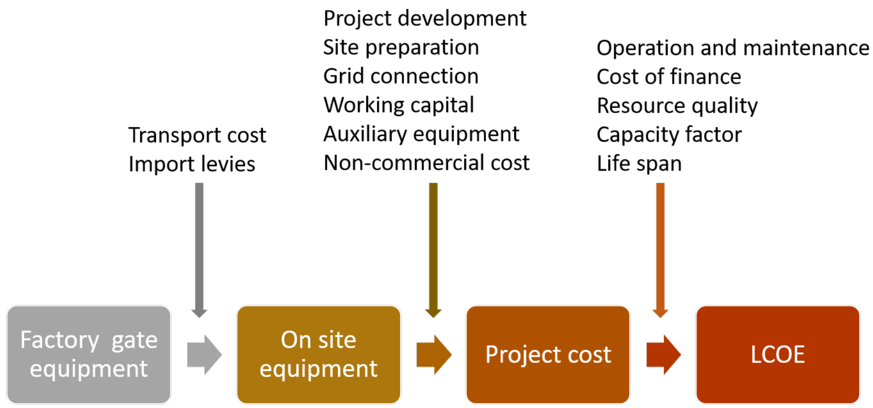

Figure 1.5: Metrics in calculation of LCOE. (Source: Taylor, Ralon, and Ilas, 2016)

between the turbines. So is the idea good or not? The answer can be obtained in economic terms by comparing the cost of energy in the two situations.

Levelized cost of energy (LCOE) is the most common metric used to calculate the cost of energy of power plants. It is the cost of per unit energy (kWh) averaged over its lifetime. The LCOE is obtained as the ratio of the discounted total cost of production and the discounted energy output. The cost of production and energy output are discounted to the start of the operation by choosing a proper discount rate. According to (Taylor, Ralon, and Ilas, 2016) the LCOE can be given as

$$\mathrm{LCOE} = \frac{\sum_{t=1}^{n} \frac{I_t + M_t}{(1+r)^t}}{\sum_{t=1}^{n} \frac{E_t}{(1+r)^t}} \tag{1.1}$$

where, I_t is the investment in the year t, M_t is the operation and maintenance expenditure in the year t, r is the rate of discount and n is the design lifetime of the offshore wind farm. By definition, the LCOE of a project is equal to the average lifetime selling price of electricity from the project. A higher electricity price means higher profit whereas electricity prices lower than LCOE means acquiring a loss on the investment. The different steps in estimation of LCOE is shown in Figure 1.5.

Depending on the scope of the analysis there can be different level of details in describing the energy production E_t, the investment I_t and the maintenance cost M_t. Typically the design lifetime of an offshore wind farm is 25 years. However, a shorter lifetime is often considered to make financial decisions. The rate of discount r depends on the cost of capital, perceived risk of the project and normally varies from market to market and over time. A discount rate of 5-10% is typically used in LCOE studies. The LCOE of different wind farms installed between 2010 to 2015 is shown in Figure 1.6

which also shows a projection until the year 2025. The numbers reproduced in this thesis is largely taken from IRENA 2016 report (Taylor, Ralon, and Ilas, 2016). It can be observed that there is a big spread in the LCOE of different projects. This is usual for a technology in its early stages. However, the projections also show that by 2025 the LCOE can be brought down to grid parity.

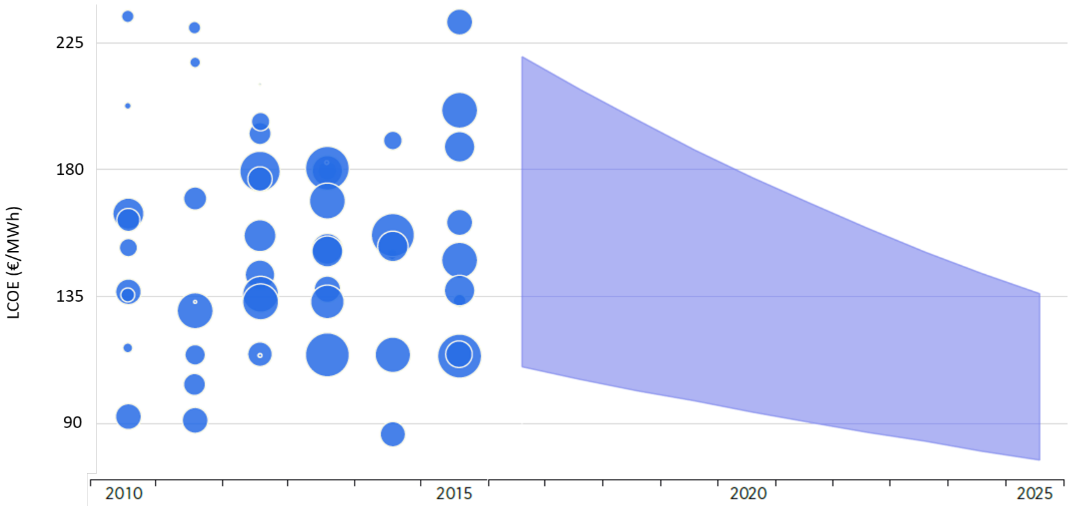

Figure 1.6: Historical LCOE of offshore wind farms and projection. (Source: Taylor, Ralon, and Ilas, 2016)

1.4 Reducing cost of energy

This section discusses the various technological innovations that can be implemented to reduce the LCOE by 2025. There is an incremental opportunity to reduce cost of energy by 2025. Through technological innovations, experience and economy of scales the the total installed cost of an offshore wind farm can reduced by about 15%. The largest opportunity of cost reduction lies with construction and installation costs that accounts for 60% of the total installed cost reduction potential of 15%. Other than that, the incremental cost reduction potential in the turbine rotor is 15% and the tower accounts for 7%. There is also a possibility of streamlining the project development phase and reducing the project development cost.

There is a range of trade-offs in identifying the greatest LCOE cost reduction potentials for offshore wind farms. Meaning, sometimes higher installed costs for some components can reduce the LCOE. For example, include higher quality and more expensive prefabricated components may reduce installation times and costs. Additionally, more expensive turbine components that deliver higher reliability will cut O&M costs and increase energy production. Larger turbine blades that are more costly, can

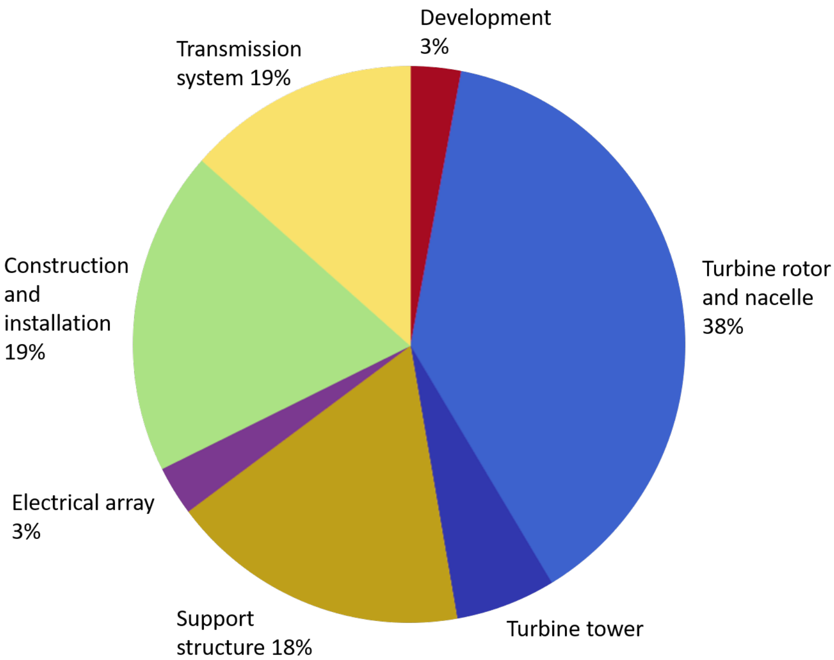

Figure 1.7: Distribution of investment expenditures for a representative offshore wind farm. (Source: Taylor, Ralon, and Ilas, 2016)

increase energy production, thus reduce LCOE. It is therefore important not to take the installed cost reductions at face value. This is particularly true for optimization between installed costs and electricity output. For example a 10% increase in capacity factor will reduce the LCOE by around 9% whereas a 10% reduction in capital costs would reduce LCOE by around 7.6% For offshore wind turbines, the main areas for innovation are improvements that focus on reducing installed costs; improving reliability, which will reduce O&M costs and improve electricity yields; and improving efficiency to increase capacity factors.

1.4.1 Construction and installation costs

Due to the high rates of offshore installation vessels and personnel the key opportunity to reduced construction costs comes from reducing the installation time. Other than this there is a range of innovations that are also expected to help reduce the installation costs.

- Increasing the maximum wind speed at which installations can be completed would provided a longer installation window, reduce number of disruptions and time spend on installation.

- Larger jack-up vessels with optimized designed could be used to install more than one frame foundation at a time thus accelerating the installation process.

- Next generation turbines should be designed so that maximum of the commissioning is done onshore. This will allow the assembly of the rotor and tower onshore in a single operation.

- Underwater noise during the piling process has an adverse effect on marine life. This can be reduced by the use of *bubble curtain* or *sleeve*. The noise reduction can lead to extended construction seasons.

Some of these innovations have already been commercially implemented. Not all of these innovations will be applicable in all situations, and commercialisation may prove more or less difficult. However, they represent significant cost reduction opportunities.

Offshore wind turbines have rapidly grown in size to large 6-8 MW turbines and are specially made for offshore installation. Continuous growth in innovations in drive-train design, blade design and innovative concepts offer opportunities to reduce installed costs. Some turbine innovations that can reduce cost of energy are:

- Modest cost reduction can be obtained by increasing the blade tip-speed ratio as it will reduce the drive-train torque. Increasing tip-speed ratio can be a problem for onshore wind turbines as it increases noise, but, this is a possibility for offshore wind turbines.

- Blade designs and manufacturing improvement can lead to cost reduction. This includes innovations and use of new materials to produce stiffer, lighter, lower cost high quality blades. Improvement in the aerodynamic design of the blades are also included in this.

- Innovations in drive-train design include direct drive drive trains, mid-speed drive trains, continuously varying drive trains and superconducting generators. These developments can lower installation costs.

- New developments in the power take-off unit can reduce installation costs and improve electricity yields. New AC (alternating current) power take-off units use advanced materials like silicon carbide or diamond to achieve greater reliability in smaller, more efficient and faster switching power conditioning units. DC (direct current) power take-off units can eliminate the need for an converter that converts the DC current from the generator to grid frequency AC current. This would save capital costs and improve reliability.

- Improvement in turbine reliability and reduction in unplanned maintenance cost can be acheived through the use of improved bearing concepts and lubrication, hydraulics and electrical systems in the hub. Back up energy source for emergency response and grid fault ride-through can help prevent unplanned outrage.

Due to the ongoing trend towards larger wind turbine the commercialization of 10 MW wind turbines is likely to take place in the early 2020s. This is will help the introduction of many of the above concepts, however, it may also necessitate the need for new innovations.

Other than the construction and installation cost of the turbines, reductions in cost of production can also be achieved through innovations in wind farm development, foundations, electrical array and onshore transmission connections. Innovations and development in offshore wind farm design can be achieved through improved identification of wind resource characteristics, improved identification sea bed characteristics and improved wind farm design software. Reduction in the cost of cables can be achieved by choosing the most suitable (smaller) cable core thickness, insulation thickness and mechanical protection. However, developers tends to demand for cables higher than industrial standards. Transmission of power over distances greater than 80 km would typically require an expensive high-voltage direct current (HVDC) system to reduce transmission losses. However, long distance HVAC systems are now being developed and proposed to avoid these incremental costs and the HVAC systems is expected to be commercialized soon.

1.4.2 Operations and maintenance costs

The potential total reduction in O&M costs is estimated to be around 44% falling from USD 141/kW per year in 2015 to USD 79/kW per year in 2025 (Taylor, Ralon, and Ilas, 2016). 57% of that is dedicated to improvements in turbine reliability and improved ease of maintenance. Reduction in O&M cost related to the electrical array accounts for another 15% of that, improved O&M systems and procedures for another 13% and other factors for 12%. Scheduled and unscheduled maintenance costs are expected to decline by 34% and 50% compared to the the costs in 2015. Some main opportunities for O&M cost reduction are:

- Improved weather forecasting and analysis methods are required to maximize energy production during the good weather period. This requires advances in the accuracy and granularity of the forecast. Heavy offshore works require reasonable predictions up to 21 days whereas present technology is accurate only up to 5 days.

- Introduction of turbine condition-based maintenance strategies can maximize energy production while minimizing unnecessary scheduled maintenance interventions. New and improved prognosis and diagnostics systems are required to reflect the risk of failure according to operating experience. The reduction in maintenance cost from this approach should more than offset the slight increase in capital cost required for data collection and analysis.
- Improvements in O&M strategies for far-from-shore wind farms include optimization of service operation vessels (SOVs) to offer better office space, workshops and welfare services to the technicians. The large SOVs should also be able to support a number of daughter vessels. Remote O&M strategies like drone based inspection and automated maintenance can replace expensive onsite maintenance. Economy of scales will also reduce O&M costs as a number of wind farms could share the same equipment and infrastructure. With further development of still larger and reliable turbines along with improved remote monitoring and automated maintenance strategies the cost of O&M is expected to reduce.

1.4.3 Improved capacity factor

Technological innovations can help to improve the overall capacity factor of offshore wind in the future. These include improved blade control and drive-train improvements. One possibility of improved blade control is to use LiDAR measurements of the inflow wind speed and orient and blades accordingly to maximize energy capture. Another possibility is to introduce active aero control on individual sectors of the blades to locally optimize the aerodynamic performance of the blades. This technology includes active flaps, activated surfaces, plasma fields and air jet boundary level control etc. These technologies can improve the energy output of individual turbines thus improving capacity factor of the entire farm.

Improvements are also possible in the drive-train, for example mid-speed drive trains and direct drive drive trains has the potential to decrease the number of critical components and reducing planned and unplanned maintenance. This will result in higher availability and therefore higher output. The ultimate result of developments in offshore wind technology and operations is to increase energy yield by around 4% between now and 2025.

1.5 Aim and organisation of the thesis

This thesis deals with the dynamics and control of spar-type floating offshore wind turbines. The motivation for the work arises from the need to improve turbine reliability and energy capture (capacity factor). In the previous section various aspects of reducing levelized cost of energy has been discussed. Two significant aspects are innovations in improving turbine reliability and energy production. Improving the reliability of the turbine means the structural and mechanical components should be able to fulfil their design life with minimum planned or unplanned maintenance. In other words, the reliability of the different components can be improved by reducing the loads on them. Energy capture (capacity factor) can be improved by innovations in active blade control strategies of passive aerodynamic optimization. This thesis deals with these two aspects of improving reliability by reducing aerodynamic loads and improving energy capture by proposing new active blade control strategies.

It must be pointed out at the beginning that this thesis proposes various control strategies that reduce structural loads and improve power production of the turbines. Estimation of the improved LCOE from the use of the proposed controllers is not in the scope of this thesis. A very wide range of information is required to estimate the LCOE of a wind farm which is not available with the author. Moreover, estimation of the LCOE of a site is a substantial task by itself. The cost benefits arising from improved fatigue life and power production is a consideration for future research.

The primary aim of the thesis is development of individual blade pitch control strategies for floating offshore wind turbines to extend their performance beyond the current state-of-the-art. The work has been divided into categories and the different aims at every level summarized below.

- Development of a high-fidelity floating offshore wind turbine model which is then used to test the proposed individual blade pitch control algorithms.
- Development of individual blade pitch control strategies to reduced structural loads and platform motion.
- Development of dual objective individual blade pitch control strategies to simultaneously reduced structural loads and regulate power production.
- Development of LIDAR based model predictive control strategy to reduce pitch actuation to reduce the long term damage equivalent loads on the pitch actuators.

The different aims of the thesis are addressed in the different chapters of this thesis and the organisation is discussed in the following paragraphs.

In Chapter 2 past works on dynamic modelling of wind turbines, active and passive structural control of wind turbines, blade pitch control strategies etc., has been reviewed. From the review of past works various gap areas are identified and discussed in details.

Floating offshore wind turbines (FOWTs) have profound dynamic characteristics. Thus it is necessary to capture this dynamic behaviour with a high degree of fidelity. Therefore a detailed model of the turbine is required. Chapter 3 is dedicated to dynamic modelling of the spar-type FOWTs. The procedure of deriving the dynamic equations of motion using Kane's method, that emerged recently as the preferred choice, is described in details. The equations of motion are derived in a systematic manner while focusing on the advantages that Kane's method brings over traditional methods like the Euler-Lagrangian energy formulation. The derived model is the verified against state-of-the-art simulator FAST (Jonkman and Buhl Jr, 2005). Often a high fidelity model brings with it a very complicated set of equations of motion, and simpler reduced order models are desired for the control systems. An investigation has been carried out to evaluate the loss of dynamics arising from this model order reduction and conclusions have been drawn based on the findings.

In Chapter 4 an novel multi-resolution wavelet individual blade pitch controller has been proposed. The primary aim of the controller is to reduce structural loads on the wind turbine components like the blades, tower and the platform. Impressive load reduction capabilities has been reported. It has been shown that this impressive load reduction comes at a cost of slightly increased wind turbine power variability. However, as past studies have reported, this slight increase in variability is negligible when an entire wind farm is considered and hence the controller has promising applications. Wave-current interactions and its effect on the dynamics and control of FOWTs has also been investigated in this chapter.

Chapter 5 proposes another individual pitch control strategy with a dual objective of structural load reduction and power regulation. The proposed controller intelligently combines an PI (proportional-integral) controller with an LQR (linear quadratic regulator) to determine the individual pitch angles. The reported reduction in structural responses and power variability is higher than any other controller available in literature. Also, unlike the existing individual pitch control strategies in literature the proposed strategy is capable of mitigating platform motion.

In Chapter 6 a non-linear model predictive individual blade pitch control strategy has been proposed and investigated. The prediction of the upstream wind field is assumed to be obtained from LIDAR measurements. The controller is designed under the optimal NMPC framework to strike a balance between the use of pitch actuation and aerodynamic load reduction/rated power tracking. It is well known that overuse of blade pitch actuators may lead to increased downtime of the the turbines. Based on this understanding, the controller is designed to reduce blade pitch actuation while maintaining or even improving power production and reducing structural vibrations compared to the baseline level.

The thesis is concluded with Chapter 7 which summarizes the work presented in this thesis and draws conclusions based on the findings. This also discusses the potential extensions to the current research in offshore wind dynamics and control.

Chapter 2

Literature review

2.1 Introduction

The literature reviewed in this thesis can be divided into three main categories. The thesis first discusses the multi-body modelling of floating floating offshore wind turbines (FOWTs). Kane's method is used in this work to derive the equations of motion. In the first part, literature available on multi-body modelling of wind turbines is reviewed. The derived multi-body model of the FOWT is then used to evaluate the performance of the different control strategies proposed in the thesis. The second part of the literature review covers the different blade pitch controllers proposed in literature. Wind turbine blades come with pitch actuators installed in them to regulate the power production. These pitch actuators can also be used to reduce aerodynamic loads on the turbine. The major contribution of thesis is the development of novel pitch control strategies that improve the dynamic characteristics of the turbine compared to the current state-of-the-art. With this in view, the second section summarizes the various blade pitch control strategies proposed in literature to date. Although active pitch control of the turbine blades can considerably reduce aerodynamic loads and hence mitigate turbine vibrations, traditionally, auxiliary dampers are used for structural vibration control of wind turbine blades and tower. Some of these investigations are reviewed in the final section.

2.2 Dynamic modelling of wind turbines

With increasing popularity of wind turbines, researchers over the world have worked actively to study the dynamic behaviour of these large rotating structures. FAST (Jonkman and Buhl Jr, 2005), an open source wind turbine simulation tool developed by NREL is one of the most popular tools used to simulate the dynamic behaviour of wind turbines subjected to wind and wave loads. FAST models the wind turbine as a multi-body system using Kane's method similar to the works in (Lee, Hodges, and Patil, 2002; Lee and Hodges, 2003). Kane's method offers a vector based approach to derive the equations of motion of a dynamic system. Unlike the traditional Euler-Lagrangian method, the analytical expressions of the kinetic and potential energy of the system are not required. Using Kane's method the equations of motion of a system can be derived directly from the kinematics of the system. This eliminates the need to manually derive the equations of motion. Parallely with FAST, Flex5 (Øye, 1996) and HAWC2 (Larsen and Hansen, 2007) was developed by DTU (Risø) to study the dynamics of wind turbines in the time domain (refer (Sarkar, Fitzgerald, and Basu, 2018)). Other than FAST, Flex5 and HAWC2, independent models of onshore and offshore wind turbines have been derived by researchers (Dinh and Basu, 2013; Murtagh, Basu, and Broderick, 2005) for specialized purposes. The effect of soil-structure interaction has also been investigated (Fitzgerald and Basu, 2016; Harte, Basu, and Nielsen, 2012). Both studies showed that there is significant impact of soil dynamics on the motion of the wind turbine tower. Thus, soil-structure interaction must be considered in the dynamic analysis of wind turbines.

Dynamics of offshore floating wind turbines were studied by (Jonkman, 2007; Karimirad and Moan, 2011, 2013; Wang, Moan, and Hansen, 2016; Waris and Ishihara, 2012). Dynamics of spar type offshore wind turbines were studied in (Karimirad and Moan, 2011, 2013). Waris and Ishihara (2012) studied the dynamics of offshore wind turbines with different kinds of heave plates and mooring systems. Stochastic dynamics of a floating vertical axis wind turbine was investigated byWang, Moan, and Hansen, 2016. Offshore wind turbines on monopiles and the involved foundation dynamics was studied by (Achmus, Kuo, and Abdel-Rahman, 2009; Arshad and O'Kelly, 2016; Carswell et al., 2015a; Carswell et al., 2015b; Damgaard, Andersen, and Ibsen, 2014; Damgaard et al., 2015; Valamanesh, Myers, and Arwade, 2015; Zuo, Bi, and Hao, 2018). Similary to onshore wind turbines, soil-dynamics has a significant effect on the dynamics of offshore wind turbines. Finite element methods to model the soil structure interaction were proposed by Achmus, Kuo, and Abdel-Rahman (2009) and Carswell et al. (2015a). Nonlinear springs based on Winkler foundation theory was used by Carswell et al. (2015b) and Arshad and O'Kelly (2016) to model the soil dynamics. A consistent lumped-parameter model obtained by the domain-transformation method and a weighted least-squares technique was used by (Damgaard, Andersen, and Ibsen, 2014; Damgaard et al., 2015) to model the foundation of a 5MW offshore wind turbine. It can be observed that different approaches has been used by researchers for dynamic modelling of flexible multi-body wind turbine and its foundation ranging from simple lumped mass models to sophisticated finite element models. The level of details and accuracy of the models vary based on the intended purpose and its selection should be made based on engineering judgement.

2.3 Pitch control of wind turbine blades

Most commercial wind turbines use proportional-integral (PI) collective blade-pitch control to regulate rotor speed in the above-rated wind speed regime. A major drawback of this type of controller is that it assumes that the blades have identical structural properties and are subject to similar aerodynamic loads which is seldom the case. Also, these controllers are designed to regulate the rotor speed and are not designed for structural vibration/load reduction. However, it is well known that blade pitch control is capable of reducing structural loads on the wind turbines. This opens up the possibility of designing controllers that use existing actuators and sensors like the blade pitch actuators to reduce structural loads/vibrations while maintaining the required rotor speed. Recently, researchers have proposed a number of pitch control strategies for structural load reduction in blades/rotor (Stol, Zhao, and Wright, 2006; Zhao and Stol, 2007), tower (Kristalny, Madjidian, and Knudsen, 2013; Nam, Kien, and La, 2013) and drive-train (De Battista, Mantz, and Christiansen, 2000; Fleming, Wingerden, and Wright, 2012). Structural load mitigation in wind turbines has become an important aspect of its design. The main focus has been on the reduction of 1P (once per revolution) loads using Individual Pitch Controllers (IPCs) that contribute mainly to the fatigue loads of the components.

Some of the earliest works on individual pitch control was presented by Bossanyi, 2003, 2005. The idea was to reduce the 1P aerodynamic loads by active pitch control. The results showed that there is an emmense pontential in load reduction that can be acheived from intelligent control algorithms. The developed individual pitch control strategies were further verified by field experiments in (Bossanyi, Fleming, and Wright, 2013). Since then, numerous individual pitch control strategies have been proposed by researchers with different control objectives. A discussion on various pitch control strategies from basic PID (proportional-derivative-integral) controllers to complex multivariable controllers like H_∞, neural network, adaptive control etc., has been presented by Mughal and Guojie, 2015. The study also focused on variable-speed-variable-pitch-control, an emerging trend in wind turbine technology and concluded that control of this nature is complex due to the highly non-linear nature of the wind turbine. An innovative ℓ_1-control scheme using two decoupled linear time-invariant models derived using Colemen Transformation to design individual and collective pitch controllers independently was proposed by Schuler et al., 2013. The individual pitch controller was designed to reduce blade root bending moments and the collective pitch controller was designed to maintain rated rotor speed. The authors reported significant load reduction without loss in energy production for onshore wind turbines. A quite similar work was presented by Jafarnejadsani and Pieper, 2015 where a gain scheduled ℓ_1-optimal control strategy for variable-speed-variable-pitch wind turbines was proposed. The controller was developed using linear models of the wind turbine at different operating points using genetic algorithm optimization. The controller was coupled to the wind turbine simulator FAST (Jonkman and Buhl Jr, 2005) and compared against a well tuned PI (proportional-integral) controller. The authors reported improved power quality and decrease in generator torque and rotor speed fluctuations.

A disturbance accommodating controller (DAC) was proposed by Cheon, Kwon, and Choi, 2014 with the aim to extend fatigue life by reducing mechanical loads on the wind turbine while maintaining the rated rotor speed. FAST (Jonkman and Buhl Jr, 2005) was used as the simulation tool and the wind turbine was subjected to stochastic wind loads. The controller was shown to perform better than the conventional collective or individual pitch controller.

Model Predictive Control has gain popularity since 1980's in industrial application and the same has been proposed for wind turbine control. LIDAR measurements can provide information about wind at various distances in-front of the wind turbine. This information was used to design a nonlinear model predictive controller by Schlipf, Schlipf, and Kühn, 2013. The controller was compared against the baseline controller and was shown to reduce extreme gust loads by 50% and lifetime fatigue loads by 30%. A nonlinear model predictive controller for floating offshore wind turbines has been proposed by Raach et al., 2014.

Petrović, Jelavić, and Baotić, 2015 discussed the development of a control algorithm to mitigate higher order dynamics arising from rotor asymmetries. The paper showed that rotor asymmetries introduce additional oscillations of both structural loads and rotor speed and standard control algorithms for reduction of structural loads cannot reduce them. The existing control algorithm for reduction of structural loads was augmented to enable reduction of structural loads caused by rotor asymmetries.

Gao and Gao, 2016 developed an optimal PI controller by optimizing the tuning parameters using a direct search optimization algorithm. The authors investigated the effect of time delay caused by the hydraulic pressure units and reported that the proposed controller had desired performance against time delays without any need of prior information about the induced delay. Ren et al., 2016 proposed a non-linear PI controller that eliminated the need of switching the controller gains in a gain scheduled PI controller. Hence, it requires only one set of PI parameters for entire operational region. Simulations showed that the proposed non-linear PI controller is better than the conventional and gain scheduled PI controllers in regulating constant power and reducing drive-train stresses.

Adaptive control was developed by Yuan and Tang, 2017 with disturbance rejection and load mitigation capabilities for onshore wind turbines. It was shown that the adaptive controller was better in load mitigation than the baseline controller employed by FAST (Jonkman and Buhl Jr, 2005) but, at a cost of degradation in power regulation. Further, it was also shown that the GSPI (gain scheduled PI) was sensitive to model uncertainties while the adaptive controller was capable of dealing with uncertainties. A fault tolerant controller (FTC) was proposed by Lan, Patton, and Zhu, 2018, that included a adaptive sliding mode observer and a baseline PI controller to estimate parametric pitch actuator faults. It was shown that the proposed FTC is able to maintain stability of wind turbines in the presence of actuator faults. The objective of the controller was to recover nominal baseline PI controller performance under actuator faults. The controller was not developed to reduce structural loads. A wavelet-LQR based individual blade pitch controller was proposed by Fitzgerald, Staino, and Basu, 2019 capable of reducing aerodynamic loads on onshore wind turbines. But again, allowing for degradation in energy production.

Namik and Stol, 2010; Namik and Stol, 2011 proposed an individual pitch State Feeback Controller (SFC) and Disturbance Accomodating Controller (DAC) for floating offshore wind turbines. In Namik and Stol, 2014 the authors demonstrated the performance of the above two controllers on a spar-buoy floating wind turbine. The authors showed that while both controllers are capable of improving power regulation, the DAC has a detrimental effect on the platform motion. The SFC was inferior compared to the DAC in power regulation, but, the platform rolling and pitching rate was similar to that of the baseline controller. The authors recommended the use of the SFC since the platform motion was not amplified. To summarize, the controllers were not capable of improving power regulation and reducing platform motion simultaneously.

The above review summaries some of the key individual pitch controllers proposed in literature that utilize innovative technology and/or complex control algorithms to optimize performance of wind turbines. The review shows that there is a wide range of published work on individual blade pitch control which proves that there is considerable interest in improving the available control strategies. The interest stems from the fact that the current state-of-the-art pitch controller are far from being optimal and there is scope of enhancement that can improve power production and simultaneously reduce aerodynamic loads on the turbines. Amongst the different controller proposed in literature perhaps the most relevant ones for this thesis are presented by Namik and Stol, 2014 and Raach et al., 2014. Namik and Stol, 2014 reported 9% reduction in tower fatigue DELs over the baseline controller. A massive 64% reduction in power error has also been reported. And, Raach et al., 2014 proposed an IPC based on a non-linear model predictive control strategy. The proposed controller was compared against the baseline controller (Jonkman and Buhl Jr, 2005). They have reported around 18% reduction in blade out-of-plane fatigue DELs and an impressive 77.6% reduction in generated power error. The aim of this thesis is to developed IPCs that outperform these state-of-the-art controllers.

2.4 Structural control of wind turbines

Along with pitch control of wind turbines, structural control of wind turbines using external dampers has been another key area of research in the last two decades. Wind turbine components, the blades and the tower are in general slender, hence, they undergo large vibrations when sujected to a turbulent wind field. Mitigating these excessive vibrations is critical for the safe operation of the turbines. In that regard, external dampers can be designed to dissipate some of the energy from the primary structure (blades and tower). Various external passive, semi-active and active dampers have been proposed in literature and some of them are reviewed here in brief. Tuned mass damper (TMD) was first proposed by Murtagh et al. (2008) for passive vibration control of wind turbine tower. They were amongst the first to consider blade-tower interaction of a rotating 3-bladed wind turbine. While rotationally sampled wind turbulence was considered in this paper the assumption of only drag forces acting on the blades was a drawback of this initial investigation. Multiple TMDs were used by Dinh and Basu (2015) to mitigate vibrations of off-shore wind turbines. The authors investigated the use of single and multiple TMDs at various levels along the spar to mitigate edgewise vibrations of the tower/nacelle. Developing this concept further, Arrigan et al. (2011) proposed an semi-active version of the TMD for flapwise vibration control of wind turbine blades. A variable stiffness TMD was tuned using Short Time Fourier Transformation (STFT) based algorithm to track the natural frequency of the blades-tower system to mitigate its flapwise vibrations. Huang et al. (2010) used similar device with STFT algorithm for edgewise vibration control of floating wind turbine blades. Colwell and Basu (2009) used passive Tuned Liquid Column Damper (TLCD) for vibration control of offshore horizontal axis wind turbine (HAWT) tower.

The authors were the first to use TLCD to mitigate tower vibrations of offshore wind turbines. A probabilistic model of joint wind-wave loads was considered in this study that correlates the sea states with wind parameters. The performance of the TLCDs under moderate and strong wind and wave loads was investigated. Buckley et al. (2017) also used TLCD for structural vibration control considering the effects of soil-structure interaction. Equivalent linearisation was used to optimize the parameters of TLCD, to minimize the variance of the along-wind response of tower. Passive and active vibration control of offshore wind turbines were investigated by Lackner and Rotea (2011a,b). The authors modified FAST (Jonkman and Buhl Jr, 2005) that incorporated two independent TMDs to offer more efficient structural control. Their study demonstrated improvement in structural response of barge and monopile supported wind turbines coupled with optimally tuned passive TMDs. Lackner and Rotea (2011b) also compared the performance of active TMDs against optimal passive TMDs in fore-aft fatigue load reduction. Their active controllers based on H_∞ control strategy showed improved fatigue load reduction over passive TMDs at the expense of active power and larger TMD strokes. Chen and Georgakis (2013) experimentally demonstrated the use of rolling-ball dampers for vibration control of wind turbine tower. Stewart and Lackner (2014) studied the impact of passive TMDs on offshore wind turbines subjected to wind-wave misalignment. The misalignment can cause large loads on the tower in its side-to-side direction. Optimally tuned passive TMDs in their proposal were capable of reducing tower fore-aft and side-side fatigue loads by approximately 5% and 40%, respectively. Semi-active TMDs were used by Dinh, Basu, and Nagarajaiah (2016) for edgewise vibration control of blade, tower and spar of a spar type floating wind turbines. They also used STFT based semi-active algorithm to tune the TMDs to the natural frequencies of the blades/tower in real time. Their algorithm showed improved performance compared to passive TMD when damage was simulated by a reduction in stiffness. Caterino (2015) and Caterino and Spizzuoco (2017) proposed a combination of spring and MR dampers at the base of the tower to reduce bending stress. Their strategy allowed a controlled increase in tower deflection to release/reduce bending stress at the base of the tower. The trade-off between the tower deflection and base moment was optimized without affecting the generator performance. Brodersen, Bjørke, and Høgsberg (2017) designed an active TMD for mitigation of fore-aft vibrations of a fixed bottom offshore wind turbine. The paper presented optimal damping and tuning relations for a tower coupled with an ATMD at the top. Sarkar and Chakraborty (2018, 2019) used semi-active MR-TLCD for along wind vibration control of wind turbine tower. A clipped optimal control strategy based on Linear Quadratic Regulator (LQR) was adopted in this study to control the damping of the MR-fluid.

It produced the semi-active control force designed to mitigate the fore-aft vibration of the tower. Semi-active TMD was developed by Sun (2018) to reduce the nacelle/tower vibration of a damaged tower under combined wind and wave loads. Their semi-active control algorithm was based on STFT to track the natural frequency of the tower considering soil-effects and damage. Simulations in this study showed better performance compared to passive TMDs when the natural frequency was altered due to damage or soil-structure interaction. Bi-directional vibration control of offshore wind turbine tower using a 3D pendulum tuned mass damper was proposed by Sun and Jahangiri (2018). They showed that the performance of tuned 3D pendulum mass damper could offer better performance compared to multiple two linear TMDs. Performance of TMD during installation of a single blade was investigated by Jiang (Jiang, 2018). Relative motion between the blade root (i.e. nacelle) and the foundation due to wind and wave loads was reduced by the external TMDs at the tower top. Active TMDs were used by Fitzgerald, Sarkar, and Staino (2018) to improve the reliability of onshore wind turbine towers. They demonstrated that the probability of the tower top displacement exceeding a threshold displacement was reduced by the installation of active TMDs, thus improving the reliability of the tower.

Besides vibration control of tower, control of blade vibration was also studied by many researchers. Active Tuned Mass Dampers (ATMDs) were used by Fitzgerald, Basu, and Nielsen (2013) to mitigate the in-plane vibration of rotating wind turbine blades exposed to turbulent wind. An innovative proposal in the form of cable connected active tuned mass dampers were used by Fitzgerald and Basu (2014) for in-plane vibration control of blades which showed promising results. Staino, Basu, and Nielsen (2012) and Tao, Basu, and Li (2018) used active tendons in the blades to control edgewise vibrations. In these studies, active tendons were installed inside the blades using a truss structure. The forces in the tendons were tuned using linear control law in real time to compensate the effects of aerodynamic loads. Semi-active control of edgewise vibration of wind turbine blades under extreme conditions by MR dampers was proposed by Chen et al. (2015). Their control strategy was based on fuzzy algorithm and proved to be efficient even when the wind changed its direction. Zhang et al. (2014) investigated the use of roller dampers in vibration mitigation of wind turbine blades. The parameters of the roller dampers were optimized first using a decoupled reduced order model and then coupled with the aeroelastic model of the wind turbine where the controller offered promising capabilities. Non-linear tuned liquid dampers (TLDs) were used by Zhang et al. (2015) for edgewise blade vibration control. The high centrifugal acceleration at the tip of the blade enabled the use of TLD with relatively small fluid mass. Two models (i.e. one sloshing mode and three sloshing modes) were studied using numerical simulation. The TLCD is optimized based on the one-mode model, which has been shown to effectively improve the dynamic response of wind turbine blades. Staino and Basu (2015) discussed the simultaneous use of active tendon and pitch control for turbine blades. Circular Liquid Column Dampers (CLCDs) were developed by Basu, Zhang, and Nielsen (2016) to mitigate edgewise vibration of the blades. It is a variant of the regular TLCD attached to the blades to achieve optimal reduction. Similar to TLDs, the CLCDs also utilized the centrifugal acceleration at the tip of the blades to counteract the gravitational force. A state-of-the-art review was presented by Njiri and Söffker (2016) which discussed various methods used for vibration control of wind turbine in the recent past. The paper reviewed various methods ranging from classical Proportional-Integral (PI) independent blade pitch controller (IPC) to robust H_2, H_∞ and model predictive control used for structural load reduction in high wind speed regions and power optimization in low wind speed region. The paper also discussed the need for control strategies to fulfill multiple objectives for power optimization and structural load reduction. Controllable deformable trailing edge flap (DTEF) were used by Zhang, Yang, and Xu (2017) for fatigue load reduction of turbine blades. This smart rotor control approach was used to turn the in-phase fluid-blade interaction into an anti-phase one at the 1P rotational frequency mode. In comparison to collective blade pitch control approaches, this method helped to reduced fatigue loads up to 30%. A new electromagnetic torsional damper was proposed by Chen et al. (2018) to enhance flutter stability of wind turbine blades. It was shown that the use of the torsional damper could increase the flutter critical rotational speed by more than 100%.

Fatigue analysis of wind turbine is critical as these machines are subjected to constant vibrations (Sutherland, 1999) and hence it is important to verify if they fulfil their design life. Fatigue life estimates for wind turbine components were investigated in (Berglind and Wisniewski, 2014; Berglind, Wisniewski, and Soltani, 2015; Kong et al., 2006; Lee et al., 2012; Ragan and Manuel, 2007). Ragan and Manuel (2007) compared rainflow cycle-counting technique with spectral techniques such as Dirlik's method to estimate wind turbine fatigue loads. Camblong et al. (2012) designed a discrete Linear Quadratic Gaussian (LQG) controller reduce the drive-train fatigue loads of a wind turbine. The most recognized approaches to estimate the damage caused by fatigue are discussed and compared by Berglind and Wisniewski (2014), with a special focus on their applicability for wind turbine control. Berglind, Wisniewski, and Soltani (2015) addresses an on-line fatigue estimation method based on hysteresis operators, and propose a model predictive control (MPC) strategy that incorporates the online fatigue estimation through the objective function with the ultimate goal to reduce the fatigue load of the wind turbine. Effect of atmospheric and wake turbulence on fatigue loads of wind turbines was studied by Lee et al. (2012). Fatigue damage of composite wind turbine blades was studied by (Kong, Bang, and Sugiyama, 2005; Marin et al., 2009; Shokrieh and Rafiee, 2006).

Chapter 3

Flexible Multibody Dynamics of Floating Offshore Wind Turbines

Modern day wind turbines are a combination of large number of flexible and rigid components which undergo large deformations. The various parts of the wind turbine come together to extract mechanical energy from the incoming wind. The blades of a multi-mega watt wind turbine are mounted on the hub which is at the tip of the low speed shaft. The shaft is often tilted up and the blades are conned to avoid tower strike during operation. The conversion of mechanical torque to electrical power has quite a few stages and involves many components. Modelling such a wind turbine requires a detailed multi-body approach. This extension consists primarily of provisions made to accommodate the fact that reference frames play a central role in connection with many of the vectors of interest in dynamics of the wind turbine. Every component of the wind turbine is thus required to be defined in its own coordinate system. The inclusion of multiple coordinate systems to model various components of the system makes the use of classical methods (like energy methods) in derivation of equations of motion difficult to implement. A vector approach is hence required to replace the classical scalar approaches. Kane's method, which emerged recently, reduces the labour needed to derive equations of motion and leads to equations that are simpler and more readily solved by computer. In this study, Kane's method is used to derive the dynamic equations of a flexible wind turbine. Throughout the study bold upper case alphabets are used for matrices and bold lower case alphabets are used for vectors.

3.1 Assumptions

Flexible multi-body dynamics has been used to model the floating offshore wind turbine. The various components of importance are the tower, the nacelle, the generator, the gear box, the low speed shaft, the hub and the blades. The tower, the blades and

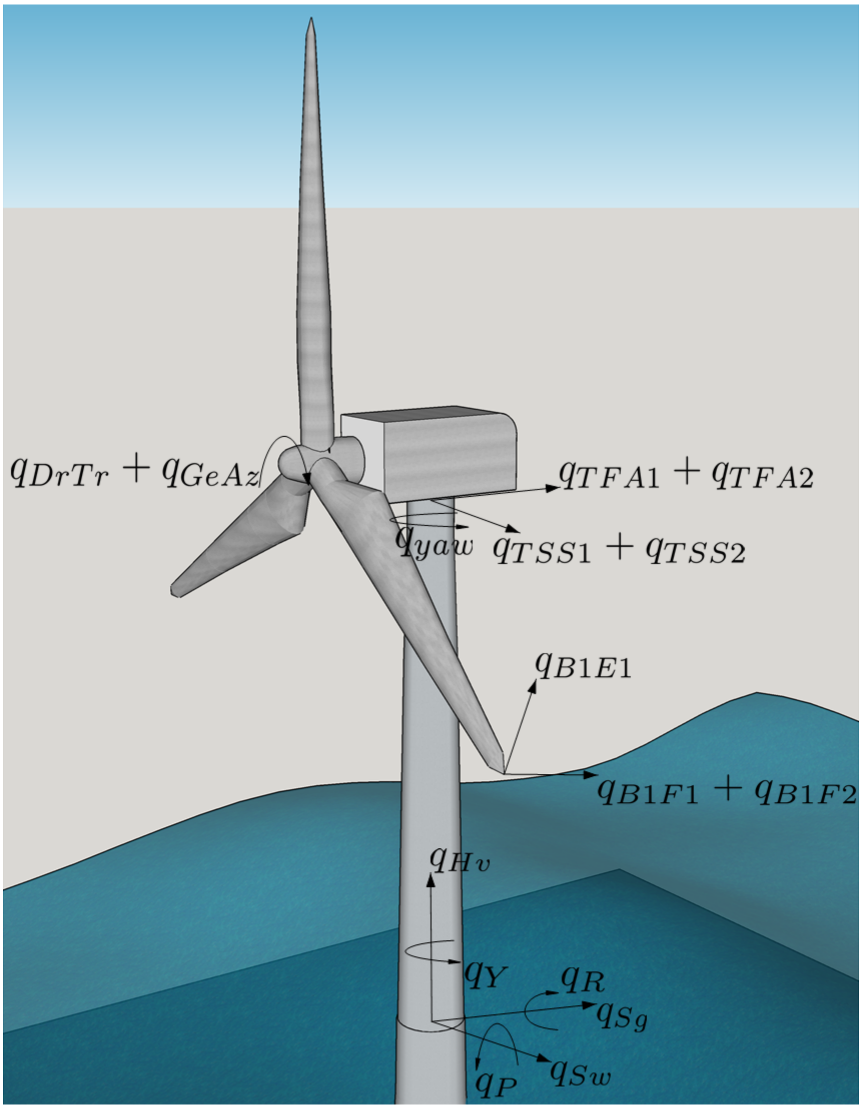

Figure 3.1: Schematic diagram of the degrees of freedom

the low speed shaft are the flexible components of the wind turbine. Modal analysis is often used to study the dynamics of flexible members. To model the tower the first two modes in fore-aft and side-to-side directions are used. For the blades the first modes in flapwise and the first mode in the edgewise direction is used. It is assumed that since these members are highly flexible and hence the first few modes will capture the dynamics with sufficient accuracy. The platform is assumed to be rigid is free to undergo large rigid body motion about the three axes. Degrees of freedom that define the motion of a full scale wind turbine are the platform motion, tower displacements, the nacelle yaw, the torsional bending of the low speed shaft, the generator azimuth angle and the elastic deformations of the three blades. The degrees of freedom used for the 3-bladed wind turbine can be written as

$$\mathbf{q} = \{q_{Sg} \quad q_{Sw} \quad q_{Hv} \quad q_{R} \quad q_{P} \quad q_{Y} \quad q_{TFA1} \quad q_{TSS1} \quad q_{TFA2} \quad q_{TSS2} \quad q_{yaw} \quad q_{GeAz} \quad q_{DrTr} \quad q_{B1F1} \quad q_{B1E1} \quad q_{B1F2} \quad q_{B2F1} \quad q_{B2E1} \quad q_{B2F2} \quad q_{B3F1} \quad q_{B3E1} \quad q_{B3F2}\}^T \tag{3.1}$$

A schematic diagram showing the degrees of freedom is provided in Figure 3.1. It is important to note here that the figure shows the degrees of freedom in an approximate manner in a global coordinate system whereas, in the detailed modelling of the wind turbine every degree of freedom is described in its local coordinate system. A 22 degrees of freedom model is derived to model the floating wind turbine. The degrees of freedom are also denoted by numbers 1 to 22 in the same sequence as presented in equation 3.1. Throughout the study the name of the DOF and its corresponding number will be used alternatively. Kinematic description of the system involves assigning coordinate systems to each component and describing its motion in the the global reference frame. In the following sections, the co-ordinate systems required for the wind turbine will be defined, followed by the kinematics of the system and finally the kinetics of the system which will also see the derivations of the equations of motion. The basic description of the kinematic and kinetics are provided in the following sections while the details are provided in Appendix A.

3.2 Coordinate Systems

As mentioned earlier different components of the wind turbine are modelled in their local reference frames. Transformation relations are to be established which relates a coordinate system to another. A combination of small angle approximation (small angle rotation) and euler angles (euler rotation) are used to link the coordinate systems. Three consecutive rotations θ_1, θ_2 and θ_3 about three mutually orthogonal axes $(\hat{\boldsymbol{X}}_{\mathbf{1}}, \hat{\boldsymbol{X}}_{\mathbf{2}}, \hat{\boldsymbol{X}}_{\mathbf{3}})$ results in a set of orthogonal axes $(\hat{\boldsymbol{x}}_{\mathbf{1}}, \hat{\boldsymbol{x}}_{\mathbf{2}}, \hat{\boldsymbol{x}}_{\mathbf{3}})$. This transformation with small angle approximation can be defined as

$$\begin{pmatrix} \hat{\boldsymbol{x}}_{\mathbf{1}} \\ \hat{\boldsymbol{x}}_{\mathbf{2}} \\ \hat{\boldsymbol{x}}_{\mathbf{3}} \end{pmatrix} \approx \underbrace{\begin{bmatrix} 1 & \theta_3 & -\theta_2 \\ -\theta_3 & 1 & \theta_1 \\ \theta_2 & -\theta_1 & 1 \end{bmatrix}}_{\boldsymbol{T}} \begin{pmatrix} \hat{\boldsymbol{X}}_{\mathbf{1}} \\ \hat{\boldsymbol{X}}_{\mathbf{2}} \\ \hat{\boldsymbol{X}}_{\mathbf{3}} \end{pmatrix} \tag{3.2}$$

The small angle approximation makes the transformation independent of the sequence of rotation. Here, the approximation sign is used since the transformation matrix $\boldsymbol{T}$ is not orthonormal and hence the resulting set of axes are not orthogonal to each other.

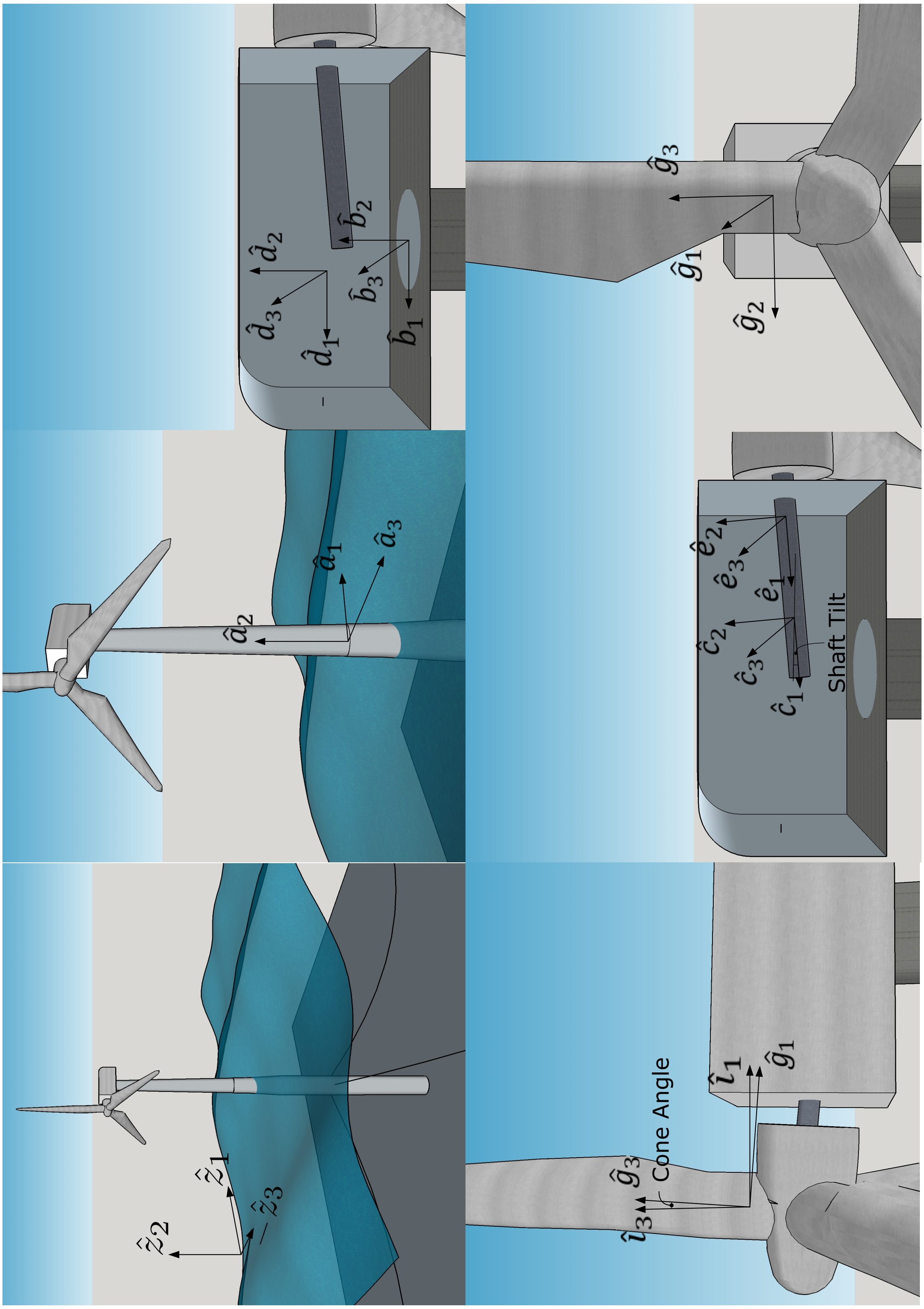

Figure 3.2: Spar-type floating offshore wind turbine and coordinate systems

The nearest orthonormal matrix can be obtained from Singular Value Decomposition (SVD) of $\boldsymbol{T}$. The nearest orthonormal matrix in Frobenius norm sense $\boldsymbol{T_O}$ is given as

$$\boldsymbol{T_O} = \boldsymbol{U}\boldsymbol{V}' \tag{3.3}$$

where, the columns of $\boldsymbol{U}$ contains the eigenvectors of $\boldsymbol{T}\boldsymbol{T}'$ and the columns of $\boldsymbol{V}$ contains eigenvectors of $\boldsymbol{T}'\boldsymbol{T}$. This follows from the result of SVD of $\boldsymbol{T}$ obtained as

$$\boldsymbol{T} = \boldsymbol{U}\boldsymbol{\Sigma}\boldsymbol{V}' \tag{3.4}$$

where, $\boldsymbol{\Sigma}$ is a diagonal matrix containing the singular values of $\boldsymbol{T}$. $\boldsymbol{\Sigma}$ can be obtained as

$$\boldsymbol{\Sigma} = \sqrt{\text{eigenvalues of } \boldsymbol{T}\boldsymbol{T}'} = \sqrt{\text{eigenvalues of } \boldsymbol{T}'\boldsymbol{T}} \tag{3.5}$$

The matrix $\boldsymbol{T_O}$ will be used to define transformations where small angle approximation is employed. The different coordinate system used are defined as follows. The different coordinate systems used in this thesis are shown in Figure 3.2 and their corresponding transformation relations are provided in Appendix A.

3.3 Kinematics

This section describes the kinematics of the wind turbine. The includes describing the position, velocity and acceleration of the each flexible and rigid component of the wind turbine. For that purpose the important points that describe the motion are as follows: Z (tower-base), Y (platform center of gravity), T (tower node), O (tower-top/base-plate/yaw bearing mass center), U (nacelle center of mass), Q (apex of conning angle), C (hub center of mass), S1 (blade nodes for blade 1), S2 (blade nodes for blade 2) and S3 (blade nodes for blade 3). The various reference frames are denoted as follows: E (earth/inertial), X (tower base), F (tower body element), B (tower-top/base-plate), N (nacelle), L (low speed shaft on rotor end), M1 (blade 1 element body), M2 (blade 2 element body), M3 (blade 3 element body) and G (high speed shaft/generator).

Two important relations provided next are used in this section to obtain the velocity and accelerations of the important points on the wind turbines.

Two points fixed on a rigid body

If P and Q are two points fixed on a rigid body B having an angular velocity ${}^{\boldsymbol{A}}\boldsymbol{\omega}^{\boldsymbol{B}}$ in A, then the velocity of Q in A, ${}^{\boldsymbol{A}}\boldsymbol{v}^{\boldsymbol{Q}}$, can be obtained from the velocity of P in A, ${}^{\boldsymbol{A}}\boldsymbol{v}^{\boldsymbol{P}}$, and the position vector of Q to P, $\boldsymbol{r}$, can be obtained as

$$ {}^{\boldsymbol{A}}\boldsymbol{v}^{\boldsymbol{P}} = {}^{\boldsymbol{A}}\boldsymbol{v}^{\boldsymbol{Q}} + {}^{\boldsymbol{A}}\boldsymbol{\omega}^{\boldsymbol{B}} \times \boldsymbol{r} \tag{3.6} $$

The acceleration of the point Q in A can be obtained as

$$ {}^{\boldsymbol{A}}\boldsymbol{a}^{\boldsymbol{P}} = {}^{\boldsymbol{A}}\boldsymbol{a}^{\boldsymbol{Q}} + {}^{\boldsymbol{A}}\boldsymbol{\omega}^{\boldsymbol{B}} \times ({}^{\boldsymbol{A}}\boldsymbol{\omega}^{\boldsymbol{B}} \times r) + {}^{\boldsymbol{A}}\boldsymbol{\alpha}^{\boldsymbol{B}} \times \boldsymbol{r} \tag{3.7} $$

where ${}^{\boldsymbol{A}}\boldsymbol{\alpha}^{\boldsymbol{B}}$ is the angular acceleration of B in A.

One point moving on a rigid body

If a point P is moving on a rigid body B while B is moving in a reference frame A, the velocity ${}^{\boldsymbol{A}}\boldsymbol{v}^{\boldsymbol{P}}$ of P in A can be obtained as

$$ {}^{\boldsymbol{A}}\boldsymbol{v}^{\boldsymbol{P}} = {}^{\boldsymbol{A}}\boldsymbol{v}^{\bar{\boldsymbol{B}}} + {}^{\boldsymbol{B}}\boldsymbol{v}^{\boldsymbol{P}} \tag{3.8} $$

where ${}^{\boldsymbol{A}}\boldsymbol{v}^{\bar{\boldsymbol{B}}}$ is the velocity in A of the point $\bar{B}$ of B that coincides with P at the instant under consideration. The acceleration of the point P in A can be obtained as

$$ {}^{\boldsymbol{A}}\boldsymbol{a}^{\boldsymbol{P}} = {}^{\boldsymbol{A}}\boldsymbol{a}^{\bar{\boldsymbol{B}}} + {}^{\boldsymbol{B}}\boldsymbol{a}^{\boldsymbol{P}} + 2{}^{\boldsymbol{A}}\boldsymbol{\omega}^{\boldsymbol{B}} \times {}^{\boldsymbol{B}}\boldsymbol{v}^{\boldsymbol{P}} \tag{3.9} $$

where, ${}^{\boldsymbol{A}}\boldsymbol{a}^{\bar{\boldsymbol{B}}}$ is the acceleration of $\bar{B}$ in A, ${}^{\boldsymbol{B}}\boldsymbol{a}^{\boldsymbol{P}}$ is the acceleration of P in B and ${}^{\boldsymbol{A}}\boldsymbol{\omega}^{\boldsymbol{B}}$ is the angular velocity of B in A. The last term $2{}^{\boldsymbol{A}}\boldsymbol{\omega}^{\boldsymbol{B}} \times {}^{\boldsymbol{B}}\boldsymbol{v}^{\boldsymbol{P}}$ is referred as the *Coriolis acceleration.*

Using these relations the position, velocity and acceleration vectors of every important point on the wind turbine is described, the partial linear velocities, the partial angular velocities and the partial linear and angular accelerations are estimated as per (Kane and Levinson, 1985). The details of these quantities are provided in Appendix A.

3.4 Kinetics

In this section the equations of motion of a 3-bladed floating offshore wind turbine will be derived. By a direct result of Newton's laws of motion, Kane's equations of motion for a simple holonomic system with 22 DOFs can be stated as follows (Kane and Levinson, 1985)

$$F_r + F_r^* = 0 \quad \text{for } r = 1 \text{ to } 22 \tag{3.10}$$

Where, F_r and F_r^* are the generalized active ad inertia forces respectively. In a set of n rigid bodies characterized by reference frame N_i and center of mass point X_i the generalized active and inertial forces are given as

$$\begin{aligned} F_r &= \sum_{i=1}^{n} {}^{\boldsymbol{E}}\boldsymbol{v}_{\boldsymbol{r}}^{\boldsymbol{X_i}} \cdot \boldsymbol{F^i} + {}^{\boldsymbol{E}}\boldsymbol{\omega}_{\boldsymbol{r}}^{\boldsymbol{N_i}} \cdot \boldsymbol{M^{N_i}} \quad \text{for } r = 1 \text{ to } 22 \\ F_r^* &= -\sum_{i=1}^{n} {}^{\boldsymbol{E}}\boldsymbol{v}_{\boldsymbol{r}}^{\boldsymbol{X_i}} \cdot \left(m^{N_i} {}^{\boldsymbol{E}}\boldsymbol{a}^{\boldsymbol{X_i}} \right) - {}^{\boldsymbol{E}}\boldsymbol{\omega}_{\boldsymbol{r}}^{\boldsymbol{N_i}} \cdot {}^{\boldsymbol{E}}\dot{\boldsymbol{H}}^{\boldsymbol{N_i}} \quad \text{for } r = 1 \text{ to } 22 \end{aligned} \tag{3.11}$$

where it is assumed that for each rigid body N_i, the active forces are applied at the center of mass point X_i. The time derivative of the angular momentum of rigid body N_i about its center of mass X_i in the inertial frame can be found as (Kane and Levinson, 1985)

$${}^{\boldsymbol{E}}\dot{\boldsymbol{H}}^{\boldsymbol{N_i}} = \bar{\bar{\boldsymbol{I}}}^{\boldsymbol{N_i}} \cdot {}^{\boldsymbol{E}}\boldsymbol{\alpha}^{\boldsymbol{N_i}} + {}^{\boldsymbol{E}}\boldsymbol{\omega}^{\boldsymbol{N_i}} \times \bar{\bar{\boldsymbol{I}}}^{\boldsymbol{N_i}} \cdot {}^{\boldsymbol{E}}\boldsymbol{\omega}^{\boldsymbol{N_i}} \tag{3.12}$$

For the wind turbine model the mass of the tower, yaw bearing, nacelle, hub, blades, generator contribute to the total generalized inertia forces as follows

$$F_r^* = F_r^*\Big|_X + F_r^*\Big|_T + F_r^*\Big|_N + F_r^*\Big|_H + F_r^*\Big|_{B1} + F_r^*\Big|_{B2} + F_r^*\Big|_{B3} + F_r^*\Big|_G \tag{3.13}$$

Generalized active forces are the forces applied directly on the wind turbine system, forces that ensure constraint relationships between the various rigid bodies and internal forces within flexible members. Forces applied directly on the wind turbine system include aerodynamic forces acting on the blades and tower; gravitational forces acting on the tower, yaw bearing, nacelle, hub, blades; generator torque, high speed shaft brake. Here it must be noted that gear box friction forces are neglected. Yaw springs and damper contribute to forces that enforce constraint relationship between rigid bodies. Internal forces within flexible members include elasticity and damping in tower, blades and drive-train. Thus generalized active forces can be given as

$$
\begin{aligned}
F_r = {} & F_r\Big|_{HydroX} + F_r\Big|_{AeroT} + F_r\Big|_{AeroB1} + F_r\Big|_{AeroB2} + F_r\Big|_{AeroB3} + F_r\Big|_{GravX} + F_r\Big|_{GravT} \\
& + F_r\Big|_{GravN} + F_r\Big|_{GravH} + F_r\Big|_{GravB1} + F_r\Big|_{GravB2} + F_r\Big|_{GravB3} + F_r\Big|_{YawSprng} \\
& + F_r\Big|_{YawDamp} + F_r\Big|_{Gen} + F_r\Big|_{Brake} + F_r\Big|_{ElasticT} + F_r\Big|_{ElasticB1} + F_r\Big|_{ElasticB2} \\
& + F_r\Big|_{ElasticB3} + F_r\Big|_{DampT} + F_r\Big|_{DampB1} + F_r\Big|_{DampB2} + F_r\Big|_{DampB3} + F_r\Big|_{ElasticDrive} \\
& + F_r\Big|_{DampDrive}
\end{aligned}
\tag{3.14}
$$

Kane's equations of motion can be written in matrix form as

$$
\mathbf{M}(\mathbf{q},t)\ddot{\mathbf{q}} + \mathbf{f}(\dot{\mathbf{q}},\mathbf{q},t) = 0 \Rightarrow \mathbf{M}(\mathbf{q},t)\ddot{\mathbf{q}} = -\mathbf{f}(\dot{\mathbf{q}},\mathbf{q},t) \tag{3.15}
$$

The above equation can be readily solved by a computer using any numerical time integration scheme. This study recommends the use of Runga-Kutta 4th order method or the Adams-Bashforth-Moulton 4-th order predictor-corrector method. The kinetic description of each individual component is provided in Appendix A.

3.5 Dynamic loads

The sources of dynamic loads on a floating offshore wind turbine are aerodynamic and hydrodynamic loads. Aerodynamic loads are the largest source of dynamic load on a FOWT, however, due to the large dimension of the floating spar it also attracts significant hydrodynamic loads. In this thesis, the aerodynamic loads are estimated using the classical Blade Element Momentum (BEM) method solved with a new approach. The hydrodynamic loads are estimated using Morison's equations which sufficiently accurate for rigid structures which undergo small motion (compared to the wavelength). The two theories are briefly described in the following.

3.5.1 Aerodynamic loads

Aerodynamic loads on the wind turbine are estimated using steady Blade Element Momentum (BEM) theory. 3D wind fields are generated using the TurbSim (Jonkman, 2009) package distributed by National Renewable Energy Laboratory (NREL), USA. The wind fields generated by the TurbSim account for vertical and horizontal wind shear and spatial coherence of the turbulent wind field. The package can be used to generate complete wind field with varying turbulence intensity levels, power-law coefficients for wind shear and the characteristic wind speeds. In this thesis, the spectral model and coherence model presented in IEC 61400-1 3$^{\text{rd}}$ ed. (Commission et al., 2005) are used as inputs in TurbSim to generate the turbulent wind fields. The IEC Kaimal spectrum is used for the three wind speed components (u, v and w).

$$S_k(f) = \frac{4\sigma^2 L_k/u_{hub}}{(1+6fL_k/u_{hub})^{5/3}} \qquad \text{for } k = u, v, w \tag{3.16}$$

This model assumes neutral atmospheric stability (i.e., Richardson Number) and is slightly different from the original spectra defined by Kaimal. In the above equation f is the cyclic frequency, L_k is the integral scale parameter and u_{hub} is the hub height wind speed. The IEC 61400-1 3$^{\text{rd}}$ defines the scale parameter as

$$L_k = \begin{cases} 8.10\Gamma_u & k = u \\ 2.70\Gamma_u & k = v \\ 0.66\Gamma_u & k = w \end{cases} \tag{3.17}$$

where the turbulence scale parameter, Γ_u is

$$\Gamma_u = 0.7 \times \text{minimum}(60\text{m}, HubHt) \tag{3.18}$$

where, $HubHt$ is the height hub from the mean sea level of the wind turbine. The relationship between the standard deviations between the three wind components is given as

$$\begin{aligned} \sigma_v &= 0.8\sigma_u \\ \sigma_w &= 0.5\sigma_u \end{aligned} \tag{3.19}$$

The velocity spectra is assumed to the invariant across the grid, however, small variations will occur due to the spatial coherence model.

The spatial coherence model for the u component of wind speed defined by IEC 61400-1 3$^{\text{rd}}$ ed. is given as

$$Coh_{i,j} = \exp\left[a\sqrt{\left(\frac{fr}{u_{hub}/r}\right) + \left(0.12\frac{r}{L_c}\right)}\right] \tag{3.20}$$

Where, r is the distance between points i and j on the grid. a is the coherence decrement parameter and L_c is the coherence scale parameter. From IEC 61400-1 3$^{\text{rd}}$

ed., the parameters a and L_c are obtained as

$$\begin{aligned} a &= 12 \\ L_c &= 5.67 \times \text{minimum}(60\text{m}, HubHt) \end{aligned} \tag{3.21}$$

The IEC 61400-1 3$^{\text{rd}}$ ed. standard doest not specify the coherence model for the v or w component of the wind speed. Therefore, TurbSim uses the following model for v and w components.

$$Coh_{i,j} = \begin{cases} 1 & i = j \\ 0 & i \neq j \end{cases} \tag{3.22}$$

The steady BEM theory used in this thesis interpolates the wind speed at the blade nodes from the TurbSim generated 3D wind field to estimate aerodynamic loads based on the quasi-static aerodynamic properties (i.e., lift and drag) of the blades. This theory is widely available in the literature (Burton et al., 2011; Hansen, 2015; Moriarty and Hansen, 2005) and hence, it is not described in this thesis. The BEM equations are solved using an approach proposed by (Ning, 2014). The major change introduced by this approach is to solve for the unknown inflow angle instead of solving for the axial and the tangential induction factors. For this purpose, different equations are used in different solution regions (e.g. momentum, empirical or propeller brake region). Furthermore, the empirical region is estimated using Glauert's correction with Buhl's modification. Adjusting different equations for each region circumvents the traditional two-point iterative procedure of solving the BEM equations as described in Ning, 2014. Prandtl's hub and tip loss correction factors are also included to account for the vortices generated by the blade tips and the hub. The model is also capable of accounting for skewed inflow using a correction on the axial induction factor proposed by Pitt and Peters as obtained from (Ning et al., 2015). The solution of the BEM equations at each section gives the elemental lift and drag forces. The elemental out-of-plane force (thrust) and in-plane force (torque) on the blade sections can be estimated from the elemental lift and drag forces. For details on the procedure please refer (Ning et al., 2015).

An overview of the BEM algorithm is presented here. The steps of the algorithm are as follows.

1. Guess and initial value for the local inflow angles.

2. Compute the local angle of attack.

3. Estimate the local lift and drag coefficients.
4. In the rotor plane, compute the normal and tangential force coefficients.
5. Compute the induction factors.
6. Check the error in the residue in the governing equation.
7. Try the next value of inflow angle until the residue approaches zero. MATLAB's `fzero` function, which employs Brent's root finding method is used here to search for the solution.

Steps 1 to 4 are straight forward. In step 5, the induction factors must be calculated. This is typically done by equating the thrust and torque coefficients from the blade element/sectional theory and momentum theory. The local thrust coefficient of an annulus of the rotor from the sectional theory is given as

$$C_T = \left(\frac{1-a}{\sin\phi}\right)^2 c_n \sigma \tag{3.23}$$

where, the normal force coefficient is given as

$$c_n = c_l \cos\phi + c_d \sin\phi \tag{3.24}$$

The local thrust coefficient predicted by the momentum theory (including hub and tip loss) is given as

$$C_T = 4a(1-a)F \tag{3.25}$$

where, F is the hub/tip loss correction. Prandtl's correction is given as

$$\begin{aligned}
f_{tip} &= \frac{B}{2}\left(\frac{R-r}{r|\sin\phi|}\right) \\
F_{tip} &= \frac{2}{\pi}\arccos(\exp(-f_{tip})) \\
f_{hub} &= \frac{B}{2}\left(\frac{r-R_{hub}}{R_{hub}|\sin\phi|}\right) \\
F_{hub} &= \frac{2}{\pi}\arccos(\exp(-f_{hub})) \\
F &= F_{tip}F_{hub}
\end{aligned} \tag{3.26}$$

Equating the two equation 3.23 and equation 3.25 the axial induction factor is obtained as

$$a(\phi) = \frac{\kappa(\phi)}{1 + \kappa(\phi)} \tag{3.27}$$

where, the dimensionless quantity κ is obtained as

$$\kappa(\phi) = \frac{\sigma c_n(\phi)}{4F(\phi)\sin^2\phi} \tag{3.28}$$

Of course, the momentum theory is not valid for the entire range of induction factors. If we consider the maximum value of induction factor for which the momentum theory is valid to be a_u, equation 3.25 is valid for $-1 < \kappa \leq a_u/(1 - a_u)$. For axial induction factors between a_u and 1.0 the thrust coefficient is obtained from Buhl's theory as

$$C_T = \left(\frac{50}{9} - 4F\right)a^2 - \left(\frac{40}{9} - 4F\right)a + \frac{8}{9} \tag{3.29}$$

According to Buhl's derivation the assumed value of $a_u = 0.4$. Similar to the momentum region, the thrust coefficient in 3.23 is equated to equation 3.29 to obtain the axial induction coefficient as

$$a(\phi) = \frac{\gamma_1 - \sqrt{\gamma_2}}{\gamma_3} \tag{3.30}$$

$$\gamma_1 = 2F\kappa - \left(\frac{10}{9} - F\right), \quad \gamma_2 = 2F\kappa - F\left(\frac{4}{3} - F\right), \quad \gamma_3 = 2F\kappa - \left(\frac{25}{9} - 2F\right) \tag{3.31}$$

This form is valid for $0.4 < a < 1.0$. Singularities arise when $\gamma_3 = 0$ or $\kappa = 25/(18F - 1)$. To avoid this singularity a small number (e.q., 1E-5) can be added or subtracted from κ and $a(\phi)$ will remain finite and introduce negligible error.

Finally, for the region where $a \geq 1.0$, the propeller brake region, the thrust coefficient from the momentum theory is obtained from a change of sign as

$$C_T = 4a(a - 1)F \tag{3.32}$$

and the axial induction factor can be obtained obtained by equating the above equation to equation 3.23 as

$$a(\phi) = \frac{\kappa(\phi)}{\kappa(\phi) - 1} \tag{3.33}$$

valid for $\kappa > 1$.

Similarly, the tangential induction factor a' can be obtained by equating the torque coefficient from the sectional theory to the torque coefficient from the momentum theory. After some simplification, the tangential induction factor is obtained as

$$a'(\phi) = \frac{\kappa'(\phi)}{1 - \kappa'(\phi)} \tag{3.34}$$

where,

$$\kappa'(\phi) = \frac{\sigma c_t}{4F \sin\phi \cos\phi} \tag{3.35}$$

and

$$c_t = c_l \sin\phi - c_d \cos\phi \tag{3.36}$$

Once the induction factors are obtained, the variables can be related to each other using the geometric relationship shown in Figure 3.3.

$$\tan\phi = \frac{1 - a}{(1 + a')\lambda_r} \tag{3.37}$$

This equation can be arranged in various ways to obtain a residue function. But as pointed out by (Ning, 2014), it is advantageous to arrange the equation in a way that the terms $(1 - a)$ and $(1 + a')$ appear at the denominator. This way the singularities occur at predefined locations such as at $\phi = 0, \pm\pi$. It is also the location where the regions separate. Therefore an bracketing approach may be adapted where the residue function can be modified to suit the region under consideration. The choice residue function proposed by (Ning, 2014) is given as

$$f(\phi) = \frac{\sin\phi}{1 - a} - \frac{\cos\phi}{\lambda_r(1 + a')} \tag{3.38}$$

The solution of the BEM equations has been be reduced from a two-dimensional fixed-point algorithm to a one dimensional root finding algorithm. The solution algorithm

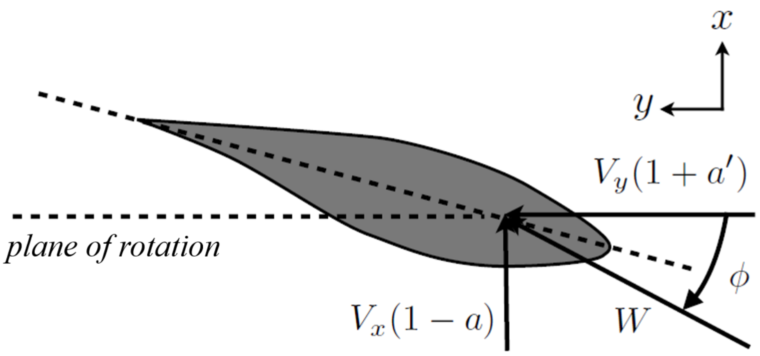

Figure 3.3: Local blade section with velocity and inflow parameters looking towards the root from the tip.

Algorithm 1 Solve for ϕ^* in the BEM equations

function $fzero(f, lb, ub)$
  return x^* where $f(x^*) = 0$ for $lb \leq x \leq ub$ and $f(lb)f(ub) < 0$
function $a(\phi)$
  if $\kappa < 2/3$ **then**
    $a \leftarrow \kappa/(1+\kappa)$
  else if $2/3 < \kappa < 1$ **then**
    $a \leftarrow (\gamma_1 - \sqrt{\gamma_2})/\gamma_3$
  else
    $a \leftarrow \kappa/(\kappa - 1)$
  end if
  return a
end function
function $f(\phi)$
  return $\sin\phi/(1 - a(\phi)) - \cos\phi(1 - \kappa'(\phi))/\lambda_r$
end function
function $f_{PB}(\phi)$
  return $\sin\phi(1 - \kappa(\phi)) - \cos\phi(1 - \kappa'(\phi))/\lambda_r$
end function
function SOLVE INFLOW ANGLE ϕ^*
  $\epsilon \leftarrow 1 \times 10^{-6}$
  if $f(\pi/2) > 0$ **then**
    $\phi^* \leftarrow fzero(f(\phi), \epsilon, pi/2)$
  else if $f_{PB}(-\pi/4) < 0$ and $f_{PB}(\epsilon) > 0$ **then**
    $\phi^* \leftarrow fzero(f_{PB}(\phi), -\pi/4, -\epsilon)$
  else
    $\phi^* \leftarrow fzero(f(\phi), pi/2, \pi)$
  end if
  return $a \leftarrow a(\phi^*)$ and $a' \leftarrow a'(\phi^*)$
end function

of the BEM equation is given in Algorithm 1.

3.5.2 Hydrodynamic loads

Morison's representation is used to estimate hydrodynamic loads on the cylindrical spar of the floating wind turbine. In conjunction with strip theory, Morison's equations can be used to compute linear wave inertia forces and non-linear viscous drag forces. The total load on the platform is then obtained by integrating the elemental forces along the depth of the platform. The forces associated with a strip dz of the platform in surge and sway direction are given as

$$\begin{aligned} \mathrm{d}F_i^P(z,t) = & \underbrace{-C_A\rho\left(\frac{\pi D(z)^2}{4}\right)\ddot{q}_i(z,t)\mathrm{d}z}_{\text{added mass}} + \underbrace{C_M\rho\left(\frac{\pi D(z)^2}{4}\right)a_i^f(z,t)\mathrm{d}z}_{\text{fluid inertial force}} \qquad \text{for } i = Sg, Sw \\ & + \underbrace{\frac{1}{2}C_D\rho D(z)\left(v_i^f(z,t)-v_i^p(z,t)\right)|v_i^f(z,t)-v_i^p(z,t)|\mathrm{d}z}_{\text{viscous drag force}} \end{aligned} \tag{3.39}$$

Where, the superscript 'P' denotes the platform and dF_i^P is the elemental force on the platform for the i^{th} degree of freedom. Sg and Sw are platform surge and sway degrees of freedom respectively. The roll and pitch moments on the platform can be given as

$$\mathrm{d}M_i^P(z,t) = \begin{cases} -\mathrm{d}F_{Sg}^P(z,t)z & i = P \\ \mathrm{d}F_{Sw}^P(z,t)z & i = R \end{cases} \tag{3.40}$$

Where, dM_i^P is the elemental moment on the platform for the i^{th} degree of freedom. The total forces and moments on the platform are obtained by integration of the elemental forces and moments along the depth of the platform. Since, the spar is symmetrical about its vertical axis, the yaw moment and heave force are assumed to be zero. Morison's representation assumes that viscous drag force dominates the total drag force and radiation damping is negligible. This is valid only for rigid platforms with small motion, which is true in this case. Equation 3.39 does not include the added mass associated with the heave motion of the platform. Hence, added mass coefficient for heave degree of freedom is included as per Dinh and Basu, 2013.

3.6 Mooring dynamics model

An open-source mooring system simulation program, named OpenMOOR (Chen, Basu, and Nielsen, 2018), is used to compute the mooring force for given reference point motion of the platform. The program is based on the model of submerged cables, as in Figure 3.4, developed by Gobat and Grosenbaugh, 2006; Tjavaras et al., 1998; Tjavaras, 1996, where the cable is modelled as an Euler beam considering the bending and torsional stiffness effects. The hydrodynamic effect is considered using the modified Morison's equation. In the case that a part of the cable is grounded on the seabed, the seabed is considered as a flat plane modelled as a visco-elastic mattress. Using OpenMOOR, the fairlead motion is computed using the multi-body dynamics and then the two-point boundary problem for each cable is solved in parallel using the generalized-α method for both spatial and temporal discretization Gobat and Grosenbaugh, 2006. The resulting non-linear algebraic equation is eventually solved using a Newton-like method with dynamic relaxation. OpenMOOR also enables the consideration of steady current with an arbitrary profile. In the present study, the wave effect on the mooring cable is neglected since the fairleads of the spar-type FOWT are deep below the mean water level. For implementation, OpenMOOR is compiled as a dynamic linking library and then coupled with the model of the FOWT.

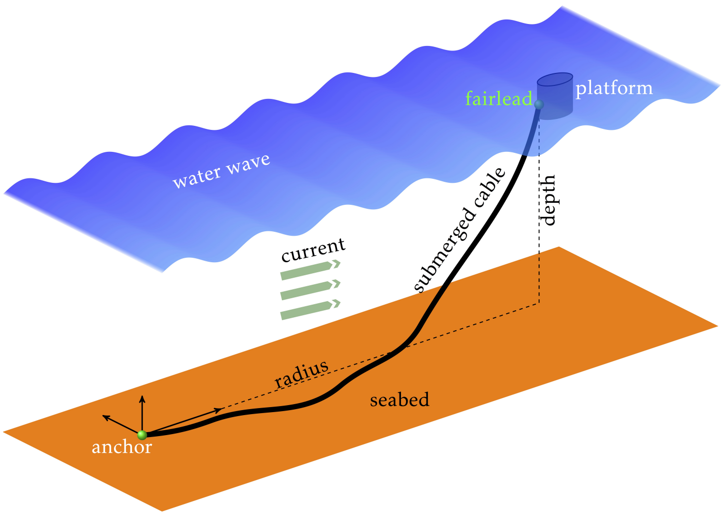

Figure 3.4: Submerged cable subjected to wave and current

3.7 Model verification results

The offshore wind turbine model developed is benchmarked against state of the art wind turbine simulator FAST (Jonkman and Buhl Jr, 2005). The spar-type offshore wind turbine defined in (Jonkman, 2010) is used for analysis. The codes for the offshore wind turbine are developed in MATLAB, 2018. The verification results are shown in Figure 3.5 and Figure 3.6. The offshore wind turbine is simulated under steady rated wind speed of 11.4 m/s in still water.

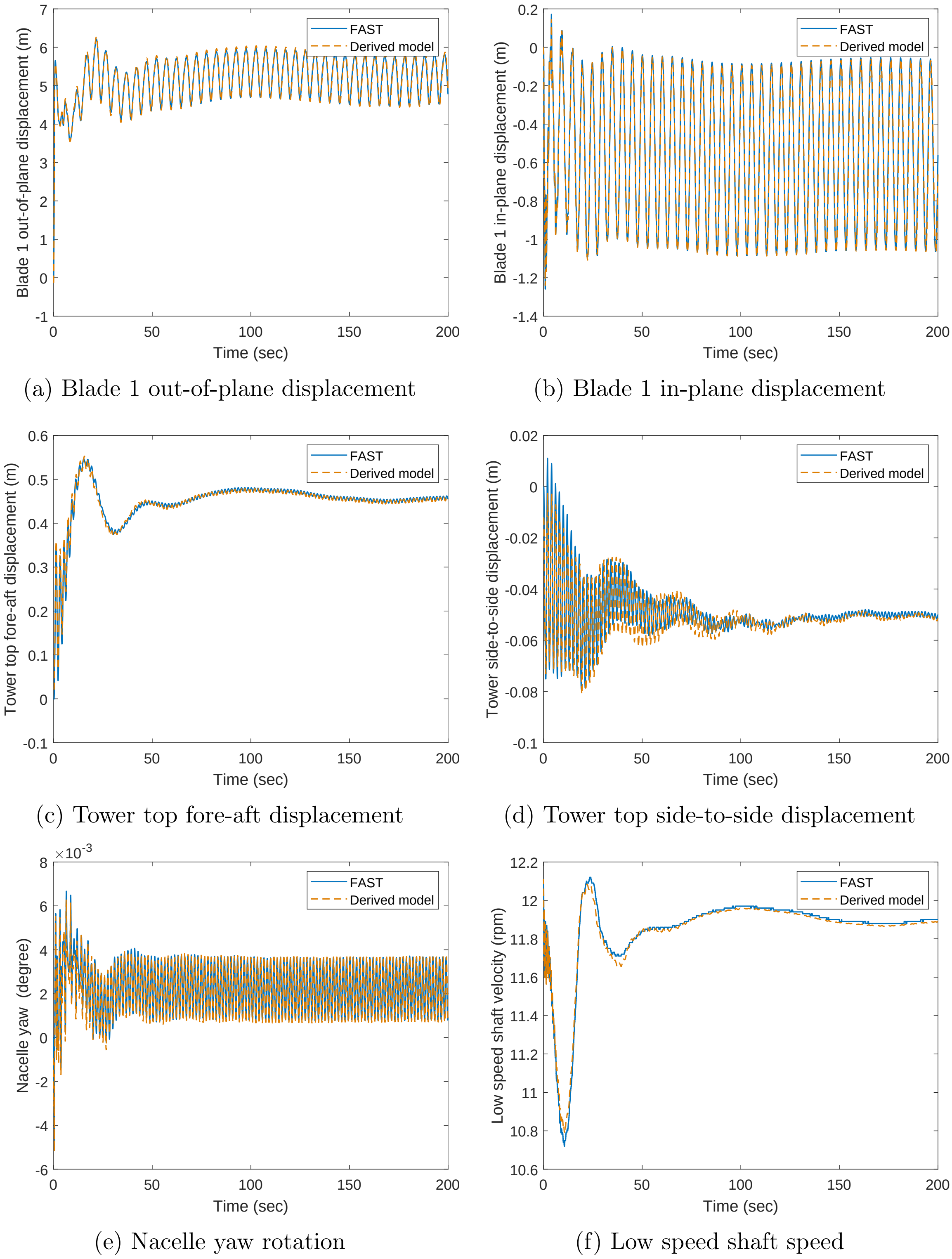

Figure 3.5: Model verification: motion of the wind turbine tower, nacelle and blades

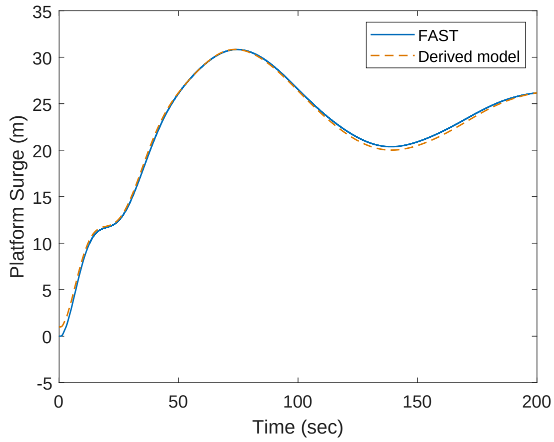

(a) Platform surge

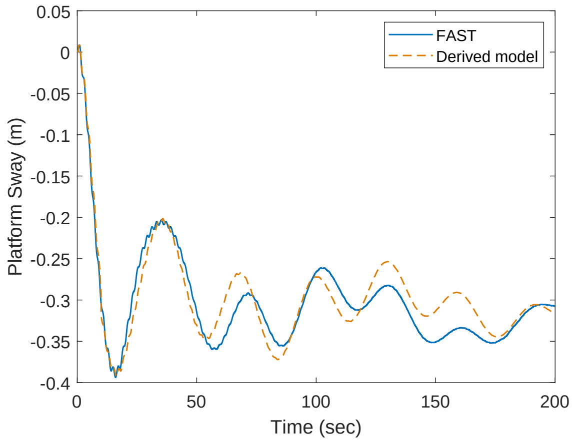

(b) Platform sway

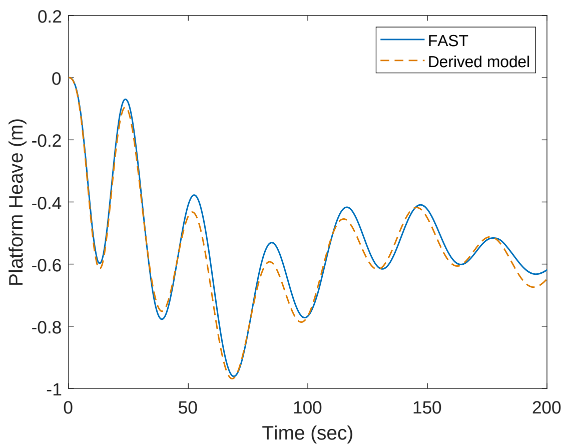

(c) Platform heave

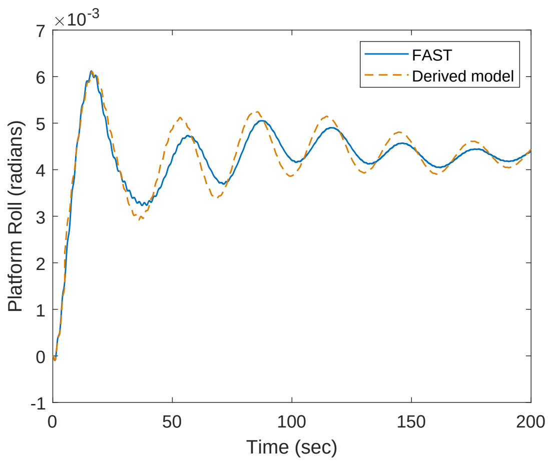

(d) Platform roll

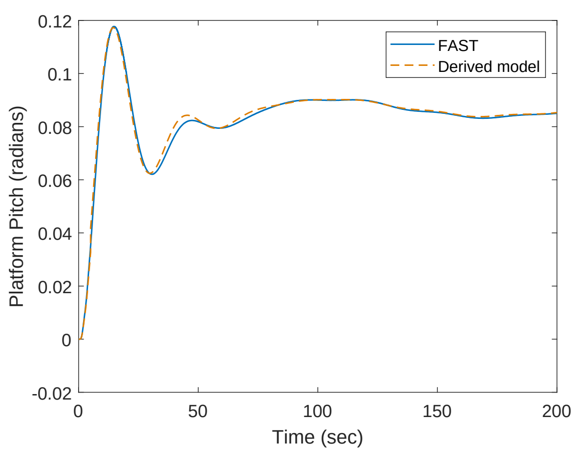

(e) Platform pitch

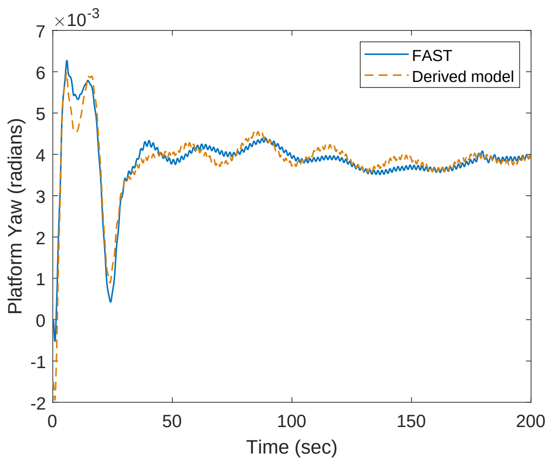

(f) Platform yaw

Figure 3.6: Model verification: motion of the wind turbine platform

An excellent similarity is observed for the wind turbine tower, nacelle and blade motion in Figure 3.5; while some dissimilarities are observed in the platform motion from Figure 3.6. The main difference is a phase shift in the response time histories. This is due to the fact that while FAST applies hydrodynamic damping from both linear potential flow theory and viscous drag forces from Morison's equation, the derived model in this thesis uses only viscous drag forces from Morison's equation. This difference in hydrodynamic damping results in a phase shift in the response time histories. Also, the degrees of freedom that experience less hydrodynamic damping like platform surge, heave or reaches steady state quickly like platform pitch, yaw is less affected by the phase shift. The platform sway and roll degrees of freedom experience a noticeable phase shift due to the difference in hydrodynamic damping. However, the mean and the frequency content of the responses remain the same which is important from a dynamic analysis point of view.

3.8 Passive TMD on Nacelle

In this section a passive Tuned Mass Damper (TMD) is installed on the nacelle to mitigate side-to-side vibrations of the tower of an onshore wind turbine. The purpose of this section is to demonstrate the procedure of installing the TMD using Kane's method and it will emphasize on the relative ease of the procedure compared to traditional energy methods.

Installing a TMD on the nacelle is simple because the kinematics of important points of the wind turbine (without the TMD) are not dependent on the position of the TMD mass. The position of the TMD mass is denote by a new generalized coordinate q_{TMD} which is also denoted by the number 23. Therefore, the kinematics of the wind turbine derived previously do not change. Only, the kinematics and kinetics of the TMD needs to be derived. The system matrices of the TMD can be then superimposed on to the overall wind turbine to obtain the system matrices of the coupled system. Here it must be noted that the TMD mass is only allowed to translate (no rotation) and hence it does not poses any angular velocity. The kinematics and kinetics are derived in Appendix A.4. Generalized active and inertia forces are superimposed on equations 3.14 and 3.13 respectively to obtain the equations of motion of the coupled system.

3.8.1 Result

The TMD place on the nacelle has a mass of 1% of the tower mass and is tuned to the natural frequency of the tower. The tower side-to-side motion with and without the TMD is shown Figure 3.7. Both steady and turbulent cases are shown in the figure.

The results clearly show that additional damping is introduced by installation of the damper and it is capable of dissipating energy from the tower.

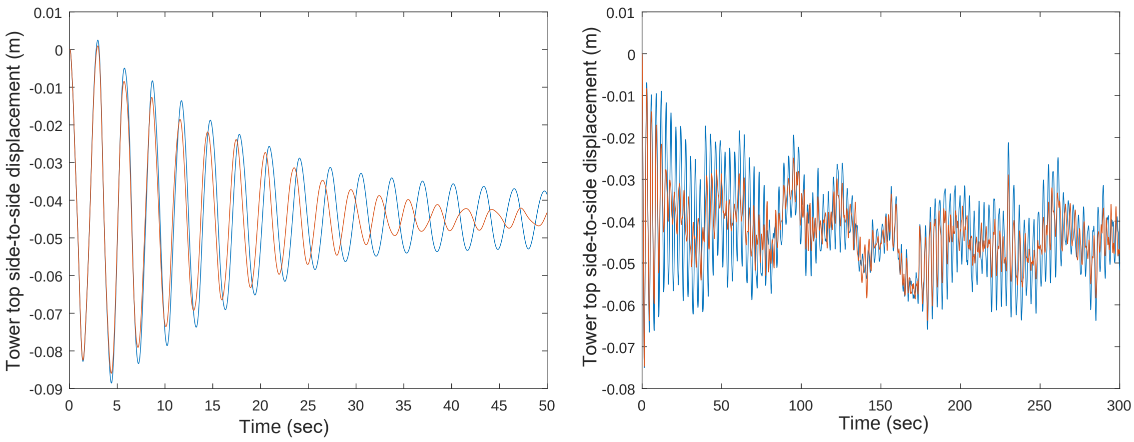

(a) Steady Wind (b) Turbulent Wind

Figure 3.7: Tower side-to-side motion with and with out the TMD

This section showed the method installing a passive damper using Kane's method. The step are similar of any other kind of damper. The procedure is extremely simple and again closed form expression of the equations of motion are not required. The coupled system equation are readily solve by a computer using any numerical time integration scheme.

3.9 Model Reduction

The wind turbine model derived in the previous chapter is a highly coupled non-linear system. The complexity of the model makes it impossible to look at the analytical equations of motion. This is where the benefit of using Kane's method was also utilized. But, under certain circumstances an analytical model of the system is desirable as it provides physical insight into the dynamics. Also, in other problems like that of control theory a simple model is beneficial. Hence, in this section model order reduction is investigated from the point of view of an onshore wind turbine. The purpose is to investigate the loss of dynamics arising from the assumptions that lead to this simplification and to make a judgment whether a reduced order model is accurate enough for dynamic analysis and subsequent investigations. Model order reduction includes reduction in the number of degrees of freedom and other assumptions that helps in reducing the complexity without loss any important information. The assumptions are summarized next.

3.9.1 Assumptions

1. Only the first mode in fore-aft and side-to-side direction has been used for the tower. Similarly, for the blades the first flapwise mode is considered to reduced the total numbers of degrees of freedom.

2. Nacelle yaw, driveshaft torsion degrees of freedom are neglected.

3. Rotational speed of the generator is assumed to be constant and hence it is removed from the list of degrees of freedom.

4. Elastic rotation of the tower and blades is neglected.

5. Axial deformation due to lateral deflection is neglected in all structural components.

6. Only two sets of reference frames are used to define the wind turbine model.

7. Blades are assumed to be neither coned nor pitched.

8. Shaft tilt and skew is neglected.

9. It is assumed that the center of mass of the nacelle, hub and blades all lie along the center line of the tower.

10. Aerodynamic loads are estimated and returned in the blade's global coordinate system instead of blade's local coordinate system.

11. Inertial effect of the generator is neglected.

12. Since the structural twist angle of the blades is small, especially towards the tip, and the blades are not pitched, it is assumed that the shape of deflection in the out-of-plane and in-plane directions of the blades can be described by the flapwise and edgewise mode shapes respectively, with sufficient accuracy.

The assumptions led to a 8 DOF system whose generalized coordinates are given as

$$q = [q_{TFA1} \quad q_{TSS1} \quad q_{B1F1} \; q_{B1E1} \quad q_{B2F1} \quad q_{B2E1} \quad q_{B3F1} \quad q_{B3E1}]' \tag{3.41}$$

Here it is very important to understand that the assumption that q_{GeAz} is not degree of freedom/generalized coordinate is a forced assumption since we use it to determine location of points of the system; and hence, by definition, it must a degree of freedom. Therefore, it is necessary that we treat the q_{GeAz} as a degree of freedom while defining the kinematics of the system. Hence, for description of kinematics of the system 9 DOFs (including q_{GeAz}) is used. Later in derivation of equations of motion we can neglect the equation of motion corresponding to q_{GeAz} and end up with a system with 8 degrees of freedom. The wind turbine system is defined using a inertial coordinate system attached to the base of the tower and a set of rotating coordinate system attached to the blades. This reduction reduces a lot of complexity while incurring some inaccuracies that can be tolerated in a simplified case. The coordinate systems, the kinematic description and the kinetic description of the wind turbine, in other words the derivation of the equations of motion are provided in Appendix B and following subsection provides the key findings from the investigation.

3.9.2 Comparison with the 22-DOF Model

In this section the blade and tower motion obtained from the reduced order model is compared with that of the full order model under steady wind at rated speed. It is accepted from the beginning that there will be some basic difference in the responses due to the assumptions made to reduce the complexity of the model. Therefore, the aim of this section is not to look for small differences but rather to look for major anomalies which may arise from deletion of important terms from the equations of motion during model reduction. The blade out-of-plane, blade in-plane, tower fore-aft and tower side-to-side motions are shown in Figure 3.8 to Figure 3.11 respectively. While there

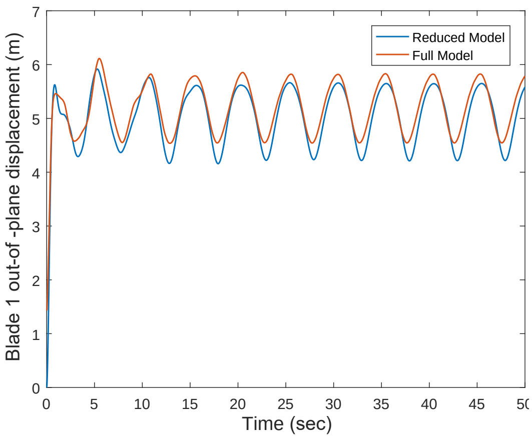

Figure 3.8: Blade Out-of-plane displacement

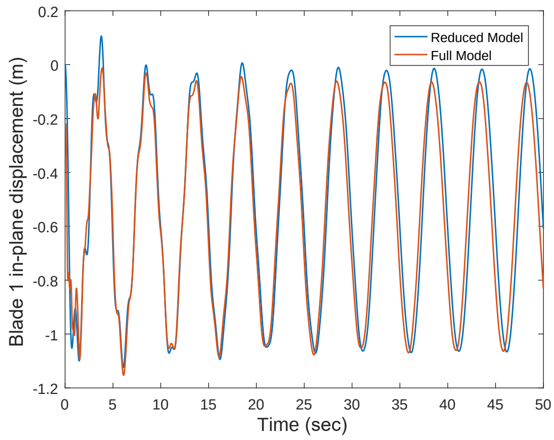

Figure 3.9: Blade In-plane displacement

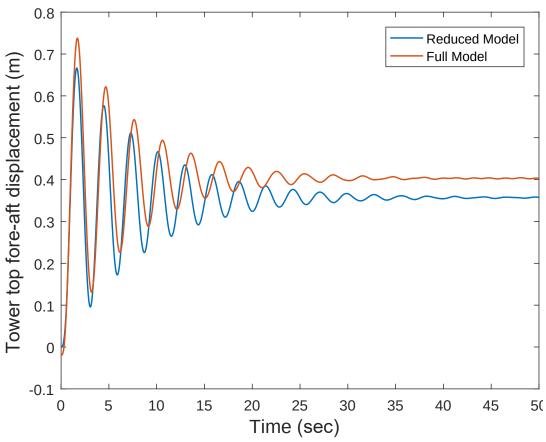

Figure 3.10: Tower Top Fore-Aft displacement

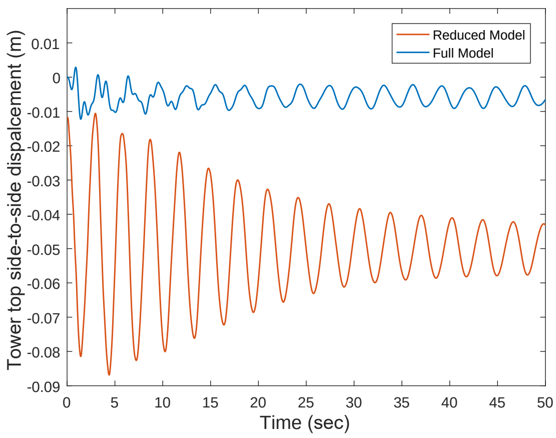

Figure 3.11: Tower Top Side-to-Side displacement

are small differences in the responses, major difference in obtained in tower side-to-side to motion. The difference in the mean displacement of the tower fore-aft motion arises from the fact that in the reduced order model the tower stiffness in higher since gravitational softening effect is not considered. Also, the combined effect of the center of gravity of the blades, hub and nacelle create a positive moment about $\hat{\boldsymbol{a}}_1$ axis. Other minor differences in the figures also arise from the fact that rotational speed is constant as opposed to the full order model which results in minor phase shifts in the responses. However, the tower side-to-side displacement time histories differ considerably from one another. This is due to the fact that the effect of rotational inertia of the rotor on the tower side-to-side displacement is completely neglected. This leads to considerable under prediction of the response.

Although in engineering a certain level of approximation is acceptable, the error in prediction of tower motion is cannot be overlooked. In this case any subsequent analysis, for example estimation of fatigue life, will incur significant errors. Thus, it is not advisable these kinds of reduced order models for analysis that require good quality prediction of the dynamic behaviour of the structure.

Chapter 4

Multi-resolution wavelet pitch controller including wave-current interactions

In this chapter a wavelet based individual pitch control strategy for spar-type Floating Offshore Wind Turbines (FOWTs) has been proposed. Its performance has been evaluated under joint wind-wave-current loads considering the effects of wave-current interactions. A multi-resolution analysis (MRA) based wavelet controller that modifies an optimal control problem cast in Linear Quadratic Regulator (LQR) form constrained to a band of frequency has been used. The weighting matrices of the LQ regulator are varied in different frequency bands depending on the emphasis to be placed on the response energy and control effort to minimize the cost functional of that frequency band. This formulation results in frequency band dependent controller gains that lead to a time-varying controller. Daubechies wavelet is used in the MRA based filter that ensures perfect decomposition of the time signal over a finite interval and fast numerical implementation for control application. The multi-resolution wavelet-LQR individual blade pitch controller is used to control blade out-of-plane vibrations with additional emphasis on the 1P frequency of the wind turbine. The emphasis on the 1P frequency along with the blade's out-of-plane natural frequency is shown to reduce aerodynamic loads corresponding to 1^{st} rotational frequency of the wind turbine which in turn reduces vibrations in other modes of the wind turbine. The proposed controller is simulated using a 5-MW baseline spar-type floating offshore wind turbine with realistic operating conditions including wave-current interactions. The controller has been proved to be effective in every analysed met-ocean condition.

Section 2.3 discusses the various pitch controllers proposed in literature. The control strategies vary from simple SISO PI controllers to sophisticated MIMO controllers using fuzzy logic or model predictive controllers. While these control strategies focus on improvement of power production and/or structural load reduction there is always a trade-off between the two conflicting requirements. The use of wavelet-LQR control strategy that is suitable for a time-varying system as described in (Basu and Nagarajaiah, 2008, 2010) has not been employed for offshore wind turbines. Recently, (Fitzgerald, Staino, and Basu, 2019) used a wavelet-LQR control strategy to minimize blade out-of-plane displacement for onshore wind turbines. However, developing a control strategy for offshore wind turbines presents additional challenges since the stability of the entire system (especially the platform roll and pitch degrees of freedom) must be considered. Further, the wave-current interaction has only been recently incorporated in the analysis of FOWTs (Chen and Basu, 2018, 2019). Considerable effects on the structural responses and fatigue loads have been observed thereof. However, the interaction effects have not been included in previous studies on vibration control of wind turbines. Besides, a simplified model for the FOWT blades and tower was used in (Chen and Basu, 2018, 2019) while the present study uses a more comprehensive model with the same number of degrees-of-freedom as FAST (Jonkman and Buhl Jr, 2005). Based on these considerations the focus of this chapter can be listed as:

- Model the effect of wave-current interaction considering different current profiles to estimate joint wave-current loads on the spar of the floating wind turbine. Further, investigate whether an underlying current has an effect on controller performance.
- Design a wavelet-LQR based individual pitch controller for the floating offshore wind turbine with the primary target of minimizing blade out-of-plane vibrations. Compare its performance against the standard baseline controller and a classical LQR based individual blade pitch controller.
- Examine controller performance in the operational region 3 of the turbine.

In the following sections, the wave-current interaction model is explained first followed by the proposed wavelet-LQR based individual pitch controller, then the performance of the controller is evaluated and the chapter is finished with conclusions drawn from this study.

4.1 Wave-current interaction model

The wave-current interaction is modelled using the Airy wave theory considering the effect of an underlying current (Huang et al., 1972; Tung and Huang, 1974). Two-dimensional flow is considered, i.e., the waves are travelling on a favourable and adverse current. For description of the flow field, a coordinate system is defined with the origin placed on the mean water level (MWL) with x the horizontal axis and z the vertical axis pointing upwards. Let the water depth be denoted by h_w The coordinate system defined in Figure 4.1 is used for the definition of the wave-current interaction model, with the origin at the mean water level (MWL) and x-axis and z-axis pointing to the horizontal direction and the vertical direction respectively.

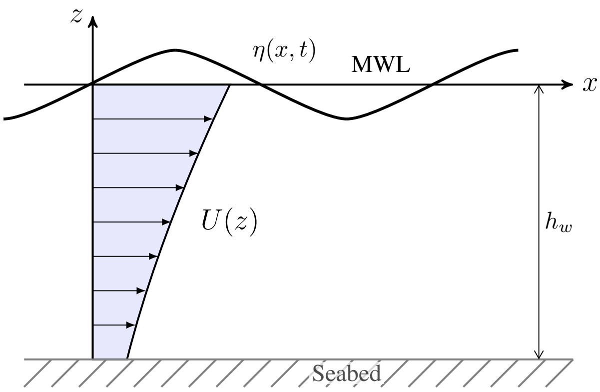

Figure 4.1: Coordinate system for wave-current interaction definition

4.1.1 Regular wave on current

Assuming small-amplitude waves travelling on a current, the flow velocity field is expressed as the summation of the flow due to surface wave and the current (Silva et al., 2016; Thomas, 1981), as

$$u_T(x,z,t) = U(z) + u(z)\cos(\kappa x - \omega t) \tag{4.1}$$

$$w_T(x,z,t) = w(z)\sin(\kappa x - \omega t) \tag{4.2}$$

where $U(z)$ is the current velocity varying with respect to z; and ω and κ denote the angular frequency and the wavenumber respectively. Note that ω is the apparent frequency with the current effect considered (Ismail, 1984). In the preceding expressions, $u_T(x,z,t)$ and $w_T(x,z,t)$ are the flow velocities in horizontal and vertical directions, while $u(x,z,t)$ and $w(x,z,t)$ are the wave velocities using the first-order term (Thomas, 1981). According to the Airy wave theory, the free surface elevation η is given as

$$\eta(x,t) = A\cos(\kappa x - \omega t) \tag{4.3}$$

where A = the surface wave amplitude. Given the free surface function, the flow velocity can be solved analytically for a uniform or linear current profile ($\mathrm{d}^2U(z)/\mathrm{d}z^2 = 0$)(see Silva et al., 2016 for details), as

$$u_T(x,z,t) = U(z) + A(\omega - \kappa U_0)\frac{\cosh\left[\kappa(z+h_w)\right]}{\sinh(\kappa h_w)}\cos(\kappa x - \omega t) \tag{4.4}$$

$$w_T(x,z,t) = A(\omega - \kappa U_0)\frac{\sinh\left[\kappa(z+h_w)\right]}{\sinh(\kappa h_w)}\sin(\kappa x - \omega t) \tag{4.5}$$

where U_0 = the current velocity at $z = 0$. The corresponding dispersion relation becomes

$$(\omega - \kappa U_0)^2 = \left[\mathrm{g}\kappa - (\omega - \kappa U_0)\frac{\mathrm{d}U}{\mathrm{d}z}\right]\tanh(\kappa h_w) \tag{4.6}$$

which is valid for both uniform and linear shear currents. The solution of the preceding equation gives the wave numbers and the flow field is then explicitly determined using equations (4.4,4.5).

4.1.2 Irregular waves on current

To consider the current effect on irregular waves, the expressions in equations (4.4,4.5) are combined with the spectral representation. The influence of the current on the wave spectrum is considered by (Huang et al., 1972)

$$S(\omega, U) = \frac{4S(\omega)}{\left(1+\sqrt{1+4\omega U/\mathrm{g}}\right)^2\sqrt{1+4\omega U/\mathrm{g}}} \tag{4.7}$$

where $S(\omega, U)$ and $S(\omega)$ denote the wave spectra with and without an underlying current respectively. It is noted that when $\omega \to -\mathrm{g}/4U$, the wave components are unable to propagate against the current and wave breaking occurs and hence the preceding expression is only valid for $1+4\omega U/g > 0$ if waves are travelling on an adverse current.

To deal with the case when wave breaking happens, an "equilibrium limit" was defined for deep water by (Hedges, 1981; Hedges, Anastasiou, and Gabriel, 1985) as

$$S_{\mathrm{ER}}(\omega, U) = \frac{A^* \mathrm{g}^2}{(\omega - kU)^5} \frac{1}{1 + 2U(\omega - \kappa U)/\mathrm{g}} \tag{4.8}$$

where the subscript ER refers to the equilibrium range and A^* is a numerical constant in the range of 0.008–0.015 (Phillips, 1977). Equation 4.8 is used instead for a given wave frequency whenever $S(\omega, U)$ is larger than $S_{\mathrm{ER}}(\omega, U)$.
For irregular waves, the water surface elevation can be expressed as

$$\eta(x, t) = \sum_{j=1}^{N} A_j \cos(k_j x - \omega_j t + \phi_j) \tag{4.9}$$

where ϕ_j is introduced as a random phase angle uniformly distributed from 0 to 2π and N denotes the number of wave components. The amplitude of the jth wave is $A_j = \sqrt{2S(\omega_j, U)\Delta\omega}$ with $\Delta\omega$ the frequency interval. Correspondingly, the flow velocities are given by

$$u_T(x, z, t) = U(z) + \sum_{j=1}^{N} A_j(\omega_j - \kappa_j U) \frac{\cosh\left[\kappa_j(z + h_w)\right]}{\sinh(\kappa_j h_w)} \cos(\kappa_j x - \omega_j t + \phi_j) \tag{4.10}$$

$$w_T(x, z, t) = \sum_{j=1}^{N} A_j(\omega_j - \kappa_j U) \frac{\sinh\left[\kappa_j(z + h_w)\right]}{\sinh(\kappa_j h_w)} \sin(\kappa_j x - \omega_j t + \phi_j) \tag{4.11}$$

The accelerations can be obtained from the preceding equations , as

$$\dot{u}_T(x, z, t) = \sum_{j=1}^{N} A_j \omega_j (\omega_j - \kappa_j U) \frac{\cosh\left[\kappa_j(z + h_w)\right]}{\sinh(\kappa_j h_w)} \sin(\kappa_j x - \omega_j t + \phi_j) \tag{4.12}$$

$$\dot{w}_T(x, z, t) = -\sum_{j=1}^{N} A_j \omega_j (\omega_j - \kappa_j U) \frac{\sinh\left[\kappa_j(z + h_w)\right]}{\sinh(k_j h_w)} \cos(\kappa_j x - \omega_j t + \phi_j) \tag{4.13}$$

where the wave-number κ_j is solved from equation (4.6) for each wave component. An instance of the Pierson-Moskowitz spectrum with and without an underlying current is shown in Figure 4.2. The parameters used are - significant wave height 10 m, peak spectral period 6 s and surface current velocity 0.609 m/s (Azcona et al., 2017). It can be observed that the magnitude and the location of the energy peak in the spectrum is altered by the underlying current.

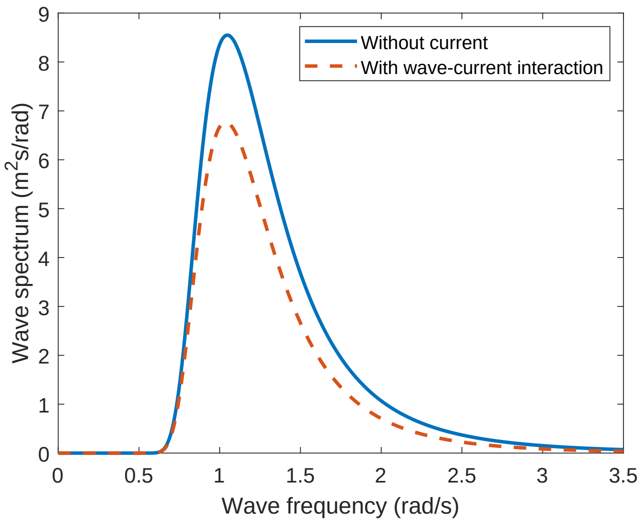

Figure 4.2: Pierson-Moskowitz spectrum with and without an underlying current

4.2 Multi-resolution wavelet-LQR pitch controller

The wavelet-LQR pitch controller is developed using a reduced order system with primary focus on reduction of blade out-of-plane displacement. With this in view, a reduced order system with four degrees of freedom (i.e., the three blade flapwise and tower fore-aft) are used. A time-varying system can be represented as

$$\dot{\mathbf{x}}(t) = \mathbf{A}(t)\mathbf{x}(t) + \mathbf{B}(t)\mathbf{u}(t) + \mathbf{F}(t) \tag{4.14}$$

with states $\mathbf{x} \in \Re^n$, control input $\mathbf{u} \in \Re^m$ and external disturbance $\mathbf{F} \in \Re^n$. The reduced order time-varying FOWT can be represented in this form, however, for controller design the closed form state-space equations are not required as will be shown subsequently. The state vector and control input vector are given as

$$\begin{aligned} &\mathbf{x} = [\mathbf{q},\ \dot{\mathbf{q}}]^T, \qquad \mathbf{q} = [q_{TFA1},\ q_{B1F1},\ q_{B2F1},\ q_{B3F1}] \\ &\mathbf{u} = [\beta_1,\ \beta_2,\ \beta_3]^T \end{aligned} \tag{4.15}$$

Wavelet transformation and integration by parts of the i^{th} equation in 4.14 with respect to a basis function ψ with scale parameter a and translation parameter b leads to

$$\frac{\partial}{\partial b} W_\psi x_i(a,b) = \sum_{k=1}^{n} W_\psi(A_{ik}x_k)(a,b) + \sum_{k=1}^{m} W_\psi(B_{ik}u_k)(a,b) + W_\psi F_i(a,b) \quad \forall a \in \Re \tag{4.16}$$

Where, $W_\psi(\cdot)(a,b)$ is the wavelet transformation of the $(\cdot)$. For a particular value of a the equation can be written as

$$W'_{\psi_a} x_i(b) = \sum_{k=1}^{n} W_{\psi_a}(A_{ik}x_k)(b) + \sum_{k=1}^{m} W_{\psi_a}(B_{ik}u_k)(b) + W_{\psi_a} F_i(b) \tag{4.17}$$

where prime denotes differentiation with respect to the translation parameter b. Looking at an individual transformation

$$W_{\psi_a}(A_{ik}x_k)(b) = \frac{1}{\sqrt{a}} \int_{t_0}^{t_c} A_{ik}(t)x_k(t)\psi(\frac{t-b}{a})\mathrm{d}t \qquad t_0 \leq b \leq t_c \tag{4.18}$$

It can be noted that, $\psi[(t-b)/a]$ is a fast decaying function localized around $t = b$ and $A_{ik}(t)$ & $B_{ik}(t)$ are slowing varying functions as compared to $\psi[(t-b)/a]$ and $x_k(t)$. Therefore $A_{ik}(t)$ can be approximated by a constant value $A_{0,ik}$ in this time interval and the wavelet transformation of the first two terms in the right hand side of equation 4.17 can be approximated as

$$\begin{aligned} W_{\psi_a}(A_{ik}x_k) &\approx A_{0,ik} W_{\psi_a} x_k(b) \\ W_{\psi_a}(B_{ik}x_k) &\approx B_{0,ik} W_{\psi_a} x_k(b) \end{aligned} \tag{4.19}$$

where, $\mathbf{A}_0$ and $\mathbf{B}_0$ are the mean (nominal matrices) excluding the time varying components. Therefore, equation 4.17 can be rewritten as

$$W'_{\psi_a}\mathbf{x}(b) = \mathbf{A}_0 W_{\psi_a}\mathbf{x}(b) + \mathbf{B}_0 W_{\psi_a}\mathbf{u}(b) + W_{\psi_a}\mathbf{F} \tag{4.20}$$

For the non-linear floating wind turbine system the linearised state matrix $\mathbf{A}_0$ and linearised control influence matrix $\mathbf{B}_0$ can be obtained from a Taylor series expansion till first order terms. The partial differentiations can be performed using the numerical central difference technique. For details on the form of the equations refer to (Jonkman and Buhl Jr, 2005). For the system defined in equation 4.20 in wavelet domain the control input can be written in a state feedback form as

$$\{W_{\psi_a}\mathbf{u}\} = -\mathbf{G_a}\{W_{\psi_a}\mathbf{x}\} \tag{4.21}$$

where, $\mathbf{G}_a$ is scale parameter dependent gain matrix, i.e., a frequency band dependent gain matrix. With the control input of the above form a minimization cost functional can be defined as

$$J_a = \int_{t_0}^{t_c} \{W_{\psi_a}\mathbf{x}\}^T \mathbf{Q}_a \{W_{\psi_a}\mathbf{x}\} + \{W_{\psi_a}\mathbf{u}\}^T \mathbf{R}_a \{W_{\psi_a}\mathbf{u}\} \tag{4.22}$$

The definition of the cost function leads to the classical LQR problem for wavelet transformed states and control input. The weighting matrices $\mathbf{Q}_a$, $\mathbf{R}_a$ are associated to the scaling parameter a and are specified for every frequency band.

Control input in time domain The control input can be obtained in time domain by inverse wavelet transformation of the control input. The control input at $t = t_c$ using the states from the interval $[t_0,\ t_c]$ can be obtained as

$$\begin{aligned} \mathbf{u}(t_c) = & - \mathbf{G}_L W_{\psi_a}^{-1} \int_0^{a_L} \int_{t_0}^{t_c} \frac{1}{a^2} \{W_{\psi_a}\mathbf{x}(t)\} \psi\left(\frac{t_c - b}{a}\right) \mathrm{d}b \mathrm{d}a \\ & - \sum_{j=L+1}^{U} \mathbf{G}_j W_{\psi_a}^{-1} \int_j^{j+1} \int_{t_0}^{t_c} \frac{1}{a^2} \{W_{\psi_a}\mathbf{x}(t)\} \psi\left(\frac{t_c - b}{a}\right) \mathrm{d}b \mathrm{d}a \end{aligned} \tag{4.23}$$

where, the scaling parameter is discretized into bands $\{0,\ a_1,\ a_2, \dots,\ a_L, \dots,\ a_U, \dots\}$. Where, a_L is the lower threshold of frequency bands, a_U is the upper is the upper threshold of frequency bands; and for higher bands $a_j > a_U$ the control input is ignored.

Since continuous wavelet transform (CWT) is not suitable for synthesis of control input from time histories of finite interval, discrete wavelet transform (DWT) based on MRA is used for exact decomposition/reconstruction of the signal. The filtered signal obtained from MRA is then used to obtain the control input in time domain as

$$\mathbf{u} = -\mathbf{G}_L\{\mathbf{x}\}_L - \sum_{j=L+1}^{U} \mathbf{G}_j\{\mathbf{x}\}_j \tag{4.24}$$

from frequency dependent control gains where, $\{\mathbf{x}\}_L$, $\{\mathbf{x}\}_{L+1}$, ..., $\{\mathbf{x}\}_U$ are the filtered signal corresponding to discretized frequency bands. The frequency band dependent controller gains $\mathbf{G}_j$ are estimated using different weighting matrices $\mathbf{Q}_j$ and $\mathbf{R}_j$ from the solution of the Algebraic Riccati Equation (ARE) associated with the nominal state and control influence matrices $\mathbf{A}_0$ and $\mathbf{B}_0$. For $j > U$ the gain matrices can be assumed to be zero matrices ($\mathbf{G} = \mathbf{0}$). The wavelet-LQR controller is compared against the classical LQR controller where the control input is estimated from gain scheduling of the unfiltered state and frequency band independent controller gain.

For every wind turbine the blade pitch angles, used as the control input, is limited by the pitching rate and maximum pitch angle that can be realized by the pitch actuators of the blades. Hence, the commanded pitch angles obtained from equation 4.24 are limited by maximum pitching rate of 8 degrees/sec and maximum pitch angle of 90 degrees for the reference wind turbine (Jonkman, 2010).

4.3 Controller performance evaluation

The non-linear aeroelastic offshore wind turbine model developed in Chapter 3 is used to simulate the dynamic behaviour of the spar-type floating offshore wind turbine. The different cases are simulated for a standard 600 sec and with a sampling rate of 40 Hz. Numerical Runga-Kutta method 'ODE 4' is used for time integration of the non-linear system. The proposed controller is compared with a baseline PI collective pitch controller and a classical LQR pitch controller to illustrate the effectiveness of the proposed control strategy. The turbulent wind field is generated using the TurbSim (Jonkman, 2009) package distributed by NREL. It has the capability of generating turbulent 3-D wind field taking into account wind shear and spatial coherence. The turbulence intensity in the wind has been assumed to be 10% in this section. Two different wind cases are investigated here, i.e., 14 m/s and 25 m/s reference wind speed at hub height. The two different wind speeds represent the bound of wind speeds where the pitch control is active (above rated wind speed), in region 3. The stochastic sea is modelled using the Pierson-Moskowitz spectrum (Pierson Jr and Moskowitz, 1964). Significant wave height is assumed to be 10 m and peak spectral period is assumed to be 6 s for all simulations. The depth-dependent wave velocity and accelerations are obtained from equations 4.10,4.11,4.12 and 4.13 with underlying current. The offshore wind turbine is simulated without current and with an underlying current of uniform and linear profile. The surface current velocity is assumed to be 0.609 m/s (Azcona et al., 2017) in the along wind direction, which is the same as the wave propagation direction. The above sea-states represent a violent ocean. For illustration purpose, the controller performance is also evaluated under moderate sea-states of $H_s = 2.25$m and $T_p = 6.25$s and presented here.

The proposed pitch controller is employed in the FOWT and simulated under the above mentioned met-ocean conditions. Its performance is compared against the baseline pitch controller and the classical LQR controller. The three controllers used are defined as follows:

1. *Baseline controller.* The baseline controller is described in (Jonkman et al., 2009) which also provides the FORTRAN source code for the control algorithm. The same was rewritten in MATLAB (MATLAB, 2018) with changes prescribed in (Jonkman, 2010).

2. *LQR controller.* The LQR pitch controller is designed using state weight matrix $\mathbf{Q} = 5 \times \mathbf{I}$ and input weight matrix $\mathbf{R} = 15000 \times \mathbf{I}$ for 14 m/s wind speed and $\mathbf{Q} = 300 \times \mathbf{I}$ and $\mathbf{R} = 15000 \times \mathbf{I}$ for 25 m/s wind speed. The weights are chosen a-priori after a few trial and errors to optimize the effort between the response states and pitch angles.

3. *Wavelet-LQR controller (W-LQR).* The advantage of the wavelet-LQR controller is that it is capable of applying different weights to different frequency bands. For that purpose, the signal from a finite internal $[t_0 \; t_c]$ is filtered using 'db6' wavelet from the Daubechies wavelets (Daubechies, 1992). The response is decomposed into 5 levels, where for a response sampled at 40 Hz, the reconstructed approximate signal at 5^{th} level contains frequencies in the band [0 Hz 1.2 Hz]. This band contains the frequencies that are required to be suppressed, i.e., the rotational frequency of the wind turbine and the blade's natural frequency. Hence, the 5^{th} band becomes the lower bound where additional emphasis is placed on the response states by relaxing the control weight of this band to $\mathbf{R}_L = 3000 \times \mathbf{I}$. All other parameters remain same as the LQR controller. Also, reconstructed detailed signals from levels 1 and 2 are disregarded in the estimation of control input.

4.3.1 Reference wind speed 14 m/s without underlying current

The responses of the offshore wind turbine using the three different controllers and without any underlying current is shown in Figure 4.3. It can be observed from Figure 4.3(a) that excellent vibration reduction is obtained using the proposed wavelet controller for the blade out-of-plane motion. The LQR controller is capable of reducing the amplitude of the response but the peaks of the response are similar to that of the baseline controller. The corresponding Fourier spectrum of the response in Figure 4.3(b) shows that the 1P rotational frequency i.e., 0.2 Hz has been effectively suppressed by the proposed controller. It is also interesting to note that the two visible peaks below 0.2 Hz in the blade out-of-plane response spectrum is the effect of dynamic coupling between the blade-tower-platform. The response of the blade is heavily affected by the pitching motion of the platform and the fore-aft motion of the

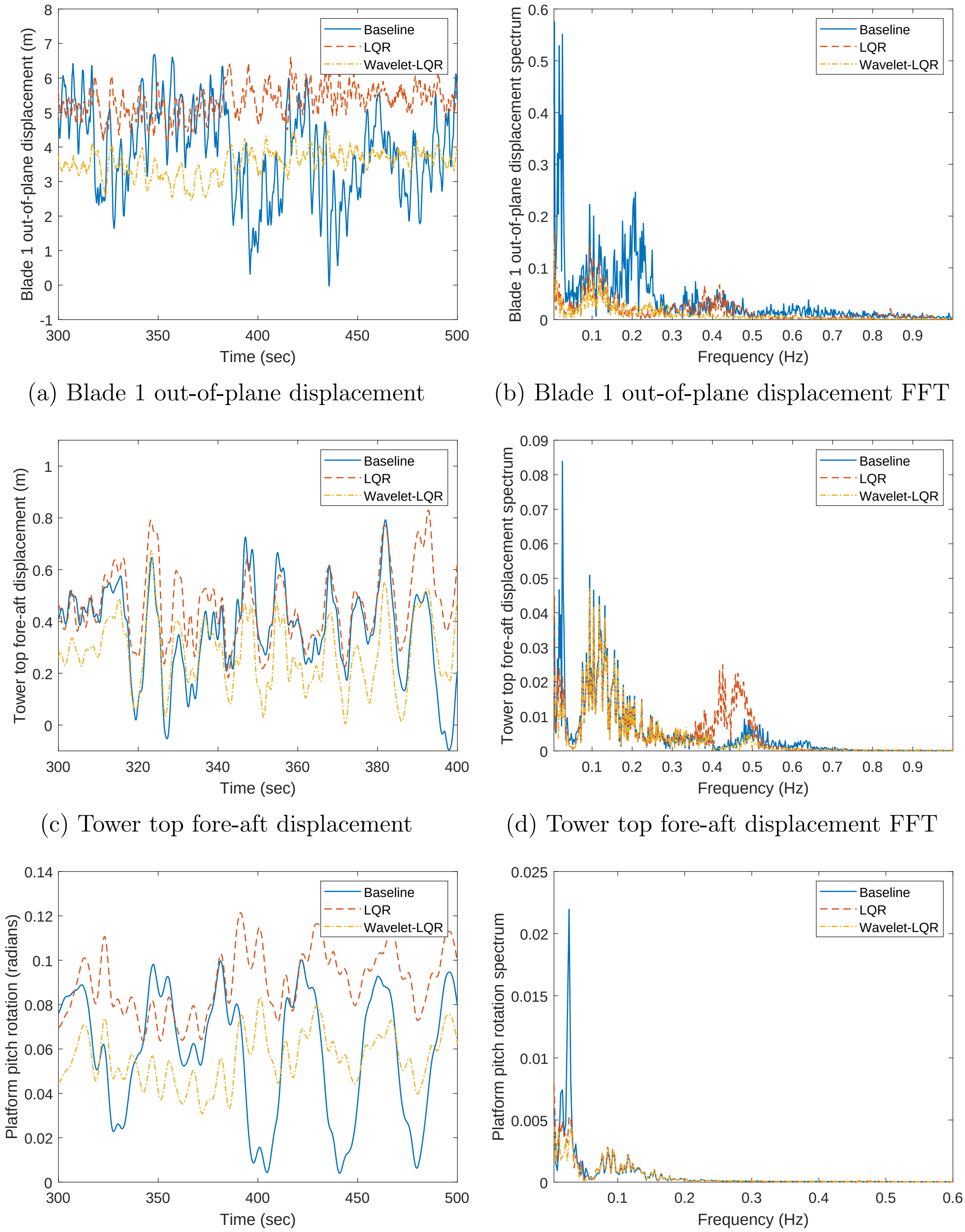

(a) Blade 1 out-of-plane displacement

(b) Blade 1 out-of-plane displacement FFT

(c) Tower top fore-aft displacement

(d) Tower top fore-aft displacement FFT

(e) Platform pitch rotation

(f) Platform pitch rotation FFT

Figure 4.3: Wind turbine motion at reference wind speed 14 m/s without underlying current

tower. However, the proposed controller is capable of suppressing these two peaks very effectively. Although the LQR controller is capable of mitigating these response frequencies, the wavelet-LQR controller performs better as is shown in the figures.

The tower fore-aft motion is shown in Figure 4.3(c) with its Fourier spectrum in Figure 4.3(d). Again, the wavelet-LQR controller performs significantly better than the baseline controller and LQR controller as can be observed from the time history. While the wavelet-LQR is capable of suppressing the various frequency peaks, the LQR controller is only capable of suppressing the lower frequency peak and higher peaks are observed in the higher frequency range. The response time history shows that, with the LQR controller, the response peaks are of greater amplitude than when the baseline controller is used.

Finally, the platform pitching motion is shown in Figure 4.3(e) with its Fourier spectrum in Figure 4.3(f). It can be observed that the pitching motion is dominated by a single frequency and it is mitigated effectively by the LQR controllers. But, again the wavelet-LQR controller performs better than the LQR controller as can be clearly observed from the two figures.

4.3.2 Reference wind speed 14 m/s with underlying current of uniform profile

The offshore wind turbine is simulated next with an underlying current of a uniform profile at the same hub-height reference wind speed of 14 m/s and the performance of the three different pitch controllers is compared in Figure 4.4. The response time histories, Fourier spectrum and controller performance are almost identical to that when the offshore wind turbine is simulated without the underlying current. The same conclusion can be made about the controller performance and is therefore not repeated. The only difference that can be observed is that the Fourier spectrum amplitudes are fractionally reduced. This is due to the fact that the underlying current decreases the wave turbulence as can be observed from the reduced peak of the wave spectrum in Figure 4.2 in the presence of an underlying current. Although this underlying current has negligible impact on the wind turbine degrees of freedom, the dynamic behaviour of the platform surge motion is heavily affected as shown in Figure 4.6. The current, when in the same direction as that of the wave, increases the platform surge motion. It can be also observed from Figure 4.6 that the underlying current reduces that turbulence in the surge motion of the platform. Since the dynamics of the surge motion much slower than the other components, it behaves as a static offset in the position of the

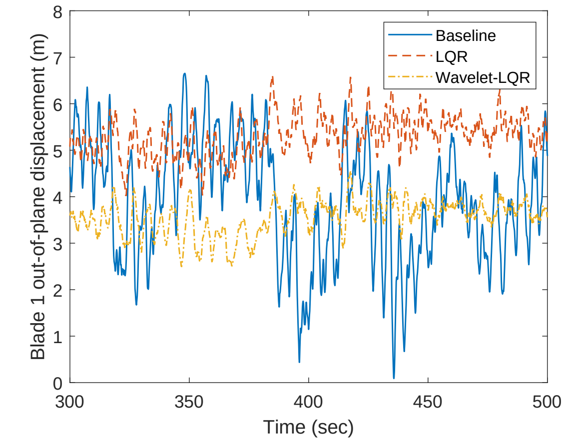

(a) Blade 1 out-of-plane displacement

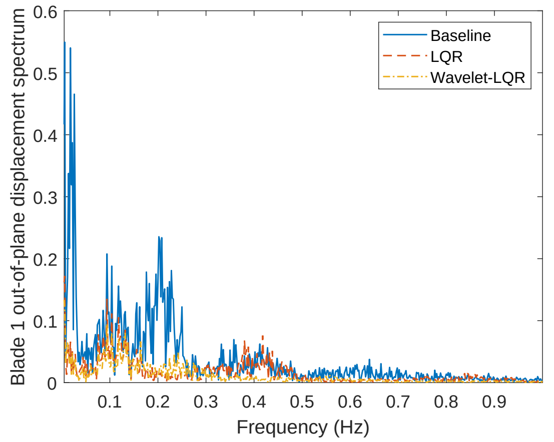

(b) Blade 1 out-of-plane displacement FFT

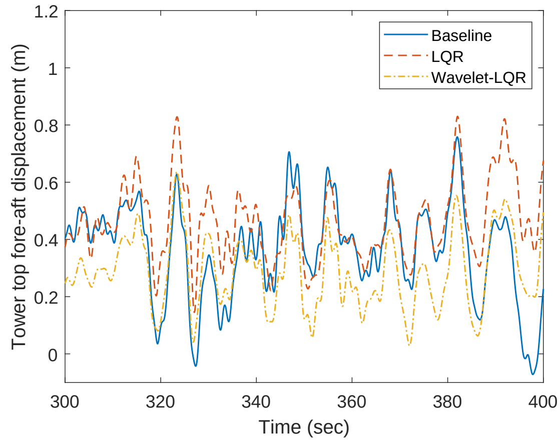

(c) Tower top fore-aft displacement

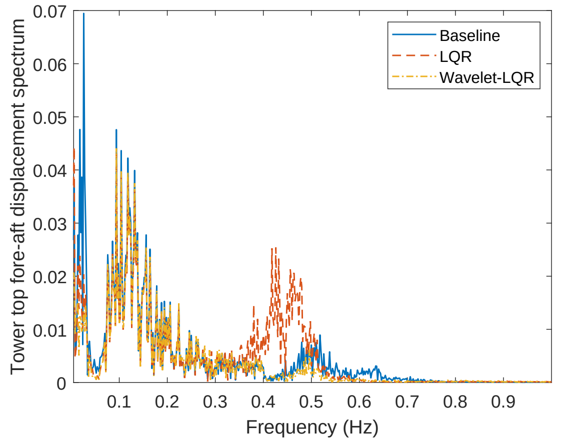

(d) Tower top fore-aft displacement FFT

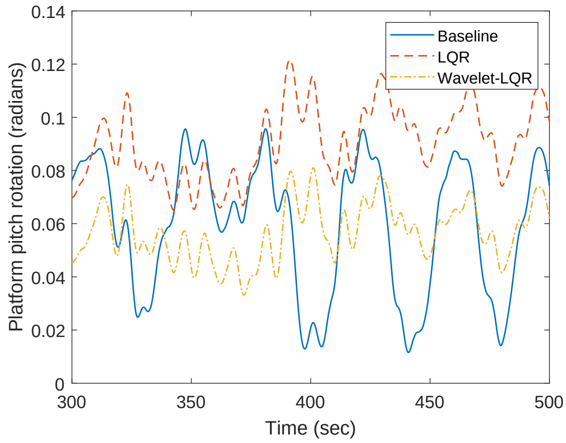

(e) Platform pitch rotation

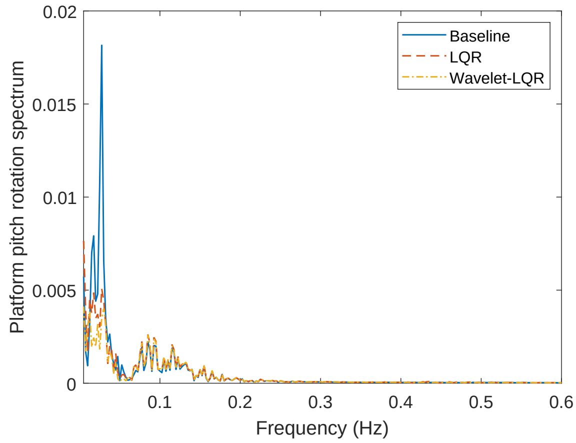

(f) Platform pitch rotation FFT

Figure 4.4: Wind turbine motion at reference wind speed 14 m/s with underlying uniform current

wind turbine without any significant effect on the dynamics of the wind turbine and the performance of the controller.

4.3.3 Reference wind speed 25 m/s with underlying current of linear profile

In this case, the performance of the three controllers is compared at a reference wind speed of 25 m/s with an underlying current of a linear profile. The response time histories for the along-wind components along with their Fourier spectrum is shown in Figure 4.5. Again, a considerable reduction in blade out-of-plane using the proposed controller can be observed in Figure 4.5(a) and the peak associated with the 1P frequency of the wind turbine is clearly seen to be suppressed in Figure 4.5(b). It can be again observed that the proposed wavelet-LQR controller performs better than the baseline controller and the LQR pitch controller. Further reduction in the tower fore-aft motion and the platform pitching motion using the wavelet-LQR controller is observed where the LQR pitch controller shows poor performance. The decrease in the response spectrum amplitudes of the tower fore-aft motion in Figure 4.5(d) and platform pitching motion in Figure 4.5(f) illustrates that the proposed controller is capable of mitigating the tower and the platform pitching motions through load reduction.

Tables 4.1 and 4.2 show the peak and the standard deviation of the blade, tower and platform motion associated with the baseline and the proposed Wavelet-LQR pitch controllers at the various met-ocean conditions considered in this chapter. The percentage reduction over the baseline controller is also shown in the tables. The choice of the two wind speeds is based on the fact that, it lies at the bounds of region 3 of operational wind speeds. It has been shown that the response peaks and standard deviations are reduced with the proposed wavelet-LQR controller in both cases. A considerable reduction is obtained at 14 m/s wind speed with the different current profiles. The results presented in Tables 4.1 and 4.2 show that at the cut-out wind speed of 25 m/s the performance of the proposed controller in mitigating the standard deviation of the responses drop slightly but promising reductions in response peaks are still observed. No significant difference in the controller performance is observed under different current profiles.

It has been shown the emphasis on 1P rotational frequency reduces the aerodynamic load associated with it and results in reduced pitching motion of the platform. However, this reduction of aerodynamic loads provides additional benefit in the form of reduced in-plane motion of the wind turbine although it is not the objective of the controller. The blade in-plane motion, tower side-to-side motion, rotor speed and platform roll of

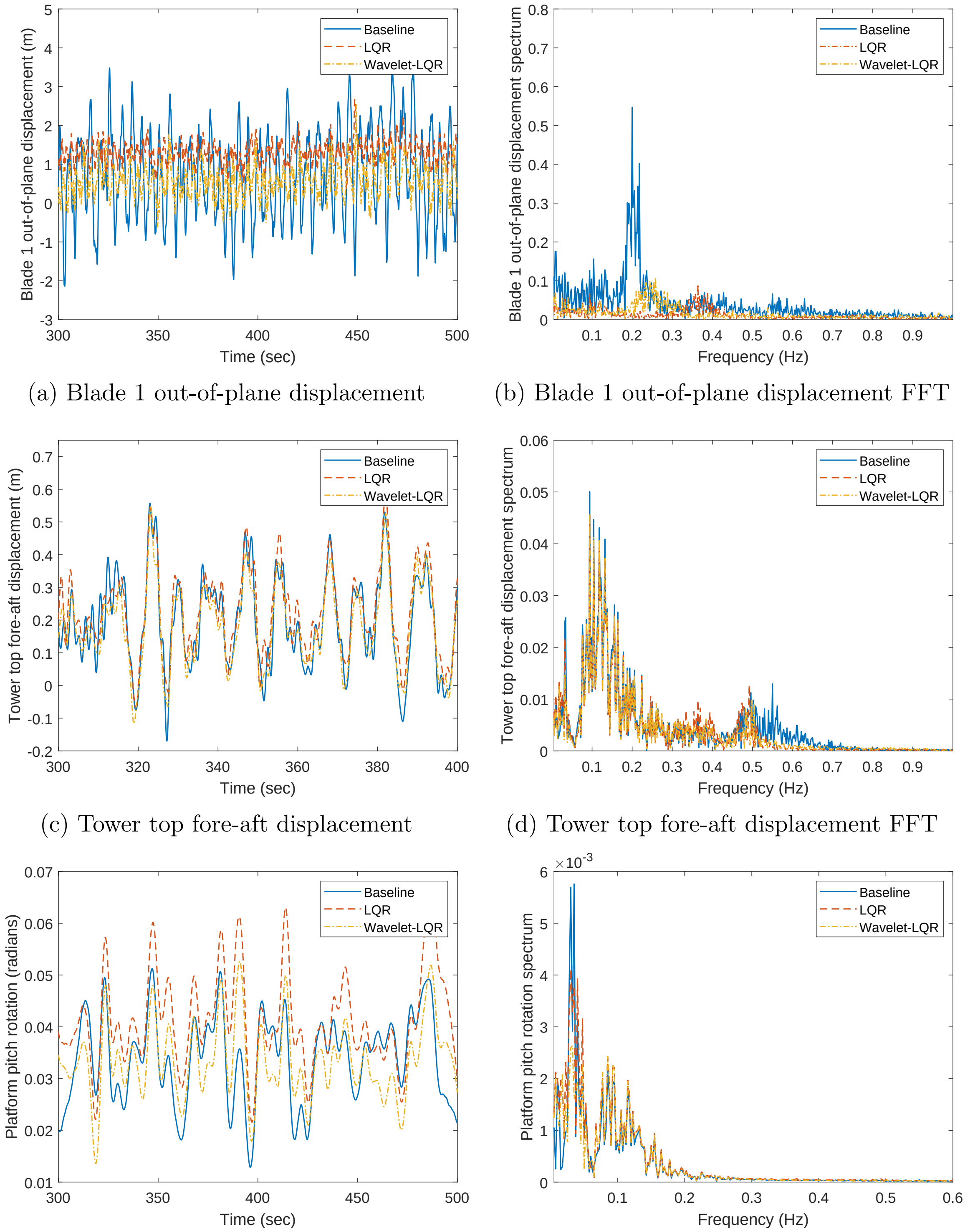

(a) Blade 1 out-of-plane displacement

(b) Blade 1 out-of-plane displacement FFT

(c) Tower top fore-aft displacement

(d) Tower top fore-aft displacement FFT

(e) Platform pitch rotation

(f) Platform pitch rotation FFT

Figure 4.5: Wind turbine motion at reference wind speed 25 m/s with underlying linear current

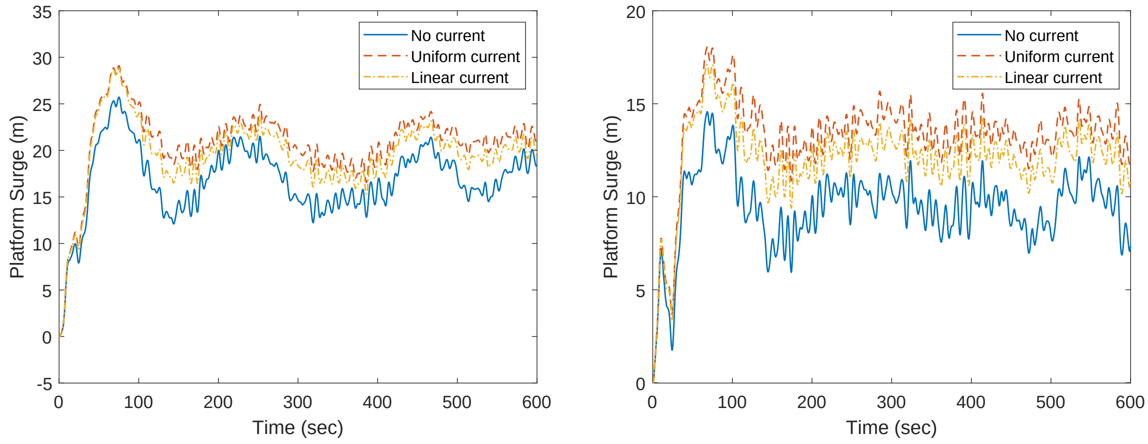

(a) Reference wind speed 14 m/s

(b) Reference wind speed 25 m/s

Figure 4.6: Static offset created by the underlying current

Table 4.1: Controller performance: peak response magnitudes

Current	Wind speed (m/s)	Blade OOP disp. (m)			Tower FA disp. (m)			Plat. pitch rot. (rads)		
		Base-line	W-LQR	$P.R$ (%)	Base-line	W-LQR	$P.R$ (%)	Base-line	W-LQR	$P.R$ (%)
W/O Current	14	6.864	4.491	35	0.807	0.755	6	0.100	0.083	17
	25	3.902	1.939	50	0.677	0.630	7	0.061	0.052	15
Uniform Current	14	6.788	4.554	33	0.778	0.705	9	0.096	0.081	15
	25	3.871	2.530	35	0.634	0.601	5	0.058	0.053	8
Linear Current	14	6.786	4.456	34	0.782	0.703	10	0.097	0.082	16
	25	3.873	2.541	34	0.638	0.586	8	0.058	0.053	10

$P.R = \left(1 - \frac{q^{\text{W-LQR}}}{q^{\text{Baseline}}}\right) 100\%$

the floating wind turbine for 14 m/s and 25 m/s are shown in Figure 4.7 and Figure 4.8 respectively. It can be observed that compared to the baseline controller the proposed wavelet-LQR controller is capable of reducing the structural vibrations by reducing the aerodynamic loads associated with 1P frequency. Further, the platform roll is also reduced thanks to the reduced load on the wind turbine. The reduction in platform pitch and roll establishes the fact that the proposed control not only ensures stability of the entire floating wind turbine but also reduces the rotation of the platform which is beneficial for power production.

It can also be observed from Figure 4.7(c) and Figure 4.8(c) that the variability in the rotor speed has increased. Although there is an increase in variability in the rotor

Table 4.2: Controller performance: response standard deviations

Current	Wind speed (m/s)	Blade OOP disp. (m)			Tower FA disp. (m)			Plat. pitch rot. (rads)		
		Base-line	W-LQR	$P.R$ (%)	Base-line	W-LQR	$P.R$ (%)	Base-line	W-LQR	$P.R$ (%)
W/O Current	14	1.212	0.320	74	0.161	0.124	23	0.023	0.011	54
	25	1.099	0.404	63	0.140	0.126	10	0.011	0.008	25
Uniform Current	14	1.176	0.316	73	0.150	0.117	22	0.020	0.010	52
	25	1.092	0.392	64	0.130	0.119	8	0.009	0.008	15
Linear Current	14	1.183	0.316	73	0.151	0.117	23	0.021	0.010	52
	25	1.091	0.388	64	0.130	0.118	9	0.009	0.007	18

$P.R = \left(1 - \frac{q^{\text{W-LQR}}}{q^{\text{Baseline}}}\right) 100\%$

speed it still tracks the rated speed of 12.1 rpm. While the baseline PI controller is designed solely to maintain the rotor speed at 12.1 rpm, the Wavelet-LQR controller is designed to reduce structural vibrations. The LQR gains are selected appropriately to keep the rotor speed around the rated value while aiming for greater load reduction. In this study, it has been found the standard deviation of the low-speed-shaft/rotor speed from 12.1 rpm using the baseline PI controller is 1.21 rpm and 1.40 rmp for wind speeds of 14 m/s and 25 m/s respectively. For the proposed Wavelet-LQR controller the standard deviations of the rotor speed for the respective wind speeds are 1.72 rpm and 1.87 rmp. While there is an increase in the standard deviation, the coefficient of variation in the worst scenario is still under 15 %. Also, as pointed out by (Fitzgerald, Staino, and Basu, 2019; Lackner, 2013), individual wind turbine power variability will be less important as an offshore wind turbine will almost certainly be situated in a large wind farm and the total output of the farm will be predominantly dictated by the spatial and temporal variations of the farm rather than the variability of a single turbine. Hence, this increase in individual wind turbine power variability is judged to be acceptable considering the promising reduction in structural loads. This trade-off between structural response mitigation and rotor speed regulation can prove to be beneficial in extending the design life of the wind turbine components. Another important aspect of the controller design is the pitching rate of the blades which demonstrates the rate of use of pitch actuators. It has been observed that the maximum pitch rate for the baseline PI pitch controller is 1.63 deg/s and 0.42 deg/s for wind speeds of 14 m/s and 25 m/s respectively. However, with the Wavelet-LQR pitch controller the maximum pitch rate is saturated at 8 deg/s which is the design specification. Hence,

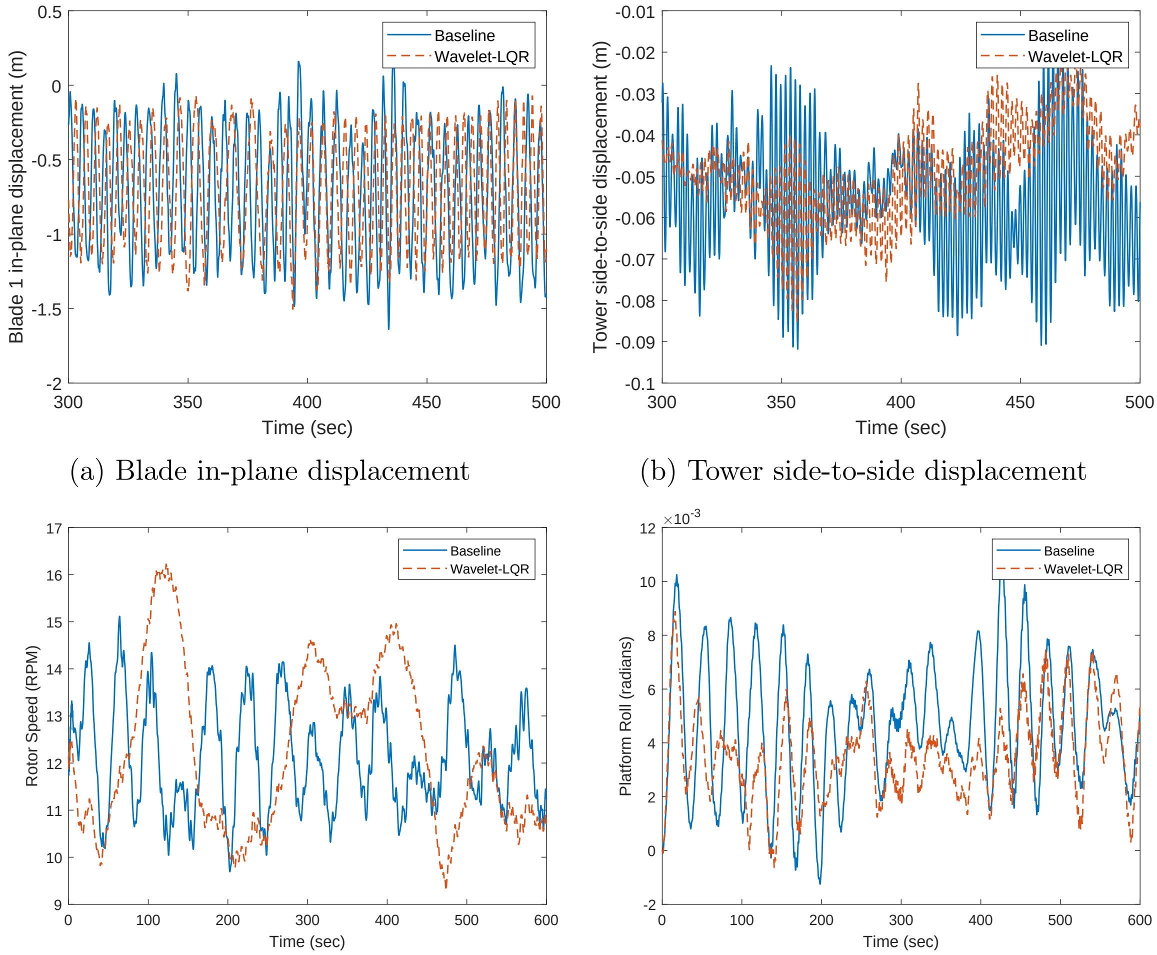

(a) Blade in-plane displacement

(b) Tower side-to-side displacement

(c) Low speed shaft/rotor speed

(d) Platform roll

Figure 4.7: Hub height reference wind speed 14 m/s and underlying current of linear profile

the improved structural response if obtained from at a cost of increased use of pitch actuation.

Lastly, as it was mentioned before the proposed controller is compared against the baseline controller at a hub height wind speed of 14 m/s, moderate sea-states and an underlying current of linear profile and is shown in Figure 4.9 and Figure 4.10. A similar observation can be made about the controller performance where a significant reduction in structural responses is achieved at a cost of increased rotor speed variability. The pitch and roll of the platform are reduced while the rotor speed still tracks the rated value. As mentioned earlier this increase in variability is judged to be acceptable given the significant amount of reduction in structural responses that is achieved.

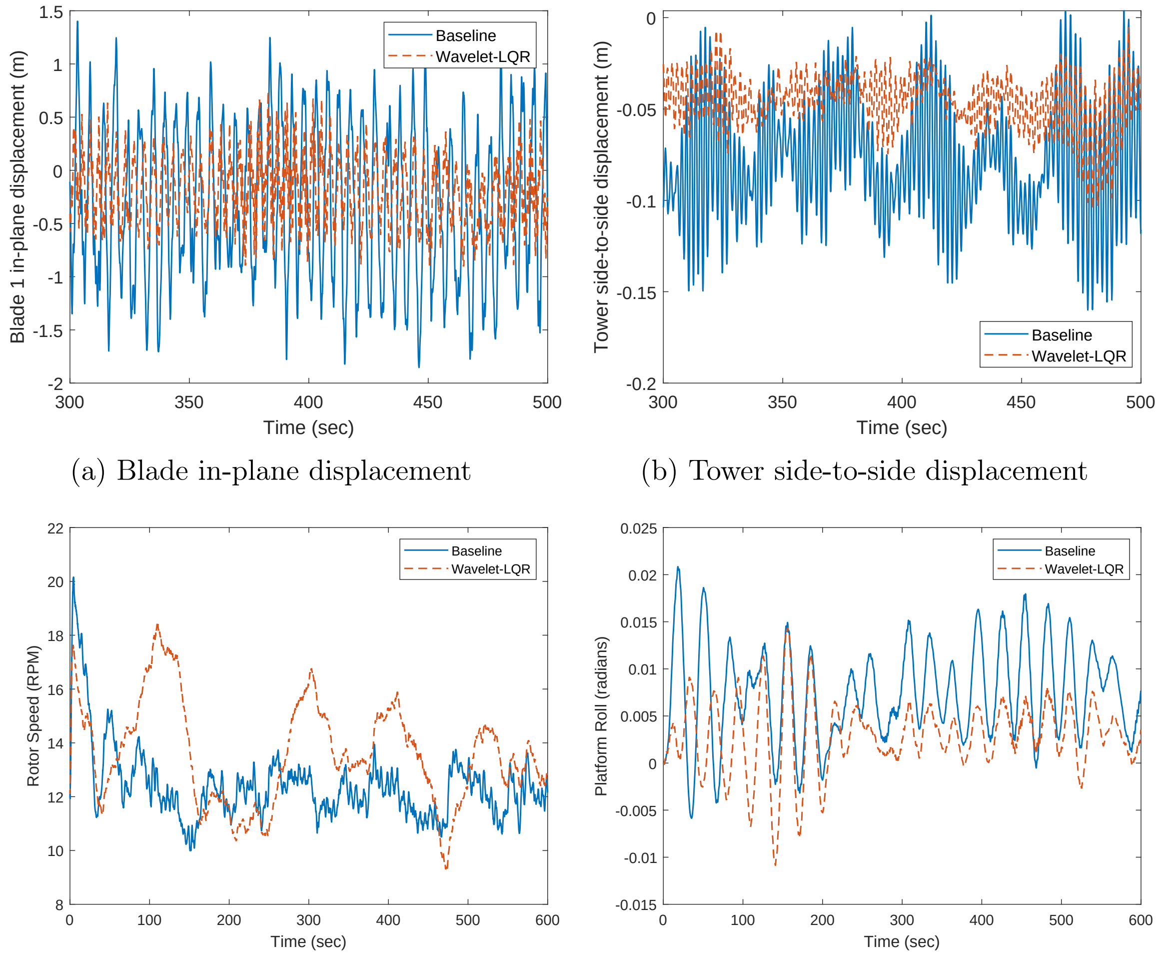

(a) Blade in-plane displacement

(b) Tower side-to-side displacement

(c) Low speed shaft/rotor speed

(d) Platform roll

Figure 4.8: Hub height reference wind speed 25 m/s and underlying current of linear profile

4.4 Conclusion

This chapter proposes the use of a wavelet-LQR based individual pitch controller for response mitigation and load reduction in a spar-type floating offshore wind turbines considering wave-current interactions. A reduced order model using the blade out-of-plane and tower fore-aft degrees of freedom is used to develop the controller. The proposed wavelet-LQR controller has the capability of assigning frequency band dependent LQR gains. This capability has been used in this study to place emphasis on the 1P frequency of the wind turbine along with the blade out-of-plane natural frequency. The controller is compared against the baseline controller and the classical LQR controller. The numerical results presented in this chapter show that the wavelet-LQR

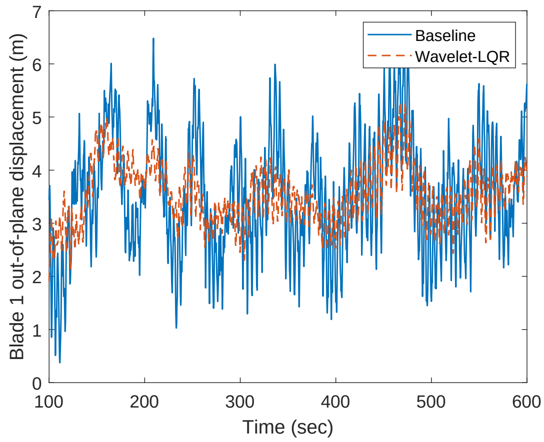

(a) Blade out-of-plane displacement

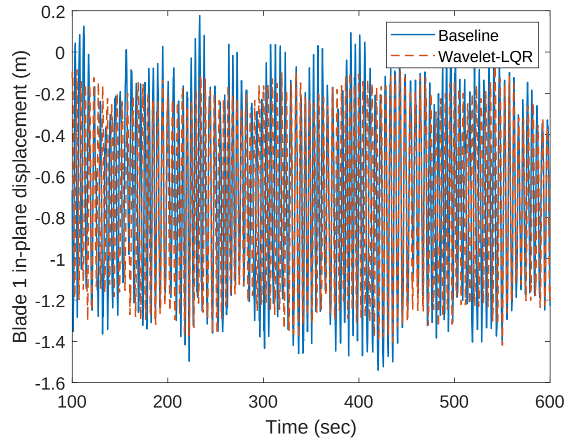

(b) Blade in-plane displacement

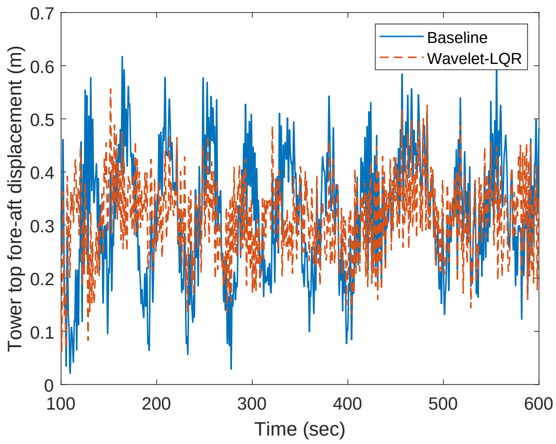

(c) Tower top fore-aft displacement

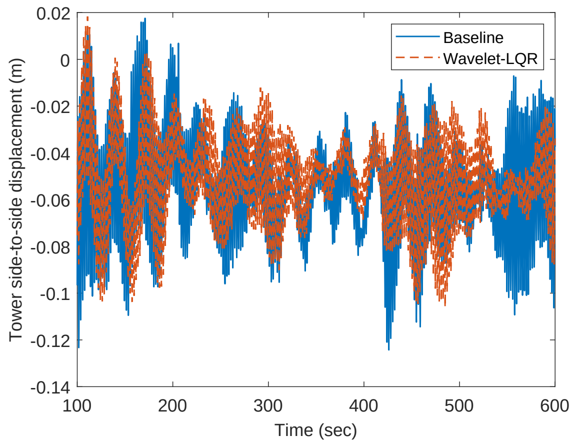

(d) Tower top side-to-side displacement

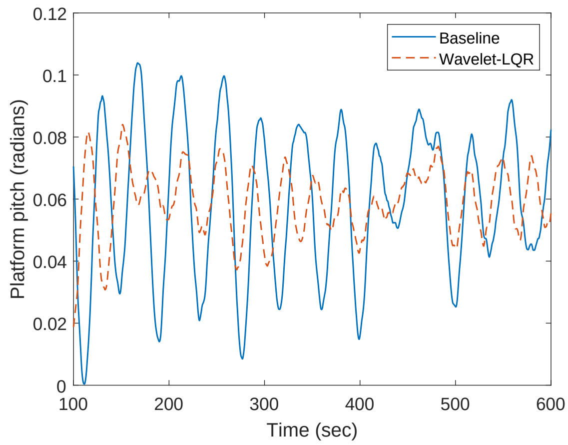

(e) Platform pitch

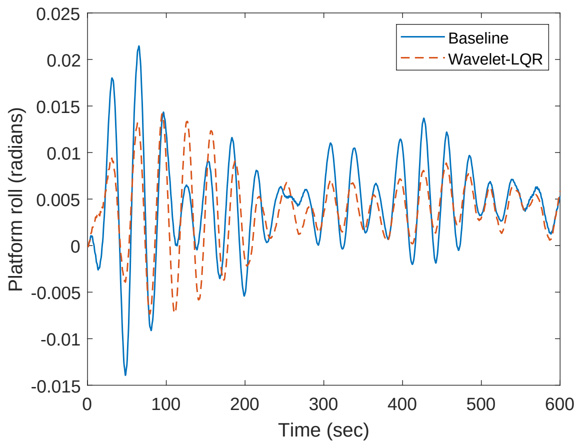

(f) Platform Roll

Figure 4.9: Hub height reference wind speed 14 m/s and underlying current of linear profile and moderate sea states

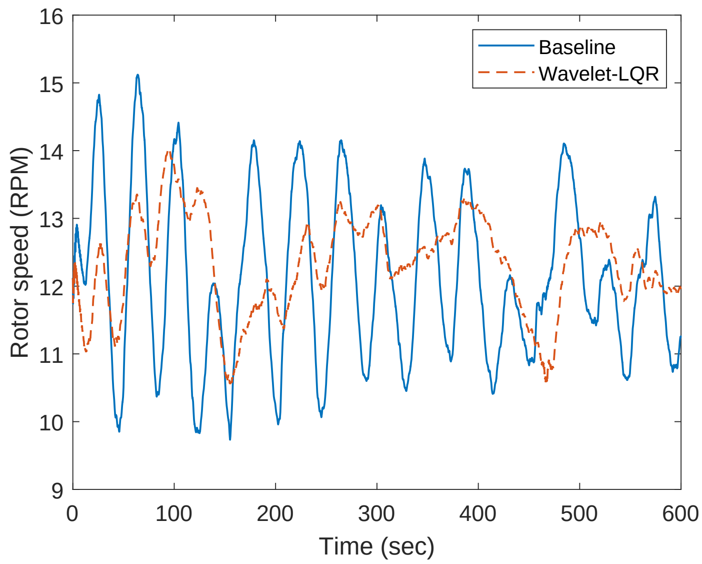

Figure 4.10: Rotor speed at wind speed 14 m/s and underlying current of linear profile and moderate sea states

controller perform better than the baseline controller and the LQR controller for different met-ocean conditions in reducing structural loads. The wind speeds are selected so that they lie on the bound of region 3 of operational wind speeds. The performance at the two different wind speeds shows that although excellent response mitigation is obtained at lower wind speed as compared to higher wind speed, better performance than the baseline controller is obtained in full range of wind speeds. The emphasis on the 1P frequency of the wind turbine reduces the aerodynamic loads which in turn reduces vibration in tower fore-aft and platform pitching motion of the wind turbine. It has been shown that the pitching of the platform contributes significantly to the dynamics of the blade and the tower. However, the proposed controller is capable of minimizing the pitching motion of the platform together with the blade out-of-plane motion and tower fore-aft motion. Additional benefit is achieved in the form of reduction of blade in-plane motion, tower side-to-side motion and platform roll that arises from aerodynamic load reduction associated with the 1P frequency of the wind turbine. The proposed controller not only ensures the stability of the entire wind turbine but also reduces the platform pitch and roll. It has been observed that this improved structural response is obtained at a cost of increased use of pitch actuation. It has also been shown that the improved structural response of the offshore wind turbine results in an increase in deviation from the rate rotor speed which leads to increased power variability. However, as has been mentioned in the previous section the significance of this individual wind turbine power variability will be further minimized when an entire wind farm is considered. This trade-off between vibration reduction and rotor speed improvement can prove to be beneficial in increasing the design life of the wind turbine components.

The investigation on wave-current interaction showed that the underlying current has no significant effect on the performance of the controller. The results presented also show the importance of wave-current interaction on offshore wind turbines.

Chapter 5

Individual blade pitch control strategy for combined load mitigation and power regulation

In the previous chapter a wavelet-LQR based individual blade pitch control strategy was proposed to alleviate aerodynamic loads on the floating offshore wind turbine. It was shown that the proposed controller was excellent in alleviating aerodynamic loads on the turbine and thus in mitigating structural responses of the wind turbine and its supporting platform. However, this was achieved at a cost of increased output power variability. It was argued that a small increase in power variability of individual turbines would be negligible when an entire wind farm is considered. And hence, the controller has practical applicability. Similar results, where structural load reduction using individual pitch controllers lead to degradation in output power quality and turbine regulation have been reported by several authors. None of the IPCs proposed in the literature to date are capable of improving platform response and some controllers even have detrimental effects on the platform motion (Namik and Stol, 2014). Thus, it is an open challenge to develop control algorithms that are not only capable of improving power production but are also capable of simultaneously reducing wind turbine and platform loads. This gap is addressed in this chapter by proposing a new individual pitch control strategy that is both simple and intuitive. The control strategy combines the benefits of a LQ controller with an integral controller to achieve the desired objectives. Unlike the IPCs available in literature the proposed controller is capable of simultaneously improving power production and alleviating structural loads. The reduced structural load on the turbine will eventually help in increasing life-span and improving stability of the spar-type FOWT.

5.1 Proposed Control Strategy

The non-linear aeroelastic model of the FOWT derived in Chapter 3 has been used in this study to simulate its dynamic behaviour subjected to a stochastic wind-wave loading environment and evaluate the performance of the controller. The full non-linear FOWT model has 22 degrees of freedom as listed in Chapter 3. Aerodynamic and hydrodynamic loads on the wind turbine are estimated using the Blade Element Momentum (BEM) theory and Morison's equation respectively. The mooring cables are modelled using MoorDyn (Hall, 2015).

The proposed controller combines a low authority LQR (linear quadratic regulator) and an integral controller to determine the individual blade pitch angles. Although the performance of the controller is evaluated using a fully non-linear model, a reduced order model is used to develop the linear quadratic regulator. The control input of the individual blade pitch angles are obtained as

$$\mathbf{\Theta} = \theta + \mathbf{\Theta}_l, \qquad \mathbf{\Theta} \in \Re^{3\times 1} \tag{5.1}$$

Where, $\theta \in \Re$ is the collective pitch angle obtained from the integral controller and $\mathbf{\Theta}_l \in \Re^{3\times 1}$ is the individual pitch angles obtained from a low authority LQ controller. Conceptually, the integral controller is designed to determine the low frequency variation in the pitch angle following the low frequency variation in the inflow wind speed and the LQ regulator mitigates the 1P frequency of the aerodynamics loads. The along wind components of the wind turbine are subjected to the majority of the aerodynamic loads and therefore the chosen degrees of freedom for the reduced order model are

$$\mathbf{q} = \{q_P \; q_{TFA1} \; q_{B1F1} \; q_{B2F1} \; q_{B3F1} \; q_\varepsilon\}^T \tag{5.2}$$

All the degrees of freedom are described in Chapter 3 except q_ε which is the generator speed error degree of freedom. More details on this degree of freedom is provided in Appendix C. The governing equations of motion are obtained using Kane's method (Kane and Levinson, 1985). The resulting non-linear equations of motion are further linearised by ignoring the quadratic and higher order terms and the final set of linearised equations are presented in Appendix C. These equations of motion are time-varying in nature. But, since the time-varying nature in the along wind direction is relatively small in magnitude, the time varying terms are further dropped assuming a frozen rotor situation. The final linear-time-invariant equations can be written in matrix form as

$$\mathbf{M}\ddot{\mathbf{q}} + \mathbf{C}\dot{\mathbf{q}} + \mathbf{K}\mathbf{q} = \mathbf{F}_{Aero}(v, \mathbf{\Theta}) + \mathbf{F}_{Hydro}(H_s, T_p) \tag{5.3}$$

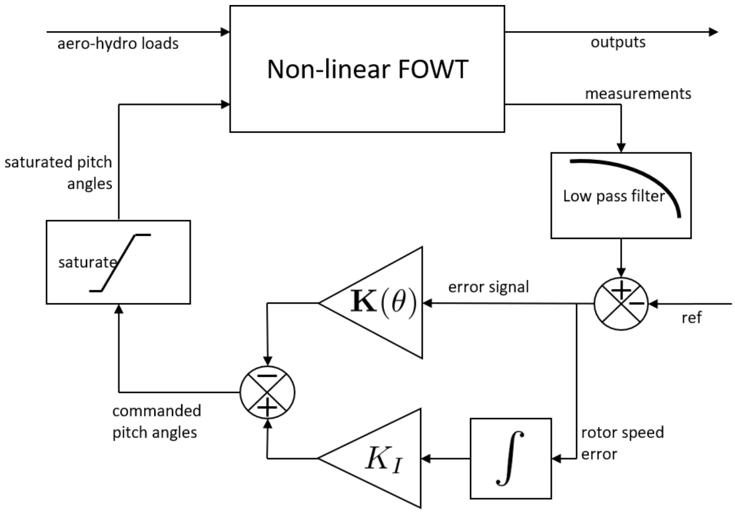

Figure 5.1: Schematic diagram of the proposed controller

In the above equation, aerodynamic loads $\mathbf{F}_{Aero}(v, \mathbf{\Theta})$ is a function of wind speed v and blade pitch angles $\mathbf{\Theta}$. The hydrodynamic loads $\mathbf{F}_{Hydro}$ is a function of significant wave height H_s and peak spectral period T_p. The second order equations of motion can be then rewritten in first order form as

$$\dot{\mathbf{x}} = \mathbf{A}\mathbf{x} + \mathbf{B}(\mathbf{\Theta})\mathbf{\Theta} + \mathbf{G}(v, \mathbf{\Theta}, H_s, T_p) \tag{5.4}$$

Here, $\mathbf{x} = [\mathbf{q}; \dot{\mathbf{q}}] \in \Re^{12\times1}$ is the state vector, the vector of individual blade pitch angles $\mathbf{\Theta} \in \Re^{3\times1}$ is the control input. Ideally, the control influence matrix $\mathbf{B}(\mathbf{\Theta})$ is a function of the individual pitch angles. However, to simplify the controller design it is assumed that the controller gain matrix derived around the collective pitch angle θ and is valid for $\mathbf{\Theta}$ (i.e., $\mathbf{B}(\mathbf{\Theta}) \approx \mathbf{B}(\theta)$). The control influence matrix is obtained from a Taylor series expansion of the aerodynamic loads around the collective pitch angle as the operating point.

$$\mathbf{F}_{Aero}(v, \theta) = \mathbf{F}_{Aero}(v_0, \theta_0) + \left.\frac{\partial \mathbf{F}_{Aero}}{\partial \theta}\right|_{(v_0,\theta_0)} \theta + \left.\frac{\partial \mathbf{F}_{Aero}}{\partial v}\right|_{(v_0,\theta_0)} v + \mathcal{O} \tag{5.5}$$

where,

$$\mathbf{B}(\theta) = \left.\frac{\partial \mathbf{F}_{Aero}}{\partial \theta}\right|_{(v_0,\theta_0)} \tag{5.6}$$

The above linearisation is performed using a numerical central difference scheme on the complete non-linear model to obtain the control influence matrix using collective pitch control strategy (i.e., equal pitch angles for three blades). Using the above linearised system matrices the steady-state (infinite-horizon) LQR is designed ignoring the external disturbance term in equation (5.4). Although a steady-state LQR is not optimal for a finite time system, this approach is a common practice (Namik and Stol, 2010; Namik and Stol, 2014) as it renders the design of the LQR simpler without the need for solving another set of differential equations for the controller. The cost function for the low-authority LQR can be given as

$$J = \int_0^\infty (\mathbf{x}^T \mathbf{Q} \mathbf{x} + \boldsymbol{\Theta}_l^T \mathbf{R} \boldsymbol{\Theta}_l) \mathrm{d}t \tag{5.7}$$

where $\mathbf{Q}$ is state weight matrix that penalizes the control system states and $\mathbf{R}$ is the input weight matrix that penalizes the control input vector. For a steady-state LQR the control input can be obtained from the solution of the Algebraic Ricatti Equation as

$$\begin{aligned} &\mathbf{PA} + \mathbf{A}^T\mathbf{P} - \mathbf{PB}(\theta)\mathbf{R}^{-1}\mathbf{B}^T\mathbf{P} + \mathbf{Q} = \mathbf{0} \\ &\boldsymbol{\Theta}_l = -\mathbf{R}^{-1}\mathbf{B}(\theta)^T\mathbf{P}\mathbf{x}(t) = -\mathbf{K}(\theta)\mathbf{x}(t) \end{aligned} \tag{5.8}$$

A schematic diagram of the controller is shown in Figure 5.1. The LQR is combined with an integral action as shown in Figure 5.1. The integral controller has been obtained from (Jonkman, 2010; Jonkman et al., 2009). It has been pointed out in (Jonkman, 2010; Jonkman et al., 2009) that the controller response frequency must be lower that the smallest response frequency of the FOWT and the wave loading frequency. This must be ensured so that the response of the FOWT is not amplified by the controller. Hence, the integral gains K_I are chosen to attain a controller-response natural frequency of 0.2 rad/s. A controller response frequency of 0.2 rad/s is lower than the platform pitch natural frequency and wave loading frequency in most sea-states and hence the controller remains positively damped. The final control input is obtained from equation (5.1).

To summarize the proposed controller, the LQR is designed to mitigate the 1P vibrations of the blades, the tower fore-aft vibrations and the platform pitch motion. The integral action guarantees convergence towards the rated speed in the above rated wind region while the LQR optimizes the dynamic characteristics of the responses. The combined action of the two controllers have proved to be very effective in optimizing the power production of a FOWT and reducing structural loads as will be shown in the following sections. It can also be observed from Figure 5.1, that the measurements are first passed through a low-pass filter to eliminate the high frequency content and

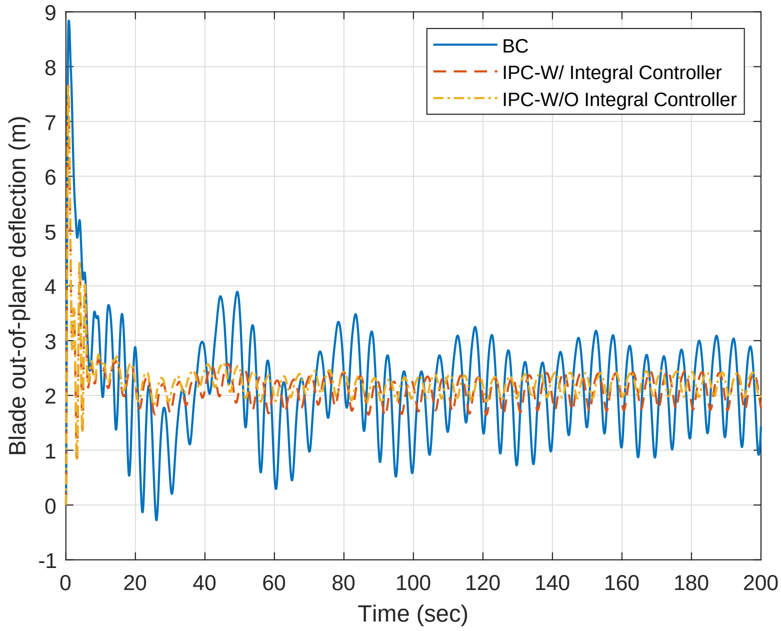

(a) Blade out-of-plane

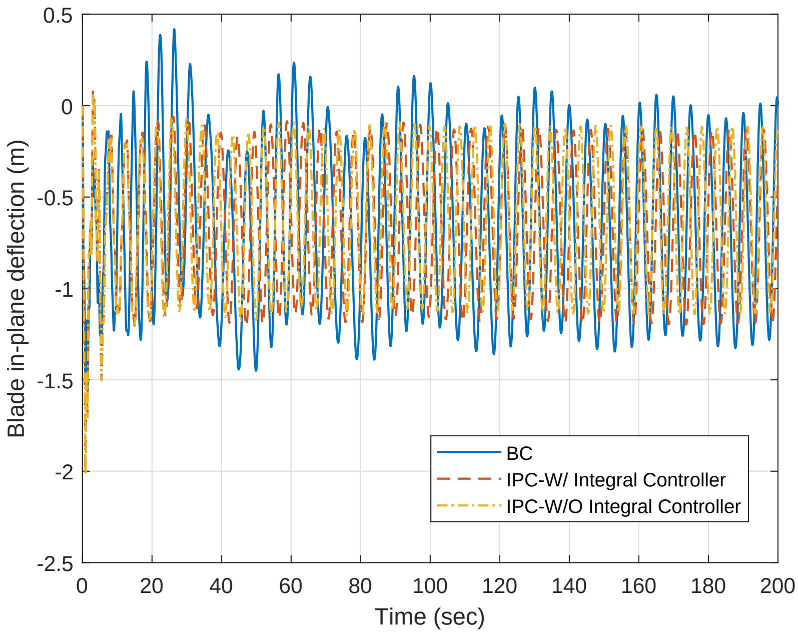

(b) Blade in-plane

Figure 5.2: FOWT subjected to steady 18 m/s hub height wind speed

the control input is saturated prior to feedback. The saturation limits are prescribed in (Jonkman, 2007) to deliver realistic control actions to the blade pitch actuators.

5.2 Controller Performance - Steady Wind

In this section the performance of proposed controller is compared against the baseline controller when the FOWT is subjected to steady wind and no wave loads. The main purpose of this section is to study the response of the FOWT and to evaluate whether the proposed IPC is capable of improving the transient behavior of the FOWT. The 5MW OC3 Hywind turbine, a spar-type FOWT, defined in (Jonkman, 2010) has been used for numerical purposes. The structural and aerodynamic properties of the tower and the blades are defined in (Jonkman et al., 2009). MATLAB, 2018 has been used as the simulation platform. A sampling rate of 40 Hz has been used for time integration using the runga-kutta 4th order method. To investigate the transient behavior the FOWT is subjected to a steady wind field with vertical shear. The hub height reference wind speed is 18 m/s and it is assumed that it is floating on still water. As mentioned in the previous section the integral gain K_I is obtained from (Jonkman, 2010). Therefore only the LQR needs to be designed by proper selection of the state weight matrix and the input weight matrix. For ease of design the control weight matrix is chosen as $\mathbf{R} = \mathbf{I}_{3\times3}$.

It is important to note here that we are aiming for a low authority controller. Unlike conventional mechanical systems, the pitch actuators cannot be used to drive the error state to zero. Designing a high authority controller will demand high pitch actuation which is not suitable for a wind turbine. Pitching of the blades will also be limited by its saturation limits. The aim is to design a low authority controller that is capable of reducing the aerodynamic loads with relatively lower pitch actuation. Therefore, the state weight matrix is chosen as $\mathbf{Q} = 0.001 \times \mathbf{I}_{12\times12}$. The state weight matrix $\mathbf{Q}$ is further modified by increasing the weights on the tower fore-aft, platform pitch and generator azimuth states to 1 to obtain the final low authority controller. It must be noted here that the selected controller weight matrices are used over the entire wind-wave loading environment without the need to retune them with changing wind speed (Jafarnejadsani and Pieper, 2015).

The numerical time history predictions are shown in Figure 5.2. The baseline controller (BC) is compared against the proposed IPC with and without the integral controller (IPC-W/ Integral Controller, and, IPC-W/O Integral Controller, respectively). Figures 5.2a through 5.2f show the structural response of the FOWT. Figure 5.2g shows the rotor speed which should track the rated speed of 12.1 rpm to optimize power production. Figure 5.2h shows the pitch angle of blade 1 and Figure 5.2i shows the generator power. It is clearly visible that the proposed controller improves the tracking of the rated rotor speed while mitigating structural loads on the FOWT. Important

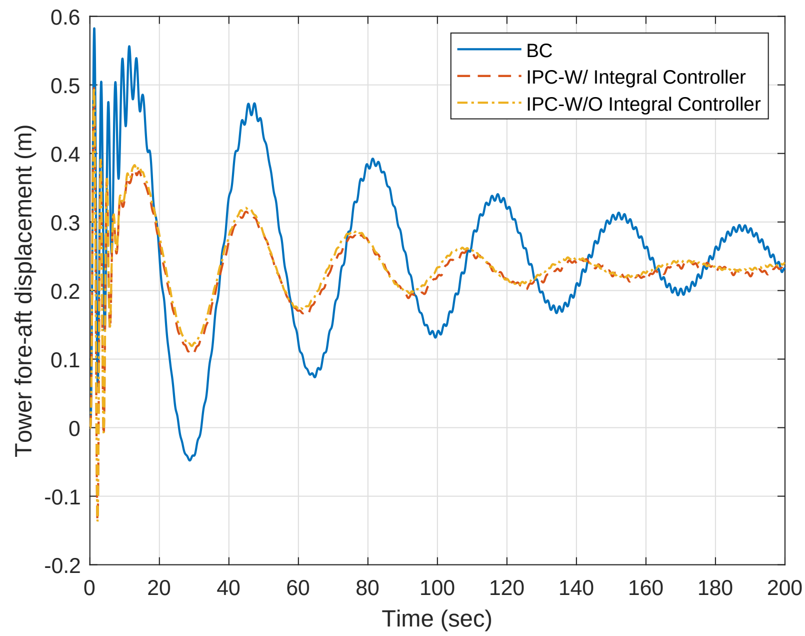

(c) Tower fore-aft

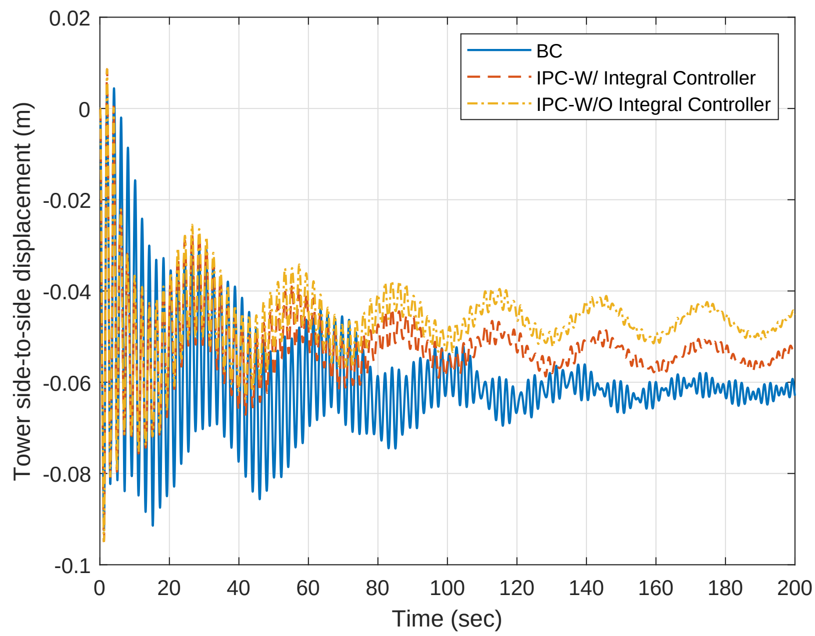

(d) Tower side-to-side

Figure 5.2: FOWT subjected to steady 18 m/s hub height wind speed

points to note from the results presented in this section are:

- The proposed controller improves dynamic response of the FOWT by reducing aerodynamic loads. Evidently, the improvement is greater in the along-wind direction since that is the objective of the LQR. But, as can be observed from

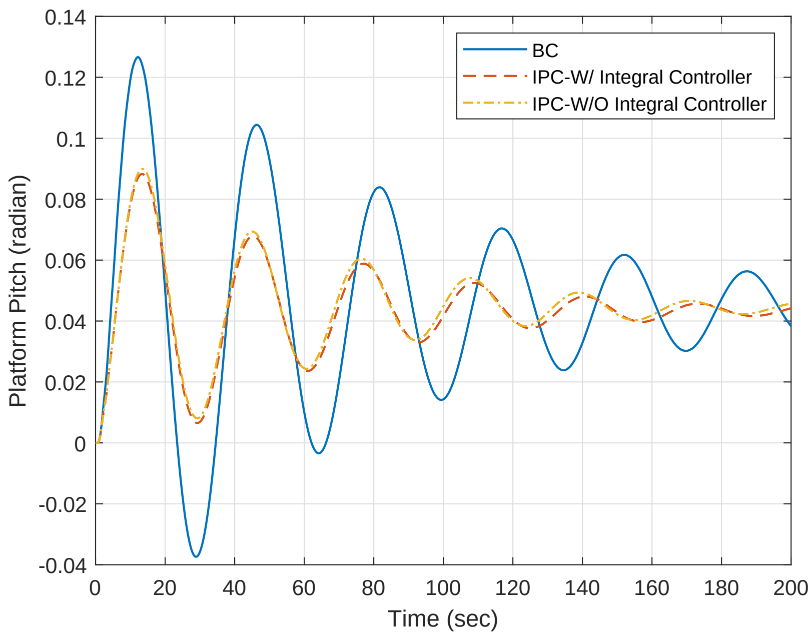

(e) Platform pitch

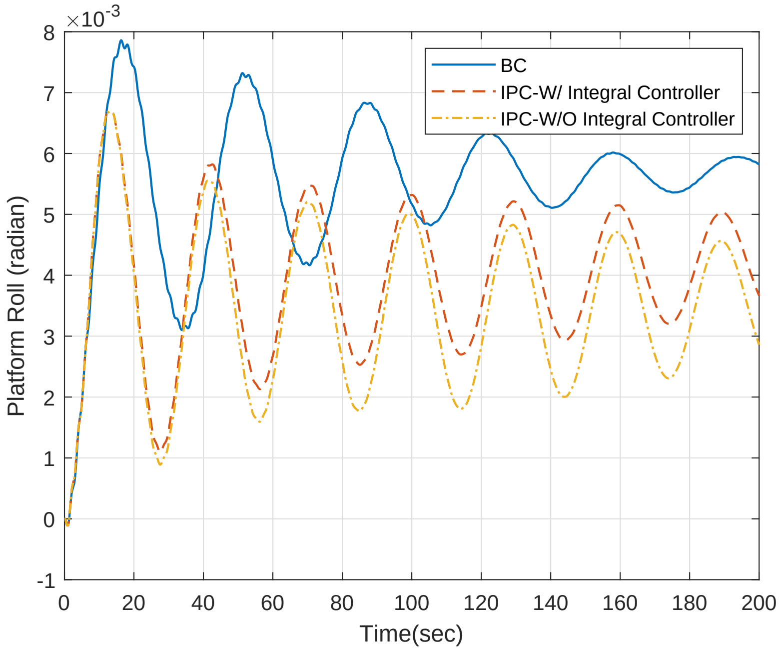

(f) Platform roll

Figure 5.2: FOWT subjected to steady 18 m/s hub height wind speed

Figure 5.2, there is reduction in the cross-wind (direction perpendicular to inflow wind) structural responses arising from the reduction in aerodynamic loads.

- The LQR without integral action fails to track the rated rotor speed, Figure 5.2g,

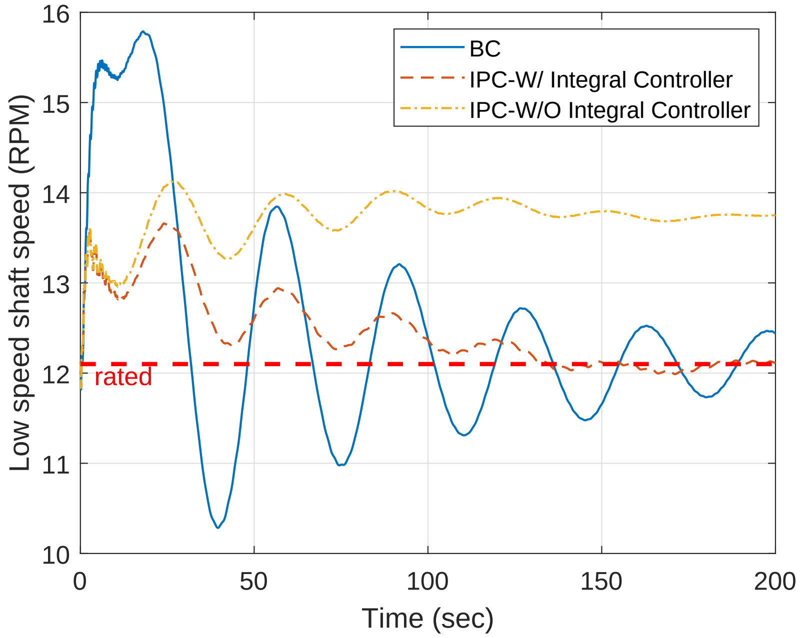

(g) Low speed shaft

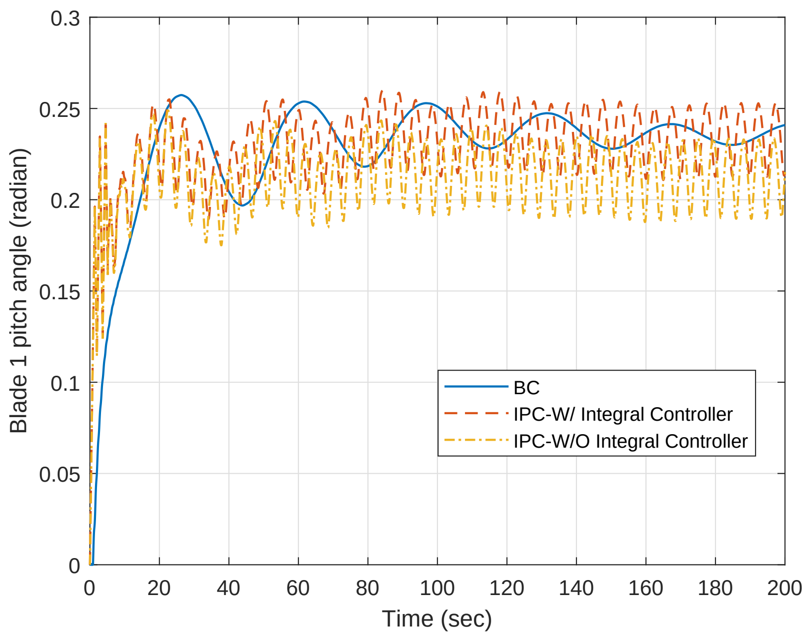

(h) Blade 1 pitch

Figure 5.2: FOWT subjected to steady 18 m/s hub height wind speed

and rated generator power, Figure 5.2i. Operating the generator at above rated condition gives rise to undesirable loads on the generator.

- Improvements in platform pitch and roll is achieved by minimizing the oscillation

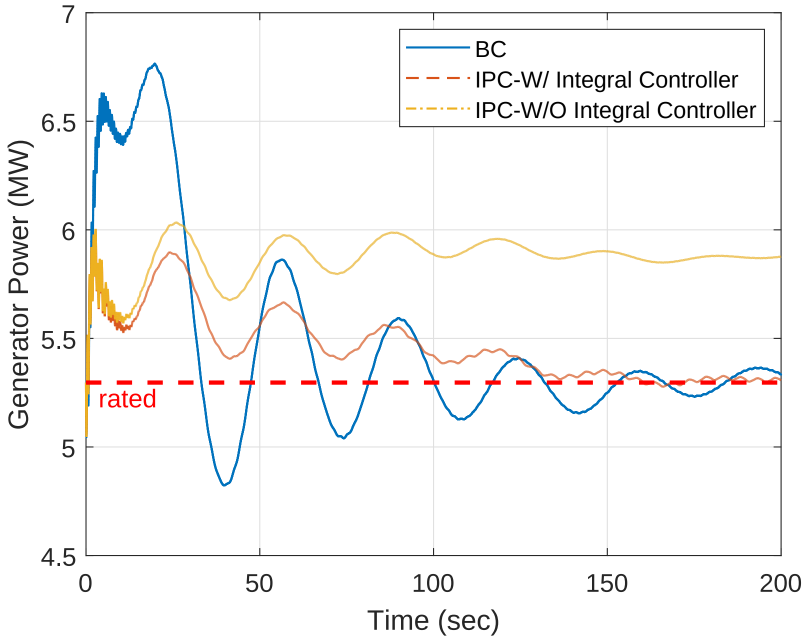

(i) Generator power

Figure 5.2: FOWT subjected to steady 18 m/s hub height wind speed

corresponding to the platform pitch/roll frequency in the blade pitch angle. This is achieved by increasing the weight on the platform pitch degree of freedom in the LQR design. It can be observed from Figure 5.2e that using the proposed IPC the platform pitch DOF reaches steady-state faster than using the baseline controller. On the other hand, the proposed IPC increases the *settling time* of the platform roll DOF. However, it will be shown in the next section that under stochastic wind-wave condition including hydrodynamic damping the proposed IPC can improve the platform roll compared to the baseline controller.

- A 1P oscillation is introduced in the blade pitch angle, see Figure 5.2h, by the proposed controller that mitigates the 1P oscillation in the aerodynamic load and hence reduces the 1P oscillations of the blades, see Figure 5.2a. Simultaneously, the integral controller ensures guaranteed tracking of the rated rotor speed by determining the low frequency variation of the pitch angle.

- It can be observed that the along-wind responses of the FOWT (blade out-of-plane displacement, tower fore-aft displacement and platform pitch rotation) reaches steady-state faster. For the cross-wind responses (blade in-plane displacement, tower side-to-side displacement and platform roll rotation) the transient behaviour is not improved, however, the steady-state displacement/rotations are reduced.

- The improvement in structural response is obtained at an expense of increased pitch actuation, however, always within saturation limits.

5.3 Controller Performance Evaluation - Stochastic wind-wave

The proposed controller is compared against the baseline controller with the FOWT subjected to stochastic wind-wave loading environment. The turbulent wind field is generated using the TurbSim (Jonkman, 2009) package. The stochastic sea is modeled by the Pierson-Moskowitz spectrum (Pierson Jr and Moskowitz, 1964). Nine different wind-wave cases including cases with misaligned wind-wave loads are investigated in this chapter. Wind-wave misalignment can often lead to increased vibrations in the cross-wind components of FOWT and hence the cases must be considered in the design of a controller. The turbulence intensity of the wind field is assumed to be 10% and the wave period for all different wave heights is assumed to be 6 s. It is also assumed that the wave height increases with increasing wind speed. The selected load cases are summarized in Table 5.1. It may be noted here that the selected load cases falls under design load case category 1.1 and 1.2 (normal and fatigue design load cases) of IEC 61400-1 3$^{\text{rd}}$ Ed. (Commission et al., 2005). Cases 2, 4 and 6 simulate wind-wave misalignment and the wave direction relative to the wind direction is given in the table.

5.3.1 Pareto Optimal Tuning

In a multi-objective controller, the ratio between weights in the cost function balances the different control objectives. To find the right balance between the control objectives it is possible to sweep across the weight ratios to form Pareto fronts (Odgaard et al., 2016). These Pareto fronts show the balance between the competitive objectives and can be used to tune the controller.

In this chapter, optimal tuning parameters are determined by comparing the performance of the controller in terms of reduction of generator power variability (Ψ_P)

and the blade out-of-plane moment Damage Equivalent Load (Ψ_{DEL}) defined in equation 5.9.

$$\begin{aligned} \Psi_P &= 1 - \frac{\sigma_{IPC}}{\sigma_{BC}} \\ \Psi_{DEL} &= \frac{\Delta_{IPC}}{\Delta_{BC}} \end{aligned} \tag{5.9}$$

Where, $\sigma_{(}\cdot)$ is the generator power error RMS and $\Delta_{(}\cdot)$ is the fatigue DEL of the blade out-of-plane bending moment. To compute the Pareto curves the state weight matrix $\mathbf{Q}$ is modified as

$$\mathbf{Q} = \begin{bmatrix} \mathbf{Q}_l(1-\rho) & \cdots \\ \cdots & \rho \end{bmatrix} \tag{5.10}$$

where $\mathbf{Q}_l = 0.001 \times \mathbf{I}_{11\times11}$. $\mathbf{Q}_l$ is further modified by increasing the weight on the platform and tower degrees of freedom to 1. $\mathbf{R}$ is left unchanged from the previous section. A sweep across the scalar tuning parameter ρ is done to obtain the Pareto curves shown in Figure 5.3. Pareto curve for 3 different load cases are compared to determine the optimal tuning parameter ρ for the entire range of wind speeds.

Optimal tuning is found by selecting a ρ that gives maximum benefits in form of power regulation without a significant increase in cost in the form of fatigue DEL. In other words, it makes sense to increase the weight ρ as long as the gradient of the Pareto curve is below a predefined small value. From visual inspection of the Pareto curves in Figure 5.3 the tuning ρ has been set to 0.6 to achieve an optimal balance between the two competitive objectives.

5.3.2 Controller performance

The summary of the results for the different load cases are provided in Table 5.3. However, prior to that, for illustration, Figure 5.4 shows the numerical time histories of the FOWT responses for load case 7. The time histories show that the proposed controller, compared to the baseline controller, is more efficient in mitigating structural responses of the wind turbine and the floating platform and tracking the rated rotor speed.

Figure 5.5 compares the fatigue DELs (Damage Equivalent Loads) of the blade out-of-plane bending moment, blade in-plane bending moment, tower fore-aft bending moment and tower side-to-side bending moment of the FOWT obtained using the baseline controller with the proposed IPC. The DELs are estimated using the classical

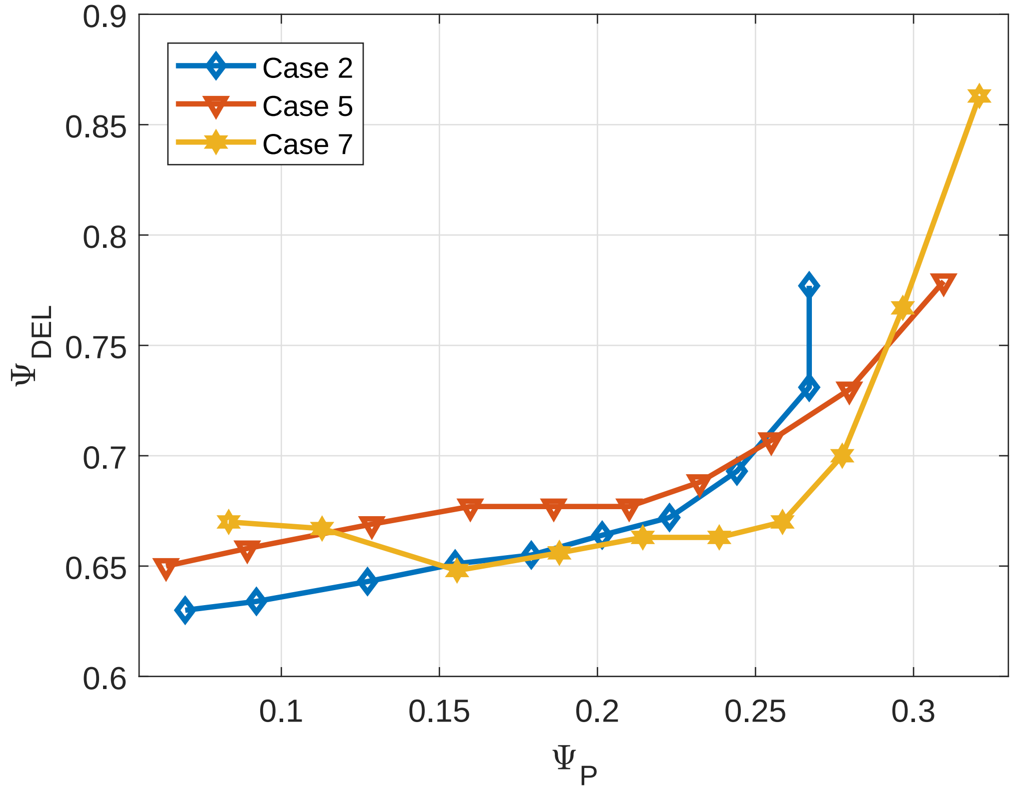

Figure 5.3: Simulated Pareto curves

rainflow counting technique (Downing and Socie, 1982). The DELs are obtained as the constant amplitude loads of fixed amplitude and a frequency of 1 Hz. The first 50 s of the time history load predictions are removed from the analysis to cater to transient effects. The figures clearly show that significant reduction in fatigue DELs can be obtained from the proposed IPC.

Next, the standard deviations of the platform pitch and roll rotations are shown in Figure 5.6. It can be observed that the proposed IPC significantly reduces platform pitch rotation for every different load case investigated here. It is also important to note that the platform roll rotation is also reduced by the proposed IPC.

It is of significant interest to note here that the RMS (root mean square) of the low speed shaft error and generator power error is reduced consistently, (see Figure 5.7a and Figure 5.7b respectively) over the different load cases. This shows that the proposed IPC is better than the baseline controller in regulating power production of the FOWT.

The wave loads effects the dynamic response of the tower most significantly. It can be observed from Figure 5.5c and Figure 5.5d that increasing wave height increases the tower base fore-aft and side-to-side moments. It can be observed from load cases

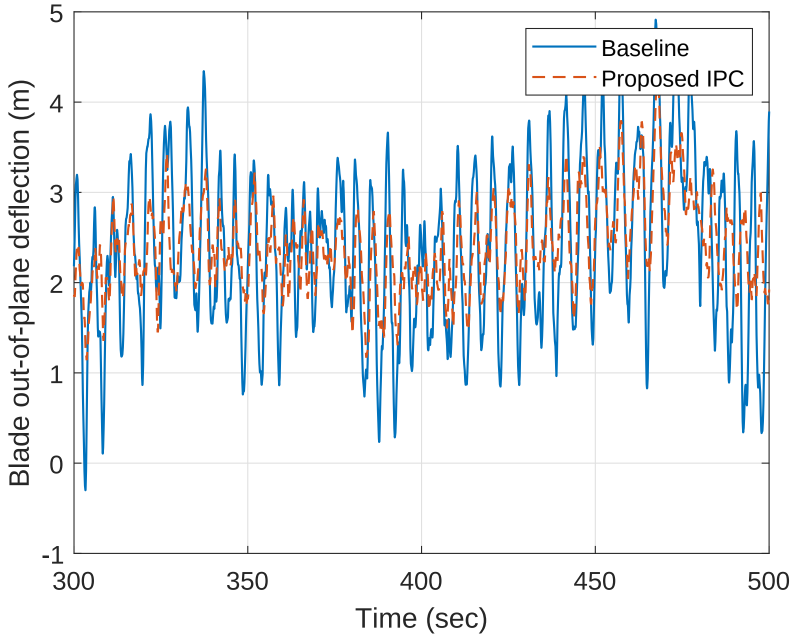

(a)

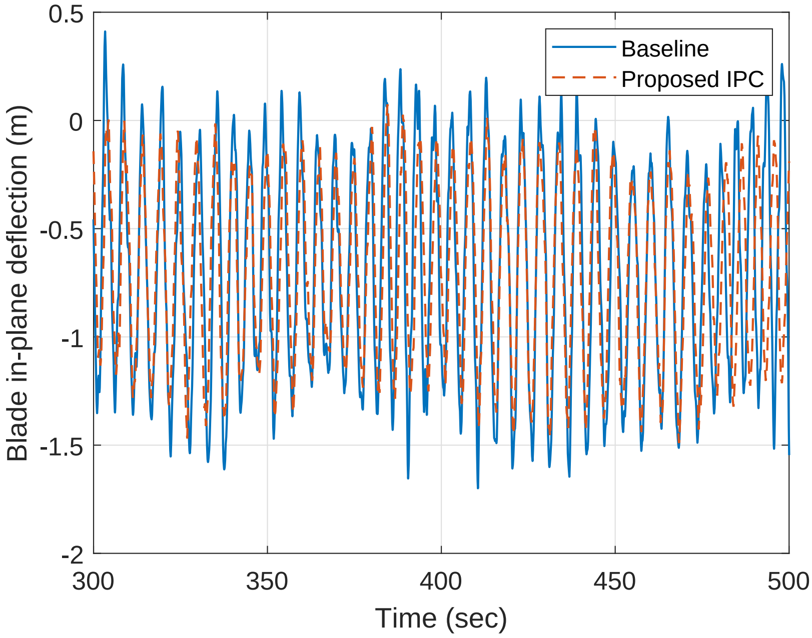

(b)

Figure 5.4: Numerical time histories for load case 7

2, 4 and 6 that the wind-wave miss-alignment significantly increases the tower side-to-side moment and decreases tower fore-aft moment. However, the proposed controller performs better than the baseline controller in achieving the design objectives for the wind-wave misalignment cases. Although wave loads influences the dynamics of the

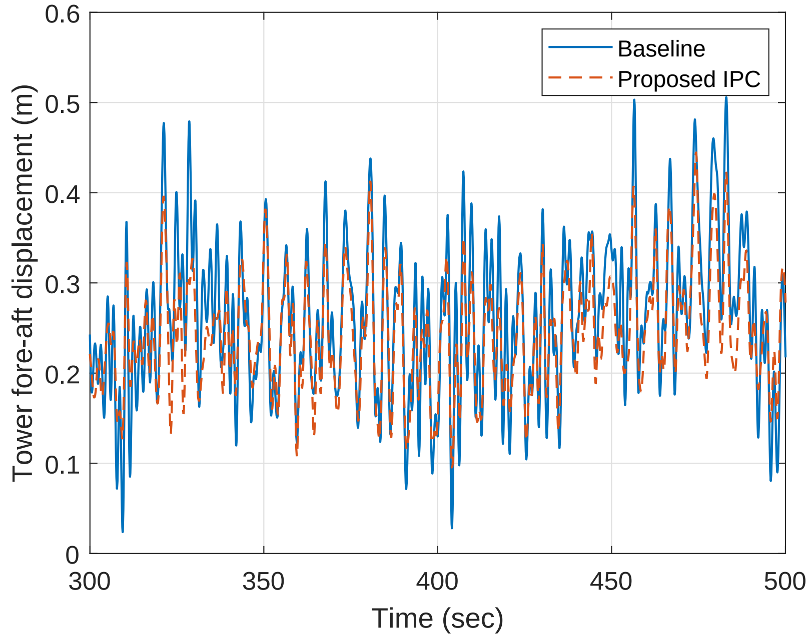

(c)

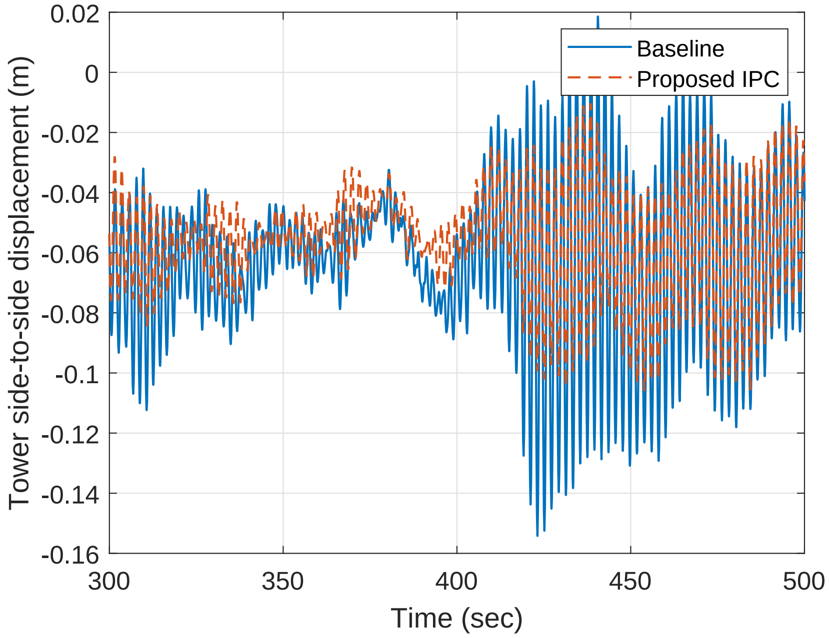

(d)

Figure 5.4: Numerical time histories for load case 7

entire FOWT its effect on the other degrees of freedom is not apparently visible from the results presented here because wind is the primary source of dynamic loads on a spar-type FOWT.

To summarize, the best case, worst case and average reduction in fatigue DELs,

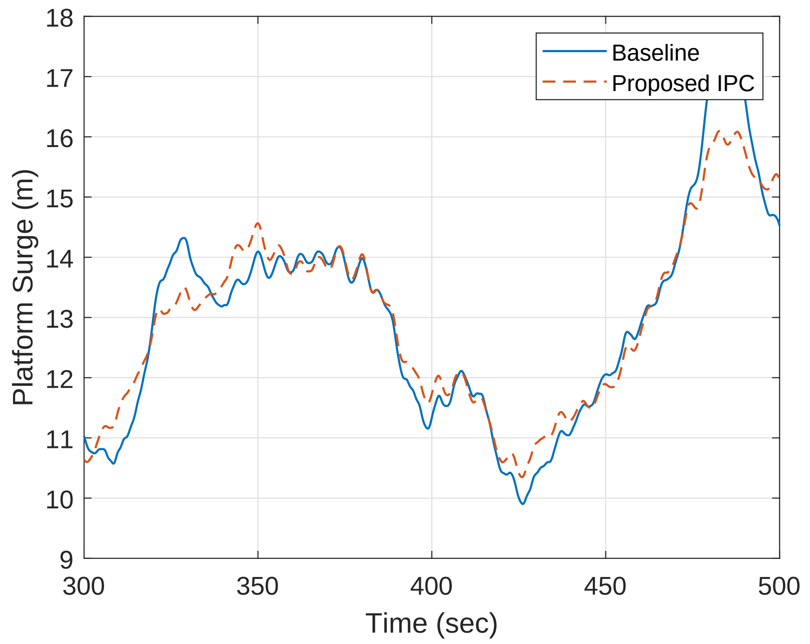

(e)

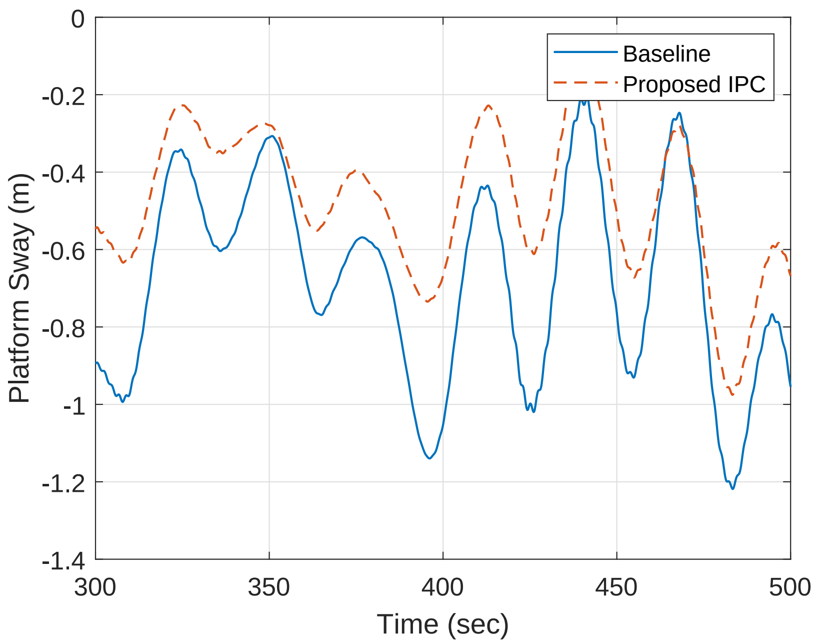

(f)

Figure 5.4: Numerical time histories for load case 7

standard deviations of the platform rotations and the RMS of the rotor speed error and generator power error achieved by the propose IPC over the baseline controller is presented in Table 5.3.

The improvements in the form of reduced loads and improved power regulation is

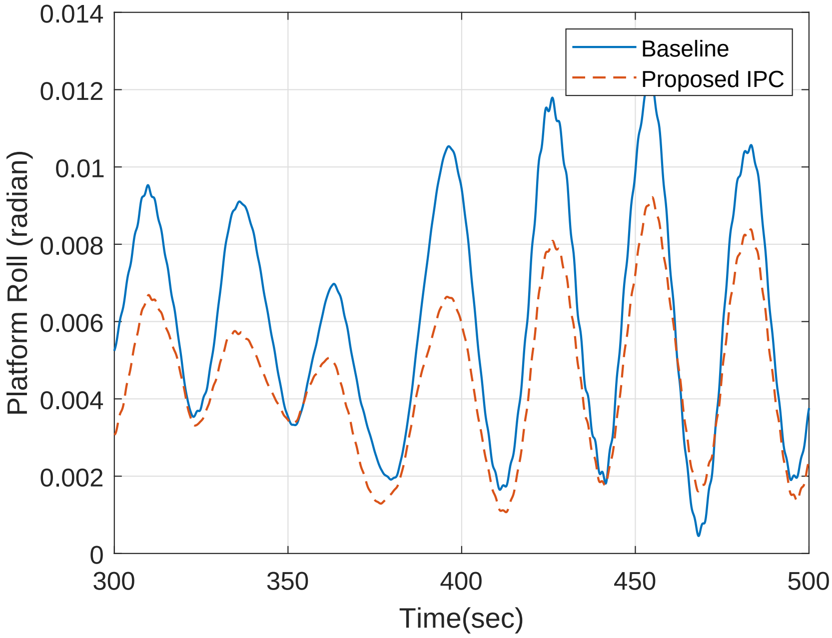

(g)

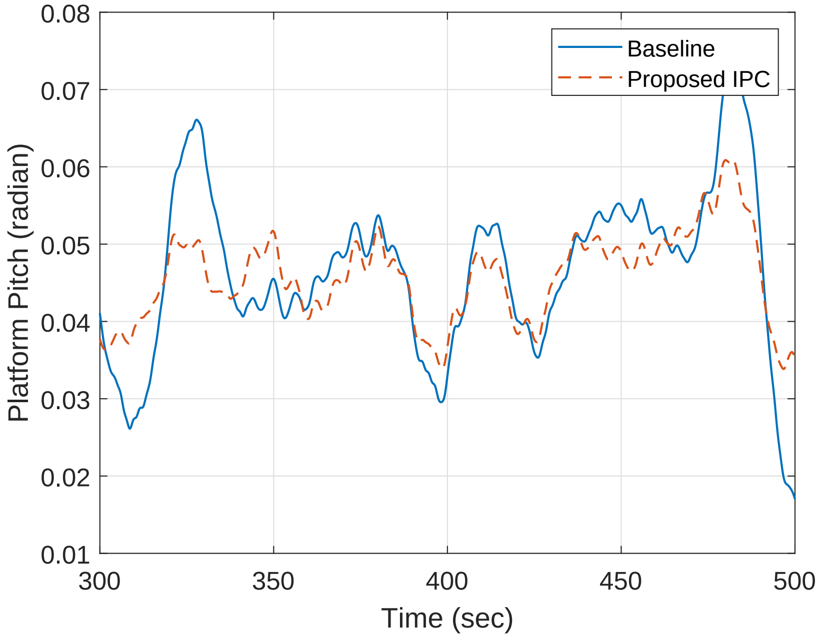

(h)

Figure 5.4: Numerical time histories for load case 7

obtained at a cost of higher pitch actuation. To evaluate this increase an equivalent constant amplitude blade pitch cycle is estimated from the time history predictions of the blade pitch angles using the rainflow counting method. The resulting pitch cycle has a constant amplitude and a frequency of 1 Hz. The constant amplitude obtained

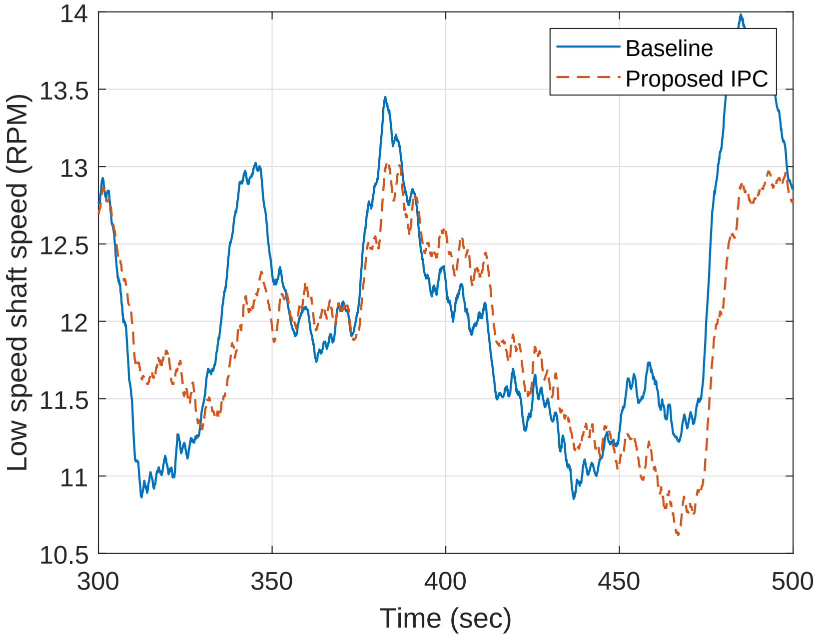

(i)

Figure 5.4: Numerical time histories for load case 7

from the baseline controller in compared against the proposed IPC and presented in Figure 5.8. It can be clearly observed that pitch actuation is higher compared to the baseline controller for all load cases. Also, using the baseline controller the blade pitch actuation reduces with wind speed, however, using the proposed IPC blade pitch actuation increases with wind speed. Although this increase may not be ideal in all situations, with reliable pitch systems the control strategy proposed in this chapter is capable of greatly improving FOWT response and power production.

5.3.3 Comparison against published literature

In this subsection, the proposed IPC is compared against the most popular IPCs available in the literature. For reasonable comparison, it is important to compare the performance of the controllers on the same 5MW OC3 Hywind spar-type offshore wind turbine Jonkman, 2010.

Namik and Stol, 2014 proposed two IPCs, one based on an SFC control strategy and another based on a DAC control strategy. The authors compared the proposed controller against the baseline controller (Jonkman and Buhl Jr, 2005). They reported 9% reduction in tower fatigue DELs over the baseline controller. A massive 64% reduction in power error has also been reported. However, as the authors have mentioned in their

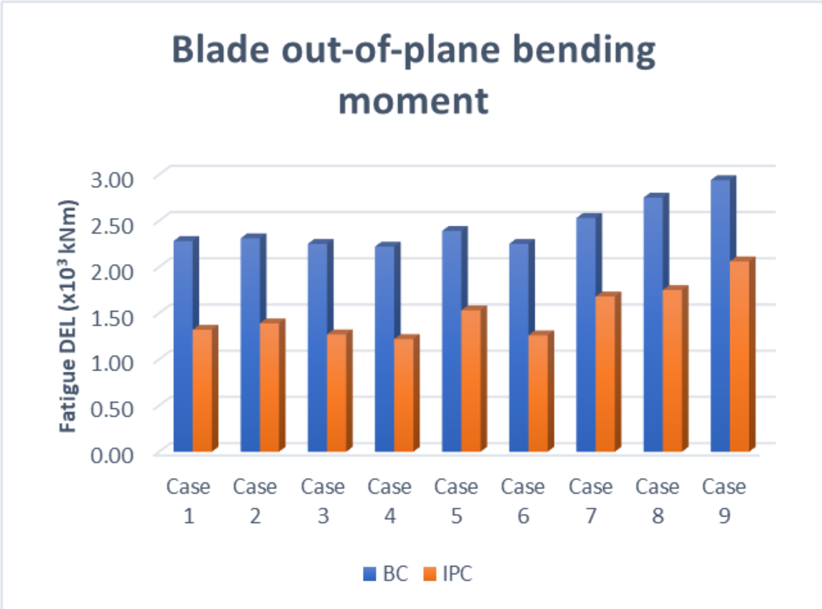

(a)

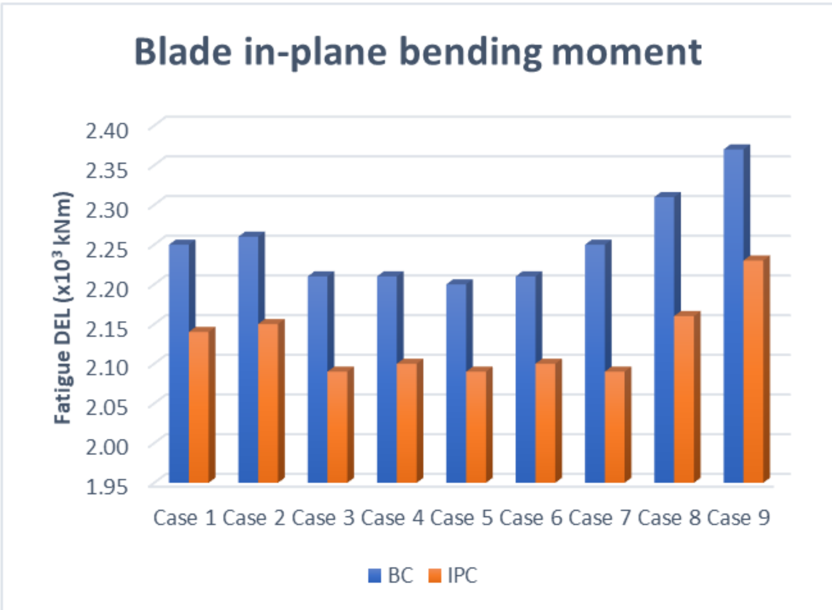

(b)

paper this is due to the use of constant power algorithm used by the generator torque controller and not due to the proposed IPCs. The authors do not report any reduction in the blade fatigue DELs or any improvement in the floating platform response. In comparison, the controller proposed in this chapter achieves greater reductions in fatigue DELs of the blades and the tower. It significantly improves the floating platform response and also improves generator power output using a control torque algorithm which is recommended by Jonkman and Buhl Jr, 2005. The reductions are provided in Table 5.3. It can be observed that the proposed controller performs significantly better

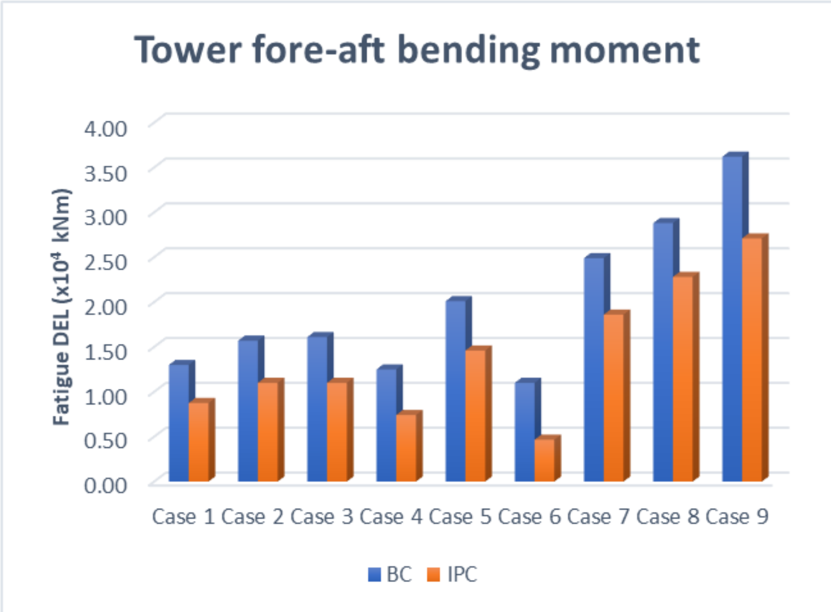

(c)

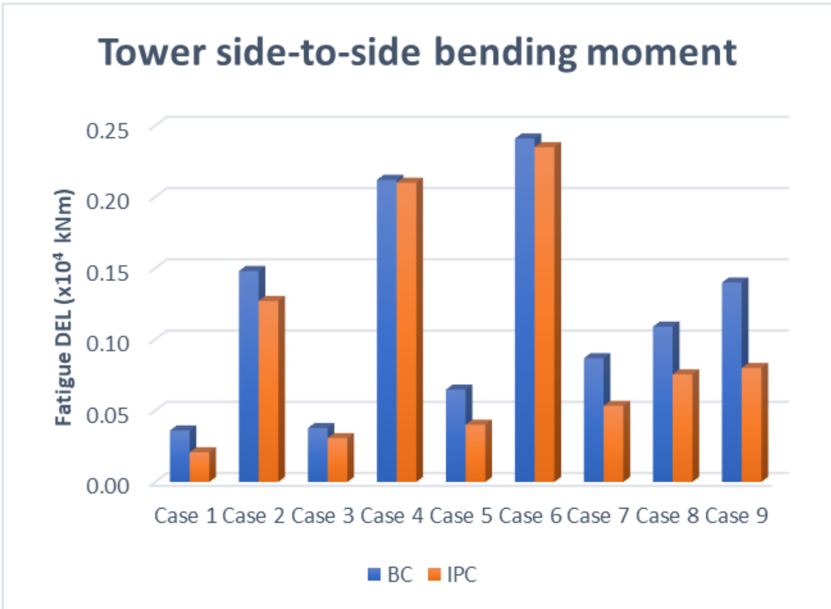

(d)

Figure 5.5: Fatigue DELs

than the one proposed in (Namik and Stol, 2014).

In another paper, Raach et al., 2014 proposed an IPC based on a nonlinear model predictive control strategy. The proposed controller was compared against the baseline controller (Jonkman and Buhl Jr, 2005). They have reported around 18% reduction in blade out-of-plane fatigue DELs and an impressive 77.6% reduction in generated

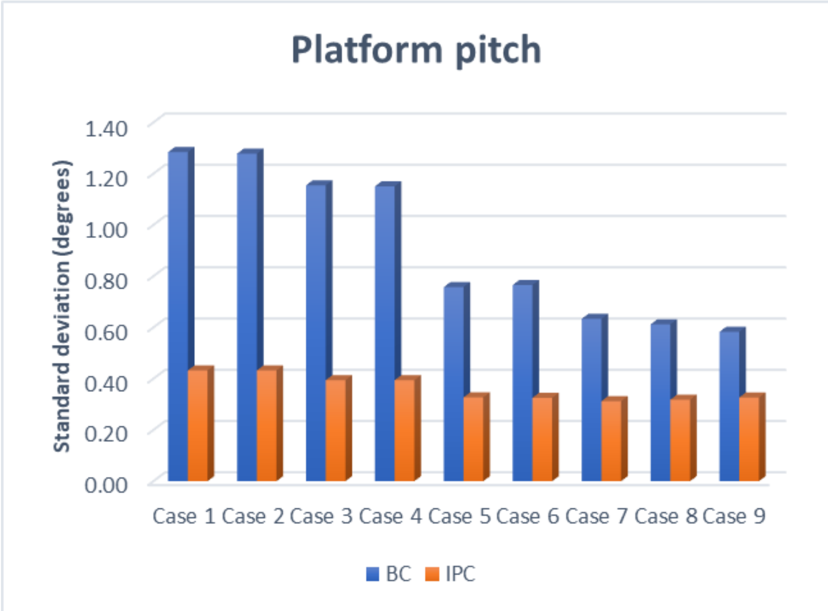

(a)

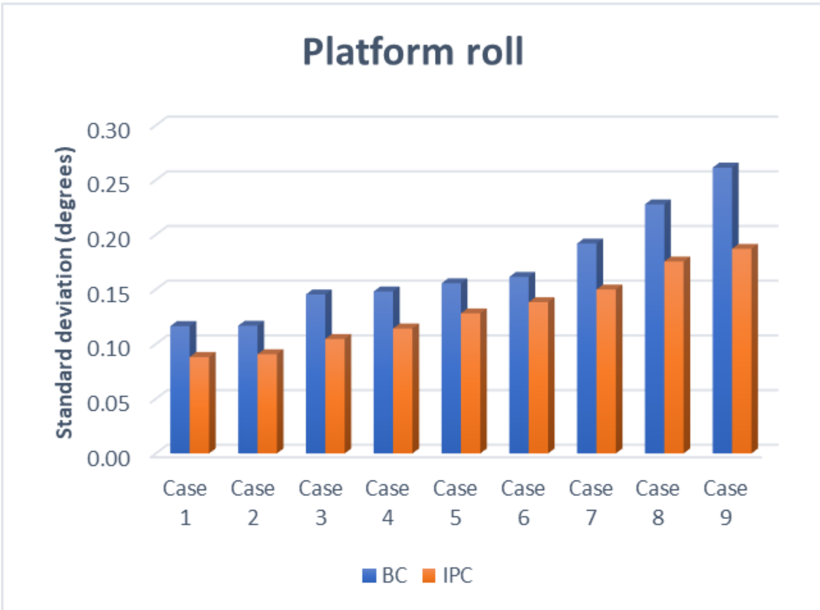

(b)

Figure 5.6: Standard deviations of platform responses

power error. In comparison, the controller proposed in this chapter is better in reducing fatigue DELs although poorer in reducing generator power error. However, this comparison is not reasonable as the NMPC controller requires 1.3s for solving the optimization problem to determine the control input. This considerable time delay will significantly affect the performance of the controller which has not been considered by the authors. Moreover, the authors consider only one load case and the performance

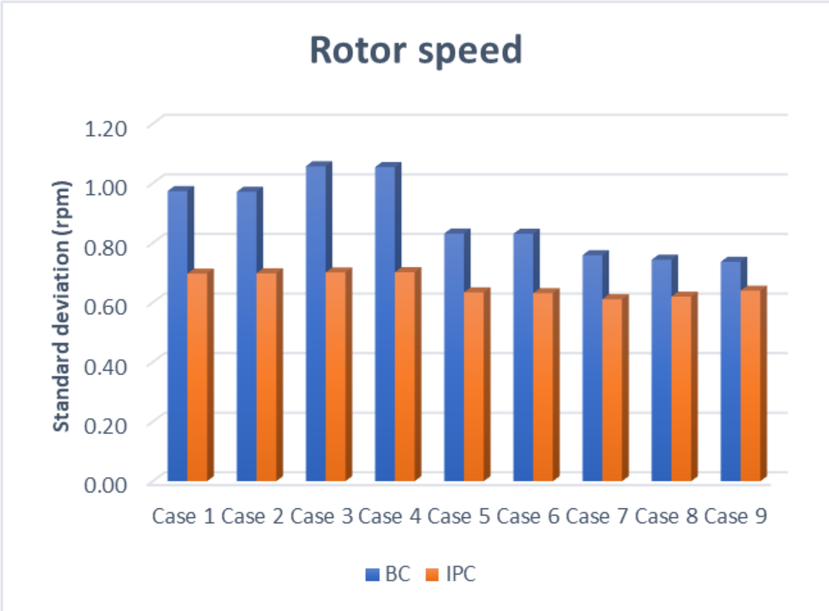

(a)

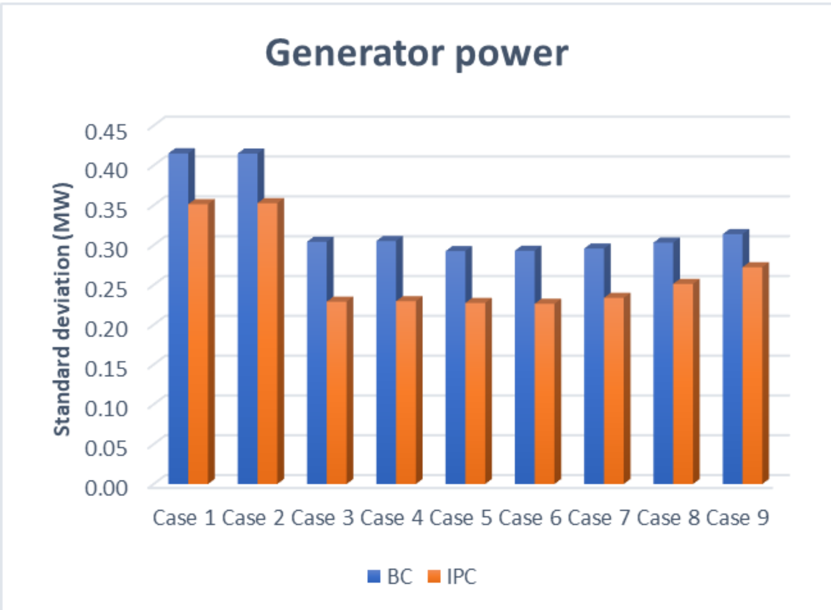

(b)

Figure 5.7: RMS of rotor speed and generator power error

of the controller over the operational region 3 has not been investigated.

5.4 Conclusion

A new individual blade pitch control strategy has been proposed in this chapter that combines a low authority LQ controller with an integral controller to achieve improved

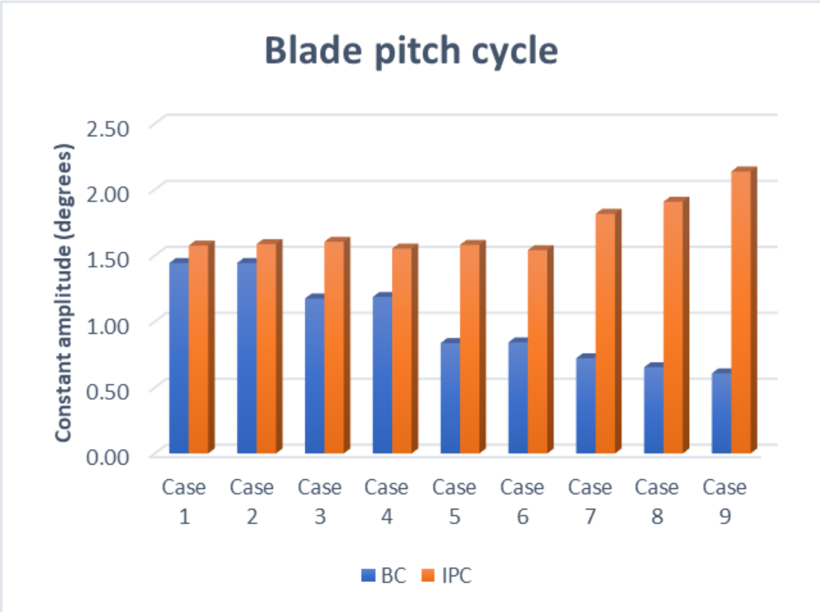

Figure 5.8: Equivalent constant amplitude pitch cycle

Table 5.1: Load Cases

Case No.	Rotor Speed (rpm)	Wind Speed v (m/s)	Wave Height H_s (m)	Wave Direction (degrees)
1	12.1	13	1	0
2	12.1	13	2	30
3	12.1	15	2	0
4	12.1	15	2	60
5	12.1	17	3	0
6	12.1	17	2	90
7	12.1	19	4	0
8	12.1	21	5	0
9	12.1	23	6	0

tracking of the rated rotor speed to optimize power regulation while simultaneously reducing aerodynamic loads on the FOWT. The proposed controller is compared against the baseline controller used by FAST (Jonkman and Buhl Jr, 2005) with the FOWT subjected to various stochastic wind-wave scenarios. It has been shown numerically that the proposed controller performs better than the existing baseline controller and other existing controllers in the literature. The important conclusions to draw from this study are

- The proposed controller is more effective compared to the baseline controller in

Table 5.2: DLC 1.2 Average fatigue DELs

Controller	Blade out-of-plane moment (kNm)	Blade in-plane moment (kNm)	Tower fore-aft moment (kNm)	Tower side-to-side moment (kNm)
BC	2.44E+003	2.25E+003	1.98E+004	1.20E+004
IPC	1.50E+003	2.13E+003	1.40E+004	9.70E+003

Table 5.3: Percentage reduction in standard deviation over baseline controller

Fatigue DELs and responses		Best case	Worst case	Average
Platform RMS	Pitch	66	44	58
	Roll	28	14	23
Fatigue DELs	Tower fore aft bending moment	58	21	32
	Tower side to side bending moment	43	1	25
	Blade out of plane bending moment	45	30	39
	Blade in plane bending moment	7	5	6
Generator error RMS	Rotor speed	34	13	25
	Generator power	25	13	20

reducing the variability in the rotor speed thus improving the power production of the FOWT. Unlike the IPCs available in literature, the proposed controller is capable of simultaneously mitigating FOWT structural responses and rotor power variability.

- The simple and intuitive nature of the controller makes it easy to design. The successful use of a reduced order model of the FOWT and a linearized approximation of the control influence matrix shows that exact information of the fully non-linear wind turbine model is not required to design an effective controller.

- The proposed controller is equally effective for cases with wind-wave misalignment.

- Significant reduction in blade vibrations and platform motion is observed. Excessive blade vibrations and platform motion are critical for functionality of the wind turbine. Hence, the reductions achieved by the proposed controller can significantly improve the performance of the FOWT.

- As shown in this chapter, this improvement in performance, notably the reduction of 1P oscillation of the aerodynamic loads is achieved at an expense of increase blade pitch actuation, especially at higher wind speeds. However, this is always well within saturation limits.

Chapter 6

Optimizing blade pitch actuation using Nonlinear Model Predictive Control

It has been shown in the previous chapters that the blade pitch control strategies aimed at reducing aerodynamic loads typically comes at the cost of increased pitch actuation. The control strategies proposed in Chapter 4 and 5 were excellent in mitigating aerodynamic loads on the turbine, hence, reducing the turbine and platform vibrations, but at a cost of increased pitch actuation. However, it is known (Valpy et al., 2017) that the blade bearings and pitch systems are a significant source of turbine downtime. Innovations that increase the load cycles on the pitch systems will only compound this problem. Design of pitch systems has evolved slowly over the last 10 years and during this time turbines have been continuously up scaled. These large wind turbines can create problems in manufacturing. One way to reduce this downtime is innovations in improving bearing concepts and lubrication, improved hydraulic and electrical systems. However, with the current pitching systems, innovations in pitch control strategies that reduce pitch actuation may a solution. It would help in reducing cost of production of expensive pitching systems.

Following the above discussion, this chapter is dedicated to the development of an individual pitch control strategy under a mathematically optimal framework to reduce pitch actuation without compromising on tracking of rated rotor speed and structural vibrations. In other words, the aim of the controller is to optimize pitch actuation, i.e., minimizing blade pitch actuation while maintaining/improving baseline performance. The controller is developed in a Non-linear Model Predictive Control (NMPC) framework. It is assumed that a preview of the inflow wind field is available in the form of LIDAR (LIght Detection And Ranging) wind speed measurements. The details on the working of a LIDAR is not in the scope of this study. The interested reader may refer (Lindelöw et al., 2008) for details on LIDAR technology. In this work the assumed LIDAR measurements are obtained directly from a wind field generated using TurbSim (Jonkman, 2009). To include the pitch actuators in the controller design, linear uncoupled single degree of freedom pitch actuator models provided by equation 6.1 are included in the 22-DOF dynamic model derived in Chapter 3.

$$m_{act}\ddot{\beta}_i + c_{act}\dot{\beta}_i + k_{act}\beta_i = k_{act}\beta_i^c \qquad \text{for } \ i = 1 \text{ to } 3 \tag{6.1}$$

Where, m_{act}, c_{act} and k_{act} are the actuator inertia, damping and stiffness terms respectively obtained from (Jonkman and Buhl Jr, 2005). The following sections present the deign of the controller followed by an evaluation of its performance.

6.1 Non-linear model predictive control of blade pitch angles

A model predictive controller predicts the future behaviour of a system based on the current measurements, disturbance preview and an internal model. The objective of the controller is to solve the optimal control problem over a selected horizon. A part of this control input is sent to the actual system, new measurements are gathered and the optimal control problem is solved again. The core of the model predictive controller is an optimization problem that minimizes a predefined cost function by optimizing the control input over a selected horizon. This basic concept of model predictive control is applicable to both linear and non-linear systems alike. Since the 1980s, linear MPC (for linear systems) has been applied successfully for many industrial applications (Findeisen, 2005). However, in certain cases the system presents strong non-linearities that cannot be neglected. In those situations non-linear model predictive control (NMPC) can significantly improve performance by considering the non-linearities of the system.

Amongst the various advantages of NMPC, perphaps the biggest one is that the controller is mathematically optimal. Further, it can handle multi-variable and non-quadratic problems; the disturbance preview can be defined dynamically; constraints on actuators and the state can be defined inherently in the problem. However, solving the optimal control (optimization) problem is not trivial and several methods exist. Two of the most popular methods are Sequential Quadratic Programming (SQP) and Interior-Point Methods (IPM). These control algorithm are not trivial and the authors suggest referring to specialized literature like (Nocedal and Wright, 2006) for thorough understanding. In this study, the solvers are borrowed from the Optimization Toolbox in (MATLAB, 2018). Several other optimization toolboxes are also available such as (Franke, 1998; Löfberg, 2004; Mosek, 2015), that can be used to solve the optimal control problem.

6.1.1 Reduced order internal model

Model predictive control contains an internal model of the system embedded in the controller that is used to predict the future state of the system for a control sequence $\mathbf{u}(\cdot)$. For continuous time system the control system is obtained in the form

$$\dot{\mathbf{x}} = f(t, \mathbf{x}, \mathbf{u}) \tag{6.2}$$

For a complicated multi-degree of freedom systems the dynamics of the overall system is often approximated by a reduced order model of the system dynamics. In this work, a nine degree of freedom reduced order internal model is used to design the controller. Since the along wind components of the wind turbine experiences the majority of the aerodynamic loads the nine degrees of freedom primarily consists of the along wind components of the wind turbine. The selected degrees of freedom are: the platform pitching degree of freedom (q_P), the tower fore-aft bending mode (q_T), the out-of-plane bending mode of the three blades (q_{Bi} for $i = 1, 2, 3$), the generator azimuth angle (q_{GeAz}) and the three blade pitch actuator motion (β_i for $i = 1, 2, 3$). The state vector can be given as

$$\mathbf{x} = [q_P,\ q_T,\ q_{B1},\ q_{B2},\ q_{B3},\ q_{GeAz},\ \beta_1,\ \beta_2,\ \beta_3]' \tag{6.3}$$

For simplicity of the internal model, the generator degree of freedom is de-coupled from the other degrees of freedom. Similarly, the blade pitch actuators are modelled as single degree of freedom linear models. The blade pitch actuators are also de-coupled from the rest of the system. A similar approach can be observed in (Schlipf, Schlipf, and Kühn, 2013). Since the platform pitching angles are small, the coupled motion of the platform, tower and blades is simplified by ignoring the quadratic and higher order

q_P terms. The final equations of motion of the internal model is obtained as

$$m_{PP}\ddot{q}_P + m_{PT}\ddot{q}_T + \sum_{i=1}^{3} m_{PBi}\ddot{q}_{Bi} + c_{PP}\dot{q}_P + k_{PP}q_P = f^P_{Aero}(u_0, \beta) \tag{6.4a}$$

$$m_{PT}\ddot{q}_P + m_{TT}\ddot{q}_T + \sum_{i=1}^{3} m_{TB}\ddot{q}_{Bi} + c_{TT}\dot{q}_T + k_{TT}q_T = f^T_{Aero}(u_0, \beta) \tag{6.4b}$$

$$m_{TBi}\ddot{q}_{Bi} + m_{BB}\ddot{q}_{Bi} + c_{BB}\dot{q}_{Bi} + k_{BB}q_{Bi} = f^{Bi}_{Aero}(u_0, \beta_i) \qquad \text{for } \; i = 1 \text{ to } 3 \tag{6.4c}$$

$$I_{DT}\ddot{q}_{GeAz} + GBRatio \cdot GenTrq(t, q_{GeAz}) = AeroTrq(u_0, \beta) \tag{6.4d}$$

$$m_{act}\ddot{\beta}_i + c_{act}\dot{\beta}_i + k_{act}\beta_i = k_{act}\beta^c_i \qquad \text{for } \; i = 1 \text{ to } 3 \tag{6.4e}$$

where, the rotational inertia of the platform can be given as

$$\begin{aligned} m_{PP} = 12H_t^2 \int_0^L \mu^B(r)\mathrm{d}r + \sum_{i=1}^{3} \Bigg[4H_t \int_0^L r\mu^B(r)\mathrm{d}r \cos(\psi_i) \\ + \int_0^L r^2\mu^B(r)\mathrm{d}r \cos^2(\psi_i) \Bigg] + H_t^2(m^N + m^H) + I_P + I_P^{AM} \end{aligned} \tag{6.5}$$

The inertial coupling between the platform and tower can be given as

$$m_{PT} = 6H_t \int_0^L \mu^B(r)\mathrm{d}r + \int_0^{H_t} h\mu^T(h)\phi_t(h)\mathrm{d}h \tag{6.6}$$

The inertial coupling between the platform and the blades can be given as

$$m_{PBi} = 2H_t \int_0^L \phi_b(r)\mu^B(r)\mathrm{d}r + \int_0^L r\phi_b(r)\mu^B(r)\mathrm{d}r \cos(\psi_i) \qquad \text{for } i = 1 \text{ to } 3 \tag{6.7}$$

The inertial coupling between the tower and the blades can be given as

$$m_{TB} = \int_0^L \phi_b(r)\mu^B(r)\mathrm{d}r \tag{6.8}$$

The translational inertia term of the tower fore-aft degree of freedom can be given as

$$m_{TT} = 3\int_0^L \mu^B(r)\mathrm{d}r + \int_0^{H_t} \phi_t^2\mu^T(h)\mathrm{d}h + m^N + m^H \tag{6.9}$$

The translational inertia term associated with blade flapwise degree of freedom can be given as

$$m_{BB} = \int_0^L \phi_b(r)^2 \mu^B(r)\mathrm{d}r \tag{6.10}$$

Where, H_t is the height of the tower and L is the length of the blades. $\mu^B(r)$ and $\mu^T(h)$ are mass per unit length of the blades and tower respectively. ψ_i is the azimuth angle of the i^{th} blade. I_P is the rotational inertia of the platform and I_P^{AM} is the hydrodynamic added mass coefficient associated with the platform pitch degree of freedom. $\phi_b(r)$ and $\phi_t(h)$ are the normalized fundamental model shapes of the blades and tower in the flapwise and fore-aft directions respectively. c_{PP} is the linear hydrodynamic damping coefficient associated with the platform pitch degree of freedom, c_{TT} and c_{BB} are structural damping coefficient of the tower and the blades respectively. k_{PP} is the summation of hydro-static and linearized mooring lines stiffness associated with the platform pitch degree of freedom. k_{TT} is the elastic stiffness of the tower and $k^i_{BB} = k^e_{BB} + k^c_{BB} + k^g_{BB}\cos(\psi_i)$ is the summation of the elastic stiffness, ,k^e_{BB}, centrifugal stiffness, k^c_{BB}, and, gravitational stiffening/softening, k^g_{BB}, of the i^{th} blade. More details on these terms can be found in (Fitzgerald, Basu, and Nielsen, 2013; Fitzgerald, Sarkar, and Staino, 2018; Sarkar and Chakraborty, 2018). The above equations can be rearranged in the form of equation 6.2 for numerical evaluation.

The aerodynamic loads on the wind turbine is usually estimated using the Blade Element Momentum (BEM) theory. However, the internal model must be as simple as possible for implementation. For this purpose the aerodynamic loads on the wind turbine are estimated a-priori. The loads are obtained as a polynomial function of the effective wind speed (u_0) and blade pitch angles (β) by polynomial surface fitting of BEM results for various wind speeds and blade pitch angles. The reduced order model requires the information of the effective wind speed experienced by the blade in a way that encapsulates the information of the total wind field that the blade is subjected to. Hence, an effective wind speed is defined as

$$u_0 = \sqrt[3]{\frac{\int_0^L u(r)^3 \frac{\partial c_p}{\partial r} r\mathrm{d}r}{\int_0^L \frac{\partial c_p}{\partial r} r\mathrm{d}r}} \tag{6.11}$$

Where, $\frac{\partial c_p}{\partial r}$ is the spanwise variation of power extraction factor obtained by modelling tip and hub losses following (Burton et al., 2011) shown in Figure 6.1. Figure 6.2 to Figure 6.5 show the aerodynamic loads on the blades, tower and platform obtained from BEM theory for different effective wind speeds and blade pitch angles.

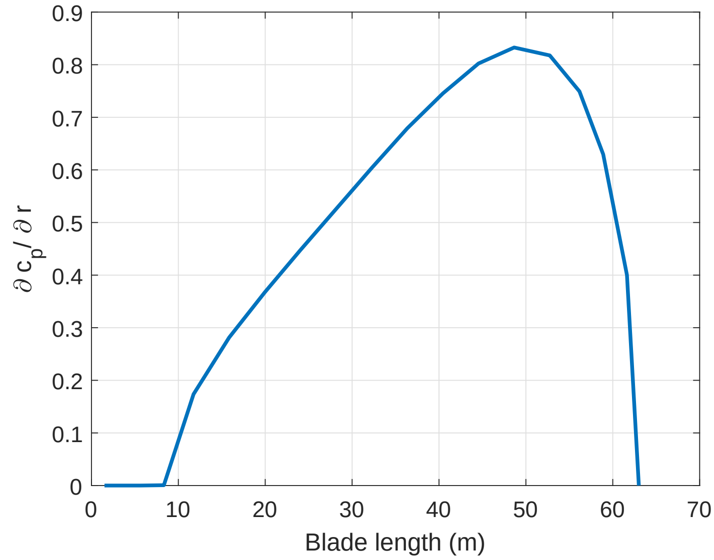

Figure 6.1: Spanwise variation of power extraction

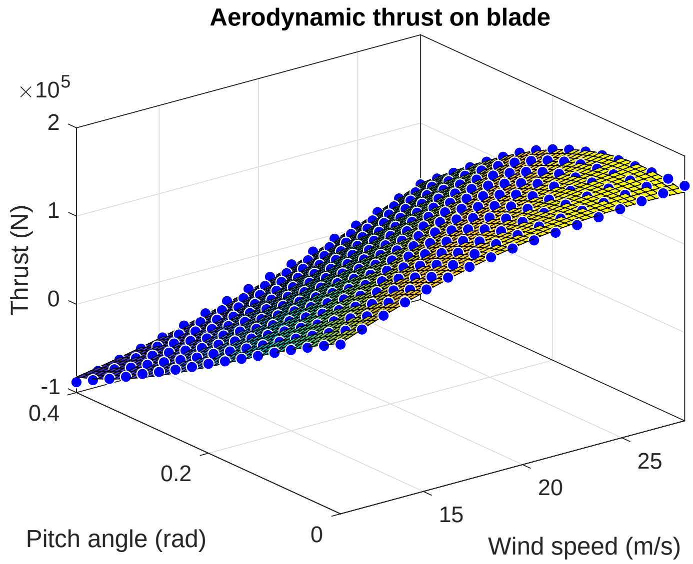

Figure 6.2: Aerodynamic thrust on the blade

6.1.2 Definition of the optimal control problem

The objective of the optimal control problem is to minimize a cost function J_{OCP} defined over a time horizon t_0 to T_f. The cost function is minimized by solving for an optimal control input trajectory $\mathbf{u}(\cdot)$ that minimizes the cost function in the presence of disturbance $\mathbf{d}(\cdot)$ subjected to a set of non-linear constraints that includes the dynamics of the internal model, the initial measurements and a set of non-linear constraints H that ensure feasible operational range. The optimization problem in continuous time

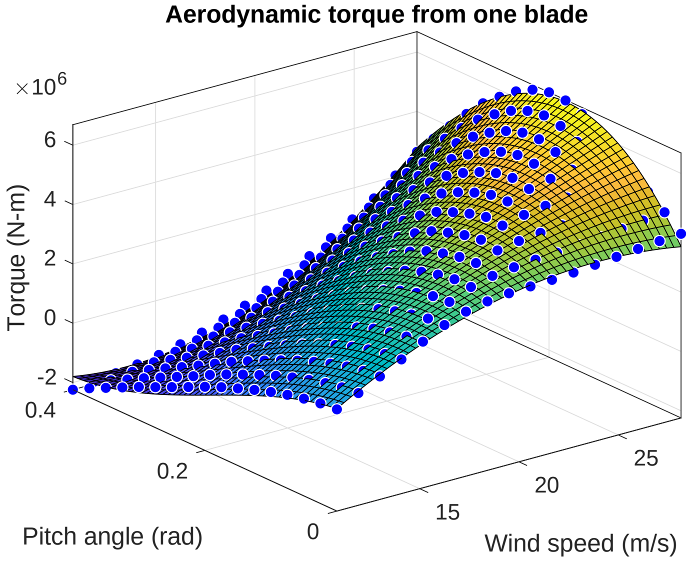

Figure 6.3: Aerodynamic torque from blade

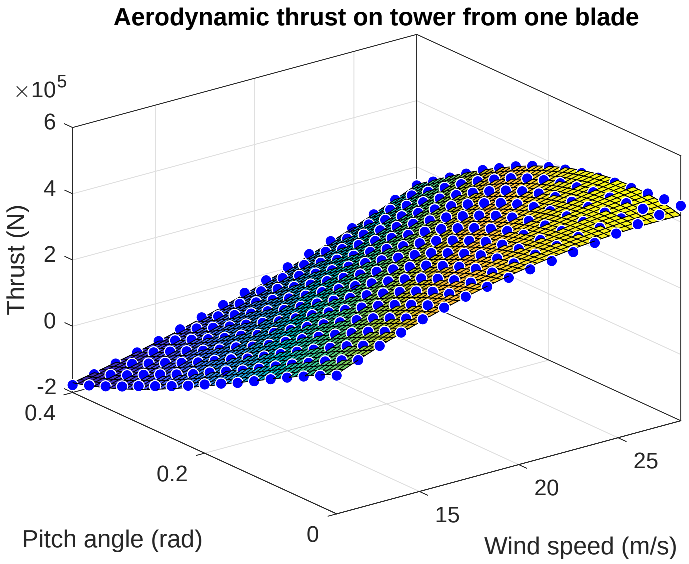

Figure 6.4: Aerodynamic thrust on tower

can be described as

$$
\begin{aligned}
& \min_{\mathbf{u}(\cdot)} J_{OCP}(\mathbf{x},\mathbf{u},\mathbf{d}) \\
\text{with:} \quad & J_{OCP}(\mathbf{x},\mathbf{u},\mathbf{d}) = \int_{t_0}^{t_0+T_f} \Pi(\mathbf{x}(\tau),\mathbf{u}(\tau),\mathbf{d}(\tau))\mathrm{d}\tau \\
\text{s.t.} \quad & \dot{\mathbf{x}} = f(\mathbf{x},\mathbf{u},\mathbf{d}) \\
& \mathbf{x}(t_0) = \mathbf{x}_0 \\
& H(\mathbf{x}(\tau),\mathbf{u}(\tau),\mathbf{d}(\tau)) \geq 0 \quad \forall \tau \in [t_0, t_0 + T_f]
\end{aligned}
\tag{6.12}
$$

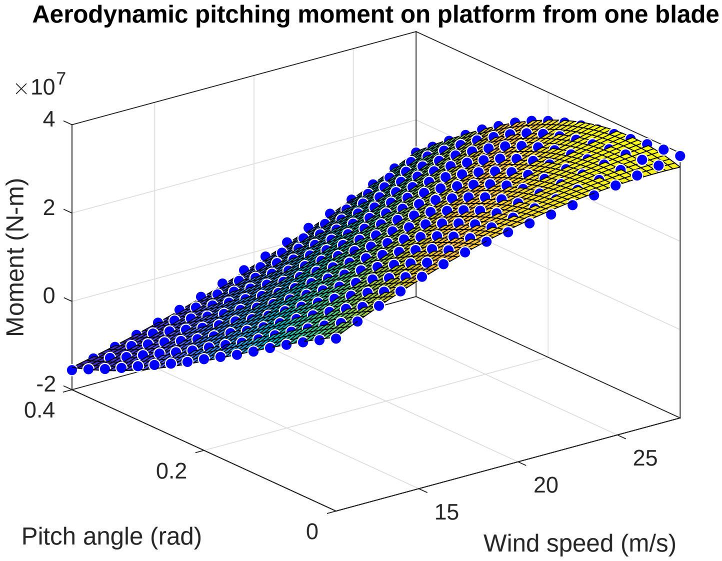

Figure 6.5: Aerodynamic pitching moment on platform

The most crucial part of designing a NMPC controller is proper mathematical description of the controller aim and then translating it into a cost function and a set of constraints. The primary aim of the present controller is to minimize blade pitch actuation while maintaining tracking of rated power at above rated wind speeds. The secondary objectives are to minimize platform pitching motion, the fore-aft bending of the tower and the flapwise bending of the blades. However, the aim of the controller is to achieve these goals at a reduced pitch actuation compared to the baseline controller.

The objective function is defined as a quadratic function of system states multiplied with independent weights to emphasise on the different control objectives. The objective function is defined as

$$\Pi(\mathbf{x}(\tau), \mathbf{u}(\tau), \mathbf{d}(\tau)) = \quad Q_1(\dot{q}_{GeAz} - \Omega_{rated})^2 \tag{6.13}$$

$$+ Q_2(P(t) - P_{rated})^2 \tag{6.14}$$

$$+ Q_3\dot{q}_T^2 \tag{6.15}$$

$$+ Q_4\dot{q}_P^2 \tag{6.16}$$

$$+ [\dot{q}_{B1}\ \dot{q}_{B2}\ \dot{q}_{B3}]\mathbf{Q}_5[\dot{q}_{B1}\ \dot{q}_{B2}\ \dot{q}_{B3}]' \tag{6.17}$$

$$+ [\dot{\beta}_1\ \dot{\beta}_2\ \dot{\beta}_3]\mathbf{Q}_6[\dot{\beta}_1\ \dot{\beta}_2\ \dot{\beta}_3]' \tag{6.18}$$

In the above equation, Ω_{rated} and P_{rated} are the rated rotor speed and power output of the 5MW FOWT. The weights Q_1 and Q_2 penalises the rotor speed error and rated power error respectively. The velocity of tower fore-aft motion is penalised with

Q_3 and the platform pitching velocity is penalised with the weight Q_4. $\mathbf{Q}_5$ and $\mathbf{Q}_6$ are diagonal matrices defined to penalise the blade flapwise velocity and blade pitch actuator velocities respectively.

Next, the set of constraints H that guarantees the feasible range of operation of the wind turbine is defined as

$$H := \begin{array}{l} \beta_i^{min} \leq \beta_i \leq \beta_i^{max} \\ -\dot{\beta}_i^{max} \leq \dot{\beta}_i \leq \dot{\beta}_i^{max} \\ T_g^{min} \leq T_g \leq T_g^{max} \\ \dot{T}_g^{max} \leq \dot{T}_g \leq \dot{T}_g^{max} \end{array} \tag{6.19}$$

where, β_i^{min} and β_i^{max} and the minimum and maximum pitch angles respectively. T_g^{min} and T_g^{max} are the minimum and maximum allowable generator torque respectively. And $\dot{\beta}_i^{max}$ and $\dot{T}_g^{max}$ are the maximum allowable pitch and torque rate respectively.

The NMPC needs a preview of the blade effective wind speed over the prediction time T_f. In simulations, this is obtained easily from TurbSim (Jonkman, 2009) wind fields using equation 6.11. In reality, nacelle mounted LIDAR systems are capable of scanning the incoming wind field. It is possible to extract a rotor effective wind speed from the raw data delivered by such a LIDAR system. This procedure is out of scope of the current study and a description is presented in (Schlipf, Schlipf, and Kühn, 2013). MATLAB's constrained non-linear programming solver `fmincon` has been used here to solve the optimal control problem. Sequential Quadratic Programming algorithm has been used in `fmincon` to minimize the cost function in equation 6.12. The prediction horizon is chosen to be $T_f = 12$ s which is a reasonable assumption (refer (Schlipf, Schlipf, and Kühn, 2013)). LIDAR measurement update rate has been assumed to be $\Delta t_L = 0.5$ s. The time steps in the NLP are set equal to $\Delta t_{NLP} = 1.2$ s, in 11 stages. This implies that the optimization is repeated with new measurements each 0.5 s to close the control loop. The differential equations are solved with a fourth-order explicit Runge-Kutta method.

Recursive elimination method is used to solve the optimal control problem in equation 6.12. In this method, the problem is divided into two sub-problems and they are solve separately using specialized methods. The fundamental principle of this method is to decouple the dynamics of the control system, equation 6.2, from the non-linear optimization problem (NLP).

The hierarchy of the problem is shown in Figure 6.6. A specialized solution method, like numerical solvers for ordinary differential equations can be used to evaluated the dynamics of the control system for a given sequence of control input $\mathbf{u}(\cdot)$ and initial

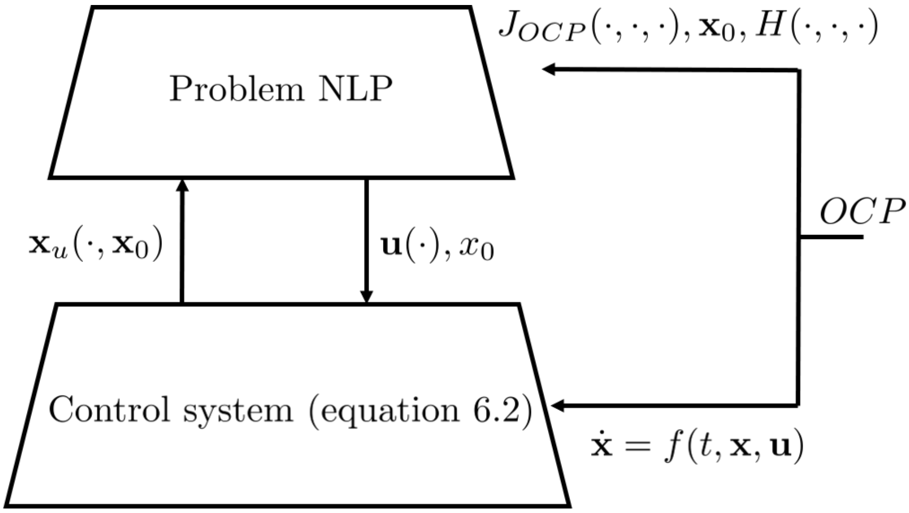

Figure 6.6: Computation hierarchy and communication of data between elements

measurements $\mathbf{x}_0$. Therefore, the interaction between the two sub-problems consists of sending the control sequence $\mathbf{u}(\cdot)$ from the NLP solver to the solver of the dynamics of the control system which in turn returns the computed state sequence $\mathbf{x}_u(\cdot,\mathbf{x}_0)$ back to the NLP solver. The communication between the two elements is also shown in Figure 6.6.

A practical challenge from an implementation point of view is that the control input obtained from NMPC is discrete in nature. Since, the pitch actuator model is stiff, applying the control inputs in their original discrete form can amplify actuator motion due to the transient effect arising from step jumps in commanded pitch angles. To avoid this problem two steps are taken. Firstly, the commanded pitch angles are obtained by interpolating between the inputs of two stages. Hence, a step change in control input is transformed into a linear change. And secondly, the control input is passed through a single-pole low-pass filter with exponential smoothing (Jonkman and Buhl Jr, 2005) to eliminate high frequency variations in the control input. These two steps are crucial for the design of the controller as the pitch actuator model is stiff and any discrete change in the control input results in amplified motion of the pitch actuators which must be avoided to fulfil the design goals.

The proof of closed loop stability of the non-linear constrained system solved by a model predictive controller is beyond the scope of this work and is quite complicated as J_{OCP} has to be a local Lyapunov function. There are theoretical approaches and practical recommendations to ensure stability, but the results presented in this section will show that there is no stability problem in this case. The NMPC controller needs the measured state vector x_0 at the start of each optimization. Here, the measurements include, velocity and rotation of platform pitch, velocity and displacement of the tower top in the fore-aft direction, the generator rotation speed, the blade flapwise velocity and displacement and the blade pitching velocity and displacement.

The long-term performance of the controller is evaluated in this chapter from fatigue load analysis on the pitch actuator, the blades and the tower. A long-term probability distribution of the met-ocean parameters is hence described in the next section. Then, the performance of the controller is evaluated numerically in Section 6.3.

6.2 Joint distribution of U_w, H_s and T_p

To estimate the long-term distribution of environmental loads a joint probability distribution of the wind speed (U_w), wave height (H_s) and wave period (T_p) is required to estimate the occurrence of each event. Every event is described by a combination of wind and wave condition. The joint probability distribution used in this study is obtained from (Li, Gao, and Moan, 2015). The paper presents the long-term joint distribution parameters for five sites, three of them facing the Atlantic ocean and two of them in the North Sea. The distribution parameters are estimated by fitting analytical distributions to hindcast wind and wave data recorded between 2001 and 2010. These long-term joint distributions can be used to estimate wind and wave power at each sites and also to estimate fatigue life of structures.

The joint distribution consists of a marginal distribution of the mean wind speed (U_w), a conditional distribution of wave height (H_s) given the wind speed (U_w) and a conditional distribution of wave period (T_p) given the wave height (H_s). A conditional distribution of T_p given H_s and U_w can be obtained, however, as shown in (Li, Gao, and Moan, 2015) the dependency of the distribution parameters for T_p on U_w is limited, specially at higher wind ranges. Hence, the authors proposed a simplified version of the distribution parameters of T_p dependent only on H_s. The resulting joint distribution can be obtained as

$$f_{U_w,H_s,T_p}(u,h,t) = f_{U_w}(u) \cdot f_{H_s|U_w}(h|u) \cdot f_{T_p|H_s}(t|h) \tag{6.20}$$

The marginal distribution of mean wind speed is approximated by a two-parameter Weibull distribution. The probability density function (PDF) is given as

$$f_{U_w}(u) = \frac{\alpha_U}{\beta_U}\left(\frac{u}{\beta_U}\right)^{\alpha_U-1} \exp\left[-\left(\frac{u}{\beta_U}\right)^{-\alpha_U}\right] \tag{6.21}$$

where, α_U and β_U are the shape and scale parameters respectively, and u is the wind speed.

The conditional distribution of H_s is given as a two-parameter Weibull distribution

$$f_{H_s|U_w}(h|u) = \frac{\alpha_H}{\beta_H}\left(\frac{h}{\beta_H}\right)^{\alpha_H - 1} \exp\left[-\left(\frac{h}{\beta_H}\right)^{\alpha_H}\right] \tag{6.22}$$

where, α_H and β_H are the shape and scale parameters of the Weibull distribution respectively, given as

$$\begin{aligned} \alpha_H &= a_1 + a_2 u^{a_3} \\ \beta_H &= b_1 + b_2 u^{b_3} \end{aligned} \tag{6.23}$$

where, $a_1,\ a_2,\ a_3,\ b_1,\ b_2$ and b_3 are the distribution parameters estimated from non-linear curve fitting to the raw data. For details please refer (Li, Gao, and Moan, 2015).

And lastly, the conditional distribution of T_p given H_s is approximated by a log-normal distribution given as

$$f_{T_p|H_s}(t|h) = \frac{1}{\sqrt{2\pi}\sigma_T t} \exp\left[-\frac{1}{2}\left(\frac{\ln(t) - \mu_T}{\sigma_T}\right)^2\right] \tag{6.24}$$

where, μ_T and σ_T are the mean and standard deviation of $\ln(t)$. To describe the conditionality of T_p on H_s, μ_T and σ_T^2 are estimated as

$$\begin{aligned} \mu_T &= c_1 + c_2 h^{c_3} \\ \sigma_T^2 &= d_1 + d_2 \exp(d_3 h) \end{aligned} \tag{6.25}$$

where, $c_1,\ c_2,\ c_3,\ d_1,\ d_2$ and d_3 are parameters estimated from non-linear curve fitting of the raw data. For more details refer (Li, Gao, and Moan, 2015).

The data used in this study corresponds to site number 14 from (Li, Gao, and Moan, 2015). The name of the site is Norway 5 and it is situated in the North Sea at a water depth of 100 m to 200 m which is ideal for spar-type floating offshore wind turbines. The parameters used in the study are summarized in Table 6.1.

6.3 Results

The performance of the controller has been evaluated using two approaches. A short term evaluation is based on time history analysis of single load cases and long term

Table 6.1: Joint probability distribution parameters

Distribution	Parameter	Associated Equation	Value
Marginal U_w	α_U	6.21	2.029
	β_U	6.21	8.920
Conditional H_s on U_w	a_1	6.23	2.136
	a_2	6.23	0.013
	a_3	6.23	1.709
	b_1	6.23	1.816
	b_2	6.23	0.024
	b_3	6.23	1.787
Conditional T_p on H_s	c_1	6.25	1.886
	c_2	6.25	0.365
	c_3	6.25	0.312
	d_1	6.25	0.001
	d_2	6.25	0.105
	d_3	6.25	-0.264

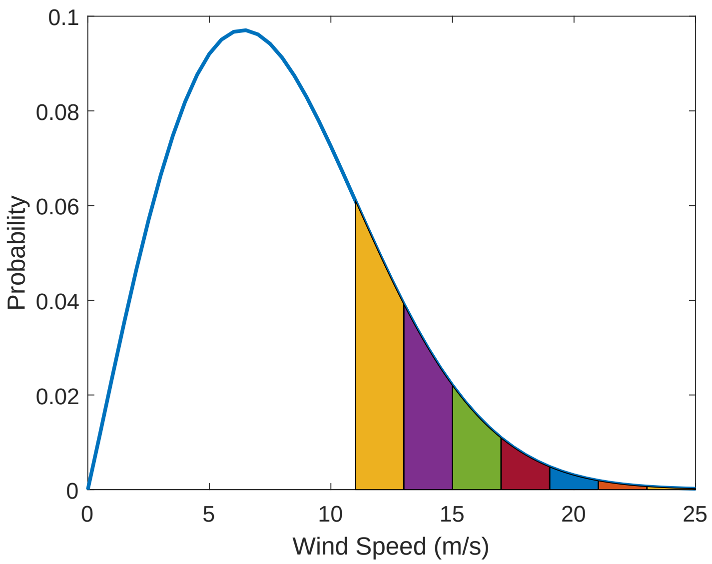

Figure 6.7: Marginal probability density function of wind speed

analysis is based on the life time Damage Equivalent Loads (DELs) on the different structural and mechanical components of the FOWT. For long term DEL evaluation the probability of occurrence of different met-ocean conditions are described in the previous section. First, the numerical results for the probability distribution function

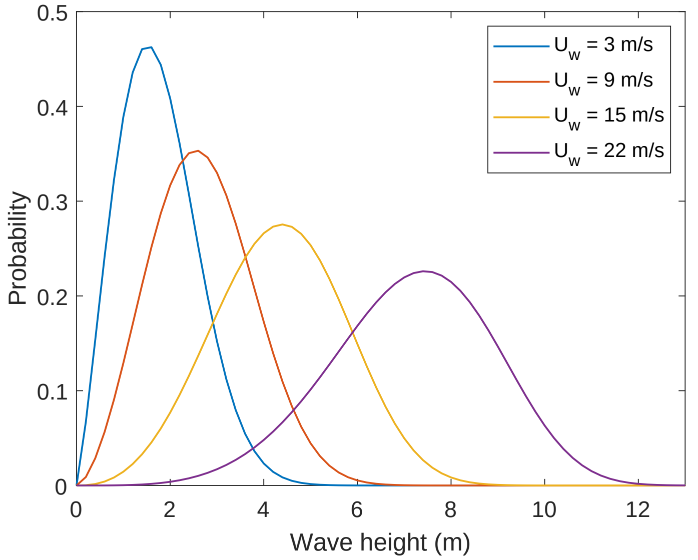

Figure 6.8: Probability density function of wave height conditional on wind speed

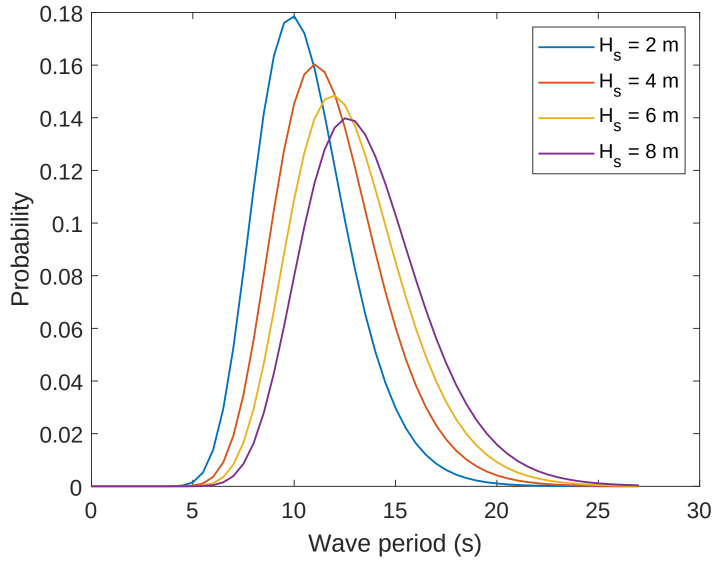

Figure 6.9: Probability density function of wave period conditional on wave height

are provided. The marginal distribution of wind speed at the chosen site shown in Figure 6.7. The conditional distributions of wave height and wave period used in this study are shown in Figure 6.8 and Figure 6.9 for a few different wind speeds and wave heights respectively. It is important to note here that the pitch controller is active only in wind speed region 3 (above rated wind speed).

For short term analysis of the FOWT responses numerical results of individual load cases are presented here. Two load cases are chosen; Load Case 1: wind speed = 12.5 m/s, wave height 3 m and wave period 11 s, and, Load Case 2: wind speed = 14.5 m/s, wave height 3 m and wave period 11 s. The two load cases are selected as they contributed most to the total probability in equation 6.20. This can be verified from Figure 6.7, Figure 6.8 and Figure 6.9. The degrees of freedom analysed are rotor speed, platform pitch and roll, blade out-of-plane and in-plane displacement, tower fore-aft and side-to-side displacement and the blade pitch angle. The blade pitch angle is the most important parameter as the controller is designed to minimize blade pitch actuation or variation of the blade pitch angles. Figure 6.10 through Figure 6.17 compares the proposed NMPC controller against the baseline controller for Load Case 1 & 2. The first thing to note is that the dynamics of the FOWT is not heavily altered by the NMPC controller compared to the baseline controller. This is because the blade pitch angle from the NMPC controller is not significantly different from the baseline controller as shown in Figure 6.17. The objective of the NMPC controller is to minimize blade actuator without compromising on power tracking while the baseline controller is design solely for power tracking. It can be observed from the results that the baseline controller tracks the rated rotor speed with almost minimum blade pitch actuation. Therefore, the scope of further reduction of blade pitch actuation is limited. However, further scope of improvement arises from from the fact that unlike the baseline PI controller the NMPC controller provides an optimal control framework and the NMPC controller uses a preview of the upstream wind and optimizes the control input based on information about the future. This information helps the controller to estimate the current input based on future wind speeds and therefore the oscillations of the blade pitch angles are reduced. This can be clearly observed in Figure 6.17. The controller also tracks the rated rotor speed with very good accuracy, specially in Load Case 2 (see Figure 6.16), with reduced pitch actuation.

Among the structural responses of the FOWT, the proposed NMPC controller considerably reduces the platform pitching motion, the tower fore-aft motion and the blade out-of-plane motion. This is obvious since these degrees of freedom are included in the design of the controller. There is a significant reduction in the platform pitching motion. This is due to the fact that the NMPC controller removes low frequency oscillations from the blade pitch angles which would otherwise excite the platform pitch degree of freedom. This leads to significantly better performance than the baseline controller.

In the cross-wind direction, the platform rolling motion is slightly reduced. Other than that, the quantitative behaviour of the blade in-plane motion and tower side-to-side motion is almost unaffected by the controller. The performance of the controller

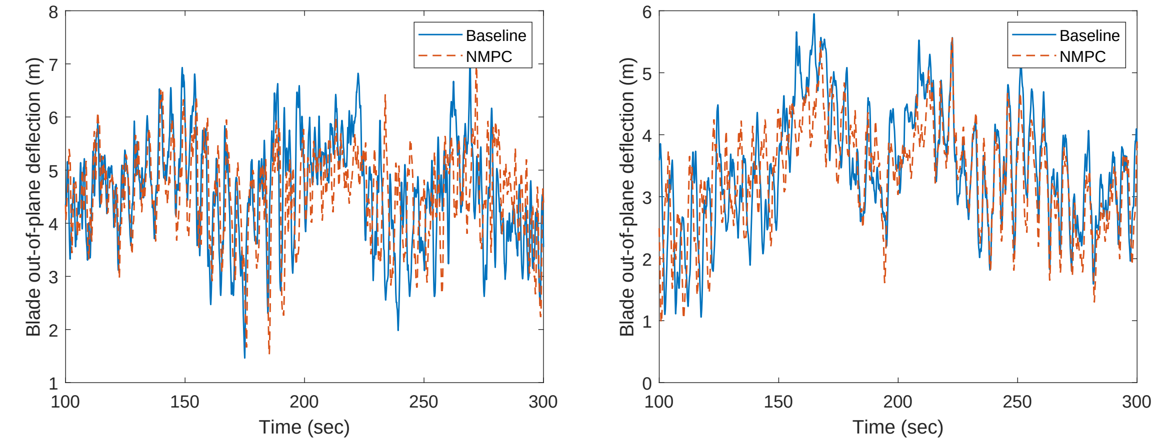

(a) Load case 1 (b) Load case 2

Figure 6.10: Blade out-of-plane displacement

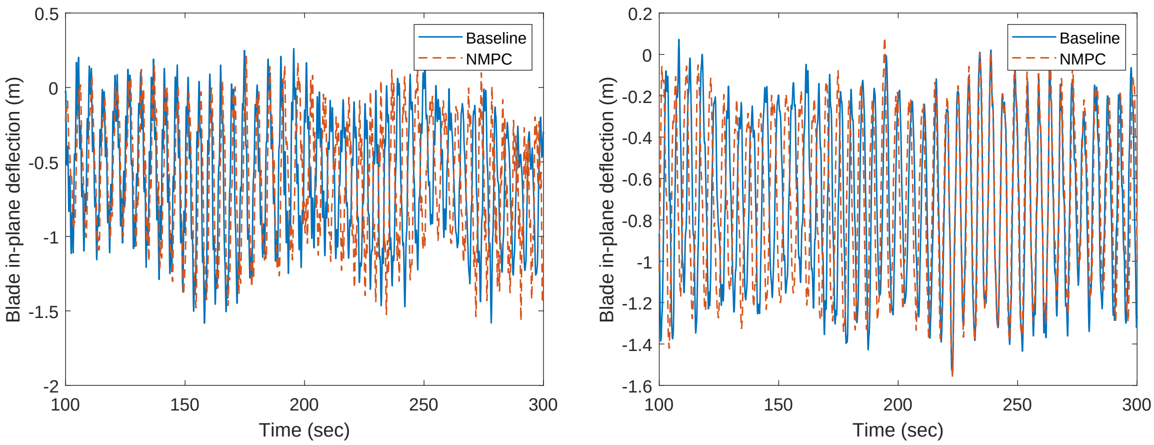

(a) Load case 1 (b) Load case 2

Figure 6.11: Blade in-plane displacement

based on the short term results can be summarized by noting that the proposed NMPC controller is capable of improving the dynamic responses of the FOWT (rotor speed tracking and vibration control) with reduced pitch actuation compared to baseline controller. To compare the two controllers quantitatively the standard deviations of the different FOWT responses are summarized in Table 6.2. These results also lead to the same conclusion.

Next, the Damage Equivalent Loads (DELs) on the pitch actuators and the blades and tower estimated from the use of the proposed NMPC controller are compared against the baseline controller. The met-ocean parameters are discretized in bins shown in Table 6.3. This discretization leads to 672 load cases. Standard 600 s time history results are generated for the different load cases using a sampling rate of 62.5 Hz. The

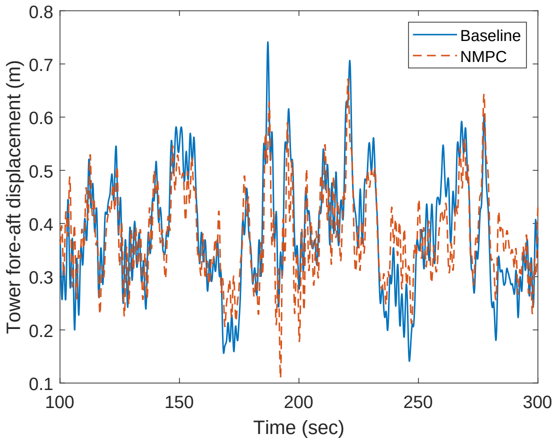

(a) Load case 1

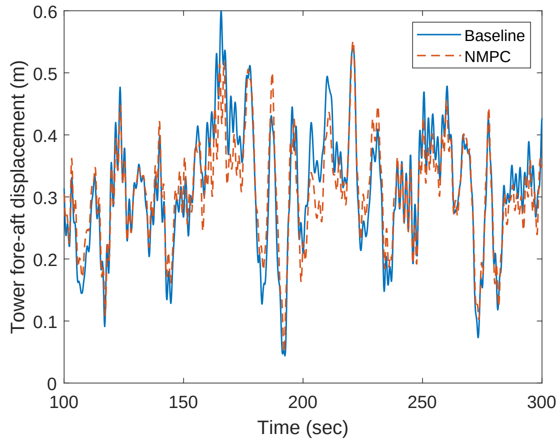

(b) Load case 2

Figure 6.12: Tower fore-aft displacement

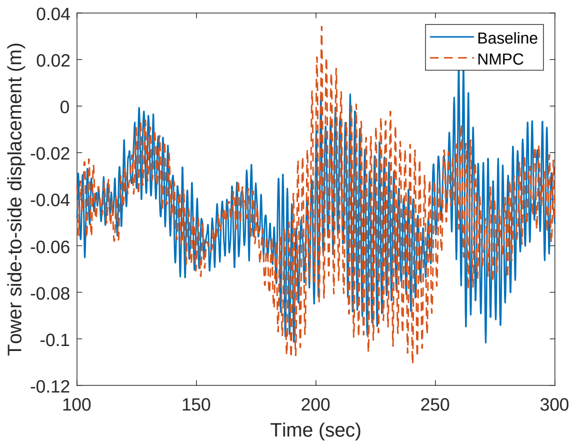

(a) Load case 1

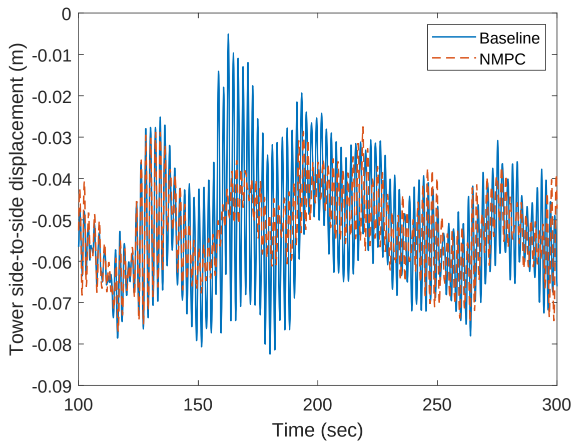

(b) Load case 2

Figure 6.13: Tower side-to-side displacement

Rainflow Counting method (Downing and Socie, 1982) is used to estimate the load cycles from the time histories and then extrapolated using the probability distribution to obtain the lifetime cycle counts. The DELs presented in this study are constant amplitude loads with a frequency of 0.2 Hz. Table 6.4 and Table 6.5 compares the DELs of the pitch actuator force, the blade flapwise moment and the tower fore-aft moment. The DELs for the blade edgewise moment and the tower side-to-side moment has not been presented as it has been shown in the previously that the controller has insignificant effect on these two responses. Table 6.4 and Table 6.5 show the aggregate and lifetime DELs obtained from the two controller. It can be observed that the proposed NMPC controller offers a reduction of 6-8% in fatigue loads over the baseline controller.

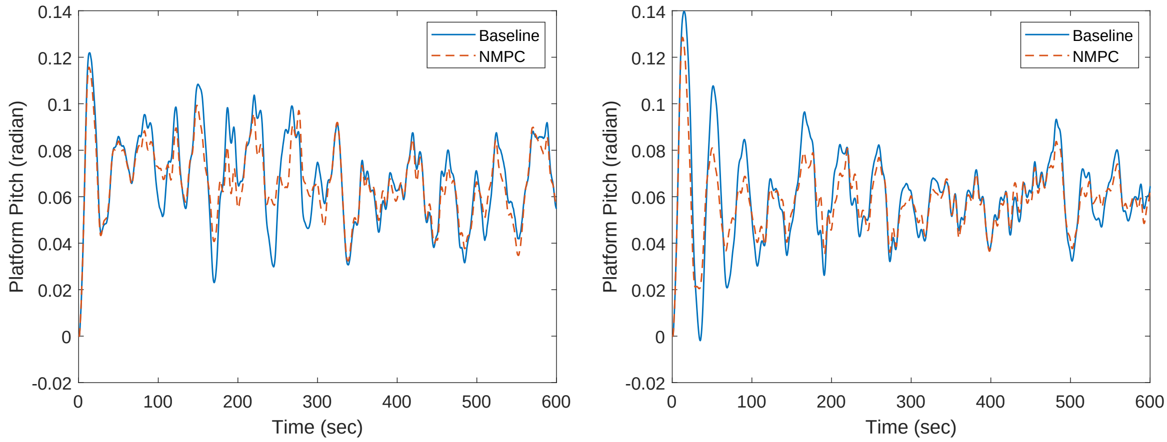

(a) Load case 1 (b) Load case 2

Figure 6.14: Platform pitch

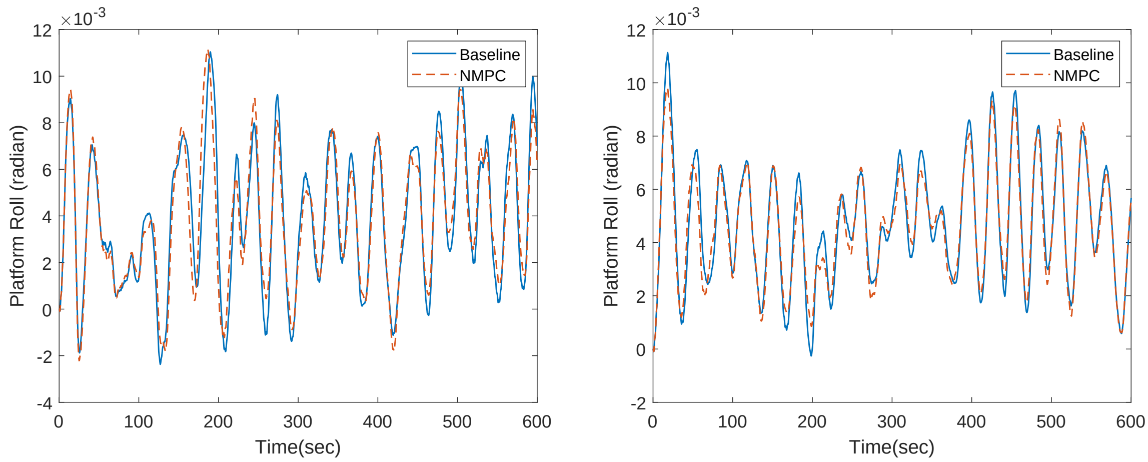

(a) Load case 1 (b) Load case 2

Figure 6.15: Platform roll

6.4 Conclusions

In this chapter a new individual blade pitch control strategy is proposed that optimizes blade pitch actuator demand. The aim of the controller is to minimize blade pitch actuation while maintaining/improving the tracking of the rated rotor speed and mitigating structural vibrations of the FOWT. The controller is derived under the mathematically optimal framework of the Non-linear Model Predictive Control (NMPC). The preview of the inflow wind to the FOWT is assumed to be available from LIDAR measurements. The details of the working of a nacelle mounted LIDAR is beyond the scope of the study and specialized literature has been referred. The proposed NMPC controller is compared against the existing baseline controller and the results the presented in two

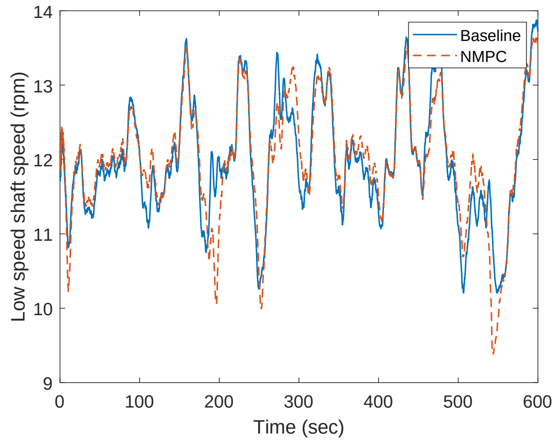

(a) Load case 1

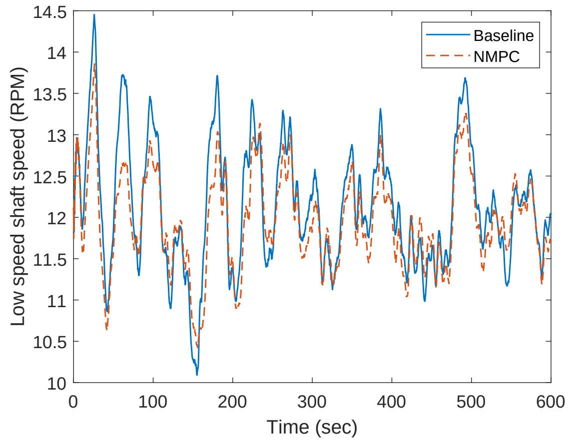

(b) Load case 2

Figure 6.16: Low-speed-shaft speed

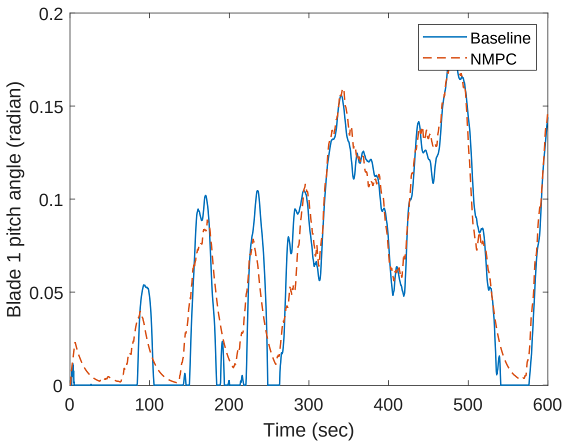

(a) Load case 1

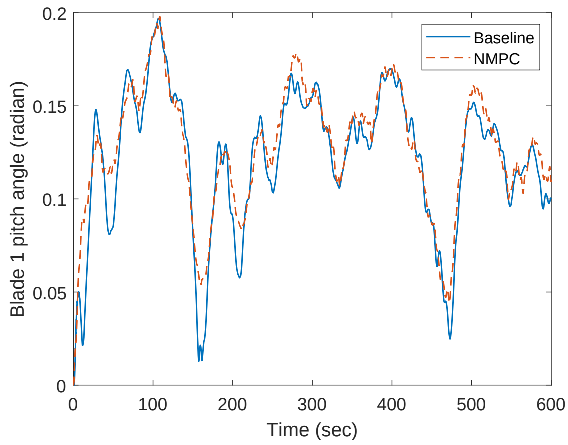

(b) Load case 2

Figure 6.17: Blade pitch angle

forms. First, short term results based on time history analysis of single load cases were presented. The results showed that the proposed controller in capable of reducing pitch actuation below the baseline level while improving tracking of rated rotor speed. It was also shown that the controller is capable of reducing blade out-of-plane vibrations, tower fore-aft vibrations and platform pitch motion considerably. This structural response reduction will improve the dynamic response of the FOWT and hence improve performance.

Assessment of long term fatigue loads showed that the proposed NMPC controller is capable of reducing aggregate and lifetime DELs on the pitch actuators, the blades in the out-of-plane direction and the tower in the fore-aft direction by 6-8% over the existing baseline controller. These results clearly show that the proposed controller is

Table 6.2: Standard deviation of wind turbine responses

Parameter	Baseline		NMPC		Reduction (%)	
	LC #1	LC #2	LC #1	LC #2	LC #1	LC #2
Rotor speed (rpm)	0.816	0.770	0.824	0.620	-0.98	19.48
Platform pitch (degree)	1.102	1.154	0.893	0.838	18.95	27.38
Platform roll (degree)	0.167	0.131	0.158	0.120	5.38	8.39
Blade pitch angle (degree)	3.271	2.248	3.042	1.956	7.00	12.99
Blade out-of-plane(m)	1.127	0.964	1.069	0.859	5.14	10.89
Blade in-plane (m)	0.395	0.410	0.394	0.405	0.25	1.22
Tower fore-aft (m)	0.101	0.099	0.090	0.082	10.89	17.17
Tower side-to-side (m)	0.019	0.014	0.020	0.014	-5.26	0.00

Table 6.3: Bin ranges and widths for met-ocean parameters

Parameter	Bin width	Bin range
Wind speed (m/s)	2	11-25
Significant wave height (m)	1	0-8
Peak spectral period (s)	2	0-27

Table 6.4: Aggregate Damage Equivalent Loads (DELs) on structural and mechanical components

Component forces/moments	Baseline	NMPC	Reduction (%)
Pitch Actuator force (kN)	3.65E+04	3.36E+04	7.9
Blade root flapwise bending moment (kNm)	1.27E+03	1.19E+03	6.3
Tower base fore-aft bending moment (kNm)	2.58E+04	2.38E+04	7.7

Table 6.5: Lifetime Damage Equivalent Loads (DELs) on structural and mechanical components

Component forces/moments	Baseline	NMPC	Reduction (%)
Pitch Actuator force (kN)	3.62E+04	3.37E+04	7.2
Blade root flapwise bending moment (kNm)	1.23E+03	1.16E+03	6.1
Tower base fore-aft bending moment (kNm)	2.61E+04	2.40E+04	7.8

better that the existing baseline controller and has promising applications in vibration mitigation and fatigue load reduction in both structural and mechanical components of the wind turbine.

It is important to mention here unlike the controllers proposed in the previous two chapters the controller proposed in this chapter is non-linear and hence stability analysis becomes an important part of the design. Classical stability analysis has not been performed for the proposed NMPC controller, however, stability is analysed/verified by numerical simulation of various met-ocean conditions encompassing the entire the wind-wave loading scenario. It has been shown that the controller performs well under every different condition and it is concluded that the proposed controller is stable.

Chapter 7

Conclusions and future works

7.1 Summary and conclusion

Any new technology is primarily driven by cost. For offshore wind technology to compete with other forms of energy, innovations are required to bring down the Levelized Cost of Energy (LCOE). As introduced in Chapter 1, the LCOE of offshore wind can be reduced from innovations in construction and installation, operation and maintenance and improvements in capacity factor. As pointed out in Chapter 1 the biggest scope of cost reduction is in construction and installation. However, further cost reduction is possible by improving reliability and capacity factor of the wind turbines. The work presented in this thesis proposes innovations that aim to reduce operation and maintenance costs and improve capacity factor of wind turbines (hence wind farms). The various pitch control strategies proposed in this thesis are designed to reduce aerodynamic loads on wind turbine components and hence, have potential to increase design lifetime of the turbine components. Pitch control strategies are also proposed to improve power regulation of the turbines. This can improve power output of the entire wind farm hence improving capacity factor of the farm. Both of which can ultimately lead to reduction in the LCOE but as mention in Chapter 1 the estimation of the reduced LCOE is not in the scope of this thesis. A comprehensive dynamic model of a floating offshore wind turbine has been derived and different individual blade pitch control strategies have been proposed and investigated. The contributions of the different chapters are now summarized.

In Chapter 3, a flexible multi-body dynamic model of a spar-type floating offshore wind turbine has been derived following Kane's method. The advantages of using Kane's method over the traditional methods, like the Euler-Lagrangian energy formulation, has been discussed. The chapter provides a detailed step by step procedure for deriving the equations of motion of a dynamic system using Kane's method. The powerful vector approach brought by Kane's method has been demonstrated and it has been shown that closed form equations of motion are not required and the equations of motion can be directly solved by a computer. This feature is extremely useful as it allows one to model complicated systems with relative ease without the need for manual manipulation of long analytical equations. This feature has been used here to derive a high fidelity model of the FOWT. Chapter 3 also shows how simple it is to extend the model to install an auxiliary device to the existing wind turbine. It has been shown that the contribution of the device can be superimposed onto the equation of motion of the turbine to obtain the coupled equation of motion. These facts demonstrate the advantages of Kane's method over the traditional Euler-Lagrangian method. The requirement for a high fidelity model has also been investigated in this chapter. It has been shown that reduced order models are unable to capture the side-to-side dynamics of onshore wind turbines and hence in-plane motion of offshore wind turbines. This emphasises the need for high-fidelity models for numerical analysis of offshore wind turbines. In Chapter 4 through to Chapter 6 the different individual blade pitch control strategies proposed in this thesis are presented.

A wavelet-LQR based individual blade pitch controller has been proposed in Chapter 4. The control algorithm was designed with the primary aim of reducing aerodynamic loads on the wind turbine. As demonstrated in the chapter, the wavelet-LQR is capable of assigning frequency band dependent controller gains that leads to a time-varying controller. This time-varying nature of the controller has been used to design the individual blade pitch controller with an emphasis on mitigating the 1P loads on the turbine. The results presented in the chapter show that the proposed controller is extremely effective in reducing aerodynamic loads which leads to reduced blade, tower and platform motion of the FOWT. Comparison against the baseline controller and a classical LQ regulator show that the proposed wavelet-LQR is better than both. However, on the downside it has been reported that the aerodynamic load reduction is obtained at a cost of increased power output variability. This is due to the fact that power tracking is not a design objective of the controller. However, it has been shown that the degradation in power tracking is not significant and it has been argued that individual wind turbine power variability will be less important as an offshore wind turbine will almost certainly be situated in a large wind farm and the total output of the farm will be predominantly dictated by the spatial and temporal variations of the farm rather than the variability of a single turbine. Hence, this increase in individual wind turbine power variability is judged to be acceptable considering the promising reduction in structural loads. This trade-off between structural response mitigation and rotor speed regulation can prove to be beneficial in extending the design life of the wind turbine components.

As observed in Chapter 4, the proposed controller led to a degradation in power tracking. This motivated the design of the new controller proposed in Chapter 5. The individual blade pitch controller proposed in this chapter is an intelligent combination of a simple PI (proportional-integral) controller and a simple LQ regulator aimed to simultaneously alleviate structural loads on the turbine and regulate power production. The novelty of this control strategy lies in the fact that it is capable of fulfilling two competitive objectives. Excellent performance, both in the sense of mitigated turbine vibrations and improved power tracking has been reported. The performance of the controller is better than any other controller available in literature and the controller is even capable of reducing platform motion. However, this improved performance is achieved at a cost of increased blade pitch actuation. In turbines with reliable blade pitch actuators the proposed control strategy can immensely improve the dynamic behaviour and power output of the turbine.

However, with the existing pitch systems, using control strategies that increase pitch actuation may lead to increased downtime of the turbines. Also, as wind turbines are being continuously up-scaled, overuse of pitch actuators will only compound this problem. A solution to this problem is innovations in pitch system to improve their reliability. Another solution is to develop new control strategies that reduce pitch actuation, without deteriorating the performance of the FOWT. In Chapter 6 this problem is addressed by proposing a new control strategy that optimizes blade pitch actuation. The aim of the controller is to minimize blade pitch actuation while maintaining/improving tracking of rated rotor speed and mitigating structural vibrations. The controller is derived under the mathematically optimal framework of Non-linear Model Predictive Control (NMPC). The preview of the inflow wind is assumed to be available from LIDAR measurements. Numerical evaluation of the controller performance showed that the controller is capable of reducing pitch actuation while improving tracking of rated rotor speed. Further improvements in the form of reduced blade out-of-plane vibration, tower fore-aft vibrations and platform pitching motion are also obtained. The proposed NMPC controller is capable of reducing aggregate and lifetime DELs (Damage Equivalent Loads) on the pitch actuators, the blades in the out-of-plane direction and the tower in the fore-aft direction by 6-8% over the existing baseline controller. These results clearly show that the proposed controller is better than the existing baseline controller and has promising applications in vibration mitigation and fatigue load reduction in both structural and mechanical components of the wind turbine.

7.2 Future works

Based on the research carried out in this thesis certain areas have been identified that require further investigation either because the area has been unexplored or the literature available on the topic is sparse. These areas primarily focus on the dynamics and control of floating offshore wind turbines. These areas are listed below in no particular order of priority.

- The various individual pitch control strategies proposed in this thesis all depend on the availability of measurements. Although sensors are commonly placed on all wind turbines and some information is readily available, the complete information required by the controllers is not available. Measurements of the structural response is generally not available. Additionally, measurements of displacements and velocities are difficult to measure. Commonly accelerometers are used to measure the accelerations of the different structural components and displacements and velocities are estimated by an observer such as the Kalman filter. Hence, one of the most important future works is the development of a Kalman filter (or any other type of observer) that is capable of accurately estimating the displacements are velocities from the acceleration measurements.

- With all numerical tools developed, an important next step is experimental verification of the numerical algorithms. Experimental verification of this type is complicated as availability of full scale FOWTs for field tests is rather expensive. However, this is essential and should be considered in future work. To start with, small scale wind turbines available for field tests may be used before deployment on actual full scale turbines.

- In the direction of detailed, holistic dynamic modelling of the FOWT the dynamic model of the FOWT must be coupled with the generator and grid dynamics. Basu, Staino, and Basu, 2014 investigated the impact of grid faults on the dynamics of onshore wind turbines. The authors, through numerical investigation, showed that electrical disturbances have a significant impact on the mechanical/structural vibrations of the turbine. Voltage sags may lead to severe vibrations that may compromise safe operation of the overall plant. Further, the authors investigated the use of flexible alternating current transmission systems (FACTS) devices to suppress the effect of electrical fault-induced vibrations. These types of grid-induced vibrations can be expected to be significant in floating offshore wind turbines as much as in onshore wind turbines. Therefore, it is important to couple the electrical and mechanical sub-systems of the wind turbine and study its dynamics in the context of the wind farm and the grid.

- Wind turbines located in the inner grids of a wind farm will be subjected to the wake of the upwind turbine. Wakes in general increase the turbulence in the wind. The formation of these wakes, the increased atmospheric turbulence and its effects on the dynamics of the wind turbine must be investigated. The increased turbulence will potentially increase fatigue loads on the wind turbines. Usually the effect of wakes is studied experimentally or using computational fluid dynamics (CFD) tools. Therefore, the wind turbine must be coupled with CFD tools to investigate its dynamics under different atmospheric conditions and evaluate the performance of the proposed control strategies.

- The effect of vorticity in presence of ocean currents can generate complex fluid motion (Basu, 2016, 2019). The dynamics of the spar can be significantly affected by the presence of vorticity (Carlson and Modarres-Sadeghi, 2018; Gabbai and Benaroya, 2005; Irani and Finn, 2004) which requires further investigation. Vortex-induced motion of spar-type FOWTs were studied by (Carlson and Modarres-Sadeghi, 2018; Duan, Hu, and Wang, 2016). It was shown that the lock-in phenomenon occurs first in the cross-flow direction followed by the in-line direction. In the absence of wind loads, the oscillation amplitudes of all wind turbine responses increases significantly with increasing current velocity, especially after locking-in. The phenomenon of lock-in happens when the vortex shedding frequency becomes close to a natural frequency of vibration of the structure. When this happens large and damaging vibrations can result. Wind load has a clear suppression effect on cross-flow and in-line vortex induced motions. It was concluded by (Carlson and Modarres-Sadeghi, 2018) that in the presence of wind loads, the effect of current is limited to the yaw and the in-line bending moment of the tower.

  However, literature available on this topic is rather sparse and substantial contribution needs to be made on this topic both in studying the dynamics and control of vortex-induced-motions in spar-type FOWTs.

- In Chapter 6 a non-linear model predictive controller has been used to design an individual blade pitch controller. As has been mentioned in the chapter the NMPC algorithm offers a mathematically optimal control framework. This strategy can be extended further to optimize the design and operation of the entire wind farm. The potential of LIDAR measurements has not been investigated extensively in this thesis. A NMPC controller combined with LIDAR-SODAR wind-wave measurements has the potential of greatly optimizing the long-term as well extreme event performance of the turbines. Investigation into optimized control algorithms is recommended. These control algorithms will be generally dictated by design requirements and innovative algorithms can help in optimizing the design.

- A wind turbine is almost always situated in a wind farm. The supervisory wind farm control can have different types of architecture like centralized, distributed or cascade control approach. Nevertheless, the wind farm control sends reference inputs to the individual turbines. In certain situations it may be required for a wind turbine to track a reference power output. An example of such situation is power derating to maximize power output of the farm. Therefore, control strategies need to be developed that are capable of simultaneously tracking a reference power and minimizing fatigue loads on the turbine. It is important to note here that the baseline controller is designed to tracked rated power and is not capable of tracking a reference power.

Appendix A

Kinematic and kinetic description of the floating offshore wind turbine

This chapter describes the coordinates systems, the kinematic and the kinetics of the floating offshore wind turbine. The various quantities defined in this chapter facilitates the development of the equations of motion of the complete non-linear system.

A.1 Coordinate systems

A set of inertial coordinate system $\hat{\boldsymbol{z}}$ is fixed to the earth. Then, a set of coordinate system is attached to the base of the tower. The transformation relation can be obtained as

$$\begin{pmatrix} \hat{\boldsymbol{a}}_{\mathbf{1}} \\ \hat{\boldsymbol{a}}_{\mathbf{2}} \\ \hat{\boldsymbol{a}}_{\mathbf{3}} \end{pmatrix} = \boldsymbol{T_O}(\theta_1 = q_R, \theta_2 = q_Y, \theta_3 = -q_P) \begin{pmatrix} \hat{\boldsymbol{z}}_{\mathbf{1}} \\ \hat{\boldsymbol{z}}_{\mathbf{2}} \\ \hat{\boldsymbol{z}}_{\mathbf{3}} \end{pmatrix} \tag{A.1}$$

where, q_R, q_Y and q_P are the roll, yaw and pitch degrees of freedom of the platform respectively. The tower element fixed coordinate system along the height of the tower can be obtained from the elastic deformation of the tower as

$$\begin{pmatrix} \hat{\boldsymbol{t}}_{\mathbf{1}}(h) \\ \hat{\boldsymbol{t}}_{\mathbf{2}}(h) \\ \hat{\boldsymbol{t}}_{\mathbf{3}}(h) \end{pmatrix} = \boldsymbol{T_O}(\theta_1 = \theta_{SS}(h), \theta_2 = 0, \theta_3 = -\theta_{FA}(h)) \begin{pmatrix} \hat{\boldsymbol{a}}_{\mathbf{1}} \\ \hat{\boldsymbol{a}}_{\mathbf{2}} \\ \hat{\boldsymbol{a}}_{\mathbf{3}} \end{pmatrix} \tag{A.2}$$

where, $\theta_{SS}(h)$ and $\theta_{FA}(h)$ are the tower rotations in the side-to-side and fore-aft directions respectively at various sections along the height of the tower. Here, the torsion of the tower is neglected. Next, the tower top/base plate coordinate system is defined as

$$\begin{pmatrix} \hat{\boldsymbol{b}}_{\mathbf{1}} \\ \hat{\boldsymbol{b}}_{\mathbf{2}} \\ \hat{\boldsymbol{b}}_{\mathbf{3}} \end{pmatrix} = \boldsymbol{T_O}(\theta_1 = \theta_{SS}(TwrHt), \theta_2 = 0, \theta_3 = -\theta_{FA}(TwrHt)) \begin{pmatrix} \hat{\boldsymbol{a}}_{\mathbf{1}} \\ \hat{\boldsymbol{a}}_{\mathbf{2}} \\ \hat{\boldsymbol{a}}_{\mathbf{3}} \end{pmatrix} \tag{A.3}$$

where, $TwrHt$ is the flexural height of the tower. The nacelle yaw coordinate system is rotated about $\hat{\boldsymbol{b}}_{\mathbf{2}}$ by the yaw angle q_{yaw} of the nacelle.

$$\begin{pmatrix} \hat{\boldsymbol{d}}_{\mathbf{1}} \\ \hat{\boldsymbol{d}}_{\mathbf{2}} \\ \hat{\boldsymbol{d}}_{\mathbf{3}} \end{pmatrix} = \begin{bmatrix} \cos(q_{yaw}) & 0 & -\sin(q_{yaw}) \\ 0 & 1 & 0 \\ \sin(q_{yaw}) & 0 & \cos(q_{yaw}) \end{bmatrix} \begin{pmatrix} \hat{\boldsymbol{b}}_{\mathbf{1}} \\ \hat{\boldsymbol{b}}_{\mathbf{2}} \\ \hat{\boldsymbol{b}}_{\mathbf{3}} \end{pmatrix} \tag{A.4}$$

The low-speed-shaft is often tilted and sometimes skewed with respect to the tower top. The coordinate system attached to the shaft can be given as

$$\begin{pmatrix} \hat{\boldsymbol{c}}_{\mathbf{1}} \\ \hat{\boldsymbol{c}}_{\mathbf{2}} \\ \hat{\boldsymbol{c}}_{\mathbf{3}} \end{pmatrix} = \begin{bmatrix} \cos(SS)\cos(ST) & \sin(ST) & -\sin(SS)\cos(ST) \\ -\cos(SS)\sin(ST) & \cos(ST) & \sin(SS)\sin(ST) \\ \sin(SS) & 0 & \cos(SS) \end{bmatrix} \begin{pmatrix} \hat{\boldsymbol{d}}_{\mathbf{1}} \\ \hat{\boldsymbol{d}}_{\mathbf{2}} \\ \hat{\boldsymbol{d}}_{\mathbf{3}} \end{pmatrix} \tag{A.5}$$

where SS and ST denotes shaft-skew and shaft-tilt angles respectively. The azimuth coordinate system is also attached to the low speed shaft but rotates with the rotor is defined next as

$$\begin{pmatrix} \hat{\boldsymbol{e}}_{\mathbf{1}} \\ \hat{\boldsymbol{e}}_{\mathbf{2}} \\ \hat{\boldsymbol{e}}_{\mathbf{3}} \end{pmatrix} = \begin{bmatrix} 1 & 0 & 0 \\ 0 & \cos(q_{DrTr} + q_{GeAz}) & \sin(q_{DrTr} + q_{GeAz}) \\ 0 & -\sin(q_{DrTr} + q_{GeAz}) & \cos(q_{DrTr} + q_{GeAz}) \end{bmatrix} \begin{pmatrix} \hat{\boldsymbol{c}}_{\mathbf{1}} \\ \hat{\boldsymbol{c}}_{\mathbf{2}} \\ \hat{\boldsymbol{c}}_{\mathbf{3}} \end{pmatrix} \tag{A.6}$$

The rotation angle is summation of the generator azimuth angle (q_{GeAz}) and the torsional rotation of the drive train (q_{DrTr}). The coordinate system for blade 1 is given as

$$\begin{pmatrix} \hat{\boldsymbol{g}}_{\mathbf{1}}^{\boldsymbol{B1}} \\ \hat{\boldsymbol{g}}_{\mathbf{2}}^{\boldsymbol{B1}} \\ \hat{\boldsymbol{g}}_{\mathbf{3}}^{\boldsymbol{B1}} \end{pmatrix} = \begin{bmatrix} 1 & 0 & 0 \\ 0 & \cos(\pi/2) & -\sin(\pi/2) \\ 0 & \sin(\pi/2) & \cos(\pi/2) \end{bmatrix} \begin{pmatrix} \hat{\boldsymbol{e}}_{\mathbf{1}} \\ \hat{\boldsymbol{e}}_{\mathbf{2}} \\ \hat{\boldsymbol{e}}_{\mathbf{3}} \end{pmatrix} \tag{A.7}$$

When blade 1 is pointing up, blade 3 is ahead of blade 2 and blade 2 is ahead of blade 1, and the blades are set 120° degrees apart. Thus the blade coordinate systems of blade 2 and 3 are given as

$$\begin{pmatrix} \hat{\boldsymbol{g}}_{\mathbf{1}}^{\boldsymbol{B1}} \\ \hat{\boldsymbol{g}}_{\mathbf{2}}^{\boldsymbol{B1}} \\ \hat{\boldsymbol{g}}_{\mathbf{3}}^{\boldsymbol{B1}} \end{pmatrix} = \begin{bmatrix} 1 & 0 & 0 \\ 0 & \cos(\pi/2 + 2\pi/3) & -\sin(\pi/2 + 2\pi/3) \\ 0 & \sin(\pi/2 + 2\pi/3) & \cos(\pi/2 + 2\pi/3) \end{bmatrix} \begin{pmatrix} \hat{\boldsymbol{e}}_{\mathbf{1}} \\ \hat{\boldsymbol{e}}_{\mathbf{2}} \\ \hat{\boldsymbol{e}}_{\mathbf{3}} \end{pmatrix} \tag{A.8}$$

$$\begin{pmatrix} \hat{\boldsymbol{g}}_{\mathbf{1}}^{\boldsymbol{B1}} \\ \hat{\boldsymbol{g}}_{\mathbf{2}}^{\boldsymbol{B1}} \\ \hat{\boldsymbol{g}}_{\mathbf{3}}^{\boldsymbol{B1}} \end{pmatrix} = \begin{bmatrix} 1 & 0 & 0 \\ 0 & \cos(\pi/2 + 4\pi/3) & -\sin(\pi/2 + 4\pi/3) \\ 0 & \sin(\pi/2 + 4\pi/3) & \cos(\pi/2 + 4\pi/3) \end{bmatrix} \begin{pmatrix} \hat{\boldsymbol{e}}_{\mathbf{1}} \\ \hat{\boldsymbol{e}}_{\mathbf{2}} \\ \hat{\boldsymbol{e}}_{\mathbf{3}} \end{pmatrix} \tag{A.9}$$

Next, the blade coned coordinate system is defined as

$$\begin{pmatrix} \hat{\boldsymbol{i}}_{\mathbf{1}}^{\boldsymbol{B1}} \\ \hat{\boldsymbol{i}}_{\mathbf{2}}^{\boldsymbol{B1}} \\ \hat{\boldsymbol{i}}_{\mathbf{3}}^{\boldsymbol{B1}} \end{pmatrix} = \begin{bmatrix} \cos(PreCone(1)) & 0 & -\sin(PreCone(1)) \\ 0 & 1 & 0 \\ \sin(PreCone(1)) & 0 & \cos(PreCone(1)) \end{bmatrix} \begin{pmatrix} \hat{\boldsymbol{g}}_{\mathbf{1}}^{\boldsymbol{B1}} \\ \hat{\boldsymbol{g}}_{\mathbf{2}}^{\boldsymbol{B1}} \\ \hat{\boldsymbol{g}}_{\mathbf{3}}^{\boldsymbol{B1}} \end{pmatrix} \tag{A.10}$$

The coned coordinate system for blade 2 and 3 can be defined similarly. The blade pitched coordinate system is defined as

$$\begin{pmatrix} \hat{\boldsymbol{j}}_{\mathbf{1}}^{\boldsymbol{B1}} \\ \hat{\boldsymbol{j}}_{\mathbf{2}}^{\boldsymbol{B1}} \\ \hat{\boldsymbol{j}}_{\mathbf{3}}^{\boldsymbol{B1}} \end{pmatrix} = \begin{bmatrix} \cos(BlPit(1)) & -\sin(BlPit(1)) & 0 \\ \sin(BlPit(1)) & \cos(BlPit(1)) & 0 \\ 0 & 0 & 1 \end{bmatrix} \begin{pmatrix} \hat{\boldsymbol{i}}_{\mathbf{1}}^{\boldsymbol{B1}} \\ \hat{\boldsymbol{i}}_{\mathbf{2}}^{\boldsymbol{B1}} \\ \hat{\boldsymbol{i}}_{\mathbf{3}}^{\boldsymbol{B1}} \end{pmatrix} \tag{A.11}$$

Where, $BlPit$ is a vector of blade pitch angles. Again, the pitched coordinate system for blades 2 and 3 can be defined similarly. The blade coordinate system aligned to the local structural axes are defined as

$$\begin{pmatrix} \hat{\boldsymbol{l}}_{\mathbf{1}}^{\boldsymbol{B1}}(r) \\ \hat{\boldsymbol{l}}_{\mathbf{2}}^{\boldsymbol{B1}}(r) \\ \hat{\boldsymbol{l}}_{\mathbf{3}}^{\boldsymbol{B1}}(r) \end{pmatrix} = \begin{bmatrix} \cos(\theta_s^{B1}(r)) & -\sin(\theta_s^{B1}(r)) & 0 \\ \sin(\theta_s^{B1}(r)) & \cos(\theta_s^{B1}(r)) & 0 \\ 0 & 0 & 1 \end{bmatrix} \begin{pmatrix} \hat{\boldsymbol{j}}_{\mathbf{1}}^{\boldsymbol{B1}} \\ \hat{\boldsymbol{j}}_{\mathbf{2}}^{\boldsymbol{B1}} \\ \hat{\boldsymbol{j}}_{\mathbf{3}}^{\boldsymbol{B1}} \end{pmatrix} \tag{A.12}$$

Here, $\theta_s^{B1}(r)$ is the structural twist angle of blade 1. The equations of $\hat{\boldsymbol{l}}^{\boldsymbol{B2}}(r)$ and $\hat{\boldsymbol{l}}^{\boldsymbol{B3}}(r)$ are similar. The blade element fixed coordinate system is given as

$$\begin{pmatrix} \hat{\boldsymbol{n}}_{\mathbf{1}}^{\boldsymbol{B1}}(r) \\ \hat{\boldsymbol{n}}_{\mathbf{2}}^{\boldsymbol{B1}}(r) \\ \hat{\boldsymbol{n}}_{\mathbf{3}}^{\boldsymbol{B1}}(r) \end{pmatrix} = \boldsymbol{T_O}(\theta_1 = \theta_x, \theta_2 = \theta_y, \theta_3 = 0) \begin{pmatrix} \hat{\boldsymbol{l}}_{\mathbf{1}}^{\boldsymbol{B1}}(r) \\ \hat{\boldsymbol{l}}_{\mathbf{2}}^{\boldsymbol{B1}}(r) \\ \hat{\boldsymbol{l}}_{\mathbf{3}}^{\boldsymbol{B1}}(r) \end{pmatrix} \tag{A.13}$$

The definition for θ_x and θ_y are blade rotations in in-plane and out-of-plane directions respectively. The element fixed coordinate system for determining and returning aerodynamic loads are given as

$$\begin{pmatrix} \hat{\boldsymbol{m}}_{\boldsymbol{1}}^{\boldsymbol{B1}}(r) \\ \hat{\boldsymbol{m}}_{\boldsymbol{2}}^{\boldsymbol{B1}}(r) \\ \hat{\boldsymbol{m}}_{\boldsymbol{3}}^{\boldsymbol{B1}}(r) \end{pmatrix} = \begin{bmatrix} \cos(BlPit(1)+\theta_s^{B1}(r)) & \sin(BlPit(1)+\theta_s^{B1}(r)) & 0 \\ -\sin(BlPit(1)+\theta_s^{B1}(r)) & \cos(BlPit(1)+\theta_s^{B1}(r)) & 0 \\ 0 & 0 & 1 \end{bmatrix} \begin{pmatrix} \hat{\boldsymbol{n}}_{\boldsymbol{1}}^{\boldsymbol{B1}}(r) \\ \hat{\boldsymbol{n}}_{\boldsymbol{2}}^{\boldsymbol{B1}}(r) \\ \hat{\boldsymbol{n}}_{\boldsymbol{3}}^{\boldsymbol{B1}}(r) \end{pmatrix} \tag{A.14}$$

The equations for $\hat{\boldsymbol{m}}^{\boldsymbol{B2}}(r)$ and $\hat{\boldsymbol{m}}^{\boldsymbol{B3}}(r)$ are similar. When the blades are not deflected this coordinate system is coincident with $\hat{\boldsymbol{i}}^{\boldsymbol{B1}}$.

A.2 Kinematics

The kinematics of the FOWT, or in other words the important points on the turbine that describe the motion of the turbine is provided in this section.

A.2.1 Position vectors

The position vectors of the various points are listed in this section. The position vector of the tower base (reference point) is given as

$$\boldsymbol{r}^{\boldsymbol{Z}} = q_{Sq}\hat{\boldsymbol{z}}_{\boldsymbol{1}} + q_{Hv}\hat{\boldsymbol{z}}_{\boldsymbol{2}} - q_{Sw}\hat{\boldsymbol{z}}_{\boldsymbol{3}} \tag{A.15}$$

The position vector of the center of gravity of the platform (Y) from the tower base (Z) is given as

$$\boldsymbol{r}^{\boldsymbol{ZY}} = (PtfmCMzt - PtfmRefzt)\hat{\boldsymbol{a}}_{\boldsymbol{2}} \tag{A.16}$$

$$\begin{aligned} \boldsymbol{r}^{\boldsymbol{ZT}} = &\left[\phi_1^{TFA}(h)q_{TFA1} + \phi_2^{TFA}(h)q_{TFA2}\right]\hat{\boldsymbol{a}}_{\boldsymbol{1}} + \Big[h - 0.5(S_{11}^{TFA}(h)q_{TFA1}^2 \\ &+ S_{22}^{TFA}(h)q_{TFA2}^2 + 2S_{12}^{TFA}(h)q_{TFA1}q_{TFA2} + S_{11}^{TSS}(h)q_{TSS1}^2 + S_{22}^{TSS}(h)q_{TSS2}^2 \\ &+ 2S_{12}^{TSS}(h)q_{TSS1}q_{TSS2})\Big]\hat{\boldsymbol{a}}_{\boldsymbol{2}} + \left[\phi_1^{TSS}(h)q_{TSS1} + \phi_2^{TFA}(h)q_{TSS2}\right]\hat{\boldsymbol{a}}_{\boldsymbol{3}} \end{aligned} \tag{A.17}$$

where, ϕ_1^{TFA}, ϕ_2^{TFA}, ϕ_1^{TSS} and ϕ_2^{TSS} are the first two mode shapes of the tower in fore-aft and side-to-side directions respectively. And

$$S_{ij}^{TFA}(h) = \int_0^h \left[\frac{\mathrm{d}\phi_i^{TFA}(h')}{\mathrm{d}h'} \frac{\mathrm{d}\phi_j^{TFA}(h')}{\mathrm{d}h'} \right] \mathrm{d}h' \quad \text{for} \quad i,j = 1,2 \tag{A.18}$$

$$S_{ij}^{TSS}(h) = \int_0^h \left[\frac{\mathrm{d}\phi_i^{TSS}(h')}{\mathrm{d}h'} \frac{\mathrm{d}\phi_j^{TSS}(h')}{\mathrm{d}h'} \right] \mathrm{d}h' \quad \text{for} \quad i,j = 1,2 \tag{A.19}$$

where, $S_{ij}^{TFA}(r)$ and $S_{ij}^{TSS}(r)$ are symmetric. The position vector for tower top/base-plate from the base of the tower is given as

$$\begin{aligned} \boldsymbol{r^{ZO}} =& \left[q_{TFA1} + q_{TFA2}\right] \boldsymbol{\hat{a}_1} + \Big[TwrHt - 0.5(S_{11}(TwrHt)^{TFA} q_{TFA1}^2 + \\ & S_{22}^{TFA}(TwrHt) q_{TFA2}^2 + 2S_{12}^{TFA}(TwrHt) q_{TFA1} q_{TFA2} + \\ & S_{11}^{TSS}(TwrHt) q_{TSS1}^2 + S_{22}^{TSS}(TwrHt) q_{TSS2}^2 + \\ & 2S_{12}^{TSS}(TwrHt) q_{TSS1} q_{TSS2}) \Big] \boldsymbol{\hat{a}_2} + \left[q_{TSS1} + q_{TSS2}\right] \boldsymbol{\hat{a}_3} \end{aligned} \tag{A.20}$$

Position vector from tower-top to nacelle center of mass is given as

$$\boldsymbol{r^{OU}} = NacCMxn\boldsymbol{\hat{d}_1} + NacCMzn\boldsymbol{\hat{d}_2} + NacMyn\boldsymbol{\hat{d}_3} \tag{A.21}$$

Position vector from tower-top to apex of coning angle is given as

$$\boldsymbol{r^{OQ}} = OverHang\boldsymbol{\hat{c}_1} + Twr2Shft\boldsymbol{\hat{d}_2} - Yaw2Shft\boldsymbol{\hat{d}_3} \tag{A.22}$$

Position vector from apex of coning angle to hub center of mass is given as

$$\boldsymbol{r^{QC}} = HubCM\boldsymbol{\hat{c}_1} \tag{A.23}$$

Position vector from apex of coning angle to blade element node for blade 1 is given as

$$\begin{aligned} \boldsymbol{r^{QS1}} =& \left[\phi_1^{B1}(r) q_{B1F1} + \phi_2^{B1}(r) q_{B1F2} + \phi_3^{B1}(r) q_{B1E1}\right] \boldsymbol{\hat{j}_1^{B1}} + \left[\psi_1^{B1}(r) q_{B1F1} \right. \\ & \left. + \psi_2^{B1}(r) q_{B1F2} + \psi_3^{B1}(r) q_{B1E1}\right] \boldsymbol{\hat{j}_2^{B1}} + \Big[r + HubRad - 0.5 \big(S_{11}^{B1}(r) q_{B1F1}^2 \\ & + S_{22}^{B1}(r) q_{B1F2} + S_{33}^{B1}(r) q_{B1E1} + 2S_{12}^{B1}(r) q_{B1F1} q_{B1F2} \\ & + 2S_{13}^{B1}(r) q_{B1F1} q_{B1E1} + 2S_{23}^{B1}(r) q_{B1F2} q_{B1E1} \big) \Big] \boldsymbol{\hat{j}_3^{B1}} \end{aligned} \tag{A.24}$$

where,

$$S_{ij}^{B1}(r) = \int_0^r \left[\frac{\mathrm{d}\phi_i^{B1}(r)}{\mathrm{d}r'} \frac{\mathrm{d}\phi_j^{B1}(r)}{\mathrm{d}r'} + \frac{\mathrm{d}\psi_i^{B1}(r)}{\mathrm{d}r'} \frac{\mathrm{d}\psi_j^{B1}(r)}{\mathrm{d}r'} \right] \mathrm{d}r' \quad \text{for } \ i,j = 1,2,3 \tag{A.25}$$

and $S_{ij}^{B1}(r) = S_{ji}^{B1}(r)$. In the above equation ϕ_1^{B1}, ϕ_2^{B1}, ϕ_3^{B1}, ψ_1^{B1}, ψ_2^{B1} and ψ_3^{B1} are the twisted mode shapes that can be obtained as

$$\phi_1^{B1}(r) = \int_0^r \left\{ \int_0^{r'} \frac{\mathrm{d}^2\phi_1^{B1F}(r'')}{\mathrm{d}r''^2} \cos(\theta_s^{B1}(r''))\mathrm{d}r'' \right\} \mathrm{d}r' \tag{A.26}$$

$$\phi_2^{B1}(r) = \int_0^r \left\{ \int_0^{r'} \frac{\mathrm{d}^2\phi_2^{B1F}(r'')}{\mathrm{d}r''^2} \cos(\theta_s^{B1}(r''))\mathrm{d}r'' \right\} \mathrm{d}r' \tag{A.27}$$

$$\phi_3^{B1}(r) = \int_0^r \left\{ \int_0^{r'} \frac{\mathrm{d}^2\phi_1^{B1E}(r'')}{\mathrm{d}r''^2} \sin(\theta_s^{B1}(r''))\mathrm{d}r'' \right\} \mathrm{d}r' \tag{A.28}$$

$$\psi_1^{B1}(r) = -\int_0^r \left\{ \int_0^{r'} \frac{\mathrm{d}^2\phi_1^{B1F}(r'')}{\mathrm{d}r''^2} \sin(\theta_s^{B1}(r''))\mathrm{d}r'' \right\} \mathrm{d}r' \tag{A.29}$$

$$\psi_2^{B1}(r) = -\int_0^r \left\{ \int_0^{r'} \frac{\mathrm{d}^2\phi_2^{B1F}(r'')}{\mathrm{d}r''^2} \sin(\theta_s^{B1}(r''))\mathrm{d}r'' \right\} \mathrm{d}r' \tag{A.30}$$

$$\psi_3^{B1}(r) = \int_0^r \left\{ \int_0^{r'} \frac{\mathrm{d}^2\phi_1^{B1E}(r'')}{\mathrm{d}r''^2} \cos(\theta_s^{B1}(r''))\mathrm{d}r'' \right\} \mathrm{d}r' \tag{A.31}$$

Equations for $\boldsymbol{r}^{\boldsymbol{QS2}}$ and $\boldsymbol{r}^{\boldsymbol{QS3}}$ are similar.

A.2.2 Angular velocities

The angular velocity of the base of the tower in the inertial (Earth) reference frame is

$$^{\boldsymbol{E}}\boldsymbol{\omega}^{\boldsymbol{X}} = \dot{q}_R \hat{\boldsymbol{z}}_{\mathbf{1}} + \dot{q}_Y \hat{\boldsymbol{z}}_{\mathbf{2}} - \dot{q}_P \hat{\boldsymbol{z}}_{\mathbf{3}} \tag{A.32}$$

Angular velocity of tower node in inertial frame of reference assuming small rotation angles is given as

$$\begin{aligned}{}^{\boldsymbol{E}}\boldsymbol{\omega}^{\boldsymbol{F}}(h) = {}^{\boldsymbol{E}}\boldsymbol{\omega}^{\boldsymbol{X}} + \Big[\frac{\mathrm{d}\phi_1^{TSS}(h)}{\mathrm{d}h}\dot{q}_{TSS1} + \frac{\mathrm{d}\phi_2^{TSS}(h)}{\mathrm{d}h}\dot{q}_{TSS2}\Big]\hat{\boldsymbol{a}}_{\boldsymbol{1}} - \Big[\frac{\mathrm{d}\phi_1^{TFA}(h)}{\mathrm{d}h}\dot{q}_{TFA1} \\ + \frac{\mathrm{d}\phi_2^{TFA}(h)}{\mathrm{d}h}\dot{q}_{TFA2}\Big]\hat{\boldsymbol{a}}_{\boldsymbol{3}}\end{aligned} \tag{A.33}$$

Angular velocity of tower-top/base-plate in inertial reference frame is

$$\begin{aligned}{}^{\boldsymbol{E}}\boldsymbol{\omega}^{\boldsymbol{B}} = {}^{\boldsymbol{E}}\boldsymbol{\omega}^{\boldsymbol{X}} + \left[\left.\frac{\mathrm{d}\phi_1^{TSS}(h)}{\mathrm{d}h}\right|_{h=TwrHt}\dot{q}_{TSS1} + \left.\frac{\mathrm{d}\phi_2^{TSS}(h)}{\mathrm{d}h}\right|_{h=TwrHt}\dot{q}_{TSS2}\right]\hat{\boldsymbol{a}}_{\boldsymbol{1}} \\ - \left[\left.\frac{\mathrm{d}\phi_1^{TFA}(h)}{\mathrm{d}h}\right|_{h=TwrHt}\dot{q}_{TFA1} + \left.\frac{\mathrm{d}\phi_2^{TFA}(h)}{\mathrm{d}h}\right|_{h=TwrHt}\dot{q}_{TFA2}\right]\hat{\boldsymbol{a}}_{\boldsymbol{3}}\end{aligned} \tag{A.34}$$

Angular velocity of nacelle in inertial reference frame

$${}^{\boldsymbol{E}}\boldsymbol{\omega}^{\boldsymbol{N}} = {}^{\boldsymbol{E}}\boldsymbol{\omega}^{\boldsymbol{B}} + \dot{q}_{yaw}\hat{\boldsymbol{d}}_{\boldsymbol{2}} \tag{A.35}$$

Angular velocity of low speed shaft at the rotor end in inertial reference frame

$${}^{\boldsymbol{E}}\boldsymbol{\omega}^{\boldsymbol{L}} = {}^{\boldsymbol{E}}\boldsymbol{\omega}^{\boldsymbol{N}} + \dot{q}_{DrTr}\hat{\boldsymbol{c}}_{\boldsymbol{1}} + \dot{q}_{GeAz}\hat{\boldsymbol{c}}_{\boldsymbol{1}} \tag{A.36}$$

Angular velocity of an element of blade 1 fixed at a distance r from the root of the blade is given as

$$\begin{aligned}{}^{\boldsymbol{E}}\boldsymbol{\omega}^{\boldsymbol{M1}}(r) = {}^{\boldsymbol{E}}\boldsymbol{\omega}^{\boldsymbol{L}} - \left[\frac{d\psi_1^{B1}(r)}{dr}\dot{q}_{B1F1} + \frac{d\psi_2^{B1}(r)}{dr}\dot{q}_{B1F2}\frac{d\psi_3^{B1}(r)}{dr}\dot{q}_{B1E1}\right]\hat{\boldsymbol{j}}_{\boldsymbol{1}}^{\boldsymbol{B1}} \\ - \left[\frac{d\phi_1^{B1}(r)}{dr}\dot{q}_{B1F1} + \frac{d\phi_2^{B1}(r)}{dr}\dot{q}_{B1F2} + \frac{d\phi_3^{B1}(r)}{dr}\dot{q}_{B1E1}\right]\hat{\boldsymbol{j}}_{\boldsymbol{2}}^{\boldsymbol{B1}}\end{aligned} \tag{A.37}$$

The angular velocities of blades 2 ${}^{\boldsymbol{E}}\boldsymbol{\omega}^{\boldsymbol{M2}}(r)$, and blade 3 ${}^{\boldsymbol{E}}\boldsymbol{\omega}^{\boldsymbol{M3}}(r)$ can be found similarly. The generator is connected to the high speed shaft which may or may not rotate in the opposite direction of the low speed shaft and since q_{GeAz} represents the position of the low speed shaft near the entrance of the gearbox, the angular velocity of the generator is given as

$${}^{\boldsymbol{E}}\boldsymbol{\omega}^{\boldsymbol{G}} = {}^{\boldsymbol{E}}\boldsymbol{\omega}^{\boldsymbol{N}} + GenDir.GBRatio.\dot{q}_{GeAz}\hat{\boldsymbol{c}}_{\boldsymbol{1}} \tag{A.38}$$

where, $GBRatio$ is the gear box ratio and

$$GenDir = \begin{cases} -1 & \text{for Gear Box Reverse} = \text{True} \\ 1 & \text{for Gear Box Reverse} = \text{False} \end{cases} \tag{A.39}$$

A.2.3 Linear Velocities

In this section the linear velocities of all important points of the wind turbine are described. The linear velocity of the tower base can be given as

$$^{\boldsymbol{E}}\boldsymbol{v}^{\boldsymbol{Z}} = \dot{q}_{Sq}\hat{\boldsymbol{z}}_{\boldsymbol{1}} + \dot{q}_{Hv}\hat{\boldsymbol{z}}_{\boldsymbol{2}} - \dot{q}_{Sw}\hat{\boldsymbol{z}}_{\boldsymbol{3}} \tag{A.40}$$

Linear velocity of tower element in inertial reference frame can be obtained from one point moving on a rigid body formula (Kane and Levinson, 1985)

$$\begin{aligned} ^{\boldsymbol{E}}\boldsymbol{v}^{\boldsymbol{T}}(h) &= {}^{\boldsymbol{E}}\boldsymbol{v}^{\boldsymbol{Z}} + {}^{\boldsymbol{E}}\boldsymbol{v}^{\bar{\boldsymbol{T}}}(h) + {}^{\boldsymbol{X}}\boldsymbol{v}^{\boldsymbol{T}}(h) \\ &= {}^{\boldsymbol{E}}\boldsymbol{v}^{\boldsymbol{Z}} + {}^{\boldsymbol{E}}\boldsymbol{\omega}^{\boldsymbol{X}}(h) \times \boldsymbol{r}^{\boldsymbol{ZT}}(h) + {}^{\boldsymbol{X}}\boldsymbol{v}^{\boldsymbol{T}}(h) \end{aligned} \tag{A.41}$$

where ${}^{\boldsymbol{E}}\boldsymbol{v}^{\bar{\boldsymbol{T}}}$ denotes the velocity in E of the point $\overline{T}$ of X that coincides with T at the instant under consideration. In the above equation ${}^{\boldsymbol{X}}\boldsymbol{v}^{\boldsymbol{T}}$ is given as

$$\begin{aligned} ^{\boldsymbol{X}}\boldsymbol{v}^{\boldsymbol{T}}(h) = {} & \left[\phi_1^{TFA}(h)\dot{q}_{TFA1} + \phi_2^{TFA}(h)\dot{q}_{TFA2}\right]\hat{\boldsymbol{a}}_{\boldsymbol{1}} - \Big[S_{11}^{TFA}(h)q_{TFA1}\dot{q}_{TFA1} \\ & + S_{22}^{TFA}(h)q_{TFA2}\dot{q}_{TFA2} + S_{12}^{TFA}(h)\Big(\dot{q}_{TFA1}q_{TFA2} + q_{TFA1}\dot{q}_{TFA2}\Big) \\ & + S_{11}^{TSS}(h)q_{TSS1}\dot{q}_{TSS1} + S_{22}^{TSS}(h)q_{TSS2}\dot{q}_{TSS2} \\ & + S_{12}^{TSS}(h)\Big(\dot{q}_{TSS1}q_{TSS2} + q_{TSS1}\dot{q}_{TSS2}\Big)\Big]\hat{\boldsymbol{a}}_{\boldsymbol{2}} + \Big[\phi_1^{TSS}(h)\dot{q}_{TSS1} \\ & + \phi_2^{TSS}(h)\dot{q}_{TSS2}\Big]\hat{\boldsymbol{a}}_{\boldsymbol{3}} \end{aligned} \tag{A.42}$$

Similarly the velocity of tower top/base plate can be given as

$$^{\boldsymbol{E}}\boldsymbol{v}^{\boldsymbol{O}} = {}^{\boldsymbol{E}}\boldsymbol{v}^{\boldsymbol{Z}} + {}^{\boldsymbol{E}}\boldsymbol{\omega}^{\boldsymbol{O}} \times \boldsymbol{r}^{\boldsymbol{ZO}}(h) + {}^{\boldsymbol{X}}\boldsymbol{v}^{\boldsymbol{O}} \tag{A.43}$$

$$
\begin{aligned}
{}^{\boldsymbol{X}}\boldsymbol{v}^{\boldsymbol{O}} &= \left[\dot{q}_{TFA1} + \dot{q}_{TFA2}\right]\hat{\boldsymbol{a}}_{\boldsymbol{1}} - \Big[S_{11}^{TFA}(TwrHt)q_{TFA1}\dot{q}_{TFA1} \\
&\quad + S_{22}^{TFA}(TwrHt)q_{TFA2}\dot{q}_{TFA2} + S_{12}^{TFA}(TwrHt)\Big(\dot{q}_{TFA1}q_{TFA2} \\
&\quad + q_{TFA1}\dot{q}_{TFA2}\Big) + S_{11}^{TSS}(TwrHt)q_{TSS1}\dot{q}_{TSS1} + S_{22}^{TSS}(TwrHt)q_{TSS2}\dot{q}_{TSS2} \\
&\quad + S_{12}^{TSS}(TwrHt)\Big(\dot{q}_{TSS1}q_{TSS2} + q_{TSS1}\dot{q}_{TSS2}\Big)\Big]\hat{\boldsymbol{a}}_{\boldsymbol{2}} + \left[\dot{q}_{TSS1} + \dot{q}_{TSS2}\right]\hat{\boldsymbol{a}}_{\boldsymbol{3}}
\end{aligned}
\tag{A.44}
$$

The linear velocity of the nacelle center of mass can be obtained from two points fixed on a rigid body formula as (Kane and Levinson, 1985)

$$
{}^{\boldsymbol{E}}\boldsymbol{v}^{\boldsymbol{U}} = {}^{\boldsymbol{E}}\boldsymbol{v}^{\boldsymbol{O}} + {}^{\boldsymbol{E}}\boldsymbol{\omega}^{\boldsymbol{N}} \times \boldsymbol{r}^{\boldsymbol{OU}} \tag{A.45}
$$

The linear velocity of apex of the coning angle is given as

$$
{}^{\boldsymbol{E}}\boldsymbol{v}^{\boldsymbol{Q}} = {}^{\boldsymbol{E}}\boldsymbol{v}^{\boldsymbol{O}} + {}^{\boldsymbol{E}}\boldsymbol{\omega}^{\boldsymbol{L}} \times \boldsymbol{r}^{\boldsymbol{OQ}} \tag{A.46}
$$

The linear velocity of center of mass of hub can be given as

$$
{}^{\boldsymbol{E}}\boldsymbol{v}^{\boldsymbol{C}} = {}^{\boldsymbol{E}}\boldsymbol{v}^{\boldsymbol{Q}} + {}^{\boldsymbol{E}}\boldsymbol{\omega}^{\boldsymbol{L}} \times \boldsymbol{r}^{\boldsymbol{QC}} \tag{A.47}
$$

Finally, the linear velocity of blade 1 element at a distance r from the root of the blade is given as

$$
{}^{\boldsymbol{E}}\boldsymbol{v}^{\boldsymbol{S1}}(r) = {}^{\boldsymbol{E}}\boldsymbol{v}^{\boldsymbol{Q}} + {}^{\boldsymbol{E}}\boldsymbol{\omega}^{\boldsymbol{L}} \times \boldsymbol{r}^{\boldsymbol{QS1}} + {}^{\boldsymbol{L}}\boldsymbol{v}^{\boldsymbol{S1}}(r) \tag{A.48}
$$

where,

$$
\begin{aligned}
{}^{\boldsymbol{L}}\boldsymbol{v}^{\boldsymbol{S1}}(r) &= \left[\phi_1^{B1}(r)\dot{q}_{B1F1} + \phi_2^{B1}\dot{q}_{B1F2} + \phi_3^{B1}\dot{q}_{B1E1}\right]\hat{\boldsymbol{j}}_{\boldsymbol{1}}^{\boldsymbol{B1}} + \Big[\psi_1^{B1}(r)\dot{q}_{B1F1} \\
&\quad + \psi_2^{B1}\dot{q}_{B1F2} + \psi_3^{B1}\dot{q}_{B1E1}\Big]\hat{\boldsymbol{j}}_{\boldsymbol{2}}^{\boldsymbol{B1}} + \Big[S_{11}^{B1}(r)q_{B1F1}\dot{q}_{B1F1} + S_{22}^{B1}(r)q_{B1F2}\dot{q}_{B1F2} \\
&\quad + S_{33}^{B1}(r)q_{B1E1}\dot{q}_{B1E1} + S_{12}^{B1}\Big(\dot{q}_{B1F1}q_{B1F2} + q_{B1F1}\dot{q}_{B1F2}\Big) \\
&\quad + S_{13}^{B1}\Big(\dot{q}_{B1F1}q_{B1E1} + q_{B1F1}\dot{q}_{B1E1}\Big) + S_{23}^{B1}\Big(\dot{q}_{B1F2}q_{B1E1} \\
&\quad + q_{B1F2}\dot{q}_{B1E1}\Big)\Big]\hat{\boldsymbol{j}}_{\boldsymbol{3}}^{\boldsymbol{B1}}
\end{aligned}
\tag{A.49}
$$

The linear velocities for blade 2, ${}^{\boldsymbol{E}}\boldsymbol{v}^{\boldsymbol{S2}}(r)$ and blade 3, ${}^{\boldsymbol{E}}\boldsymbol{v}^{\boldsymbol{S3}}(r)$ can be obtained similarly.

A.2.4 Partial Angular Velocities

According to (Kane and Levinson, 1985) all linear velocities can be written as a combination of the partial velocities as

$$ {}^{\boldsymbol{E}}\boldsymbol{\omega}^{\boldsymbol{N_i}}(\dot{q},q,t) = \sum_{r=1}^{22} {}^{\boldsymbol{E}}\boldsymbol{\omega}_{\boldsymbol{r}}^{\boldsymbol{N_i}}(q,t)u_r + {}^{\boldsymbol{E}}\boldsymbol{\omega}_{\boldsymbol{t}}^{\boldsymbol{N_i}}(q,t) \tag{A.50} $$

for each rigid body N_i in the system. Where ${}^{\boldsymbol{E}}\boldsymbol{\omega}_{\boldsymbol{r}}^{\boldsymbol{N_i}}(q,t)$ are the partial angular velocities. u_r are called generalized speeds according to (Kane and Levinson, 1985) and in general their choice is arbitrary and it brings the linear velocities in A.2.2 and A.2.3 into particular advantageous form. ${}^{\boldsymbol{E}}\boldsymbol{\omega}_{\boldsymbol{t}}^{\boldsymbol{N_i}}$ contains the terms that do not fall into the linear superposition form. Here, time derivatives of the DOFs in equation 3.1 are chosen as the generalized speeds (i.e. $u_r = \dot{q}_r$). This choice of generalized speeds makes renders all the ${}^{\boldsymbol{E}}\boldsymbol{\omega}_{\boldsymbol{t}}^{\boldsymbol{N_i}}(q,t)$ terms are zeros as will be shown. Following equation A.32 the partial angular velocities for the platform can be given as

$$ \begin{aligned} {}^{\boldsymbol{E}}\boldsymbol{\omega}_{\boldsymbol{r}}^{\boldsymbol{X}} &= \begin{cases} \hat{\boldsymbol{z}}_{\boldsymbol{1}} & \text{for } r = R \\ -\hat{\boldsymbol{z}}_{\boldsymbol{3}} & \text{for } r = P \\ \hat{\boldsymbol{z}}_{\boldsymbol{2}} & \text{for } r = Y \\ 0 & \text{otherwise} \end{cases} \\ {}^{\boldsymbol{E}}\boldsymbol{\omega}_{\boldsymbol{t}}^{\boldsymbol{X}} &= 0 \end{aligned} \tag{A.51} $$

The partial angular velocities for a tower element at a height h from the base of the tower is given as

$$ \begin{aligned} {}^{\boldsymbol{E}}\boldsymbol{\omega}_{\boldsymbol{r}}^{\boldsymbol{F}}(h) &= {}^{\boldsymbol{E}}\boldsymbol{\omega}_{\boldsymbol{r}}^{\boldsymbol{X}} + \begin{cases} \dfrac{-d\phi_1^{TFA}(h)}{dh}\hat{\boldsymbol{a}}_{\boldsymbol{3}} & \text{for } r = TFA1 \\ \dfrac{d\phi_1^{TSS}(h)}{dh}\hat{\boldsymbol{a}}_{\boldsymbol{1}} & \text{for } r = TSS1 \\ \dfrac{-d\phi_2^{TFA}(h)}{dh}\hat{\boldsymbol{a}}_{\boldsymbol{3}} & \text{for } r = TFA2 \\ \dfrac{d\phi_2^{TSS}(h)}{dh}\hat{\boldsymbol{a}}_{\boldsymbol{1}} & \text{for } r = TSS2 \\ 0 & \text{otherwise} \end{cases} \\ {}^{\boldsymbol{E}}\boldsymbol{\omega}_{\boldsymbol{t}}^{\boldsymbol{F}}(h) &= 0 \end{aligned} \tag{A.52} $$

Partial angular velocities for tower-top/base-plate can be given as

$$
\begin{aligned}
{}^{E}\boldsymbol{\omega}_{\boldsymbol{r}}^{\boldsymbol{B}} &= {}^{E}\boldsymbol{\omega}_{\boldsymbol{r}}^{\boldsymbol{X}} + \begin{cases} \left.\dfrac{-d\phi_1^{TFA}}{dh}\right|_{h=TwrHt} \hat{\boldsymbol{a}}_{\boldsymbol{3}} & \text{for } r = TFA1 \\ \left.\dfrac{d\phi_1^{TSS}}{dh}\right|_{h=TwrHt} \hat{\boldsymbol{a}}_{\boldsymbol{1}} & \text{for } r = TSS1 \\ \left.\dfrac{-d\phi_2^{TFA}}{dh}\right|_{h=TwrHt} \hat{\boldsymbol{a}}_{\boldsymbol{3}} & \text{for } r = TFA2 \\ \left.\dfrac{d\phi_2^{TSS}}{dh}\right|_{h=TwrHt} \hat{\boldsymbol{a}}_{\boldsymbol{1}} & \text{for } r = TSS2 \\ 0 & \text{otherwise} \end{cases} \\
{}^{E}\boldsymbol{\omega}_{\boldsymbol{t}}^{\boldsymbol{B}} &= 0
\end{aligned} \tag{A.53}
$$

Partial angular velocities for nacelle can be given as

$$
\begin{aligned}
{}^{E}\boldsymbol{\omega}_{\boldsymbol{r}}^{\boldsymbol{N}} &= {}^{E}\boldsymbol{\omega}_{\boldsymbol{r}}^{\boldsymbol{B}} + \begin{cases} \hat{\boldsymbol{d}}_{\boldsymbol{2}} & \text{for } r = yaw \\ 0 & \text{otherwise} \end{cases} \\
{}^{E}\boldsymbol{\omega}_{\boldsymbol{t}}^{\boldsymbol{N}} &= 0
\end{aligned} \tag{A.54}
$$

Partial angular velocities for low speed shaft can be given as

$$
\begin{aligned}
{}^{E}\boldsymbol{\omega}_{\boldsymbol{r}}^{\boldsymbol{L}} &= {}^{E}\boldsymbol{\omega}_{\boldsymbol{r}}^{\boldsymbol{N}} + \begin{cases} \hat{\boldsymbol{c}}_{\boldsymbol{1}} & \text{for } r = GeAz \\ \hat{\boldsymbol{c}}_{\boldsymbol{1}} & \text{for } r = DrTr \\ 0 & \text{otherwise} \end{cases} \\
{}^{E}\boldsymbol{\omega}_{\boldsymbol{t}}^{\boldsymbol{L}} &= 0
\end{aligned} \tag{A.55}
$$

Partial angular velocities for blade 1 element can be given as

$$
\begin{aligned}
{}^{E}\boldsymbol{\omega}_{\boldsymbol{r}}^{\boldsymbol{M1}}(r) &= {}^{E}\boldsymbol{\omega}_{\boldsymbol{r}}^{\boldsymbol{L}} + \begin{cases} -\dfrac{d\psi_1^{B1}(r)}{dr}\hat{\boldsymbol{j}}_{\boldsymbol{1}}^{\boldsymbol{B1}} + \dfrac{d\phi_1^{B1}(r)}{dr}\hat{\boldsymbol{j}}_{\boldsymbol{2}}^{\boldsymbol{B1}} & \text{for } r = B1F1 \\ -\dfrac{d\psi_3^{B1}(r)}{dr}\hat{\boldsymbol{j}}_{\boldsymbol{1}}^{\boldsymbol{B1}} + \dfrac{d\phi_3^{B1}(r)}{dr}\hat{\boldsymbol{j}}_{\boldsymbol{2}}^{\boldsymbol{B1}} & \text{for } r = B1E1 \\ -\dfrac{d\psi_2^{B1}(r)}{dr}\hat{\boldsymbol{j}}_{\boldsymbol{1}}^{\boldsymbol{B1}} + \dfrac{d\phi_2^{B1}(r)}{dr}\hat{\boldsymbol{j}}_{\boldsymbol{2}}^{\boldsymbol{B1}} & \text{for } r = B1F2 \\ 0 & \text{otherwise} \end{cases} \\
{}^{E}\boldsymbol{\omega}_{\boldsymbol{t}}^{\boldsymbol{M1}}(r) &= 0
\end{aligned} \tag{A.56}
$$

The equations for ${}^{\boldsymbol{E}}\boldsymbol{\omega}_{\boldsymbol{r}}^{\boldsymbol{M2}}(r)$ and ${}^{\boldsymbol{E}}\boldsymbol{\omega}_{\boldsymbol{r}}^{\boldsymbol{M3}}(r)$ are similar. Finally, the partial angular velocities for the generator is given as

$$
\begin{aligned}
{}^{\boldsymbol{E}}\boldsymbol{\omega}_{\boldsymbol{r}}^{\boldsymbol{G}} &= {}^{\boldsymbol{E}}\boldsymbol{\omega}_{\boldsymbol{r}}^{\boldsymbol{N}} + \begin{cases} GenDir.GBRatio.\hat{\boldsymbol{c}}_{\boldsymbol{1}} & \text{for } r = GeAz \\ 0 & \text{otherwise} \end{cases} \\
{}^{\boldsymbol{E}}\boldsymbol{\omega}_{\boldsymbol{t}}^{\boldsymbol{G}} &= 0
\end{aligned}
\tag{A.57}
$$

A.2.5 Partial Linear Velocities

Similar to A.2.4 the linear velocities of each point X_i in the system can be written in the form

$$
{}^{\boldsymbol{E}}\boldsymbol{v}^{\boldsymbol{X_i}}(\dot{q}, q, t) = \sum_{r=1}^{16} {}^{\boldsymbol{E}}\boldsymbol{v}_{\boldsymbol{r}}^{\boldsymbol{X_i}}(q, t) u_r + {}^{\boldsymbol{E}}\boldsymbol{v}_{\boldsymbol{t}}^{\boldsymbol{X_i}}(q, t) \tag{A.58}
$$

where, ${}^{\boldsymbol{E}}\boldsymbol{v}_{\boldsymbol{r}}^{\boldsymbol{X_i}}(q, t)$ are the partial linear velocities, u_r are the generalized speeds and ${}^{\boldsymbol{E}}\boldsymbol{v}_{\boldsymbol{t}}^{\boldsymbol{X_i}}$ contains the remaining terms. Again, the choice of generalized speeds u_r renders all the ${}^{\boldsymbol{E}}\boldsymbol{v}_{\boldsymbol{t}}^{\boldsymbol{X_i}}(q, t)$ terms as zeros. Following the same approach as the previous section the partial linear velocities of the tower base can be obtained as

$$
\begin{aligned}
{}^{\boldsymbol{E}}\boldsymbol{v}_{\boldsymbol{r}}^{\boldsymbol{Z}} &= \begin{cases} \hat{\boldsymbol{z}}_{\boldsymbol{1}} & \text{for } r = Sg \\ -\hat{\boldsymbol{z}}_{\boldsymbol{3}} & \text{for } r = Sw \\ \hat{\boldsymbol{z}}_{\boldsymbol{2}} & \text{for } r = Hv \\ 0 & \text{otherwise} \end{cases} \\
{}^{\boldsymbol{E}}\boldsymbol{v}_{\boldsymbol{t}}^{\boldsymbol{Z}} &= 0
\end{aligned}
\tag{A.59}
$$

The partial linear velocities for the platform centre of mass can be obtained as

$$
\begin{aligned}
{}^{\boldsymbol{E}}\boldsymbol{v}_{\boldsymbol{r}}^{\boldsymbol{Y}} &= {}^{\boldsymbol{E}}\boldsymbol{v}_{\boldsymbol{r}}^{\boldsymbol{Z}} + \begin{cases} {}^{\boldsymbol{E}}\boldsymbol{\omega}_{\boldsymbol{r}}^{\boldsymbol{X}} \times \boldsymbol{r}^{\boldsymbol{ZY}} & \text{for } r = R,\ P,\ Y \\ 0 & \text{otherwise} \end{cases} \\
{}^{\boldsymbol{E}}\boldsymbol{v}_{\boldsymbol{t}}^{\boldsymbol{Z}} &= 0
\end{aligned}
\tag{A.60}
$$

The partial linear velocities for the tower element can be given as

$$
\begin{aligned}
{}^{E}\boldsymbol{v}_{\boldsymbol{r}}^{\boldsymbol{T}}(h) &= \begin{cases} \phi_1^{TFA}(h)\hat{\boldsymbol{a}}_{\boldsymbol{1}} - \left[S_{11}^{TFA}(h)q_{TFA1} + S_{12}^{TFA}(h)q_{TFA2}\right]\hat{\boldsymbol{a}}_{\boldsymbol{2}} & \text{for } r = TFA1 \\ \phi_1^{TSS}(h)\hat{\boldsymbol{a}}_{\boldsymbol{3}} - \left[S_{11}^{TSS}(h)q_{TSS1} + S_{12}^{TSS}(h)q_{TSS2}\right]\hat{\boldsymbol{a}}_{\boldsymbol{2}} & \text{for } r = TSS1 \\ \phi_2^{TFA}(h)\hat{\boldsymbol{a}}_{\boldsymbol{1}} - \left[S_{22}^{TFA}(h)q_{TFA2} + S_{12}^{TFA}(h)q_{TFA1}\right]\hat{\boldsymbol{a}}_{\boldsymbol{2}} & \text{for } r = TFA2 \\ \phi_2^{TSS}(h)\hat{\boldsymbol{a}}_{\boldsymbol{3}} - \left[S_{22}^{TSS}(h)q_{TSS2} + S_{12}^{TSS}(h)q_{TSS1}\right]\hat{\boldsymbol{a}}_{\boldsymbol{2}} & \text{for } r = TSS2 \\ 0 & \text{otherwise} \end{cases} \\
{}^{E}\boldsymbol{v}_{\boldsymbol{t}}^{\boldsymbol{T}}(h) &= 0
\end{aligned}
\tag{A.61}
$$

Partial linear velocities for tower top

$$
\begin{aligned}
{}^{E}\boldsymbol{v}_{\boldsymbol{r}}^{\boldsymbol{O}} &= \begin{cases} \hat{\boldsymbol{a}}_{\boldsymbol{1}} - \left[S_{11}^{TFA}(TwrHt)q_{TFA1} + S_{12}^{TFA}(TwrHt)q_{TFA2}\right]\hat{\boldsymbol{a}}_{\boldsymbol{2}} & \text{for } r = TFA1 \\ \hat{\boldsymbol{a}}_{\boldsymbol{3}} - \left[S_{11}^{TSS}(TwrHt)q_{TSS1} + S_{12}^{TSS}(TwrHt)q_{TSS2}\right]\hat{\boldsymbol{a}}_{\boldsymbol{2}} & \text{for } r = TSS1 \\ \hat{\boldsymbol{a}}_{\boldsymbol{1}} - \left[S_{22}^{TFA}(TwrHt)q_{TFA2} + S_{12}^{TFA}(TwrHt)q_{TFA1}\right]\hat{\boldsymbol{a}}_{\boldsymbol{2}} & \text{for } r = TFA2 \\ \hat{\boldsymbol{a}}_{\boldsymbol{3}} - \left[S_{22}^{TSS}(TwrHt)q_{TSS2} + S_{12}^{TSS}(TwrHt)q_{TSS1}\right]\hat{\boldsymbol{a}}_{\boldsymbol{2}} & \text{for } r = TSS2 \\ 0 & \text{otherwise} \end{cases} \\
{}^{E}\boldsymbol{v}_{\boldsymbol{t}}^{\boldsymbol{O}} &= 0
\end{aligned}
\tag{A.62}
$$

Partial linear velocities for nacelle center of mass is given as

$$
\begin{aligned}
{}^{E}\boldsymbol{v}_{\boldsymbol{r}}^{\boldsymbol{U}} &= {}^{E}\boldsymbol{v}_{\boldsymbol{r}}^{\boldsymbol{O}} + \begin{cases} {}^{E}\boldsymbol{\omega}_{\boldsymbol{r}}^{\boldsymbol{N}} \times \boldsymbol{r}^{\boldsymbol{OU}} & \text{for } r = 1 \text{ to } 11 \\ 0 & \text{otherwise} \end{cases} \\
{}^{E}\boldsymbol{v}_{\boldsymbol{t}}^{\boldsymbol{U}} &= 0
\end{aligned}
\tag{A.63}
$$

Partial linear velocities for apex of coning angle is given as

$$
\begin{aligned}
{}^{E}\boldsymbol{v}_{\boldsymbol{r}}^{\boldsymbol{Q}} &= {}^{E}\boldsymbol{v}_{\boldsymbol{r}}^{\boldsymbol{O}} + \begin{cases} {}^{E}\boldsymbol{\omega}_{\boldsymbol{r}}^{\boldsymbol{L}} \times \boldsymbol{r}^{\boldsymbol{OQ}} & \text{for } r = 1 \text{ to } 13 \\ 0 & \text{otherwise} \end{cases} \\
{}^{E}\boldsymbol{v}_{\boldsymbol{t}}^{\boldsymbol{Q}} &= 0
\end{aligned}
\tag{A.64}
$$

Partial linear velocities for hub center of mass is given as

$$
\begin{aligned}
{}^{E}\boldsymbol{v}_{\boldsymbol{r}}^{\boldsymbol{C}} &= {}^{E}\boldsymbol{v}_{\boldsymbol{r}}^{\boldsymbol{Q}} + \begin{cases} {}^{E}\boldsymbol{\omega}_{\boldsymbol{r}}^{\boldsymbol{L}} \times \boldsymbol{r}^{\boldsymbol{QC}} & \text{for } r = 1 \text{ to } 13 \\ 0 & \text{otherwise} \end{cases} \\
{}^{E}\boldsymbol{v}_{\boldsymbol{t}}^{\boldsymbol{C}} &= 0
\end{aligned}
\tag{A.65}
$$

Partial linear velocities for blade 1 element is given as

$$
\begin{aligned}
{}^{E}\boldsymbol{v}_{\boldsymbol{r}}^{\boldsymbol{S1}}(r) &= {}^{E}\boldsymbol{v}_{\boldsymbol{r}}^{\boldsymbol{Q}} \\
&+ \begin{cases} {}^{E}\boldsymbol{\omega}_{\boldsymbol{r}}^{\boldsymbol{L}} \times \boldsymbol{r}^{\boldsymbol{QS1}} & r = 1 \text{ to } 13 \\ \phi_1^{B1}(r)\hat{\boldsymbol{j}}_{\boldsymbol{1}}^{\boldsymbol{B1}} + \psi_1^{B1}(r)\hat{\boldsymbol{j}}_{\boldsymbol{2}}^{\boldsymbol{B1}} - \Big[S_{11}^{B1}(r)q_{B1F1} + S_{12}^{B1}(r)q_{B1F1} & \\ +S_{13}^{B1}(r)q_{B1E1}\Big]\hat{\boldsymbol{j}}_{\boldsymbol{3}}^{\boldsymbol{B1}} & r = B1F1 \\ \phi_3^{B1}(r)\hat{\boldsymbol{j}}_{\boldsymbol{1}}^{\boldsymbol{B1}} + \psi_3^{B1}(r)\hat{\boldsymbol{j}}_{\boldsymbol{2}}^{\boldsymbol{B1}} - \Big[S_{33}^{B1}(r)q_{B1E1} + S_{23}^{B1}(r)q_{B1F2} & \\ +S_{13}^{B1}(r)q_{B1F1}\Big]\hat{\boldsymbol{j}}_{\boldsymbol{3}}^{\boldsymbol{B1}} & r = B1E1 \\ \phi_2^{B1}(r)\hat{\boldsymbol{j}}_{\boldsymbol{1}}^{\boldsymbol{B1}} + \psi_2^{B1}(r)\hat{\boldsymbol{j}}_{\boldsymbol{2}}^{\boldsymbol{B1}} - \Big[S_{22}^{B1}(r)q_{B1F2} + S_{12}^{B1}(r)q_{B1F1} & \\ +S_{23}^{B1}(r)q_{B1E1}\Big]\hat{\boldsymbol{j}}_{\boldsymbol{3}}^{\boldsymbol{B1}} & r = B1F2 \\ 0 & \text{otherwise} \end{cases} \\
{}^{E}\boldsymbol{v}_{\boldsymbol{t}}^{\boldsymbol{S1}}(r) &= 0
\end{aligned}
\tag{A.66}
$$

Equations for ${}^{E}\boldsymbol{v}_{\boldsymbol{r}}^{\boldsymbol{S2}}(r)$ and ${}^{E}\boldsymbol{v}_{\boldsymbol{r}}^{\boldsymbol{S3}}(r)$ can be obtained similarly.

A.2.6 Angular Accelerations

For every rigid body N_i in the system the angular acceleration can be written as

$$
{}^{E}\boldsymbol{\alpha}^{\boldsymbol{N_i}}(\ddot{q}, \dot{q}, q, t) = \sum_{r=1}^{22} {}^{E}\boldsymbol{\omega}_{\boldsymbol{r}}^{\boldsymbol{N_i}}(q,t)\ddot{q}_r + \sum_{r=1}^{22} \frac{\mathrm{d}}{\mathrm{d}t}\{{}^{E}\boldsymbol{\omega}_{\boldsymbol{r}}^{\boldsymbol{N_i}}(q,t)\}\dot{q}_r + \frac{\mathrm{d}}{\mathrm{d}t}\{{}^{E}\boldsymbol{\omega}_{\boldsymbol{t}}^{\boldsymbol{N_i}}(q,t)\} \tag{A.67}
$$

Only the $\dfrac{\mathrm{d}}{\mathrm{d}t}\{{}^{E}\boldsymbol{\omega}_{\boldsymbol{r}}^{\boldsymbol{N_i}}(q,t)\}$ terms are to be derived as all the other terms are known at this stage. These terms will be named as the partial angular accelerations. The partial angular acceleration terms for the tower-base can be obtained as

$$
\begin{aligned}
&\frac{\mathrm{d}}{\mathrm{d}t}\{{}^{\boldsymbol{E}}\boldsymbol{\omega}_{\boldsymbol{r}}^{\boldsymbol{X}}\} = 0 \quad \text{for } r = 1 \text{ to } 22 \\
&\frac{\mathrm{d}}{\mathrm{d}t}\{{}^{\boldsymbol{E}}\boldsymbol{\omega}_{\boldsymbol{t}}^{\boldsymbol{X}}\} = 0
\end{aligned}
\tag{A.68}
$$

The partial angular acceleration terms for the tower element is given as

$$
\begin{aligned}
&\frac{\mathrm{d}}{\mathrm{d}t}\{{}^{\boldsymbol{E}}\boldsymbol{\omega}_{\boldsymbol{r}}^{\boldsymbol{F}}(h)\} = \begin{cases} {}^{\boldsymbol{E}}\boldsymbol{\omega}^{\boldsymbol{X}} \times {}^{\boldsymbol{E}}\boldsymbol{\omega}_{\boldsymbol{r}}^{\boldsymbol{F}}(h) = 0 & \text{for } r = 1 \text{ to } 10 \\ 0 & \text{otherwise} \end{cases} \\
&\frac{\mathrm{d}}{\mathrm{d}t}\{{}^{\boldsymbol{E}}\boldsymbol{\omega}_{\boldsymbol{t}}^{\boldsymbol{F}}(h)\} = 0
\end{aligned}
\tag{A.69}
$$

The partial angular acceleration terms for the tower-top/base-plate is given as

$$
\begin{aligned}
&\frac{\mathrm{d}}{\mathrm{d}t}\{{}^{\boldsymbol{E}}\boldsymbol{\omega}_{\boldsymbol{r}}^{\boldsymbol{B}}\} = \begin{cases} {}^{\boldsymbol{E}}\boldsymbol{\omega}^{\boldsymbol{X}} \times {}^{\boldsymbol{E}}\boldsymbol{\omega}_{\boldsymbol{r}}^{\boldsymbol{B}} & \text{for } r = 1 \text{ to } 10 \\ 0 & \text{otherwise} \end{cases} \\
&\frac{\mathrm{d}}{\mathrm{d}t}\{{}^{\boldsymbol{E}}\boldsymbol{\omega}_{\boldsymbol{t}}^{\boldsymbol{B}}\} = 0
\end{aligned}
\tag{A.70}
$$

The partial angular acceleration terms for the nacelle is given as

$$
\begin{aligned}
&\frac{\mathrm{d}}{\mathrm{d}t}\{{}^{\boldsymbol{E}}\boldsymbol{\omega}_{\boldsymbol{r}}^{\boldsymbol{N}}\} = \frac{d}{dt}\{{}^{\boldsymbol{E}}\boldsymbol{\omega}_{\boldsymbol{r}}^{\boldsymbol{B}}\} + \begin{cases} {}^{\boldsymbol{E}}\boldsymbol{\omega}^{\boldsymbol{B}} \times {}^{\boldsymbol{E}}\boldsymbol{\omega}_{\boldsymbol{yaw}}^{\boldsymbol{N}} & \text{for } r = yaw \\ 0 & \text{otherwise} \end{cases} \\
&\frac{\mathrm{d}}{\mathrm{d}t}\{{}^{\boldsymbol{E}}\boldsymbol{\omega}_{\boldsymbol{t}}^{\boldsymbol{N}}\} = 0
\end{aligned}
\tag{A.71}
$$

The partial angular acceleration terms for the low speed shaft is given as

$$
\begin{aligned}
&\frac{\mathrm{d}}{\mathrm{d}t}\{{}^{\boldsymbol{E}}\boldsymbol{\omega}_{\boldsymbol{r}}^{\boldsymbol{L}}\} = \frac{d}{dt}\{{}^{\boldsymbol{E}}\boldsymbol{\omega}_{\boldsymbol{r}}^{\boldsymbol{N}}\} + \begin{cases} {}^{\boldsymbol{E}}\boldsymbol{\omega}^{\boldsymbol{N}} \times {}^{\boldsymbol{E}}\boldsymbol{\omega}_{\boldsymbol{GeAz}}^{\boldsymbol{L}} & \text{for } r = GeAz \\ {}^{\boldsymbol{E}}\boldsymbol{\omega}^{\boldsymbol{N}} \times {}^{\boldsymbol{E}}\boldsymbol{\omega}_{\boldsymbol{DrTr}}^{\boldsymbol{L}} & \text{for } r = DrTr \\ 0 & \text{otherwise} \end{cases} \\
&\frac{\mathrm{d}}{\mathrm{d}t}\{{}^{\boldsymbol{E}}\boldsymbol{\omega}_{\boldsymbol{t}}^{\boldsymbol{L}}\} = 0
\end{aligned}
\tag{A.72}
$$

The partial angular acceleration terms for blade element is given as

$$\begin{aligned}
\frac{\mathrm{d}}{\mathrm{d}t}\{{}^{\boldsymbol{E}}\boldsymbol{\omega}_{\boldsymbol{r}}^{\boldsymbol{M1}}\} &= \frac{d}{dt}\{{}^{\boldsymbol{E}}\boldsymbol{\omega}_{\boldsymbol{r}}^{\boldsymbol{L}}\} + \begin{cases} {}^{\boldsymbol{E}}\boldsymbol{\omega}^{\boldsymbol{L}} \times {}^{\boldsymbol{E}}\boldsymbol{\omega}_{\boldsymbol{B1F1}}^{\boldsymbol{M1}} & \text{for } r = B1F1 \\ {}^{\boldsymbol{E}}\boldsymbol{\omega}^{\boldsymbol{L}} \times {}^{\boldsymbol{E}}\boldsymbol{\omega}_{\boldsymbol{B1E1}}^{\boldsymbol{M1}} & \text{for } r = B1E1 \\ {}^{\boldsymbol{E}}\boldsymbol{\omega}^{\boldsymbol{L}} \times {}^{\boldsymbol{E}}\boldsymbol{\omega}_{\boldsymbol{B1F2}}^{\boldsymbol{M1}} & \text{for } r = B1F2 \\ 0 & \text{otherwise} \end{cases} \\
\frac{\mathrm{d}}{\mathrm{d}t}\{{}^{\boldsymbol{E}}\boldsymbol{\omega}_{\boldsymbol{t}}^{\boldsymbol{M1}}\} &= 0
\end{aligned} \tag{A.73}$$

Equations for $\frac{\mathrm{d}}{\mathrm{d}t}\{{}^{\boldsymbol{E}}\boldsymbol{\omega}_{\boldsymbol{r}}^{\boldsymbol{M2}}\}$ and $\frac{\mathrm{d}}{\mathrm{d}t}\{{}^{\boldsymbol{E}}\boldsymbol{\omega}_{\boldsymbol{r}}^{\boldsymbol{M3}}\}$ can be found similarly. Lastly, the partial angular acceleration terms for the generator can be given as

$$\begin{aligned}
\frac{\mathrm{d}}{\mathrm{d}t}\{{}^{\boldsymbol{E}}\boldsymbol{\omega}_{\boldsymbol{r}}^{\boldsymbol{G}}\} &= \frac{\mathrm{d}}{\mathrm{d}t}\{{}^{\boldsymbol{E}}\boldsymbol{\omega}_{\boldsymbol{r}}^{\boldsymbol{N}}\} + \begin{cases} {}^{\boldsymbol{E}}\boldsymbol{\omega}^{\boldsymbol{N}} \times {}^{\boldsymbol{E}}\boldsymbol{\omega}_{\boldsymbol{GeAz}}^{\boldsymbol{G}} & \text{for } r = GeAz \\ 0 & \text{otherwise} \end{cases} \\
\frac{\mathrm{d}}{\mathrm{d}t}\{{}^{\boldsymbol{E}}\boldsymbol{\omega}_{\boldsymbol{t}}^{\boldsymbol{G}}\} &= 0
\end{aligned} \tag{A.74}$$

A.2.7 Linear Accelerations

The linear acceleration of each point X_i in the system can be represented as

$$ {}^{\boldsymbol{E}}\boldsymbol{a}^{\boldsymbol{X_i}} = \sum_{r=1}^{22} {}^{\boldsymbol{E}}\boldsymbol{v}_{\boldsymbol{r}}^{\boldsymbol{X_i}}(q,t)\ddot{q}_r + \sum_{r=1}^{22} \frac{\mathrm{d}}{\mathrm{d}t}\{{}^{\boldsymbol{E}}\boldsymbol{v}_{\boldsymbol{r}}^{\boldsymbol{X_i}}(q,t)\}\dot{q}_r + \frac{\mathrm{d}}{\mathrm{d}t}\{{}^{\boldsymbol{E}}\boldsymbol{v}_{\boldsymbol{t}}^{\boldsymbol{X_i}}(q,t)\} \tag{A.75}$$

The terms $\frac{d}{dt}\{{}^{\boldsymbol{E}}\boldsymbol{v}_{\boldsymbol{r}}^{\boldsymbol{X_i}}\}$ are all vector functions of $(\dot{q}, q, t)$ and are the only terms needed to be estimated and all terms $\frac{\mathrm{d}}{\mathrm{d}t}\{{}^{\boldsymbol{E}}\boldsymbol{v}_{\boldsymbol{t}}^{\boldsymbol{X_i}}\}$ are zeros as will be shown. The partial linear acceleration terms for the platform centre of mass can be obtained as

$$\begin{aligned}
\frac{\mathrm{d}}{\mathrm{d}t}\{{}^{\boldsymbol{E}}\boldsymbol{v}_{\boldsymbol{r}}^{\boldsymbol{Y}}\} &= \begin{cases} {}^{\boldsymbol{E}}\boldsymbol{\omega}_{\boldsymbol{r}}^{\boldsymbol{X}} \times \left({}^{\boldsymbol{E}}\boldsymbol{\omega}_{\boldsymbol{r}}^{\boldsymbol{X}} \times \boldsymbol{r}^{\boldsymbol{ZY}}\right) & \text{for } r = 1 \text{ to } 3 \\ 0 & \text{otherwise} \end{cases} \\
\frac{\mathrm{d}}{\mathrm{d}t}\{{}^{\boldsymbol{E}}\boldsymbol{v}_{\boldsymbol{t}}^{\boldsymbol{Y}}\} &= 0
\end{aligned} \tag{A.76}$$

The partial linear acceleration terms for the tower element can be given as

$$\frac{\mathrm{d}}{\mathrm{d}t}\{{}^{\boldsymbol{E}}\boldsymbol{v}_{\boldsymbol{r}}^{\boldsymbol{T}}(h)\} = \begin{cases} -\left[S_{11}^{TFA}(h)\dot{q}_{TFA1} + S_{12}^{TFA}(h)\dot{q}_{TFA2}\right]\hat{\boldsymbol{a}}_{\boldsymbol{2}} & \text{for } r = TFA1 \\ -\left[S_{11}^{TSS}(h)\dot{q}_{TSS1} + S_{12}^{TSS}(h)\dot{q}_{TSS2}\right]\hat{\boldsymbol{a}}_{\boldsymbol{2}} & \text{for } r = TSS1 \\ -\left[S_{22}^{TFA}(h)\dot{q}_{TFA2} + S_{12}^{TFA}(h)\dot{q}_{TFA1}\right]\hat{\boldsymbol{a}}_{\boldsymbol{2}} & \text{for } r = TFA2 \\ -\left[S_{22}^{TSS}(h)\dot{q}_{TSS2} + S_{12}^{TSS}(h)\dot{q}_{TSS1}\right]\hat{\boldsymbol{a}}_{\boldsymbol{2}} & \text{for } r = TSS2 \\ 0 & \text{otherwise} \end{cases}$$

$$\frac{\mathrm{d}}{\mathrm{d}t}\{{}^{\boldsymbol{E}}\boldsymbol{v}_{\boldsymbol{t}}^{\boldsymbol{T}}(h)\} = 0 \tag{A.77}$$

The partial linear acceleration terms for the tower-top/base-plate can be given as

$$\frac{\mathrm{d}}{\mathrm{d}t}\{{}^{\boldsymbol{E}}\boldsymbol{v}_{\boldsymbol{r}}^{\boldsymbol{O}}\} = \begin{cases} -\Big[S_{11}^{TFA}(TwrHt)\dot{q}_{TFA1} & \\ +S_{12}^{TFA}(TwrHt)\dot{q}_{TFA2}\Big]\hat{\boldsymbol{a}}_{\boldsymbol{2}} & \text{for } r = TFA1 \\ -\Big[S_{11}^{TSS}(TwrHt)\dot{q}_{TSS1} & \\ +S_{12}^{TSS}(TwrHt)\dot{q}_{TSS2}\Big]\hat{\boldsymbol{a}}_{\boldsymbol{2}} & \text{for } r = TSS1 \\ -\Big[S_{22}^{TFA}(TwrHt)\dot{q}_{TFA2} & \\ +S_{12}^{TFA}(TwrHt)\dot{q}_{TFA1}\Big]\hat{\boldsymbol{a}}_{\boldsymbol{2}} & \text{for } r = TFA2 \\ -\Big[S_{22}^{TSS}(TwrHt)\dot{q}_{TSS2} & \\ +S_{12}^{TSS}(TwrHt)\dot{q}_{TSS1}\Big]\hat{\boldsymbol{a}}_{\boldsymbol{2}} & \text{for } r = TSS2 \\ 0 & \text{otherwise} \end{cases}$$

$$\frac{\mathrm{d}}{\mathrm{d}t}\{{}^{\boldsymbol{E}}\boldsymbol{v}_{\boldsymbol{t}}^{\boldsymbol{T}}\} = 0 \tag{A.78}$$

The partial linear acceleration terms for the nacelle center of mass given as

$$\frac{\mathrm{d}}{\mathrm{d}t}\{{}^{\boldsymbol{E}}\boldsymbol{v}_{\boldsymbol{r}}^{\boldsymbol{U}}\} = \frac{\mathrm{d}}{\mathrm{d}t}\{{}^{\boldsymbol{E}}\boldsymbol{v}_{\boldsymbol{r}}^{\boldsymbol{O}}\} + \begin{cases} \frac{\mathrm{d}}{\mathrm{d}t}\{{}^{\boldsymbol{E}}\boldsymbol{\omega}_{\boldsymbol{r}}^{\boldsymbol{N}}\} \times \boldsymbol{r}^{\boldsymbol{OU}} + {}^{\boldsymbol{E}}\boldsymbol{\omega}_{\boldsymbol{r}}^{\boldsymbol{N}} \times \left({}^{\boldsymbol{E}}\boldsymbol{\omega}^{\boldsymbol{N}} \times \boldsymbol{r}^{\boldsymbol{OU}}\right) & r = 1 \text{ to } 11 \\ 0 & \text{otherwise} \end{cases}$$

$$\frac{\mathrm{d}}{\mathrm{d}t}\{{}^{\boldsymbol{E}}\boldsymbol{v}_{\boldsymbol{t}}^{\boldsymbol{U}}\} = 0 \tag{A.79}$$

The partial linear acceleration terms for the apex of coning angle are given as

$$\begin{aligned}
&\frac{\mathrm{d}}{\mathrm{d}t}\{{}^{\boldsymbol{E}}\boldsymbol{v}_{\boldsymbol{r}}^{\boldsymbol{Q}}\} = \frac{\mathrm{d}}{\mathrm{d}t}\{{}^{\boldsymbol{E}}\boldsymbol{v}_{\boldsymbol{r}}^{\boldsymbol{O}}\} + \begin{cases} \frac{\mathrm{d}}{\mathrm{d}t}\{{}^{\boldsymbol{E}}\boldsymbol{\omega}_{\boldsymbol{r}}^{\boldsymbol{L}}\} \times \boldsymbol{r}^{\boldsymbol{OQ}} + {}^{\boldsymbol{E}}\boldsymbol{\omega}_{\boldsymbol{r}}^{\boldsymbol{L}} \times \left({}^{\boldsymbol{E}}\boldsymbol{\omega}^{\boldsymbol{L}} \times \boldsymbol{r}^{\boldsymbol{OQ}}\right) & r = 1 \text{ to } 13 \\ 0 & \text{otherwise} \end{cases} \\
&\frac{\mathrm{d}}{\mathrm{d}t}\{{}^{\boldsymbol{E}}\boldsymbol{v}_{\boldsymbol{t}}^{\boldsymbol{Q}}\} = 0
\end{aligned} \tag{A.80}$$

The partial linear acceleration terms for the hub center of mass are given as

$$\begin{aligned}
&\frac{\mathrm{d}}{\mathrm{d}t}\{{}^{\boldsymbol{E}}\boldsymbol{v}_{\boldsymbol{r}}^{\boldsymbol{C}}\} = \frac{\mathrm{d}}{\mathrm{d}t}\{{}^{\boldsymbol{E}}\boldsymbol{v}_{\boldsymbol{r}}^{\boldsymbol{Q}}\} + \begin{cases} \frac{\mathrm{d}}{\mathrm{d}t}\{{}^{\boldsymbol{E}}\boldsymbol{\omega}_{\boldsymbol{r}}^{\boldsymbol{L}}\} \times \boldsymbol{r}^{\boldsymbol{QC}} + {}^{\boldsymbol{E}}\boldsymbol{\omega}_{\boldsymbol{r}}^{\boldsymbol{L}} \times \left({}^{\boldsymbol{E}}\boldsymbol{\omega}^{\boldsymbol{L}} \times \boldsymbol{r}^{\boldsymbol{QC}}\right) & r = 1 \text{ to } 13 \\ 0 & \text{otherwise} \end{cases} \\
&\frac{\mathrm{d}}{\mathrm{d}t}\{{}^{\boldsymbol{E}}\boldsymbol{v}_{\boldsymbol{t}}^{\boldsymbol{C}}\} = 0
\end{aligned} \tag{A.81}$$

The partial linear acceleration terms for blade 1 element are given as

$$\begin{aligned}
&\frac{\mathrm{d}}{\mathrm{d}t}\{{}^{\boldsymbol{E}}\boldsymbol{v}_{\boldsymbol{r}}^{\boldsymbol{S1}}(r)\} = \frac{\mathrm{d}}{\mathrm{d}t}\{{}^{\boldsymbol{E}}\boldsymbol{v}_{\boldsymbol{r}}^{\boldsymbol{Q}}\} \\
&\qquad + \begin{cases} \frac{\mathrm{d}}{\mathrm{d}t}\{{}^{\boldsymbol{E}}\boldsymbol{\omega}_{\boldsymbol{r}}^{\boldsymbol{L}}\} \times \boldsymbol{r}^{\boldsymbol{QS1}} + {}^{\boldsymbol{E}}\boldsymbol{\omega}_{\boldsymbol{r}}^{\boldsymbol{L}} \times \left({}^{\boldsymbol{L}}\boldsymbol{v}^{\boldsymbol{S1}}(r) + {}^{\boldsymbol{E}}\boldsymbol{\omega}^{\boldsymbol{L}} \times \boldsymbol{r}^{\boldsymbol{QS1}}\right) & r = 1 \text{ to } 13 \\ -\left[S_{11}^{B1}(r)\dot{q}_{B1F1} + S_{12}^{B1}(r)\dot{q}_{B1F1} + S_{13}^{B1}(r)\dot{q}_{B1E1}\right]\hat{\boldsymbol{j}}_{\boldsymbol{3}}^{\boldsymbol{B1}} & \\ +{}^{\boldsymbol{E}}\boldsymbol{\omega}^{\boldsymbol{L}} \times {}^{\boldsymbol{E}}\boldsymbol{v}_{\boldsymbol{B1F1}}^{\boldsymbol{S1}} & r = B1F1 \\ -\left[S_{33}^{B1}(r)\dot{q}_{B1E1} + S_{13}^{B1}(r)\dot{q}_{B1F1} + S_{23}^{B1}(r)\dot{q}_{B1F2}\right]\hat{\boldsymbol{j}}_{\boldsymbol{3}}^{\boldsymbol{B1}} & \\ +{}^{\boldsymbol{E}}\boldsymbol{\omega}^{\boldsymbol{L}} \times {}^{\boldsymbol{E}}\boldsymbol{v}_{\boldsymbol{B1E1}}^{\boldsymbol{S1}} & r = B1E1 \\ -\left[S_{22}^{B1}(r)\dot{q}_{B1F2} + S_{12}^{B1}(r)\dot{q}_{B1F1} + S_{23}^{B1}(r)\dot{q}_{B1E1}\right]\hat{\boldsymbol{j}}_{\boldsymbol{3}}^{\boldsymbol{B1}} & \\ +{}^{\boldsymbol{E}}\boldsymbol{\omega}^{\boldsymbol{L}} \times {}^{\boldsymbol{E}}\boldsymbol{v}_{\boldsymbol{B1F2}}^{\boldsymbol{S1}} & r = B1F2 \\ 0 & \text{otherwise} \end{cases} \\
&\frac{\mathrm{d}}{\mathrm{d}t}\{{}^{\boldsymbol{E}}\boldsymbol{v}_{\boldsymbol{t}}^{\boldsymbol{S1}}(r)\} = 0
\end{aligned} \tag{A.82}$$

Equations for $\frac{\mathrm{d}}{\mathrm{d}t}\{{}^{\boldsymbol{E}}\boldsymbol{v}_{\boldsymbol{r}}^{\boldsymbol{S2}}(r)\}$ and $\frac{\mathrm{d}}{\mathrm{d}t}\{{}^{\boldsymbol{E}}\boldsymbol{v}_{\boldsymbol{r}}^{\boldsymbol{S3}}(r)\}$ can be obtained similarly.

A.3 Kinetics

The kinetic of the FOWT and the resulting equations of motion of the wind turbine system is provided in this section.

A.3.1 Platform

The mass of the platform brings about generalized inertia forces. The generalized active forces associated with the platform arise from the gravitational forces, hydrostatic forces, mooring lines and hydrodynamic forces including the effect of added mass. The generalized inertia forces associated with the platform is given as

$$F_r^*\Big|_X = {}^{\boldsymbol{E}}\boldsymbol{v}_{\boldsymbol{r}}^{\boldsymbol{Y}} \cdot (-m^X {}^{\boldsymbol{E}}\boldsymbol{a}^{\boldsymbol{Y}}) + {}^{\boldsymbol{E}}\boldsymbol{\omega}_{\boldsymbol{r}}^{\boldsymbol{X}} \cdot (-{}^{\boldsymbol{E}}\dot{\boldsymbol{H}}^{\boldsymbol{X}}) \tag{A.83}$$

or

$$F_r^*\Big|_X = {}^{\boldsymbol{E}}\boldsymbol{v}_{\boldsymbol{r}}^{\boldsymbol{Y}} \cdot (-m^X {}^{\boldsymbol{E}}\boldsymbol{a}^{\boldsymbol{Y}}) + {}^{\boldsymbol{E}}\boldsymbol{\omega}_{\boldsymbol{r}}^{\boldsymbol{X}} \cdot (-\bar{\bar{\boldsymbol{I}}}^{\boldsymbol{X}} \cdot {}^{\boldsymbol{E}}\boldsymbol{\alpha}^{\boldsymbol{X}} - {}^{\boldsymbol{E}}\boldsymbol{\omega}^{\boldsymbol{X}} \times \bar{\bar{\boldsymbol{I}}}^{\boldsymbol{X}} \cdot {}^{\boldsymbol{E}}\boldsymbol{\omega}^{\boldsymbol{X}}) \tag{A.84}$$

where

$$\bar{\bar{\boldsymbol{I}}}^{\boldsymbol{X}} = PtfrmRIner\hat{\boldsymbol{a}}_{\boldsymbol{1}}\hat{\boldsymbol{a}}_{\boldsymbol{1}} + PtfrmYIner\hat{\boldsymbol{a}}_{\boldsymbol{2}}\hat{\boldsymbol{a}}_{\boldsymbol{2}} + PtfrmPIner\hat{\boldsymbol{a}}_{\boldsymbol{3}}\hat{\boldsymbol{a}}_{\boldsymbol{3}} \tag{A.85}$$

Therefore,

$$\begin{aligned} F_r^*\Big|_X = {}& {}^{\boldsymbol{E}}\boldsymbol{v}_{\boldsymbol{r}}^{\boldsymbol{Y}} \cdot \Big[- m^X \Big\{ \Big(\sum_{i=1}^{6} {}^{\boldsymbol{E}}\boldsymbol{v}_i^{\boldsymbol{Y}} \ddot{q}_i \Big) + \Big(\sum_{i=4}^{6} \frac{\mathrm{d}}{\mathrm{d}t}({}^{\boldsymbol{E}}\boldsymbol{v}_i^{\boldsymbol{Y}}) \dot{q}_i \Big) \Big\} \Big] \\ & + {}^{\boldsymbol{E}}\boldsymbol{\omega}_{\boldsymbol{r}}^{\boldsymbol{X}} \cdot \Big[- \bar{\bar{\boldsymbol{I}}}^{\boldsymbol{X}} \cdot \Big(\sum_{i=4}^{6} {}^{\boldsymbol{E}}\boldsymbol{\omega}_{\boldsymbol{i}}^{\boldsymbol{X}} \ddot{q}_i \Big) - {}^{\boldsymbol{E}}\boldsymbol{\omega}^{\boldsymbol{X}} \times \bar{\bar{\boldsymbol{I}}}^{\boldsymbol{X}} \cdot {}^{\boldsymbol{E}}\boldsymbol{\omega}^{\boldsymbol{X}} \Big] \end{aligned} \tag{A.86}$$

The elements of the system matrices can be obtained as

$$\begin{aligned} [\mathbf{M}(\mathbf{q},t)]\Big|_X(k,l) &= m^X {}^{\boldsymbol{E}}\boldsymbol{v}_{\boldsymbol{k}}^{\boldsymbol{Y}} \cdot {}^{\boldsymbol{E}}\boldsymbol{v}_{\boldsymbol{l}}^{\boldsymbol{Y}} + {}^{\boldsymbol{E}}\boldsymbol{\omega}_{\boldsymbol{k}}^{\boldsymbol{X}} \bar{\bar{\boldsymbol{I}}}^{\boldsymbol{X}} {}^{\boldsymbol{E}}\boldsymbol{\omega}_{\boldsymbol{l}}^{\boldsymbol{X}} && \text{for } k,l = 1 \text{ to } 6 \\ &= 0 && \text{otherwise} \\ [\mathbf{f}(\dot{\mathbf{q}},\mathbf{q},t)]\Big|_X(k) &= -m^X {}^{\boldsymbol{E}}\boldsymbol{v}_{\boldsymbol{k}}^{\boldsymbol{Y}} \cdot \Big[\sum_{i=4}^{6} \frac{\mathrm{d}}{\mathrm{d}t}({}^{\boldsymbol{E}}\boldsymbol{v}_i^{\boldsymbol{Y}}) \dot{q}_i \Big] \\ &\quad - {}^{\boldsymbol{E}}\boldsymbol{\omega}_{\boldsymbol{k}}^{\boldsymbol{X}} \cdot ({}^{\boldsymbol{E}}\boldsymbol{\omega}^{\boldsymbol{X}} \times \bar{\bar{\boldsymbol{I}}}^{\boldsymbol{X}} \cdot {}^{\boldsymbol{E}}\boldsymbol{\omega}^{\boldsymbol{X}}) && \text{for } k = 1 \text{ to } 6 \\ &= 0 && \text{otherwise} \end{aligned} \tag{A.87}$$

where, the indices k, l are used to denote the row and column respectively of the matrix. Hydrodynamic and hydrostatic forces contribute to the generalized active forces. These forces can be written as

$$F_r\Big|_{HydroX} = {}^{E}\boldsymbol{v}_{\boldsymbol{k}}^{\boldsymbol{Y}} \cdot \boldsymbol{F}_{\boldsymbol{HydroX}}^{\boldsymbol{Y}} + {}^{E}\boldsymbol{\omega}_{\boldsymbol{r}}^{\boldsymbol{X}} \cdot \boldsymbol{M}_{\boldsymbol{HydroX}}^{\boldsymbol{Y}} \qquad \text{for 1 to 22} \tag{A.88}$$

where $\boldsymbol{F}_{\boldsymbol{HydroX}}^{\boldsymbol{Y}}$ and $\boldsymbol{M}_{\boldsymbol{HydroX}}^{\boldsymbol{Y}}$ are the forces and moments acting at the platform center of mass. These forces can be transformed to forces at the base of the wind turbine as

$$\boldsymbol{F}_{\boldsymbol{HydroX}}^{\boldsymbol{Z}} = \boldsymbol{F}_{\boldsymbol{HydroX}}^{\boldsymbol{Y}} \tag{A.89}$$

and

$$\boldsymbol{M}_{\boldsymbol{HydroX}}^{\boldsymbol{Y}} = \boldsymbol{M}_{\boldsymbol{HydroX}}^{\boldsymbol{Z}} + \boldsymbol{r}^{\boldsymbol{YZ}} \times \boldsymbol{F}_{\boldsymbol{HydroX}}^{\boldsymbol{Z}} = \boldsymbol{M}_{\boldsymbol{HydroX}}^{\boldsymbol{Z}} - \boldsymbol{r}^{\boldsymbol{ZY}} \times \boldsymbol{F}_{\boldsymbol{HydroX}}^{\boldsymbol{Z}} \tag{A.90}$$

But since, ${}^{E}\boldsymbol{v}_{\boldsymbol{r}}^{\boldsymbol{Y}} = {}^{E}\boldsymbol{v}_{\boldsymbol{r}}^{\boldsymbol{Z}} + {}^{E}\boldsymbol{\omega}_{\boldsymbol{r}}^{\boldsymbol{X}} \times \boldsymbol{r}^{\boldsymbol{ZY}}$, the generalized active forces can be written as

$$F_r\Big|_{HydroX} = {}^{E}\boldsymbol{v}_{\boldsymbol{r}}^{\boldsymbol{Z}} + {}^{E}\boldsymbol{\omega}_{\boldsymbol{r}}^{\boldsymbol{X}} \times \boldsymbol{r}^{\boldsymbol{ZY}} \cdot \boldsymbol{F}_{\boldsymbol{HydroX}}^{\boldsymbol{Z}} + {}^{E}\boldsymbol{\omega}_{\boldsymbol{r}}^{\boldsymbol{X}} \cdot \boldsymbol{M}_{\boldsymbol{HydroX}}^{\boldsymbol{Z}} - \boldsymbol{r}^{\boldsymbol{ZY}} \times \boldsymbol{F}_{\boldsymbol{HydroX}}^{\boldsymbol{Z}} \quad \text{for 1 to 22} \tag{A.91}$$

This simplifies to

$$F_r\Big|_{HydroX} = {}^{E}\boldsymbol{v}_{\boldsymbol{k}}^{\boldsymbol{Z}} \cdot \boldsymbol{F}_{\boldsymbol{HydroX}}^{\boldsymbol{Z}} + {}^{E}\boldsymbol{\omega}_{\boldsymbol{r}}^{\boldsymbol{X}} \cdot \boldsymbol{M}_{\boldsymbol{HydroX}}^{\boldsymbol{Z}} \qquad \text{for 1 to 22} \tag{A.92}$$

Other than the motion of the liquid the hydrodynamic forces and moments also depend on the motion of the platform. The forces and moments can be written as

$$\boldsymbol{F}_{\boldsymbol{HydroX}}^{\boldsymbol{Z}} = \left(\sum_{i=1}^{6} \boldsymbol{F}_{\boldsymbol{HydroX_j}}^{\boldsymbol{Z}} \ddot{q}_j\right) + \boldsymbol{F}_{\boldsymbol{HydroX_t}}^{\boldsymbol{Z}} \tag{A.93}$$

and

$$\boldsymbol{M}_{\boldsymbol{HydroX}}^{\boldsymbol{Z}} = \left(\sum_{i=1}^{6} \boldsymbol{M}_{\boldsymbol{HydroX_j}}^{\boldsymbol{Z}} \ddot{q}_j\right) + \boldsymbol{M}_{\boldsymbol{HydroX_t}}^{\boldsymbol{Z}} \tag{A.94}$$

Where, $\boldsymbol{F^{Z}_{HydroX_t}}$ and $\boldsymbol{M^{Z}_{HydroX_t}}$ are the hydrodynamic forces and moments that do not depend of the acceleration of the platform. Thus,

$$\begin{aligned} F_r\Big|_{HydroX} &= {}^{\boldsymbol{E}}\boldsymbol{v_k^Z} \cdot \left[\left(\sum_{i=1}^{6} \boldsymbol{F^{Z}_{HydroX_j}}\ddot{q}_j\right) + \boldsymbol{F^{Z}_{HydroX_t}}\right] \\ &+ {}^{\boldsymbol{E}}\boldsymbol{\omega_r^X} \cdot \left[\left(\sum_{i=1}^{6} \boldsymbol{M^{Z}_{HydroX_j}}\ddot{q}_j\right) + \boldsymbol{M^{Z}_{HydroX_t}}\right] \qquad \text{for } r = 1 \text{ to } 22 \end{aligned} \tag{A.95}$$

Finally, the system matrices can be obtained as

$$\begin{aligned} [\mathbf{M}(\mathbf{q},t)]\Big|_{HydroX}(k,l) &= -{}^{\boldsymbol{E}}\boldsymbol{v_k^Z} \cdot \boldsymbol{F^{Z}_{HydroX_l}} - {}^{\boldsymbol{E}}\boldsymbol{\omega_k^X} \cdot \boldsymbol{M^{Z}_{HydroX_l}} & k,l = 1 \text{ to } 6 \\ &= 0 & \text{otherwise} \\ f(\dot{q},q,t)\Big|_{HydroX}(k) &= {}^{\boldsymbol{E}}\boldsymbol{v_k^Z} \cdot \boldsymbol{F^{Z}_{HydroX_t}} + {}^{\boldsymbol{E}}\boldsymbol{\omega_k^X} \cdot \boldsymbol{M^{Z}_{HydroX_t}} & k = 1 \text{ to } 6 \\ &= 0 & \text{otherwise} \end{aligned} \tag{A.96}$$

Gravitational force contribute to the generalized active forces on the platform. These forces can be written as

$$F_r\Big|_{GravX} = {}^{\boldsymbol{E}}\boldsymbol{v_k^Y} \cdot (-m^X g \boldsymbol{\hat{z}_2}) \tag{A.97}$$

where, g is acceleration due to gravity. The system matrices can be obtained as

$$\begin{aligned} [\mathbf{M}(\mathbf{q},t)]\Big|_{GravX}(k,l) &= 0 & \text{for all} \\ f(\dot{q},q,t)\Big|_{GravX}(k) &= -m^X g^{\boldsymbol{E}}\boldsymbol{v_k^Y} \cdot \boldsymbol{\hat{z}_2} & k = 1 \text{ to } 6 \\ &= 0 & \text{otherwise} \end{aligned} \tag{A.98}$$

A.3.2 Tower

The distributed properties of the tower bring about generalized inertia forces and generalized active forces associated with tower mass, elasticity, damping and aerodynamics. The generalized inertia forces associated with the tower mass can be obtained as

$$F_r^*\Big|_T = -\int_0^{TwrHt} \mu^T(h)^{\boldsymbol{E}}\boldsymbol{v_r^T}(h) \cdot {}^{\boldsymbol{E}}\boldsymbol{a^T}(h)\mathrm{d}h - YBR.{}^{\boldsymbol{E}}\boldsymbol{v_r^O} \cdot {}^{\boldsymbol{E}}\boldsymbol{a^O} \quad \text{for } r = 1 \text{ to } 4 \tag{A.99}$$

where, YBM is the yaw bearing mass. The above equation can be rewritten as

$$F_r^*\Big|_T = -\int_0^{TwrHt} \mu^T(h)^{\boldsymbol{E}}\boldsymbol{v}_{\boldsymbol{r}}^{\boldsymbol{T}}(h)\cdot\left[\Big(\sum_{i=1}^{4}{}^{\boldsymbol{E}}\boldsymbol{v}_{\boldsymbol{i}}^{\boldsymbol{T}}(h)\ddot{q}_i\Big)+\Big(\sum_{i=1}^{4}\frac{d}{dt}\{{}^{\boldsymbol{E}}\boldsymbol{v}_{\boldsymbol{i}}^{\boldsymbol{T}}(h)\}\dot{q}_i\right]\mathrm{d}h$$
$$-\,YBM.{}^{\boldsymbol{E}}\boldsymbol{v}_{\boldsymbol{r}}^{\boldsymbol{O}}\cdot\left[\Big(\sum_{i=1}^{4}{}^{\boldsymbol{E}}\boldsymbol{v}_{\boldsymbol{i}}^{\boldsymbol{O}}\ddot{q}_i\Big)+\Big(\sum_{i=1}^{4}\frac{d}{dt}\{{}^{\boldsymbol{E}}\boldsymbol{v}_{\boldsymbol{i}}^{\boldsymbol{O}}\}\dot{q}_i\right] \quad \text{for } r = 1 \text{ to } 10 \tag{A.100}$$

Thus, the elements of the system matrices can be found as

$$\begin{aligned}
[\mathbf{M}(\mathbf{q},t)]\Big|_T(k,l) &= \int_0^{TwrHt}\mu^T(h)^{\boldsymbol{E}}\boldsymbol{v}_{\boldsymbol{k}}^{\boldsymbol{T}}(h)\cdot{}^{\boldsymbol{E}}\boldsymbol{v}_{\boldsymbol{l}}^{\boldsymbol{T}}(h)\mathrm{d}h \\
&\quad + YBM.{}^{\boldsymbol{E}}\boldsymbol{v}_{\boldsymbol{k}}^{\boldsymbol{O}}\cdot{}^{\boldsymbol{E}}\boldsymbol{v}_{\boldsymbol{l}}^{\boldsymbol{O}} && \text{for } k,l = 1 \text{ to } 10 \\
&= 0 && \text{otherwise} \\
\{-\mathbf{f}(\dot{\mathbf{q}},\mathbf{q},t)\}\Big|_T(k) &= -\int_0^{TwrHt}\mu^T(h)^{\boldsymbol{E}}\boldsymbol{v}_{\boldsymbol{k}}^{\boldsymbol{T}}(h)\cdot\Big(\sum_{i=1}^{4}\frac{d}{dt}\{{}^{\boldsymbol{E}}\boldsymbol{v}_{\boldsymbol{i}}^{\boldsymbol{T}}(h)\}\dot{q}_i\Big)\mathrm{d}h \\
&\quad - YBM.{}^{\boldsymbol{E}}\boldsymbol{v}_{\boldsymbol{k}}^{\boldsymbol{O}}\cdot\Big(\sum_{i=1}^{4}\frac{d}{dt}\{{}^{\boldsymbol{E}}\boldsymbol{v}_{\boldsymbol{i}}^{\boldsymbol{O}}\}\dot{q}_i\Big) && \text{for } k = 1 \text{ to } 10 \\
&= 0 && \text{otherwise}
\end{aligned} \tag{A.101}$$

Generalized active forces arise from the elasticity and damping of the flexible members. The generalized elastic forces can be obtained from the potential energy stored in the member as

$$F_r\Big|_{ElasticT} = \frac{\partial V^T}{\partial q_r} \quad \text{for } r = 1 \text{ to } 10 \tag{A.102}$$

$$\{-f(\dot{q},q,t)\}\Big|_T(k) = \begin{cases} -k_{11}^{TFA}q_{TFA1} - k_{12}^{TFA}q_{TFA2} & \text{for } k = 7 \\ -k_{11}^{TSS}q_{TSS1} - k_{12}^{TSS}q_{TSS2} & \text{for } k = 8 \\ -k_{21}^{TFA}q_{TFA1} - k_{22}^{TFA}q_{TFA2} & \text{for } k = 9 \\ -k_{21}^{TSS}q_{TSS1} - k_{22}^{TFA}q_{TSS2} & \text{for } k = 10 \\ 0 & \text{otherwise} \end{cases} \tag{A.103}$$

where, k_{ij}^{TFA} and k_{ij}^{TSS} are the generalized stiffness of the tower in the fore-aft and side-to-side directions respectively when gravitational de-stiffening effects are not included

$$
\begin{aligned}
k_{ij}^{TFA} &= \int_0^{TwrHt} EI^{TFA}(h)\frac{\mathrm{d}^2\phi_i^{TFA}}{\mathrm{d}h^2}\frac{\mathrm{d}^2\phi_j^{TFA}}{\mathrm{d}h^2}\mathrm{d}h \quad \text{for } i,j=1,2 \\
k_{ij}^{TSS} &= \int_0^{TwrHt} EI^{TSS}(h)\frac{\mathrm{d}^2\phi_i^{TSS}}{\mathrm{d}h^2}\frac{\mathrm{d}^2\phi_j^{TSS}}{\mathrm{d}h^2}\mathrm{d}h \quad \text{for } i,j=1,2
\end{aligned}
\tag{A.104}
$$

Using Rayleigh damping technique where the damping is assumed to be proportional to the stiffness the generalized active forces arising from the damping in the member can be obtained as

$$
\{-f(\dot{q},q,t)\}\Big|_T(k) = \begin{cases}
-\frac{\zeta_1^{TFA}k_{11}^{TFA}}{\pi f_1^{TFA}}\dot{q}_{TFA1} - \frac{\zeta_2^{TFA}k_{12}^{TFA}}{\pi f_2^{TFA}}\dot{q}_{TFA2} & \text{for } k=7 \\
-\frac{\zeta_1^{TSS}k_{11}^{TSS}}{\pi f_1^{TSS}}\dot{q}_{TSS1} - \frac{\zeta_2^{TSS}k_{12}^{TSS}}{\pi f_2^{TSS}}\dot{q}_{TSS2} & \text{for } k=8 \\
-\frac{\zeta_1^{TFA}k_{21}^{TFA}}{\pi f_1^{TFA}}\dot{q}_{TFA1} - \frac{\zeta_2^{TFA}k_{22}^{TFA}}{\pi f_2^{TFA}}\dot{q}_{TFA2} & \text{for } k=9 \\
-\frac{\zeta_1^{TSS}k_{21}^{TFA}}{\pi f_1^{TSS}}\dot{q}_{TSS1} - \frac{\zeta_2^{TFA}k_{22}^{TSS}}{\pi f_2^{TSS}}\dot{q}_{TSS2} & \text{for } k=10 \\
0 & \text{otherwise}
\end{cases}
\tag{A.105}
$$

where ζ_i^{TFA} and ζ_i^{TSS} represents the structural damping ratio of the tower for the i^{th} mode in the fore-aft and side-to-side direction respectively. And, f_i^{TFA} and f_i^{TSS} represent the natural frequency of the tower for the i^{th} mode of the tower in the fore-aft and side-to-side directions respectively without the tower-top mass or gravitational de-stiffening effects. These terms can be obtained as

$$
\begin{aligned}
f_i^{TFA} &= \frac{1}{2\pi}\sqrt{\frac{k_{ii}^{TFA}}{m_{ii}^{TFA}}} \\
f_i^{TSS} &= \frac{1}{2\pi}\sqrt{\frac{k_{ii}^{TSS}}{m_{ii}^{TSS}}}
\end{aligned}
\tag{A.106}
$$

where, m_{ii}^{TFA} and m_{ii}^{TSS} represents the generalized mass of the tower for i^{th} mode in fore-aft and side-to-side directions respectively without tower-top mass effects as follows

$$
\begin{aligned}
m_{ii}^{TFA} &= \int_0^{TwrHt} \mu^T(h)\phi_i^{TFA}(h)\phi_j^{TFA}(h)\mathrm{d}h \\
m_{ii}^{TSS} &= \int_0^{TwrHt} \mu^T(h)\phi_i^{TSS}(h)\phi_j^{TSS}(h)\mathrm{d}h
\end{aligned}
\tag{A.107}
$$

Generalized active force arising from gravity acting on the tower is given as

$$F_r\Big|_{GravT} = \int_0^{TwrHt} {}^{\boldsymbol{E}}\boldsymbol{v}_{\boldsymbol{r}}^{\boldsymbol{T}}(h) \cdot \{-\mu_T(h) g \hat{\boldsymbol{z}}_{\boldsymbol{2}}\}\, dh - YBM.g.{}^{\boldsymbol{E}}\boldsymbol{v}_{\boldsymbol{r}}^{\boldsymbol{O}} \cdot \hat{\boldsymbol{z}}_{\boldsymbol{2}} \quad \text{for } r = 1 \text{ to } 10 \tag{A.108}$$

Thus,

$$\begin{aligned}
[\mathbf{M}(\mathbf{q},t)]\Big|_{GravT}(k,l) &= 0 && \forall\ k,l \\
\{-\mathbf{f}(\dot{\mathbf{q}},\mathbf{q},t)\}\Big|_{GravT}(k) &= -\int_0^{TwrHt} {}^{\boldsymbol{E}}\boldsymbol{v}_{\boldsymbol{k}}^{\boldsymbol{T}}(h) \cdot \{\mu_T(h) g \hat{\boldsymbol{z}}_{\boldsymbol{2}}\}\, dh \\
&\quad - YBM.g.{}^{\boldsymbol{E}}\boldsymbol{v}_{\boldsymbol{k}}^{\boldsymbol{O}} \cdot \hat{\boldsymbol{z}}_{\boldsymbol{2}} && \text{for } k = 1 \text{ to } 10 \\
&= 0 && \text{otherwise}
\end{aligned} \tag{A.109}$$

Generalized active forces due to aerodynamic loads on the tower can be given as

$$F_r\Big|_{AeroT} = \int_0^{TwrHt} \left[{}^{\boldsymbol{E}}\boldsymbol{v}_{\boldsymbol{r}}^{\boldsymbol{T}}(h) \cdot \boldsymbol{F}_{\boldsymbol{AeroT}}^{\boldsymbol{T}}(h) + {}^{\boldsymbol{E}}\boldsymbol{\omega}_{\boldsymbol{r}}^{\boldsymbol{F}}(h) \cdot \boldsymbol{M}_{\boldsymbol{AeroT}}^{\boldsymbol{F}}(h)\right] \mathrm{d}h \quad \text{for } r = 1 \text{ to } 10 \tag{A.110}$$

where, $\boldsymbol{F}_{\boldsymbol{AeroT}}^{\boldsymbol{T}}(h)$ and $\boldsymbol{M}_{\boldsymbol{AeroT}}^{\boldsymbol{F}}(h)$ are aerodynamic forces and moments applied on the tower expressed per unit length. Thus,

$$\begin{aligned}
[\mathbf{M}(\mathbf{q},t)]\Big|_{AeroT}(k,l) &= 0 && \forall\ k,l \\
\{-\mathbf{f}(\dot{\mathbf{q}},\mathbf{q},t)\}\Big|_{GravT}(k) &= \int_0^{TwrHt} \left[{}^{\boldsymbol{E}}\boldsymbol{v}_{\boldsymbol{r}}^{\boldsymbol{T}}(h) \cdot \boldsymbol{F}_{\boldsymbol{AeroT}}^{\boldsymbol{T}}(h)\right. \\
&\quad \left. + {}^{\boldsymbol{E}}\boldsymbol{\omega}_{\boldsymbol{r}}^{\boldsymbol{F}}(h) \cdot \boldsymbol{M}_{\boldsymbol{AeroT}}^{\boldsymbol{F}}(h)\right] \mathrm{d}h && \text{for } k = 1 \text{ to } 10 \\
&= 0 && \text{otherwise}
\end{aligned} \tag{A.111}$$

A.3.3 Yaw bearing

The yaw spring and damper bring about generalized active forces. The generalized active force from the yaw spring

$$F_r\Big|_{YawSpring} = \begin{cases} -YawSpring.(q_{yaw} - q_{yaw0}) & \text{for } r = Yaw \\ 0 & \text{otherwise} \end{cases} \tag{A.112}$$

where, q_{yaw0} is the initial neutral position of the yaw bearing. And the generalized active force from the yaw damper

$$F_r\Big|_{YawDamp} = \begin{cases} -YawDamp.\dot{q}_{yaw} & \text{for } r = Yaw \\ 0 & \text{otherwise} \end{cases} \tag{A.113}$$

Thus, the elements of the system matrices are

$$\begin{aligned} [\mathbf{M}(\mathbf{q},t)]\Big|_{YawBear}(k,l) &= 0 && \forall\ k,l \\ \{-\mathbf{f}(\dot{\mathbf{q}},\mathbf{q},t)\}\Big|_{YawBear}(k) &= -\,YawSpring.(q_{yaw}-q_{yaw0}) - YawDamp.\dot{q}_{yaw} && \text{for } k = 11 \\ &= 0 && \text{otherwise} \end{aligned} \tag{A.114}$$

A.3.4 Nacelle

The rigid lump mass of the nacelle brings about generalized inertia forces and generalized active forces associated with nacelle weight. Generalized inertia forces can be given as

$$F_r^*\Big|_N = {}^{\boldsymbol{E}}\boldsymbol{v}_{\boldsymbol{r}}^{\boldsymbol{U}} \cdot \Big(-m^N\,{}^{\boldsymbol{E}}\boldsymbol{a}^{\boldsymbol{U}}\Big) - {}^{\boldsymbol{E}}\boldsymbol{\omega}_{\boldsymbol{r}}^{\boldsymbol{N}} \cdot {}^{\boldsymbol{E}}\dot{\boldsymbol{H}}^{\boldsymbol{N}} \quad \text{for } r = 1 \text{ to } 11 \tag{A.115}$$

Or,

$$F_r^*\Big|_N = {}^{\boldsymbol{E}}\boldsymbol{v}_{\boldsymbol{r}}^{\boldsymbol{U}} \cdot \Big(-m^N\,{}^{\boldsymbol{E}}\boldsymbol{a}^{\boldsymbol{U}}\Big) - {}^{\boldsymbol{E}}\boldsymbol{\omega}_{\boldsymbol{r}}^{\boldsymbol{N}} \cdot \Big(\bar{\bar{\boldsymbol{I}}}^{\boldsymbol{N}} \cdot {}^{\boldsymbol{E}}\boldsymbol{\alpha}^{\boldsymbol{N}} + {}^{\boldsymbol{E}}\boldsymbol{\omega}^{\boldsymbol{N}} \times \bar{\bar{\boldsymbol{I}}}^{\boldsymbol{N}} \cdot {}^{\boldsymbol{E}}\boldsymbol{\omega}^{\boldsymbol{N}}\Big) \quad \text{for } r = 1 \text{ to } 11 \tag{A.116}$$

where m^N is the nacelle mass and the inertia dyadic can be obtained as

$$\bar{\bar{\boldsymbol{I}}}^{\boldsymbol{N}} = \Big[NacYIner - m^N\Big(NacCMxn^2 + NacCMyn^2\Big)\Big]\,\hat{\boldsymbol{d}}_{\boldsymbol{2}}\hat{\boldsymbol{d}}_{\boldsymbol{2}} \tag{A.117}$$

using parallel axis theorem. The generalized inertia force can then be written as

$$
\begin{aligned}
F_r^*\Big|_N = {}^{\boldsymbol{E}}\boldsymbol{v}_{\boldsymbol{r}}^{\boldsymbol{U}} \cdot \Bigg[-m^N \Bigg\{ \Bigg(\sum_{i=1}^{5} {}^{\boldsymbol{E}}\boldsymbol{v}_{\boldsymbol{i}}^{\boldsymbol{U}} \dot{q}_i \Bigg) + \Bigg(\sum_{i=1}^{5} \frac{d}{dt}({}^{\boldsymbol{E}}\boldsymbol{v}_{\boldsymbol{i}}^{\boldsymbol{U}}) \dot{q}_i \Bigg) \Bigg\} \Bigg] \\
+ {}^{\boldsymbol{E}}\boldsymbol{\omega}_{\boldsymbol{r}}^{\boldsymbol{N}} \Bigg[- \bar{\bar{\boldsymbol{I}}}^{\boldsymbol{N}} \cdot \Bigg\{ \Bigg(\sum_{i=1}^{5} {}^{\boldsymbol{E}}\boldsymbol{\omega}_{\boldsymbol{i}}^{\boldsymbol{N}} \ddot{q}_i \Bigg) + \Bigg(\sum_{i=1}^{5} \frac{d}{dt}({}^{\boldsymbol{E}}\boldsymbol{\omega}_{\boldsymbol{i}}^{\boldsymbol{N}}) \dot{q}_i \Bigg) \Bigg\} \\
- {}^{\boldsymbol{E}}\boldsymbol{\omega}^{\boldsymbol{N}} \times \bar{\bar{\boldsymbol{I}}}^{\boldsymbol{N}} \cdot {}^{\boldsymbol{E}}\boldsymbol{\omega}^{\boldsymbol{N}} \Bigg] \qquad r = 1 \text{ to } 11
\end{aligned}
\tag{A.118}
$$

Thus, the elements of the system matrices are

$$
\begin{aligned}
[\mathbf{M}(\mathbf{q}, t)]\Big|_N (k, l) &= m^N {}^{\boldsymbol{E}}\boldsymbol{v}_{\boldsymbol{k}}^{\boldsymbol{U}} \cdot {}^{\boldsymbol{E}}\boldsymbol{v}_{\boldsymbol{l}}^{\boldsymbol{U}} + {}^{\boldsymbol{E}}\boldsymbol{\omega}_{\boldsymbol{k}}^{\boldsymbol{N}} \cdot \bar{\bar{\boldsymbol{I}}}^{\boldsymbol{N}} \cdot {}^{\boldsymbol{E}}\boldsymbol{\omega}_{\boldsymbol{l}}^{\boldsymbol{N}} && \text{for } k, l = 1 \text{ to } 11 \\
&= 0 && \text{otherwise} \\
\{-\mathbf{f}(\dot{\mathbf{q}}, \mathbf{q}, t)\}\Big|_N (k) &= -m^N {}^{\boldsymbol{E}}\boldsymbol{v}_{\boldsymbol{k}}^{\boldsymbol{U}} \cdot \sum_{i=1}^{1} 1 \frac{d}{dt}({}^{\boldsymbol{E}}\boldsymbol{v}_{\boldsymbol{i}}^{\boldsymbol{U}}) \dot{q}_i \\
&\quad - {}^{\boldsymbol{E}}\boldsymbol{\omega}_{\boldsymbol{k}}^{\boldsymbol{N}} \cdot \Bigg[- \bar{\bar{\boldsymbol{I}}}^{\boldsymbol{N}} \cdot \Bigg\{ \sum_{i=1}^{1} 1 \frac{d}{dt}({}^{\boldsymbol{E}}\boldsymbol{\omega}_{\boldsymbol{i}}^{\boldsymbol{N}}) \dot{q}_i \Bigg\} \\
&\quad - {}^{\boldsymbol{E}}\boldsymbol{\omega}^{\boldsymbol{N}} \times \bar{\bar{\boldsymbol{I}}}^{\boldsymbol{N}} \cdot {}^{\boldsymbol{E}}\boldsymbol{\omega}^{\boldsymbol{N}} \Bigg] && \text{for } k = 1 \text{ to } 11 \\
&= 0 && \text{otherwise}
\end{aligned}
\tag{A.119}
$$

The generalized active force brought about by the gravitational force is given as

$$
F_r\Big|_N = {}^{\boldsymbol{E}}\boldsymbol{v}_{\boldsymbol{r}}^{\boldsymbol{U}} \cdot \left(-m^N g \hat{\boldsymbol{z}}_{\boldsymbol{2}}\right) \qquad \text{for } r = 1 \text{ to } 11
\tag{A.120}
$$

Thus, the elements of the system matrices are

$$
\begin{aligned}
[\mathbf{M}(\mathbf{q}, t)]\Big|_{GravN} (k, l) &= 0 && \forall\ k, l \\
\{-\mathbf{f}(\dot{\mathbf{q}}, \mathbf{q}, t)\}\Big|_{GravN} (k) &= {}^{\boldsymbol{E}}\boldsymbol{v}_{\boldsymbol{k}}^{\boldsymbol{U}} \cdot \left(-m^N g \hat{\boldsymbol{z}}_{\boldsymbol{2}}\right) && \text{for } k = 1 \text{ to } 11 \\
&= 0 && \text{otherwise}
\end{aligned}
\tag{A.121}
$$

A.3.5 Hub

The rigid lump mass of the hub brings about generalized inertia forces and generalized active forces associated with the hub weight. Generalized inertia forces are given as

$$
F_r^*\Big|_H = {}^{\boldsymbol{E}}\boldsymbol{v}_{\boldsymbol{r}}^{\boldsymbol{C}} \cdot \Big(- m^H {}^{\boldsymbol{E}}\boldsymbol{a}^{\boldsymbol{C}} \Big) - {}^{\boldsymbol{E}}\boldsymbol{\omega}_{\boldsymbol{r}}^{\boldsymbol{H}} \cdot {}^{\boldsymbol{E}}\dot{\boldsymbol{H}}^{\boldsymbol{H}} \qquad \text{for } r = 1 \text{ to } 13
\tag{A.122}
$$

Or,

$$F_r^*\Big|_H = {}^{\boldsymbol{E}}\boldsymbol{v}_{\boldsymbol{r}}^{\boldsymbol{C}} \cdot \Big(-m^H {}^{\boldsymbol{E}}\boldsymbol{a}^{\boldsymbol{C}}\Big) - {}^{\boldsymbol{E}}\boldsymbol{\omega}_{\boldsymbol{r}}^{\boldsymbol{H}} \cdot \Big(\bar{\bar{\boldsymbol{I}}}^{\boldsymbol{H}} \cdot {}^{\boldsymbol{E}}\boldsymbol{\alpha}^{\boldsymbol{H}} + {}^{\boldsymbol{E}}\boldsymbol{\omega}^{\boldsymbol{H}} \times \bar{\bar{\boldsymbol{I}}}^{\boldsymbol{H}} \cdot {}^{\boldsymbol{E}}\boldsymbol{\omega}^{\boldsymbol{H}}\Big) \quad \text{for } r = 1 \text{ to } 13 \tag{A.123}$$

where m^H is the hub mass and the inertia dyadic can be given as

$$\bar{\bar{\boldsymbol{I}}}^{\boldsymbol{H}} = \Big[HubIner - m^H\Big(HubCM^2\Big)\Big]\,\hat{\boldsymbol{e}}_{\boldsymbol{1}}\hat{\boldsymbol{e}}_{\boldsymbol{1}} \tag{A.124}$$

using parallel axis theorem. The generalized inertia force can then be written as

$$\begin{aligned} F_r^*\Big|_H = {}^{\boldsymbol{E}}\boldsymbol{v}_{\boldsymbol{r}}^{\boldsymbol{C}} \cdot &\left[-m^H\left\{\left(\sum_{i=1}^{7} {}^{\boldsymbol{E}}\boldsymbol{v}_{\boldsymbol{i}}^{\boldsymbol{C}}\ddot{q}_i\right) + \left(\sum_{i=1}^{7}\frac{d}{dt}({}^{\boldsymbol{E}}\boldsymbol{v}_{\boldsymbol{i}}^{\boldsymbol{C}})\dot{q}_i\right)\right\}\right] \\ &+ {}^{\boldsymbol{E}}\boldsymbol{\omega}_{\boldsymbol{r}}^{\boldsymbol{H}}\left[-\bar{\bar{\boldsymbol{I}}}^{\boldsymbol{H}} \cdot \left\{\left(\sum_{i=1}^{7} {}^{\boldsymbol{E}}\boldsymbol{\omega}_{\boldsymbol{i}}^{\boldsymbol{H}}\ddot{q}_i\right) + \left(\sum_{i=1}^{7}\frac{d}{dt}({}^{\boldsymbol{E}}\boldsymbol{\omega}_{\boldsymbol{i}}^{\boldsymbol{H}})\dot{q}_i\right)\right\}\right. \\ &\left. - {}^{\boldsymbol{E}}\boldsymbol{\omega}^{\boldsymbol{H}} \times \bar{\bar{\boldsymbol{I}}}^{\boldsymbol{H}} \cdot {}^{\boldsymbol{E}}\boldsymbol{\omega}^{\boldsymbol{H}}\right] \qquad r = 1 \text{ to } 13 \end{aligned} \tag{A.125}$$

Thus, the elements of the system matrices are

$$\begin{aligned} [\mathbf{M}(\mathbf{q},t)]\Big|_H(k,l) &= m^H {}^{\boldsymbol{E}}\boldsymbol{v}_{\boldsymbol{k}}^{\boldsymbol{C}} \cdot {}^{\boldsymbol{E}}\boldsymbol{v}_{\boldsymbol{l}}^{\boldsymbol{C}} + {}^{\boldsymbol{E}}\boldsymbol{\omega}_{\boldsymbol{k}}^{\boldsymbol{H}} \cdot \bar{\bar{\boldsymbol{I}}}^{\boldsymbol{H}} \cdot {}^{\boldsymbol{E}}\boldsymbol{\omega}_{\boldsymbol{l}}^{\boldsymbol{H}} \quad \text{for } k,l = 1 \text{ to } 7 \\ &= 0 \qquad \text{otherwise} \\ \{-\mathbf{f}(\dot{\mathbf{q}},\mathbf{q},t)\}\Big|_H(k) &= -m^H {}^{\boldsymbol{E}}\boldsymbol{v}_{\boldsymbol{k}}^{\boldsymbol{C}} \cdot \sum_{i=1}^{7}\frac{d}{dt}({}^{\boldsymbol{E}}\boldsymbol{v}_{\boldsymbol{i}}^{\boldsymbol{C}})\dot{q}_i \\ &\quad - {}^{\boldsymbol{E}}\boldsymbol{\omega}_{\boldsymbol{k}}^{\boldsymbol{H}} \cdot \left[-\bar{\bar{\boldsymbol{I}}}^{\boldsymbol{H}} \cdot \left\{\sum_{i=1}^{7}\frac{d}{dt}({}^{\boldsymbol{E}}\boldsymbol{\omega}_{\boldsymbol{i}}^{\boldsymbol{H}})\dot{q}_i\right\}\right. \\ &\quad \left. - {}^{\boldsymbol{E}}\boldsymbol{\omega}^{\boldsymbol{H}} \times \bar{\bar{\boldsymbol{I}}}^{\boldsymbol{H}} \cdot {}^{\boldsymbol{E}}\boldsymbol{\omega}^{\boldsymbol{H}}\right] \qquad \text{for } k = 1 \text{ to } 7 \\ &= 0 \qquad \text{otherwise} \end{aligned} \tag{A.126}$$

The generalized active force brought about by the gravitational force is given as

$$F_r\Big|_H = {}^{\boldsymbol{E}}\boldsymbol{v}_{\boldsymbol{r}}^{\boldsymbol{C}} \cdot \left(-m^H g\hat{\boldsymbol{z}}_{\boldsymbol{2}}\right) \qquad \text{for } r = 1 \text{ to } 13 \tag{A.127}$$

Thus, the elements of the system matrices are

$$
\begin{aligned}
\left[\mathbf{M}(\mathbf{q},t)\right]\Big|_{GravH}(k,l) &= 0 && \forall\ k,l \\
\{-\mathbf{f}(\dot{\mathbf{q}},\mathbf{q},t)\}\Big|_{GravH}(k) &= {}^{\boldsymbol{E}}\boldsymbol{v}_{\boldsymbol{k}}^{\boldsymbol{C}} \cdot \left(-m^H g\hat{\boldsymbol{z}}_{\mathbf{2}}\right) && \text{for } k = 1 \text{ to } 13 \\
&= 0 && \text{otherwise}
\end{aligned}
\tag{A.128}
$$

A.3.6 Blades

In this section the system matrices for blade 1 is derived. The procedure for blades 2 and 3 is similar and is not repeated here. The distributed properties of blade 1 brings about generalized inertia forces and generalized active forces associated with the blade mass, elasticity, damping, weight and aerodynamic loads. Generalized inertia forces associated with the blade mass can be given as

$$
F_r^*\Big|_{B1} = -\int_0^{BldLen} \mu^{B1}(r)\,{}^{\boldsymbol{E}}\boldsymbol{v}_{\boldsymbol{r}}^{\boldsymbol{S1}}(r) \cdot {}^{\boldsymbol{E}}\boldsymbol{a}^{\boldsymbol{S1}}(r)\mathrm{d}r \quad \text{for } r = 1 \text{ to } 16 \tag{A.129}
$$

Or,

$$
\begin{aligned}
F_r^*\Big|_{B1} = -\int_0^{BldLen} \mu^{B1}(r)\,{}^{\boldsymbol{E}}\boldsymbol{v}_{\boldsymbol{r}}^{\boldsymbol{S1}}(r) \cdot \Bigg[&\sum_{i=1}^{16} {}^{\boldsymbol{E}}\boldsymbol{v}_{\boldsymbol{i}}^{\boldsymbol{S1}}(r)\ddot{q}_i \\
&+ \sum_{i=1}^{16} \frac{d}{dt}\{{}^{\boldsymbol{E}}\boldsymbol{v}_{\boldsymbol{i}}^{\boldsymbol{S1}}(r)\}\dot{q}_i \Bigg]\mathrm{d}r \quad \text{for } r = 1 \text{ to } 16
\end{aligned}
\tag{A.130}
$$

Thus, the elements of the system matrices can be found as

$$
\begin{aligned}
\left[\mathbf{M}(\mathbf{q},t)\right]\Big|_{B1}(k,l) &= \int_0^{BldLen} \mu^{B1}(r)\,{}^{\boldsymbol{E}}\boldsymbol{v}_{\boldsymbol{k}}^{\boldsymbol{S1}}(r) \cdot {}^{\boldsymbol{E}}\boldsymbol{v}_{\boldsymbol{l}}^{\boldsymbol{S1}}(r)\mathrm{d}r && \text{for } k,l = 1 \text{ to } 16 \\
&= 0 && \text{otherwise} \\
\{-\mathbf{f}(\dot{\mathbf{q}},\mathbf{q},t)\}\Big|_{B1}(k) &= -\int_0^{BldLen} \mu^{B1}(r)\,{}^{\boldsymbol{E}}\boldsymbol{v}_{\boldsymbol{k}}^{\boldsymbol{S1}}(r) \\
&\quad \cdot \left(\sum_{i=1}^{10} \frac{d}{dt}\{{}^{\boldsymbol{E}}\boldsymbol{v}_{\boldsymbol{i}}^{\boldsymbol{S1}}(r)\}\dot{q}_i\right)\mathrm{d}r && \text{for } k = 1 \text{ to } 16 \\
&= 0 && \text{otherwise}
\end{aligned}
\tag{A.131}
$$

The generalized elastic forces can be obtained from the potential energy stored in the member as

$$F_r\Big|_{ElasticB1} = \frac{\partial V^{B1}}{\partial q_r} \quad \text{for } r = 1 \text{ to } 16 \tag{A.132}$$

$$\{-\mathbf{f}(\dot{\mathbf{q}}, \mathbf{q}, t)\}\Big|_{ElasticB1}(k) = \begin{cases} -k_{11}^{B1F} q_{B1F1} - k_{12}^{B1F} q_{B1F2} & \text{for } k = 14 \\ -k_{11}^{B1E} q_{B1E1} & \text{for } k = 15 \\ -k_{22}^{B1F} q_{B1F2} - k_{21}^{B1F} q_{B1F1} & \text{for } k = 16 \\ 0 & \text{otherwise} \end{cases} \tag{A.133}$$

where, k_{ij}^{B1F} and k_{ij}^{B1E} are the generalized stiffness of the blade in the local flapwise and edgewise directions respectively when gravitational de-stiffening and centrifugal stiffening effects are not included. These terms can be obtained as

$$\begin{aligned} k_{ij}^{B1F} &= \int_0^{BldLen} EI^{B1F}(r) \left[\frac{\mathrm{d}^2\phi_i^{B1F}(r)}{\mathrm{d}r^2}\right] \left[\frac{\mathrm{d}^2\phi_j^{B1F}(r)}{\mathrm{d}r^2}\right] \mathrm{d}r \qquad \text{for } i, j = 1, 2 \\ k_{11}^{B1E} &= \int_0^{BldLen} EI^{B1E}(r) \left[\frac{\mathrm{d}^2\phi_1^{B1E}(r)}{\mathrm{d}r^2}\right]^2 \mathrm{d}r \end{aligned} \tag{A.134}$$

Using Rayleigh damping technique where the damping is assumed proportional to the stiffness the generalized active forces arising from the damping in the member can be obtained as

$$\{-\mathbf{f}(\dot{\mathbf{q}}, \mathbf{q}, t)\}\Big|_{DampB1}(k) = \begin{cases} -\frac{\zeta_1^{B1F} k_{11}^{B1F}}{\pi f_1^{B1F}} \dot{q}_{B1F1} - \frac{\zeta_2^{B1F} k_{22}^{B1F}}{\pi f_2^{B1F}} \dot{q}_{B1F2} & \text{for } k = 14 \\ -\frac{\zeta_1^{B1E} k_{11}^{B1E}}{\pi f_1^{B1E}} \dot{q}_{B1E1} & \text{for } k = 15 \\ -\frac{\zeta_1^{B2F} k_{22}^{B1F}}{\pi f_2^{B1F}} \dot{q}_{B1F2} - \frac{\zeta_1^{B1F} k_{11}^{B1F}}{\pi f_1^{B1F}} \dot{q}_{B1F1} & \text{for } k = 16 \\ 0 & \text{otherwise} \end{cases} \tag{A.135}$$

where ζ_i^{B1F} and ζ_i^{B1E} represents the structural damping ratio of the blade in the flapwise and edgewise directions respectively. And, f_i^{B1F} and f_i^{B1E} represent the natural frequency of the blade for the first mode in the flapwise and edgewise directions respectively without the centrifugal stiffening or gravitational de-stiffening effects. These terms can be given as

$$
\begin{aligned}
f_1^{B1F} &= \frac{1}{2\pi}\sqrt{\frac{k_{11}^{B1F}}{m_{11}^{B1F}}} \qquad f_2^{B1F} = \frac{1}{2\pi}\sqrt{\frac{k_{22}^{B1F}}{m_{22}^{B1F}}} \\
f_1^{B1E} &= \frac{1}{2\pi}\sqrt{\frac{k_{11}^{B1E}}{m_{11}^{B1E}}}
\end{aligned}
\tag{A.136}
$$

where, m_{ii}^{TFA} and m_{ii}^{TSS} represents the generalized mass of the blade for first two modes in flapwise and edgewise directions respectively as follows

$$
\begin{aligned}
m_{ii}^{B1F} &= \int_0^{BldLen} \mu^{B1}(r)\left[\phi_i^{B1F}(r)\right]^2 \mathrm{d}r \qquad \text{for } i = 1,2 \\
m_{ii}^{B1E} &= \int_0^{BldLen} \mu^{B1}(r)\left[\phi_i^{B1E}(r)\right]^2 \mathrm{d}r \qquad \text{for } i = 1
\end{aligned}
\tag{A.137}
$$

Generalized active force arising from gravity acting on the blade is given by

$$
F_r\Big|_{GravB1} = \int_0^{BldLen} {}^{\boldsymbol{E}}\boldsymbol{v}_{\boldsymbol{r}}^{\boldsymbol{S1}}(r)\cdot\{-\mu_{B1}(r)g\hat{\boldsymbol{z}}_{\boldsymbol{2}}\}\,\mathrm{d}r \quad \text{for } r = 1 \text{ to } 16 \tag{A.138}
$$

Thus, the elements of the system matrices are

$$
\begin{aligned}
[\mathbf{M}(\mathbf{q},t)]\Big|_{GravB1}(k,l) &= 0 && \forall\ k,l \\
\{-\mathbf{f}(\dot{\mathbf{q}},\mathbf{q},t)\}\Big|_{GravB1}(k) &= -\int_0^{BldLen} {}^{\boldsymbol{E}}\boldsymbol{v}_{\boldsymbol{k}}^{\boldsymbol{S1}}(r)\cdot\{\mu_{B1}(r)g\hat{\boldsymbol{z}}_{\boldsymbol{2}}\}\,\mathrm{d}h && \text{for } k = 1 \text{ to } 16 \\
&= 0 && \text{otherwise}
\end{aligned}
\tag{A.139}
$$

Generalized active forces due to aerodynamic loads on the blade can be given as

$$
F_r\Big|_{AeroB1} = \int_0^{BldLen} \left[{}^{\boldsymbol{E}}\boldsymbol{v}_{\boldsymbol{r}}^{\boldsymbol{S1}}(r)\cdot\boldsymbol{F}_{\boldsymbol{AeroB1}}^{\boldsymbol{S1}}(r) + {}^{\boldsymbol{E}}\boldsymbol{\omega}_{\boldsymbol{r}}^{\boldsymbol{M1}}(r)\cdot\boldsymbol{M}_{\boldsymbol{AeroB1}}^{\boldsymbol{M1}}(r)\right]\mathrm{d}r \quad \text{for } r = 1 \text{ to } 16 \tag{A.140}
$$

where, $\boldsymbol{F}_{\boldsymbol{AeroB1}}^{\boldsymbol{S1}}(r)$ and $\boldsymbol{M}_{\boldsymbol{AeroB1}}^{\boldsymbol{M1}}(r)$ are aerodynamic forces and pitching moments applied on the point $S1$ on the blade receptively expressed per unit length. $\boldsymbol{M}_{\boldsymbol{AeroB1}}^{\boldsymbol{M1}}(r)$ can include effect of both direct aerodynamic pitching moments (i.e. C_m) and aerodynamic pitching moments caused by an aerodynamic offset (i.e. moments due to aerodynamic lift and drag acting at a distance away from the center of mass of the blade element along the aerodynamic cord). The system matrices can be obtained as

$$
\begin{aligned}
[\mathbf{M}(\mathbf{q},t)]\Big|_{AeroB1}(k,l) &= 0 && \forall\ k,l \\
\{-\mathbf{f}(\dot{\mathbf{q}},\mathbf{q},t)\}\Big|_{AeroB1}(k) &= \int_0^{BldLen} \left[{}^{\boldsymbol{E}}\boldsymbol{v}_{\boldsymbol{r}}^{\boldsymbol{S1}}(r)\cdot \boldsymbol{F}_{\boldsymbol{AeroB1}}^{\boldsymbol{S1}}(r)\right. \\
&\quad \left. + {}^{\boldsymbol{E}}\boldsymbol{\omega}_{\boldsymbol{r}}^{\boldsymbol{M1}}(r)\cdot \boldsymbol{M}_{\boldsymbol{AeroB1}}^{\boldsymbol{M1}}(r)\right] \mathrm{d}r && \text{for } k=1 \text{ to } 10 \\
&= 0 && \text{otherwise}
\end{aligned}
\tag{A.141}
$$

Similar to blade 1, the distributed properties of blade 2 and blade 3 bring about generalized inertia forces and generalized active forces associated with blade elasticity, blade damping, blade weight, and aerodynamic loads. The equations for $F_r^*\Big|_{B2}$, $F_r^*\Big|_{B3}$, $F_r\Big|_{ElasticB2}$, $F_r\Big|_{ElasticB3}$, $F_r\Big|_{DampB2}$, $F_r\Big|_{DampB3}$, $F_r\Big|_{GravB2}$, $F_r\Big|_{GravB3}$, $F_r\Big|_{AeroB2}$ and $F_r\Big|_{AeroB3}$ can be found similarly.

A.3.7 Drive-train

The inertia of the drive-train brings about generalized inertia forces and the load in the generator, high speed shaft brake and the flexibility of the low speed shaft bring about generalized active forces. Note that it is assumed that the rotor is spinning about positive $\hat{\boldsymbol{c}}$ axis. This is a simply gearbox model which assumes that the gearbox rotates about the shaft axis (i.e. the gear box may not be skewed with respect to the shaft) and there is no friction between the gears. If there is no gearbox, $GBRatio = GenDir = 1$. The mechanical torque within the generator is applied to the high speed shaft equally and oppositely to the structure that rotates with the rotor, therefore,

$$
F_r\Big|_{Gen} = \left({}^{\boldsymbol{E}}\boldsymbol{\omega}_{\boldsymbol{r}}^{\boldsymbol{G}} - {}^{\boldsymbol{E}}\boldsymbol{\omega}_{\boldsymbol{r}}^{\boldsymbol{N}}\right)\cdot \boldsymbol{M}_{\boldsymbol{Gen}}^{\boldsymbol{G}} \qquad \text{for } r = 1 \text{ to } 12 \tag{A.142}
$$

Thus,

$$
F_r\Big|_{Gen} = \begin{cases} {}^{\boldsymbol{E}}\boldsymbol{\omega}_{\boldsymbol{GeAz}}^{\boldsymbol{G}}\cdot \boldsymbol{M}_{\boldsymbol{Gen}}^{\boldsymbol{G}} & \text{for } r = GeAz \\ 0 & \text{otherwise} \end{cases} \tag{A.143}
$$

where, the mechanical torque can be given as

$$
\boldsymbol{M}_{\boldsymbol{Gen}}^{\boldsymbol{G}} = -GenDir.T^{Gen}(GBRatio.\dot{q}_{GeAz},t)\hat{\boldsymbol{c}}_{\mathbf{1}} \tag{A.144}
$$

A positive T^{Gen} represents a load (positive power extracted) whereas a negative T^{Gen} represents a motoring-up (negative power extracted, or power input). Thus, the generalized active forces can be obtained as

$$F_r\Big|_{Gen} = \begin{cases} -GBRatio.T^{Gen}(GBRatio.\dot{q}_{GeAz}, t) & \text{for } r = GeAz \\ 0 & \text{otherwise} \end{cases} \tag{A.145}$$

Thus,

$$\begin{aligned} [\mathbf{M}(\mathbf{q},t)]\Big|_{Gen}(k,l) &= 0 && \forall\ k,l \\ \{-\mathbf{f}(\dot{\mathbf{q}},\mathbf{q},t)\}\Big|_{Gen}(k) &= -GBRatio.T^{Gen}(GBRatio.\dot{q}_{GeAz}, t) && \text{for } k = 12 \\ &= 0 && \text{otherwise} \end{aligned} \tag{A.146}$$

Similarly, the mechanical torque applied to the high-speed shaft from the high-speed shaft brake is applied equally and oppositely to the structure that rotates with the rotor. Thus,

$$F_r\Big|_{Brake} = \begin{cases} {}^{\boldsymbol{E}}\boldsymbol{\omega}^{\boldsymbol{G}}_{\boldsymbol{GeAz}} \cdot \boldsymbol{M}^{\boldsymbol{G}}_{\boldsymbol{Brake}} & \text{for } r = GeAz \\ 0 & \text{otherwise} \end{cases} \tag{A.147}$$

where, $\boldsymbol{M}^{G}_{Brake}$ is the torque applied by the brakes given as

$$\boldsymbol{M}^{\boldsymbol{G}}_{\boldsymbol{Brake}} = -GenDir.T^{Brake}(t)\hat{\boldsymbol{c}}_{\boldsymbol{1}} \tag{A.148}$$

where, $T^{Brake}(t) = HSSBrake.\tau(t)$ is the brake torque represented as a function of time, $HSSBrake$ is the fully deployed HSS-brake torque and $\tau(t)$ is a function of time that determines the initiation of the brakes and the time of full deployment. The transnational inertia of the drive-train is to be incorporated into the structure that rotates with the nacelle, then the high speed shaft generator inertia generalized force is given as

$$F^*_r\Big|_G = -{}^{\boldsymbol{E}}\boldsymbol{\omega}^{\boldsymbol{G}}_{\boldsymbol{r}} \cdot {}^{\boldsymbol{E}}\dot{\boldsymbol{H}}^{\boldsymbol{G}} \quad \text{for } r = 1 \text{ to } 12 \tag{A.149}$$

Or,

$$F^*_r\Big|_G = -{}^{\boldsymbol{E}}\boldsymbol{\omega}^{\boldsymbol{G}}_{\boldsymbol{r}} \cdot \left(\bar{\bar{\boldsymbol{I}}}^{\boldsymbol{G}} \cdot {}^{\boldsymbol{E}}\boldsymbol{\alpha}^{\boldsymbol{G}} + {}^{\boldsymbol{E}}\boldsymbol{\omega}^{\boldsymbol{G}} \times \bar{\bar{\boldsymbol{I}}}^{\boldsymbol{G}} \cdot {}^{\boldsymbol{E}}\boldsymbol{\omega}^{\boldsymbol{G}}\right) \quad \text{for } r = 1 \text{ to } 12 \tag{A.150}$$

where, the inertia dyadic can be given as

$$\bar{\bar{\boldsymbol{I}}}^{\boldsymbol{G}} = GenIner\hat{\boldsymbol{c}}_{\boldsymbol{1}}\hat{\boldsymbol{c}}_{\boldsymbol{1}} \tag{A.151}$$

The generalized inertia force can then be written as

$$\begin{aligned} F_r^*\Big|_G = -{}^{\boldsymbol{E}}\boldsymbol{\omega}_{\boldsymbol{r}}^{\boldsymbol{G}}\Bigg[- \bar{\bar{\boldsymbol{I}}}^{\boldsymbol{G}} \cdot \left\{ \left(\sum_{i=1}^{1} 2^{\boldsymbol{E}}\boldsymbol{\omega}_{\boldsymbol{i}}^{\boldsymbol{G}} \ddot{q}_i \right) + \left(\sum_{i=1}^{1} 2\frac{d}{dt}({}^{\boldsymbol{E}}\boldsymbol{\omega}_{\boldsymbol{i}}^{\boldsymbol{G}}) \dot{q}_i \right) \right\} \\ -{}^{\boldsymbol{E}}\boldsymbol{\omega}^{\boldsymbol{G}} \times \bar{\bar{\boldsymbol{I}}}^{\boldsymbol{G}} \cdot {}^{\boldsymbol{E}}\boldsymbol{\omega}^{\boldsymbol{G}} \Bigg] \qquad \text{for } r = 1 \text{ to } 12 \end{aligned} \tag{A.152}$$

Since, $\hat{\boldsymbol{c}}_{\boldsymbol{1}} \cdot \frac{d}{dt}({}^{\boldsymbol{E}}\boldsymbol{\omega}_{\boldsymbol{GeAz}}^{\boldsymbol{G}}) \simeq \hat{\boldsymbol{c}}_{\boldsymbol{1}} \cdot ({}^{\boldsymbol{E}}\boldsymbol{\omega}^{\boldsymbol{N}} \times \hat{\boldsymbol{c}}_{\boldsymbol{1}}) = {}^{\boldsymbol{E}}\boldsymbol{\omega}^{\boldsymbol{N}} \cdot (\hat{\boldsymbol{c}}_{\boldsymbol{1}} \times \hat{\boldsymbol{c}}_{\boldsymbol{1}}) = 0$ (the first $\hat{\boldsymbol{c}}_{\boldsymbol{1}}$ comes from $\bar{\bar{\boldsymbol{I}}}^{\boldsymbol{G}}$). This simplifies the equation as

$$F_r^*\Big|_G = -{}^{\boldsymbol{E}}\boldsymbol{\omega}_{\boldsymbol{r}}^{\boldsymbol{G}} \cdot \left[-\bar{\bar{\boldsymbol{I}}}^{\boldsymbol{G}} \cdot \left\{ \left(\sum_{i=1}^{1} 2^{\boldsymbol{E}}\boldsymbol{\omega}_{\boldsymbol{i}}^{\boldsymbol{G}} \ddot{q}_i \right) + \left(\sum_{i=1}^{1} 1\frac{d}{dt}({}^{\boldsymbol{E}}\boldsymbol{\omega}_{\boldsymbol{i}}^{\boldsymbol{G}}) \dot{q}_i \right) \right\} - {}^{\boldsymbol{E}}\boldsymbol{\omega}^{\boldsymbol{G}} \times \bar{\bar{\boldsymbol{I}}}^{\boldsymbol{G}} \cdot {}^{\boldsymbol{E}}\boldsymbol{\omega}^{\boldsymbol{G}} \right] \tag{A.153}$$

Or,

$$F_r^*\Big|_G = \begin{cases} = -{}^{\boldsymbol{E}}\boldsymbol{\omega}_{\boldsymbol{r}}^{\boldsymbol{N}} \cdot \bar{\bar{\boldsymbol{I}}}^{\boldsymbol{G}} \cdot \left\{ \left(\sum_{i=1}^{1} 2^{\boldsymbol{E}}\boldsymbol{\omega}_{\boldsymbol{i}}^{\boldsymbol{G}} \ddot{q}_i \right) + \left(\sum_{i=1}^{1} 1\frac{d}{dt}({}^{\boldsymbol{E}}\boldsymbol{\omega}_{\boldsymbol{i}}^{\boldsymbol{N}}) \dot{q}_i \right) \right\} & \\ -{}^{\boldsymbol{E}}\boldsymbol{\omega}_{\boldsymbol{r}}^{\boldsymbol{N}} \cdot \left({}^{\boldsymbol{E}}\boldsymbol{\omega}^{\boldsymbol{G}} \times \bar{\bar{\boldsymbol{I}}}^{\boldsymbol{G}} \cdot {}^{\boldsymbol{E}}\boldsymbol{\omega}^{\boldsymbol{G}} \right) & \text{for } r = 1 \text{ to } 5 \\ = -GenDir.GenIner.GBRatio\left\{ \left(\sum_{i=1}^{1} 1^{\boldsymbol{E}}\boldsymbol{\omega}_{\boldsymbol{i}}^{\boldsymbol{N}} \ddot{q}_i \right) \right. & \\ \left. + \left(\sum_{i=1}^{1} 1\frac{d}{dt}({}^{\boldsymbol{E}}\boldsymbol{\omega}_{\boldsymbol{i}}^{\boldsymbol{N}}) \dot{q}_i \right) \right\} \cdot \hat{\boldsymbol{c}}_{\boldsymbol{1}} - GenIner.GBRatio^2.\ddot{q}_{GeAz} & \\ -GenDir.GBRatio\hat{\boldsymbol{c}}_{\boldsymbol{1}} \cdot \left({}^E\omega^G \times \bar{\bar{I}}^G \cdot {}^E\omega^G \right) & \text{for } r = GeAz \\ = 0 & \text{otherwise} \end{cases} \tag{A.154}$$

Again, $\hat{\boldsymbol{c}}_{\mathbf{1}} \boldsymbol{\cdot} ({}^{\boldsymbol{E}}\boldsymbol{\omega}^{\boldsymbol{G}} \times \hat{\boldsymbol{c}}_{\mathbf{1}}) = {}^{\boldsymbol{E}}\boldsymbol{\omega}^{\boldsymbol{G}} \boldsymbol{\cdot} (\hat{\boldsymbol{c}}_{\mathbf{1}} \times \hat{\boldsymbol{c}}_{\mathbf{1}}) = 0$ (the first $\hat{\boldsymbol{c}}_{\mathbf{1}}$ coming from $\bar{\bar{\boldsymbol{I}}}^{\boldsymbol{G}}$) , this simplifies again as follows:

$$F_r^*\Big|_G = \begin{cases} = -{}^{\boldsymbol{E}}\boldsymbol{\omega}_{\boldsymbol{r}}^{\boldsymbol{N}} \boldsymbol{\cdot} \bar{\bar{\boldsymbol{I}}}^{\boldsymbol{G}} \boldsymbol{\cdot} \left\{ \left(\sum_{i=1}^{1} 2{}^{\boldsymbol{E}}\boldsymbol{\omega}_{\boldsymbol{i}}^{\boldsymbol{G}} \ddot{q}_i \right) + \left(\sum_{i=1}^{1} 1 \frac{d}{dt}({}^{\boldsymbol{E}}\boldsymbol{\omega}_{\boldsymbol{i}}^{\boldsymbol{N}}) \dot{q}_i \right) \right\} & \\ -{}^{\boldsymbol{E}}\boldsymbol{\omega}_{\boldsymbol{r}}^{\boldsymbol{N}} \boldsymbol{\cdot} \left({}^{\boldsymbol{E}}\boldsymbol{\omega}^{\boldsymbol{G}} \times \bar{\bar{\boldsymbol{I}}}^{\boldsymbol{G}} \boldsymbol{\cdot} {}^{\boldsymbol{E}}\boldsymbol{\omega}^{\boldsymbol{G}} \right) & \text{for } r = 1 \text{ to } 11 \\ = -GenDir.GenIner.GBRatio \left\{ \left(\sum_{i=1}^{1} 1{}^{\boldsymbol{E}}\boldsymbol{\omega}_{\boldsymbol{i}}^{\boldsymbol{N}} \ddot{q}_i \right) \right. & \\ \left. + \left(\sum_{i=1}^{1} 1 \frac{d}{dt}({}^{\boldsymbol{E}}\boldsymbol{\omega}_{\boldsymbol{i}}^{\boldsymbol{N}}) \dot{q}_i \right) \right\} \boldsymbol{\cdot} \hat{\boldsymbol{c}}_{\mathbf{1}} - GenIner.GBRatio^2.\ddot{q}_{GeAz} & \text{for } r = GeAz \\ = 0 & \text{otherwise} \end{cases} \tag{A.155}$$

The terms associated with DOFs 1 to 11 represents the fact that the rate of change of angular momentum of the generator can be considered as an additional torque on the structure that rotates with the nacelle (i.e in addition to the torque on the structure transmitted from the low speed shaft). Thus, the system matrices are

$$\begin{aligned} [\mathbf{M}(\mathbf{q},t)]\Big|_G(k,l) &= {}^{\boldsymbol{E}}\boldsymbol{\omega}_{\boldsymbol{k}}^{\boldsymbol{G}} \boldsymbol{\cdot} \bar{\bar{\boldsymbol{I}}}^{\boldsymbol{G}} \boldsymbol{\cdot} {}^{\boldsymbol{E}}\boldsymbol{\omega}_{\boldsymbol{l}}^{\boldsymbol{G}} && \text{for } k,l = 1 \text{ to } 12 \\ &= 0 && \text{otherwise} \\ \{-\mathbf{f}(\dot{\mathbf{q}},\mathbf{q},t)\}\Big|_G(k) &= -{}^{\boldsymbol{E}}\boldsymbol{\omega}_{\boldsymbol{k}}^{\boldsymbol{G}} \boldsymbol{\cdot} \left[\bar{\bar{\boldsymbol{I}}}^{\boldsymbol{G}} \boldsymbol{\cdot} \left\{ \sum_{i=1}^{5} \frac{d}{dt}({}^{\boldsymbol{E}}\boldsymbol{\omega}_{\boldsymbol{i}}^{\boldsymbol{N}}) \dot{q}_i \right\} \right. \\ &\quad \left. + {}^{\boldsymbol{E}}\boldsymbol{\omega}^{\boldsymbol{G}} \times \bar{\bar{\boldsymbol{I}}}^{\boldsymbol{G}} \boldsymbol{\cdot} {}^{\boldsymbol{E}}\boldsymbol{\omega}^{\boldsymbol{G}} \right] && \text{for } k = 1 \text{ to } 11 \\ &= -{}^{\boldsymbol{E}}\boldsymbol{\omega}_{\boldsymbol{k}}^{\boldsymbol{G}} \boldsymbol{\cdot} \bar{\bar{\boldsymbol{I}}}^{\boldsymbol{G}} \boldsymbol{\cdot} \left\{ \sum_{i=1}^{5} \frac{d}{dt}({}^{\boldsymbol{E}}\boldsymbol{\omega}_{\boldsymbol{i}}^{\boldsymbol{N}}) \dot{q}_i \right\} && \text{for } k = 12 \\ &= 0 && \text{otherwise} \end{aligned} \tag{A.156}$$

The elasticity of the low speed shaft brings about generalized active force which can be obtained from the stored potential energy as

$$F_r\Big|_{ELasticDrive} = \frac{\partial V_{Drive}}{\partial q_r} \quad \text{for } r = 1 \text{ to } 13 \tag{A.157}$$

where, $V_{Drive} = \frac{1}{2} DTTorSpr.q_{DrTr}^2$. Hence,

$$[\mathbf{M}(\mathbf{q}, t)]\Big|_{DriveTrain}(k, l) = 0 \quad \forall\, k, l \tag{A.158}$$

and

$$\{-\mathbf{f}(\dot{\mathbf{q}}, \mathbf{q}, t)\}\Big|_{Drivetrain}(k) = \begin{cases} -DTTorSpr.q_{DrTr} & \text{for } k = 13 \\ 0 & \text{otherwise} \end{cases} \tag{A.159}$$

Likewise, the generalized active forces from the damping in the drive-train can be obtained as

$$\{-\mathbf{f}(\dot{\mathbf{q}}, \mathbf{q}, t)\}\Big|_{Drivetrain}(k) = \begin{cases} -DTTorDmp.\dot{q}_{DrTr} & \text{for } k = 13 \\ 0 & \text{otherwise} \end{cases} \tag{A.160}$$

Here, it must be noted that similar to the HSS brake, the mechanical friction in the gearbox will exert a torque on the high speed shaft. In this study, the mechanical friction torque is neglected and it is assumed that the gearbox operates with 100% efficiency. The final system matrices $\mathbf{M}(\mathbf{q}, t)$ and $-\mathbf{f}(\dot{\mathbf{q}}, \mathbf{q}, t)$ are obtained by summing up the contributions of the different components of the floating offshore wind turbine. It is worth noting here that terms of $\mathbf{M}(\mathbf{q}, t)$ and $-\mathbf{f}(\dot{\mathbf{q}}, \mathbf{q}, t)$ can be evaluated directly using a computer and a-priori closed form knowledge of equations of motion are not required. This has particular advantage for complex structures with large number of components and reference frames which makes the evaluation of closed form equations practically impossible.

A.4 Kinematics and kinetics of TMD mass

The kinematics and the kinetics of the TMD mass are provided in this section. The resulting mass matrix and force vector can be superimposed onto the floating wind turbine system equations to obtain the equations of motion of the coupled system.

A.4.1 Position Vector

The position vector from tower top to the center of mass of the TMD denoted by point D is defined as

$$\boldsymbol{r}^{\boldsymbol{OD}} = h_{TMD}\hat{\boldsymbol{d}}_{\boldsymbol{2}} + q_{TMD}\hat{\boldsymbol{d}}_{\boldsymbol{3}} \tag{A.161}$$

where, h_{TMD} is the vertical distance of the TMD mass center of gravity from tower top and q_{TMD} is the new generalized coordinate that describes the motion of the TMD mass.

A.4.2 Linear Velocity Vector

The linear velocity vector of the TMD mass is given as

$$ {}^{\boldsymbol{E}}\boldsymbol{v}^{\boldsymbol{D}} = {}^{\boldsymbol{E}}\boldsymbol{v}^{\boldsymbol{O}} + {}^{\boldsymbol{N}}\boldsymbol{v}^{\boldsymbol{D}} + {}^{\boldsymbol{E}}\boldsymbol{\omega}^{\boldsymbol{N}} \times \boldsymbol{r}^{\boldsymbol{OD}} \tag{A.162} $$

A.4.3 Partial Linear Velocities

Partial linear velocities of the TMD mass are given as

$$ \begin{aligned} {}^{\boldsymbol{E}}\boldsymbol{v}^{\boldsymbol{D}}_{\boldsymbol{r}} &= {}^{\boldsymbol{E}}\boldsymbol{v}^{\boldsymbol{O}}_{\boldsymbol{r}} + \begin{cases} {}^{\boldsymbol{E}}\boldsymbol{\omega}^{\boldsymbol{N}}_{r} \times \boldsymbol{r}^{\boldsymbol{OD}} & \text{for } r = 1 \text{ to } 11 \\ \hat{\boldsymbol{d}}_{\boldsymbol{3}} & \text{for } r = 23 \\ 0 & \text{otherwise} \end{cases} \\ {}^{\boldsymbol{E}}\boldsymbol{v}^{\boldsymbol{D}}_{\boldsymbol{t}} &= 0 \end{aligned} \tag{A.163} $$

A.4.4 Linear Accelerations

The acceleration of the TMD mass is again written in terms of partial linear acceleration as

$$ {}^{\boldsymbol{E}}\boldsymbol{a}^{\boldsymbol{D}} = \sum_{r=1}^{23} {}^{\boldsymbol{E}}\boldsymbol{v}^{\boldsymbol{D}}_{\boldsymbol{r}} \ddot{q}_r + \sum_{r=1}^{23} \frac{d}{dt}({}^{\boldsymbol{E}}\boldsymbol{v}^{\boldsymbol{D}}_{\boldsymbol{r}}) \dot{q}_r \tag{A.164} $$

The partial linear acceleration terms are given as

$$ \frac{d}{dt}({}^{\boldsymbol{E}}\boldsymbol{v}^{\boldsymbol{D}}_{\boldsymbol{r}}) = \frac{d}{dt}({}^{\boldsymbol{E}}\boldsymbol{v}^{\boldsymbol{O}}_{\boldsymbol{r}}) + \begin{cases} \frac{d}{dt}({}^{\boldsymbol{E}}\boldsymbol{\omega}^{\boldsymbol{N}}_{\boldsymbol{r}}) \times \boldsymbol{r}^{\boldsymbol{OD}} + {}^{\boldsymbol{E}}\boldsymbol{\omega}^{\boldsymbol{N}}_{\boldsymbol{r}} \times ({}^{\boldsymbol{E}}\boldsymbol{\omega}^{\boldsymbol{N}} \times \boldsymbol{r}^{\boldsymbol{OD}}) & \text{for } r = 1 \text{ to } 5 \\ {}^{\boldsymbol{E}}\boldsymbol{\omega}^{\boldsymbol{N}} \times \hat{\boldsymbol{d}}_{\boldsymbol{3}} & \text{for } r = 17 \\ 0 & \text{otherwise} \end{cases} \tag{A.165} $$

A.4.5 Kinetics & Equations of Motion

The TMD will bring about generalized active and inertial forces will can be summed up with the generalized active and inertial forces of the overall wind turbine system to obtain the final equations of motion.

The generalized inertial forces can be given as

$$F_r^*\Big|_{TMD} = {}^{\boldsymbol{E}}\boldsymbol{v}_{\boldsymbol{r}}^{\boldsymbol{D}} \cdot (-m_{TMD}{}^{\boldsymbol{E}}\boldsymbol{a}^{\boldsymbol{D}}) \qquad \text{for } r = 1 \text{ to } 23 \tag{A.166}$$

$$\begin{aligned} F_r^*\Big|_{TMD} = {}^{\boldsymbol{E}}\boldsymbol{v}_{\boldsymbol{r}}^{\boldsymbol{D}} \cdot \Bigg[- m_{TMD}\Bigg\{ &\left(\sum_{i=1}^{11} {}^{\boldsymbol{E}}\boldsymbol{v}_{\boldsymbol{i}}^{\boldsymbol{D}} \ddot{q}_i + {}^{\boldsymbol{E}}\boldsymbol{v}_{\boldsymbol{TMD}}^{\boldsymbol{D}} \ddot{q}_{TMD} \right) \\ + &\left(\sum_{i=1}^{11} \frac{d}{dt}({}^{\boldsymbol{E}}\boldsymbol{v}_{\boldsymbol{i}}^{\boldsymbol{D}}) \dot{q}_i + \frac{d}{dt}({}^{\boldsymbol{E}}\boldsymbol{v}_{\boldsymbol{TMD}}^{\boldsymbol{D}}) \dot{q}_{TMD} \right) \Bigg\} \Bigg] \qquad \text{for } r = 1 \text{ to } 23 \end{aligned} \tag{A.167}$$

The system matrices are obtained as

$$\begin{aligned} [\mathbf{M}(\mathbf{q},t)]\Big|_{TMD}(k,l) &= m_{TMD}{}^{\boldsymbol{E}}\boldsymbol{v}_{\boldsymbol{k}}^{\boldsymbol{D}} \cdot {}^{\boldsymbol{E}}\boldsymbol{v}_{\boldsymbol{l}}^{\boldsymbol{D}} && \text{for } k,l = 1 \text{ to } 11, 23 \\ &= 0 && \text{otherwise} \\ \{-\mathbf{f}(\dot{\mathbf{q}},\mathbf{q},t)\}\Big|_{TMD}(k) &= -m_{TMD}{}^{\boldsymbol{E}}\boldsymbol{v}_{\boldsymbol{k}}^{\boldsymbol{D}} \cdot \Bigg[\sum_{i=1}^{11} \frac{d}{dt}({}^{\boldsymbol{E}}\boldsymbol{v}_{\boldsymbol{i}}^{\boldsymbol{D}}) \dot{q}_i \\ &\quad + \frac{d}{dt}({}^{\boldsymbol{E}}\boldsymbol{v}_{\boldsymbol{TMD}}^{\boldsymbol{D}}) \dot{q}_{TMD} \Bigg] && \text{for } k,l = 1 \text{ to } 11, 23 \\ &= 0 && \text{otherwise} \end{aligned} \tag{A.168}$$

Gravitational force on the TMD brings about generalized active forces on the TMD

$$F_r\Big|_{TMD} = {}^{\boldsymbol{E}}\boldsymbol{v}_{\boldsymbol{k}}^{\boldsymbol{D}} \cdot (-m_{TMD} g \hat{\boldsymbol{z}}_{\boldsymbol{2}}) \tag{A.169}$$

$$\begin{aligned} [\mathbf{M}(\mathbf{q},t)]\Big|_{GravTMD}(k,l) &= 0 && \forall k,l \\ \{-f(\dot{q},q,t)\}\Big|_{TMDGrav}(k) &= {}^{\boldsymbol{E}}\boldsymbol{v}_{\boldsymbol{k}}^{\boldsymbol{D}} \cdot (-m_{TMD} g \hat{\boldsymbol{z}}_{\boldsymbol{2}}) && \text{for } k,l = 1 \text{ to } 11, 23 \end{aligned} \tag{A.170}$$

The spring and the damper attached to the TMD brings about generalized active force given as

$$\{-f(\dot{q},q,t)\}\Big|_{TMDElastic}(k) = \frac{\partial V^{TMD}}{\partial q_r} = -k_{TMD} q_{TMD} \qquad \text{for } k = 23 \tag{A.171}$$

Using Rayleigh damping technique the damping is assumed to be proportional to the stiffness. The generalized active forces arising from the damping is given as

$$\{-f(\dot{q}, q, t)\}\Big|_{TMDDamp}(k) = -\frac{\zeta_{TMD} k_{TMD}}{\pi f_{TMD}} \dot{q}_{TMD} \qquad \text{for } k = 23 \tag{A.172}$$

Where m_{TMD}, k_{TMD}, f_{TMD} and ζ_{TMD} is the damper mass, stiffness, frequency of the TMD in Hz and damping ratio respectively. Including these terms in the system matrices of the wind turbine forms the global system matrices of the wind turbine with the TMD placed on the nacelle. The following section shows some preliminary results of vibration control of wind turbine tower.

Appendix B

Kinematic and kinetic description of the reduced degree of freedom system

B.1 Coordinate Systems for Reduced Order Model

A set of inertial coordinate system $\hat{\boldsymbol{z}}$ is fixed to the earth/base of tower. For a onshore wind turbine the base is fixed to the earth and hence the tower base coordinate system is equal to the inertial coordinate system

$$\begin{pmatrix} \hat{\boldsymbol{a}}_\mathbf{1} \\ \hat{\boldsymbol{a}}_\mathbf{2} \\ \hat{\boldsymbol{a}}_\mathbf{3} \end{pmatrix} = \begin{pmatrix} \hat{\boldsymbol{z}}_\mathbf{1} \\ \hat{\boldsymbol{z}}_\mathbf{2} \\ \hat{\boldsymbol{z}}_\mathbf{3} \end{pmatrix} \tag{B.1}$$

The azimuth coordinate system is also attached to the low speed shaft but rotates with the rotor is defined next as

$$\begin{pmatrix} \hat{\boldsymbol{e}}_\mathbf{1} \\ \hat{\boldsymbol{e}}_\mathbf{2} \\ \hat{\boldsymbol{e}}_\mathbf{3} \end{pmatrix} = \begin{bmatrix} 1 & 0 & 0 \\ 0 & \cos(q_{GeAz}) & \sin(q_{GeAz}) \\ 0 & -\sin(q_{GeAz}) & \cos(q_{GeAz}) \end{bmatrix} \begin{pmatrix} \hat{\boldsymbol{a}}_\mathbf{1} \\ \hat{\boldsymbol{a}}_\mathbf{2} \\ \hat{\boldsymbol{a}}_\mathbf{3} \end{pmatrix} \tag{B.2}$$

The rotation angle (generator azimuth angle, q_{GeAz}) is assumed to be constant. The coordinate system for blade 1 is given as

$$\begin{pmatrix} \hat{\boldsymbol{g}}_\mathbf{1}^{\boldsymbol{B1}} \\ \hat{\boldsymbol{g}}_\mathbf{2}^{\boldsymbol{B1}} \\ \hat{\boldsymbol{g}}_\mathbf{3}^{\boldsymbol{B1}} \end{pmatrix} = \begin{bmatrix} 1 & 0 & 0 \\ 0 & \cos(\pi/2) & -\sin(\pi/2) \\ 0 & \sin(\pi/2) & \cos(\pi/2) \end{bmatrix} \begin{pmatrix} \hat{\boldsymbol{e}}_\mathbf{1} \\ \hat{\boldsymbol{e}}_\mathbf{2} \\ \hat{\boldsymbol{e}}_\mathbf{3} \end{pmatrix} \tag{B.3}$$

When blade 1 is pointing up, blade 3 is ahead of blade 2 and blade 2 is ahead of blade 1, and the blades are set 120° degrees apart. Thus the blade coordinate systems of blade 2 and 3 are given as

$$\begin{pmatrix} \hat{\boldsymbol{g}}_{\boldsymbol{1}}^{\boldsymbol{B1}} \\ \hat{\boldsymbol{g}}_{\boldsymbol{2}}^{\boldsymbol{B1}} \\ \hat{\boldsymbol{g}}_{\boldsymbol{3}}^{\boldsymbol{B1}} \end{pmatrix} = \begin{bmatrix} 1 & 0 & 0 \\ 0 & \cos(\pi/2 + 2\pi/3) & -\sin(\pi/2 + 2\pi/3) \\ 0 & \sin(\pi/2 + 2\pi/3) & \cos(\pi/2 + 2\pi/3) \end{bmatrix} \begin{pmatrix} \hat{\boldsymbol{e}}_{\boldsymbol{1}} \\ \hat{\boldsymbol{e}}_{\boldsymbol{2}} \\ \hat{\boldsymbol{e}}_{\boldsymbol{3}} \end{pmatrix} \tag{B.4}$$

$$\begin{pmatrix} \hat{\boldsymbol{g}}_{\boldsymbol{1}}^{\boldsymbol{B1}} \\ \hat{\boldsymbol{g}}_{\boldsymbol{2}}^{\boldsymbol{B1}} \\ \hat{\boldsymbol{g}}_{\boldsymbol{3}}^{\boldsymbol{B1}} \end{pmatrix} = \begin{bmatrix} 1 & 0 & 0 \\ 0 & \cos(\pi/2 + 4\pi/3) & -\sin(\pi/2 + 4\pi/3) \\ 0 & \sin(\pi/2 + 4\pi/3) & \cos(\pi/2 + 4\pi/3) \end{bmatrix} \begin{pmatrix} \hat{\boldsymbol{e}}_{\boldsymbol{1}} \\ \hat{\boldsymbol{e}}_{\boldsymbol{2}} \\ \hat{\boldsymbol{e}}_{\boldsymbol{3}} \end{pmatrix} \tag{B.5}$$

The aerodynamic loads are determined and returned in the blades global coordinates ($\hat{\boldsymbol{g}}^{\boldsymbol{B1}}, \hat{\boldsymbol{g}}^{\boldsymbol{B2}}$ & $\hat{\boldsymbol{g}}^{\boldsymbol{B3}}$) itself. There are no provisions made to estimate the loads in blade element local coordinates.

B.2 Kinematics of Reduced Order Model

This section describes the kinematics of the reduced order model. For that purpose the important points that describes the motion remain the same. But, the assumptions made lead to certain simplifications that will be shown in the following.

B.2.1 Position vectors

The position vectors of the various points are given in the following. The position vector of a tower node at a distance h from the base of the tower is given as

$$\boldsymbol{r}^{\boldsymbol{ZT}}(h) = \left[\phi_1^{TFA}(h) q_{TFA1}\right] \hat{\boldsymbol{a}}_{\boldsymbol{1}} + h\hat{\boldsymbol{a}}_{\boldsymbol{2}} + \left[\phi_1^{TSS}(h) q_{TSS1}\right] \hat{\boldsymbol{a}}_{\boldsymbol{3}} \tag{B.6}$$

It is important to note hear how the axial deformation due to lateral deflection has been neglected and only the first modes are used to define the fore-aft and side-to-side motion of the tower. The position vector of the tower top from the tower base is given as

$$\boldsymbol{r}^{\boldsymbol{ZO}} = [q_{TFA1}]\, \hat{\boldsymbol{a}}_{\boldsymbol{1}} + TwrHt\hat{\boldsymbol{a}}_{\boldsymbol{2}} + [q_{TSS1}]\, \hat{\boldsymbol{a}}_{\boldsymbol{3}} \tag{B.7}$$

Position vector from tower-top to nacelle center of mass following from the assumptions made is given as

$$\boldsymbol{r}^{\boldsymbol{OU}} = 0\hat{\boldsymbol{d}}_{\boldsymbol{1}} + 0\hat{\boldsymbol{d}}_{\boldsymbol{2}} + 0\hat{\boldsymbol{d}}_{\boldsymbol{3}} \tag{B.8}$$

Similarly, position vector from tower-top to apex of coning angle is given as

$$\boldsymbol{r^{OQ}} = 0\boldsymbol{\hat{c}_1} + 0\boldsymbol{\hat{d}_2} - 0\boldsymbol{\hat{d}_3} \tag{B.9}$$

Again, position vector from apex of coning angle to hub center of mass is given as

$$\boldsymbol{r^{QC}} = 0\boldsymbol{\hat{c}_1} \tag{B.10}$$

With the assumed simplifications the position vector from apex of coning angle to blade element node for blade 1 is given as

$$\begin{aligned} \boldsymbol{r^{QS1}} = & \left[\phi_1^{B1F1}(r) q_{B1F1}\right] \boldsymbol{\hat{g}_1^{B1}} + \left[\phi_1^{B1E1}(r) q_{B1E1}\right] \boldsymbol{\hat{g}_2^{B1}} \\ & + \Big[r + HubRad\Big] \boldsymbol{\hat{g}_3^{B1}} \end{aligned} \tag{B.11}$$

Where, ϕ_1^{B1F1} and ϕ_1^{B1E1} are the first flapwise and edgewise mode shapes respectively. Axial deflection of the blades have been neglected. Equations for $\boldsymbol{r^{QS2}}$ and $\boldsymbol{r^{QS3}}$ are similar.

B.2.2 Angular velocities

The rotation of the tower and blades are neglected. Hence, this section is largely simplified and the only angular velocity arises from the azimuthal rotation of blades

$$^{\boldsymbol{E}}\boldsymbol{\omega^X} = 0 \tag{B.12}$$

Angular velocity of tower node is neglected

$$^{\boldsymbol{E}}\boldsymbol{\omega^F}(h) = 0\boldsymbol{\hat{a}_1} - 0\boldsymbol{\hat{a}_3} \tag{B.13}$$

Angular velocity of tower-top/base-plate becomes zero

$$^{\boldsymbol{E}}\boldsymbol{\omega^B} = 0\boldsymbol{\hat{a}_1} - 0\boldsymbol{\hat{a}_3} \tag{B.14}$$

Angular velocity of nacelle in inertial reference frame where nacelle yaw is neglected

$$^{\boldsymbol{E}}\boldsymbol{\omega^N} = {}^{\boldsymbol{E}}\boldsymbol{\omega^B} + 0\boldsymbol{\hat{a}_2} \tag{B.15}$$

Angular velocity of low speed shaft at the rotor end in inertial reference frame where drive-train torsion is neglected becomes

$$^{\boldsymbol{E}}\boldsymbol{\omega}^{\boldsymbol{L}} = {}^{\boldsymbol{E}}\boldsymbol{\omega}^{\boldsymbol{N}} + \dot{q}_{GeAz}\hat{\boldsymbol{c}}_{\boldsymbol{1}} \tag{B.16}$$

Angular velocity of blade 1 element

$$^{\boldsymbol{E}}\boldsymbol{\omega}^{\boldsymbol{M1}}(r) = {}^{\boldsymbol{E}}\boldsymbol{\omega}^{\boldsymbol{L}} - 0\hat{\boldsymbol{g}}_{\boldsymbol{1}}^{\boldsymbol{B1}} - 0\hat{\boldsymbol{g}}_{\boldsymbol{2}}^{\boldsymbol{B1}} \tag{B.17}$$

$^{\boldsymbol{E}}\boldsymbol{\omega}^{\boldsymbol{M2}}(r)$ and $^{\boldsymbol{E}}\boldsymbol{\omega}^{\boldsymbol{M3}}(r)$ can be found similarly. The generator is neglected.

B.2.3 Linear Velocities

Linear velocity of tower element in inertial reference frame can be obtained from one point moving on a rigid body formula as (Kane and Levinson, 1985)

$$\begin{aligned} ^{\boldsymbol{E}}\boldsymbol{v}^{\boldsymbol{T}} &= {}^{\boldsymbol{E}}\boldsymbol{v}^{\overline{\boldsymbol{T}}} + {}^{\boldsymbol{X}}\boldsymbol{v}^{\boldsymbol{T}} \\ &= {}^{\boldsymbol{E}}\boldsymbol{\omega}^{\boldsymbol{X}} \times \boldsymbol{r}^{\boldsymbol{ZT}} + {}^{\boldsymbol{X}}\boldsymbol{v}^{\boldsymbol{T}} \end{aligned} \tag{B.18}$$

where $^{\boldsymbol{E}}\boldsymbol{v}^{\overline{\boldsymbol{T}}}$ denotes the velocity in E of the point $\overline{T}$ of X that coincides with T at the instant under consideration. For a fixed base wind turbine $^{\boldsymbol{E}}\boldsymbol{\omega}^{\boldsymbol{X}} = 0$ therefore, $^{\boldsymbol{E}}\boldsymbol{v}^{\boldsymbol{T}} = {}^{\boldsymbol{X}}\boldsymbol{v}^{\boldsymbol{T}}$ given as

$$^{\boldsymbol{X}}\boldsymbol{v}^{\boldsymbol{T}}(h) = \left[\phi_1^{TFA}(h)\dot{q}_{TFA1}\right]\hat{\boldsymbol{a}}_{\boldsymbol{1}} - 0\hat{\boldsymbol{a}}_{\boldsymbol{2}} + \left[\phi_1^{TSS}(h)\dot{q}_{TSS1}\right]\hat{\boldsymbol{a}}_{\boldsymbol{3}} \tag{B.19}$$

Similarly the velocity of tower top/base plate can be given as

$$^{\boldsymbol{X}}\boldsymbol{v}^{\boldsymbol{O}} = [\dot{q}_{TFA1}]\,\hat{\boldsymbol{a}}_{\boldsymbol{1}} - 0\hat{\boldsymbol{a}}_{\boldsymbol{2}} + [\dot{q}_{TSS1}]\,\hat{\boldsymbol{a}}_{\boldsymbol{3}} \tag{B.20}$$

Linear velocity of the nacelle center of mass can be obtained from two points fixed on a rigid body formula as (Kane and Levinson, 1985). Since all of the position vectors are assumed to be zeros the resulting vectors multiplications are vastly simplified.

$$^{\boldsymbol{E}}\boldsymbol{v}^{\boldsymbol{U}} = {}^{\boldsymbol{E}}\boldsymbol{v}^{\boldsymbol{O}} + {}^{\boldsymbol{E}}\boldsymbol{\omega}^{\boldsymbol{N}} \times \boldsymbol{r}^{\boldsymbol{OU}} \tag{B.21}$$

Linear velocity of apex of the coning angle is given as

$$^{\boldsymbol{E}}\boldsymbol{v}^{\boldsymbol{Q}} = {}^{\boldsymbol{E}}\boldsymbol{v}^{\boldsymbol{O}} + {}^{\boldsymbol{E}}\boldsymbol{\omega}^{\boldsymbol{L}} \times \boldsymbol{r}^{\boldsymbol{OQ}} \tag{B.22}$$

Linear velocity of center of mass of hub can be given as

$$^{\boldsymbol{E}}\boldsymbol{v}^{\boldsymbol{C}} = {}^{\boldsymbol{E}}\boldsymbol{v}^{\boldsymbol{Q}} + {}^{\boldsymbol{E}}\boldsymbol{\omega}^{\boldsymbol{L}} \times \boldsymbol{r}^{\boldsymbol{QC}} \tag{B.23}$$

Finally, the linear velocity of blade 1 element is given as

$$^{\boldsymbol{E}}\boldsymbol{v}^{\boldsymbol{S1}}(r) = {}^{\boldsymbol{E}}\boldsymbol{v}^{\boldsymbol{Q}} + {}^{\boldsymbol{E}}\boldsymbol{\omega}^{\boldsymbol{L}} \times \boldsymbol{r}^{\boldsymbol{QS1}} + {}^{\boldsymbol{L}}\boldsymbol{v}^{\boldsymbol{S1}}(r) \tag{B.24}$$

where,

$$^{\boldsymbol{L}}\boldsymbol{v}^{\boldsymbol{S1}}(r) = \left[\phi_1^{B1F1}(r)\dot{q}_{B1F1}\right]\hat{\boldsymbol{g}}_{\boldsymbol{1}}^{\boldsymbol{B1}} + \left[\phi_1^{B1E1}(r)\dot{q}_{B1E1}\right]\hat{\boldsymbol{g}}_{\boldsymbol{2}}^{\boldsymbol{B1}} + 0\hat{\boldsymbol{g}}_{\boldsymbol{3}}^{\boldsymbol{B1}} \tag{B.25}$$

The linear velocities for blade 2, $^{\boldsymbol{E}}\boldsymbol{v}^{\boldsymbol{S2}}(r)$ and blade 3, $^{\boldsymbol{E}}\boldsymbol{v}^{\boldsymbol{S3}}(r)$ can be obtained similarly.

B.2.4 Partial Angular Velocities

According to (Kane and Levinson, 1985) all linear velocities can be written as a combination of the partial velocities as

$$^{\boldsymbol{E}}\boldsymbol{\omega}^{\boldsymbol{N_i}}(\dot{q}, q, t) = \sum_{r=1}^{9} {}^{\boldsymbol{E}}\boldsymbol{\omega}_{\boldsymbol{r}}^{\boldsymbol{N_i}}(q, t)u_r + {}^{\boldsymbol{E}}\boldsymbol{\omega}_{\boldsymbol{t}}^{\boldsymbol{N_i}}(q, t) \tag{B.26}$$

for each rigid body N_i in the system. Where $^{\boldsymbol{E}}\boldsymbol{\omega}_{\boldsymbol{r}}^{\boldsymbol{N_i}}(q, t)$ are the partial angular velocities. u_r are called generalized speeds according to (Kane and Levinson, 1985) and in general their choice brings the linear velocities in A.2.2 and A.2.3 into particular advantageous form. Here, time derivatives of the DOFs in equation 3.1 are chosen as the generalized speeds (i.e. $u_r = \dot{q}_r$). The choice of generalized speeds renders all the $^{\boldsymbol{E}}\boldsymbol{\omega}_{\boldsymbol{t}}^{\boldsymbol{N_i}}(q, t)$ terms as zeros as will be shown.

The partial angular velocities for the platform can be given

$$\begin{aligned} &^{\boldsymbol{E}}\boldsymbol{\omega}_{\boldsymbol{r}}^{\boldsymbol{X}} = 0 \qquad \text{for } \; r = 1 \text{ to } 9 \\ &^{\boldsymbol{E}}\boldsymbol{\omega}_{\boldsymbol{t}}^{\boldsymbol{X}} = 0 \end{aligned} \tag{B.27}$$

All partial angular velocities for the platform are zeros since the platform is fixed to the base. The partial angular velocities for the tower element is given as

$$\begin{aligned} &^{\boldsymbol{E}}\boldsymbol{\omega}_{\boldsymbol{r}}^{\boldsymbol{F}}(h) = {}^{\boldsymbol{E}}\boldsymbol{\omega}_{\boldsymbol{r}}^{\boldsymbol{X}} + 0 \quad \text{for } \; r = 1 \text{ to } n \\ &^{\boldsymbol{E}}\boldsymbol{\omega}_{\boldsymbol{t}}^{\boldsymbol{F}}(h) = 0 \end{aligned} \tag{B.28}$$

The partial angular velocities for tower-top/base-plate can be given as

$$\begin{aligned} {}^{\boldsymbol{E}}\boldsymbol{\omega}_{\boldsymbol{r}}^{\boldsymbol{B}} &= {}^{\boldsymbol{E}}\boldsymbol{\omega}_{\boldsymbol{r}}^{\boldsymbol{X}} + 0 \quad \text{for} \ \ r = 1 \text{ to } 9 \\ {}^{\boldsymbol{E}}\boldsymbol{\omega}_{\boldsymbol{t}}^{\boldsymbol{B}} &= 0 \end{aligned} \tag{B.29}$$

The partial angular velocities for nacelle can be given as

$$\begin{aligned} {}^{\boldsymbol{E}}\boldsymbol{\omega}_{\boldsymbol{r}}^{\boldsymbol{N}} &= {}^{\boldsymbol{E}}\boldsymbol{\omega}_{\boldsymbol{r}}^{\boldsymbol{B}} + 0 \quad \text{for all} \\ {}^{\boldsymbol{E}}\boldsymbol{\omega}_{\boldsymbol{t}}^{\boldsymbol{N}} &= 0 \end{aligned} \tag{B.30}$$

The partial angular velocities for low speed shaft can be given as

$$\begin{aligned} {}^{\boldsymbol{E}}\boldsymbol{\omega}_{\boldsymbol{r}}^{\boldsymbol{L}} &= {}^{\boldsymbol{E}}\boldsymbol{\omega}_{\boldsymbol{r}}^{\boldsymbol{N}} + \begin{cases} \boldsymbol{\hat{e}_1} & \text{for } r = GeAz \\ 0 & \text{otherwise} \end{cases} \\ {}^{\boldsymbol{E}}\boldsymbol{\omega}_{\boldsymbol{t}}^{\boldsymbol{L}} &= 0 \end{aligned} \tag{B.31}$$

The partial angular velocities for blade 1 element can be given as

$$\begin{aligned} {}^{\boldsymbol{E}}\boldsymbol{\omega}_{\boldsymbol{r}}^{\boldsymbol{M1}}(r) &= {}^{\boldsymbol{E}}\boldsymbol{\omega}_{\boldsymbol{r}}^{\boldsymbol{L}} + 0 \quad \text{for all} \\ {}^{\boldsymbol{E}}\boldsymbol{\omega}_{\boldsymbol{t}}^{\boldsymbol{M1}}(r) &= 0 \end{aligned} \tag{B.32}$$

The equations for ${}^{\boldsymbol{E}}\boldsymbol{\omega}_{\boldsymbol{r}}^{\boldsymbol{M2}}(r)$ and ${}^{\boldsymbol{E}}\boldsymbol{\omega}_{\boldsymbol{r}}^{\boldsymbol{M3}}(r)$ are similar. It can be observed in this sub-section that the complexity of these quantities has been greatly reduced.

B.2.5 Partial Linear Velocities

Similar to A.2.4 the linear velocities of each point X_i in the system can be written in the form

$${}^{\boldsymbol{E}}\boldsymbol{v}^{\boldsymbol{X_i}}(\dot{q}, q, t) = \sum_{r=1}^{9} {}^{\boldsymbol{E}}\boldsymbol{v}_{\boldsymbol{r}}^{\boldsymbol{X_i}}(q,t)u_r + {}^{\boldsymbol{E}}\boldsymbol{v}_{\boldsymbol{t}}^{\boldsymbol{X_i}}(q,t) \tag{B.33}$$

where, ${}^{\boldsymbol{E}}\boldsymbol{v}_{\boldsymbol{r}}^{\boldsymbol{X_i}}(q,t)$ are the partial linear velocities. Again, the choice of generalized speeds u_r renders all the ${}^{\boldsymbol{E}}\boldsymbol{v}_{\boldsymbol{t}}^{\boldsymbol{N_i}}(q,t)$ terms as zeros as will be shown. The partial linear velocities for the tower element can be given as

$$
\begin{aligned}
{}^{E}\boldsymbol{v}_{\boldsymbol{r}}^{\boldsymbol{T}}(h) &= \begin{cases} \phi_1^{TFA}(h)\hat{\boldsymbol{a}}_{\boldsymbol{1}} & \text{for } r = TFA1 \\ \phi_1^{TSS}(h)\hat{\boldsymbol{a}}_{\boldsymbol{3}} & \text{for } r = TSS1 \\ 0 & \text{otherwise} \end{cases} \\
{}^{E}\boldsymbol{v}_{\boldsymbol{t}}^{\boldsymbol{T}}(h) &= 0
\end{aligned} \tag{B.34}
$$

The partial linear velocities for tower top

$$
\begin{aligned}
{}^{E}\boldsymbol{v}_{\boldsymbol{r}}^{\boldsymbol{O}} &= \begin{cases} \hat{\boldsymbol{a}}_{\boldsymbol{1}} & \text{for } r = TFA1 \\ \hat{\boldsymbol{a}}_{\boldsymbol{3}} & \text{for } r = TSS1 \\ 0 & \text{otherwise} \end{cases} \\
{}^{E}\boldsymbol{v}_{\boldsymbol{t}}^{\boldsymbol{O}} &= 0
\end{aligned} \tag{B.35}
$$

The partial linear velocities for nacelle center of mass is given as

$$
\begin{aligned}
{}^{E}\boldsymbol{v}_{\boldsymbol{r}}^{\boldsymbol{U}} &= {}^{E}\boldsymbol{v}_{\boldsymbol{r}}^{\boldsymbol{O}} + \begin{cases} {}^{E}\boldsymbol{\omega}_{\boldsymbol{r}}^{\boldsymbol{N}} \times \boldsymbol{r}^{\boldsymbol{OU}} & \text{for } r = 1 \text{ to } 2 \\ 0 & \text{otherwise} \end{cases} \\
{}^{E}\boldsymbol{v}_{\boldsymbol{t}}^{\boldsymbol{U}} &= 0
\end{aligned} \tag{B.36}
$$

The partial linear velocities for apex of coning angle is given as

$$
\begin{aligned}
{}^{E}\boldsymbol{v}_{\boldsymbol{r}}^{\boldsymbol{Q}} &= {}^{E}\boldsymbol{v}_{\boldsymbol{r}}^{\boldsymbol{O}} + \begin{cases} {}^{E}\boldsymbol{\omega}_{\boldsymbol{r}}^{\boldsymbol{L}} \times \boldsymbol{r}^{\boldsymbol{OQ}} & \text{for } r = 1 \text{ to } 2 \\ \hat{\boldsymbol{e}}_{\boldsymbol{1}} \times \boldsymbol{r}^{\boldsymbol{OQ}} & \text{for } GeAz \\ 0 & \text{otherwise} \end{cases} \\
{}^{E}\boldsymbol{v}_{\boldsymbol{t}}^{\boldsymbol{Q}} &= 0
\end{aligned} \tag{B.37}
$$

The partial linear velocities for hub center of mass is given as

$$
\begin{aligned}
{}^{E}\boldsymbol{v}_{\boldsymbol{r}}^{\boldsymbol{C}} &= {}^{E}\boldsymbol{v}_{\boldsymbol{r}}^{\boldsymbol{Q}} + \begin{cases} {}^{E}\boldsymbol{\omega}_{\boldsymbol{r}}^{\boldsymbol{L}} \times \boldsymbol{r}^{\boldsymbol{QC}} & \text{for } r = 1 \text{ to } 2 \\ \hat{\boldsymbol{e}}_{\boldsymbol{1}} \times \boldsymbol{r}^{\boldsymbol{QC}} & \text{for } GeAz \\ 0 & \text{otherwise} \end{cases} \\
{}^{E}\boldsymbol{v}_{\boldsymbol{t}}^{\boldsymbol{C}} &= 0
\end{aligned} \tag{B.38}
$$

The partial linear velocities for blade 1 element is given as

$$
\begin{aligned}
{}^{E}\boldsymbol{v}^{\boldsymbol{S1}}_{\boldsymbol{r}}(r) &= {}^{E}\boldsymbol{v}^{\boldsymbol{Q}}_{\boldsymbol{r}} + \begin{cases} {}^{E}\boldsymbol{\omega}^{\boldsymbol{L}}_{\boldsymbol{r}} \times \boldsymbol{r}^{\boldsymbol{QS1}} & \text{for } r = 1 \text{ to } 2 \\ \hat{\boldsymbol{e}}_{\boldsymbol{1}} \times \boldsymbol{r}^{\boldsymbol{QC}} & \text{for } GeAz \\ \phi_1^{B1F1}(r)\hat{\boldsymbol{g}}^{\boldsymbol{B1}}_{\boldsymbol{1}} + \phi_1^{B1S1}(r)\hat{\boldsymbol{g}}^{\boldsymbol{B1}}_{\boldsymbol{2}} & \text{for } r = B1F1 \\ \phi_2^{B1F1}(r)\hat{\boldsymbol{g}}^{\boldsymbol{B1F1}}_{\boldsymbol{1}} + \phi_2^{B1S1}(r)\hat{\boldsymbol{g}}^{\boldsymbol{B1}}_{\boldsymbol{2}} & \text{for } r = B1E1 \\ 0 & \text{otherwise} \end{cases} \\
{}^{E}\boldsymbol{v}^{\boldsymbol{S1}}_{\boldsymbol{t}}(r) &= 0
\end{aligned}
\tag{B.39}
$$

Equations for ${}^{E}\boldsymbol{v}^{\boldsymbol{S2}}_{\boldsymbol{t}}(r)$ and ${}^{E}\boldsymbol{v}^{\boldsymbol{S3}}_{\boldsymbol{t}}(r)$ can be obtained similarly.

B.2.6 Angular Accelerations

For every rigid body N_i in the system the angular acceleration can be written as

$$
{}^{E}\boldsymbol{\alpha}^{\boldsymbol{N_i}}(\ddot{q},\dot{q},q,t) = \sum_{r=1}^{9} {}^{E}\boldsymbol{\omega}^{\boldsymbol{N_i}}_{\boldsymbol{r}}(q,t)\ddot{q}_r + \sum_{r=1}^{9} \frac{\mathrm{d}}{\mathrm{d}t}\{{}^{E}\boldsymbol{\omega}^{\boldsymbol{N_i}}_{\boldsymbol{r}}(q,t)\}\dot{q}_r + \frac{\mathrm{d}}{\mathrm{d}t}\{{}^{E}\boldsymbol{\omega}^{\boldsymbol{N_i}}_{\boldsymbol{t}}(q,t)\} \tag{B.40}
$$

Only the terms $\dfrac{d}{dt}\{{}^{E}\boldsymbol{\omega}^{\boldsymbol{N_i}}_{\boldsymbol{r}}(q,t)\}$ to be found since the other terms are known at this stage. The partial angular acceleration terms for the platform/tower-base

$$
\begin{aligned}
&\frac{\mathrm{d}}{\mathrm{d}t}\{{}^{E}\boldsymbol{\omega}^{\boldsymbol{X}}_{\boldsymbol{r}}\} = 0 \quad \text{for all} \\
&\frac{\mathrm{d}}{\mathrm{d}t}\{{}^{E}\boldsymbol{\omega}^{\boldsymbol{X}}_{\boldsymbol{t}}\} = 0
\end{aligned}
\tag{B.41}
$$

The partial angular acceleration terms for the tower element is given as

$$
\begin{aligned}
&\frac{\mathrm{d}}{\mathrm{d}t}\{{}^{E}\boldsymbol{\omega}^{\boldsymbol{F}}_{\boldsymbol{r}}(h)\} = 0 \quad \text{for all} \\
&\frac{\mathrm{d}}{\mathrm{d}t}\{{}^{E}\boldsymbol{\omega}^{\boldsymbol{F}}_{\boldsymbol{t}}(h)\} = 0
\end{aligned}
\tag{B.42}
$$

The partial angular acceleration terms for the tower-top/base-plate is given as

$$
\begin{aligned}
&\frac{\mathrm{d}}{\mathrm{d}t}\{{}^{E}\boldsymbol{\omega}^{\boldsymbol{B}}_{\boldsymbol{r}}\} = 0 \quad \text{for all} \\
&\frac{\mathrm{d}}{\mathrm{d}t}\{{}^{E}\boldsymbol{\omega}^{\boldsymbol{B}}_{\boldsymbol{t}}\} = 0
\end{aligned}
\tag{B.43}
$$

The partial angular acceleration terms for the nacelle is given as

$$\begin{aligned}
&\frac{\mathrm{d}}{\mathrm{d}t}\{{}^{\boldsymbol{E}}\boldsymbol{\omega}_{\boldsymbol{r}}^{\boldsymbol{N}}\} = \frac{\mathrm{d}}{\mathrm{d}t}\{{}^{\boldsymbol{E}}\boldsymbol{\omega}_{\boldsymbol{r}}^{\boldsymbol{B}}\} + 0 \quad \text{for all} \\
&\frac{\mathrm{d}}{\mathrm{d}t}\{{}^{\boldsymbol{E}}\boldsymbol{\omega}_{\boldsymbol{t}}^{\boldsymbol{N}}\} = 0
\end{aligned} \tag{B.44}$$

The partial angular acceleration terms for the low speed shaft is given as

$$\begin{aligned}
&\frac{\mathrm{d}}{\mathrm{d}t}\{{}^{\boldsymbol{E}}\boldsymbol{\omega}_{\boldsymbol{r}}^{\boldsymbol{L}}\} = \frac{\mathrm{d}}{\mathrm{d}t}\{{}^{\boldsymbol{E}}\boldsymbol{\omega}_{\boldsymbol{r}}^{\boldsymbol{N}}\} + \begin{cases} {}^{\boldsymbol{E}}\boldsymbol{\omega}^{\boldsymbol{N}} \times {}^{\boldsymbol{E}}\boldsymbol{\omega}_{\boldsymbol{GeAz}}^{\boldsymbol{L}} = 0 & \text{for } r = GeAz \\ 0 & \text{otherwise} \end{cases} \\
&\frac{\mathrm{d}}{\mathrm{d}t}\{{}^{\boldsymbol{E}}\boldsymbol{\omega}_{\boldsymbol{t}}^{\boldsymbol{L}}\} = 0
\end{aligned} \tag{B.45}$$

The partial angular acceleration terms for blade element is given as

$$\begin{aligned}
&\frac{\mathrm{d}}{\mathrm{d}t}\{{}^{\boldsymbol{E}}\boldsymbol{\omega}_{\boldsymbol{r}}^{\boldsymbol{M1}}\} = \frac{\mathrm{d}}{\mathrm{d}t}\{{}^{\boldsymbol{E}}\boldsymbol{\omega}_{\boldsymbol{r}}^{\boldsymbol{L}}\} + \begin{cases} {}^{\boldsymbol{E}}\boldsymbol{\omega}^{\boldsymbol{L}} \times {}^{\boldsymbol{E}}\boldsymbol{\omega}_{\boldsymbol{B1F1}}^{\boldsymbol{M1}} = 0 & \text{for } r = B1F1 \\ {}^{\boldsymbol{E}}\boldsymbol{\omega}^{\boldsymbol{L}} \times {}^{\boldsymbol{E}}\boldsymbol{\omega}_{\boldsymbol{B1E1}}^{\boldsymbol{M1}} = 0 & \text{for } r = B1E1 \\ 0 & \text{otherwise} \end{cases} \\
&\frac{\mathrm{d}}{\mathrm{d}t}\{{}^{\boldsymbol{E}}\boldsymbol{\omega}_{\boldsymbol{t}}^{\boldsymbol{M1}}\} = 0
\end{aligned} \tag{B.46}$$

Equations for $\frac{\mathrm{d}}{\mathrm{d}t}\{{}^{\boldsymbol{E}}\boldsymbol{\omega}_{\boldsymbol{r}}^{\boldsymbol{M2}}\}$ and $\frac{\mathrm{d}}{\mathrm{d}t}\{{}^{\boldsymbol{E}}\boldsymbol{\omega}_{\boldsymbol{r}}^{\boldsymbol{M3}}\}$ can be found similarly.

B.2.7 Linear Accelerations

Linear accelerator for each point X_i in the system can be represented as

$${}^{\boldsymbol{E}}\boldsymbol{a}^{\boldsymbol{X_i}} = \sum_{r=1}^{9} {}^{\boldsymbol{E}}\boldsymbol{v}_{\boldsymbol{r}}^{\boldsymbol{X_i}}(q,t)\ddot{q}_r + \sum_{r=1}^{9} \frac{\mathrm{d}}{\mathrm{d}t}\{{}^{\boldsymbol{E}}\boldsymbol{v}_{\boldsymbol{r}}^{\boldsymbol{X_i}}(q,t)\}\dot{q}_r + \frac{\mathrm{d}}{\mathrm{d}t}\{{}^{\boldsymbol{E}}\boldsymbol{v}_{\boldsymbol{t}}^{\boldsymbol{X_i}}(q,t)\} \tag{B.47}$$

The only terms required to be found are $\frac{\mathrm{d}}{\mathrm{d}t}\{{}^{\boldsymbol{E}}\boldsymbol{v}_{\boldsymbol{r}}^{\boldsymbol{X_i}}\}$ which are vector functions of $(\dot{q}, q, t)$ and all the $\frac{\mathrm{d}}{\mathrm{d}t}\{{}^{\boldsymbol{E}}\boldsymbol{v}_{\boldsymbol{t}}^{\boldsymbol{X_i}}\}$ terms are zeros as will be shown. The partial linear acceleration terms for the tower element can be given as

$$\begin{aligned}
&\frac{\mathrm{d}}{\mathrm{d}t}\{{}^{\boldsymbol{E}}\boldsymbol{v}_{\boldsymbol{r}}^{\boldsymbol{T}}(h)\} = 0 \quad \text{for all} \\
&\frac{\mathrm{d}}{\mathrm{d}t}\{{}^{\boldsymbol{E}}\boldsymbol{v}_{\boldsymbol{t}}^{\boldsymbol{T}}(h)\} = 0
\end{aligned} \tag{B.48}$$

The partial linear acceleration terms for the tower-top/base-plate can be given as

$$\begin{aligned}
&\frac{\mathrm{d}}{\mathrm{d}t}\{{}^{\boldsymbol{E}}\boldsymbol{v}_{\boldsymbol{r}}^{\boldsymbol{O}}\} = 0 \quad \text{for all} \\
&\frac{\mathrm{d}}{\mathrm{d}t}\{{}^{\boldsymbol{E}}\boldsymbol{v}_{\boldsymbol{t}}^{\boldsymbol{T}}\} = 0
\end{aligned} \tag{B.49}$$

The partial linear acceleration terms for the nacelle center of mass given as

$$\begin{aligned}
&\frac{\mathrm{d}}{\mathrm{d}t}\{{}^{\boldsymbol{E}}\boldsymbol{v}_{\boldsymbol{r}}^{\boldsymbol{U}}\} = \frac{\mathrm{d}}{\mathrm{d}t}\{{}^{\boldsymbol{E}}\boldsymbol{v}_{\boldsymbol{r}}^{\boldsymbol{O}}\} + 0 \quad \text{for all} \\
&\frac{\mathrm{d}}{\mathrm{d}t}\{{}^{\boldsymbol{E}}\boldsymbol{v}_{\boldsymbol{t}}^{\boldsymbol{U}}\} = 0
\end{aligned} \tag{B.50}$$

The partial linear acceleration terms for the apex of coning angle are given as

$$\begin{aligned}
&\frac{\mathrm{d}}{\mathrm{d}t}\{{}^{\boldsymbol{E}}\boldsymbol{v}_{\boldsymbol{r}}^{\boldsymbol{Q}}\} = \frac{\mathrm{d}}{\mathrm{d}t}\{{}^{\boldsymbol{E}}\boldsymbol{v}_{\boldsymbol{r}}^{\boldsymbol{O}}\} + \begin{cases} 0 & r = 1 \text{ to } 2 \\ \frac{\mathrm{d}}{\mathrm{d}t}\{{}^{\boldsymbol{E}}\boldsymbol{\omega}_{\boldsymbol{r}}^{\boldsymbol{L}}\} \times \boldsymbol{r}^{\boldsymbol{OQ}} + {}^{\boldsymbol{E}}\boldsymbol{\omega}_{\boldsymbol{r}}^{\boldsymbol{L}} \times \left({}^{\boldsymbol{E}}\boldsymbol{\omega}^{\boldsymbol{L}} \times \boldsymbol{r}^{\boldsymbol{OQ}}\right) & r = GeAz \\ 0 & \text{otherwise} \end{cases} \\
&\frac{\mathrm{d}}{\mathrm{d}t}\{{}^{\boldsymbol{E}}\boldsymbol{v}_{\boldsymbol{t}}^{\boldsymbol{Q}}\} = 0
\end{aligned} \tag{B.51}$$

The partial linear acceleration terms for the hub center of mass are given as

$$\begin{aligned}
&\frac{\mathrm{d}}{\mathrm{d}t}\{{}^{\boldsymbol{E}}\boldsymbol{v}_{\boldsymbol{r}}^{\boldsymbol{C}}\} = \frac{\mathrm{d}}{\mathrm{d}t}\{{}^{\boldsymbol{E}}\boldsymbol{v}_{\boldsymbol{r}}^{\boldsymbol{Q}}\} + \begin{cases} 0 & r = 1 \text{ to } 2 \\ \frac{\mathrm{d}}{\mathrm{d}t}\{{}^{\boldsymbol{E}}\boldsymbol{\omega}_{\boldsymbol{r}}^{\boldsymbol{L}}\} \times \boldsymbol{r}^{\boldsymbol{QC}} + {}^{\boldsymbol{E}}\boldsymbol{\omega}_{\boldsymbol{r}}^{\boldsymbol{L}} \times \left({}^{\boldsymbol{E}}\boldsymbol{\omega}^{\boldsymbol{L}} \times \boldsymbol{r}^{\boldsymbol{QC}}\right) & r = GeAz \\ 0 & \text{otherwise} \end{cases} \\
&\frac{\mathrm{d}}{\mathrm{d}t}\{{}^{\boldsymbol{E}}\boldsymbol{v}_{\boldsymbol{t}}^{\boldsymbol{C}}\} = 0
\end{aligned} \tag{B.52}$$

The partial linear acceleration terms for blade 1 element are given as

$$\begin{aligned}
\frac{\mathrm{d}}{\mathrm{d}t}\{{}^{E}\boldsymbol{v}^{\boldsymbol{S1}}_{\boldsymbol{r}}(r)\} &= \frac{\mathrm{d}}{\mathrm{d}t}\{{}^{E}\boldsymbol{v}^{\boldsymbol{Q}}_{\boldsymbol{r}}\} + \begin{cases} 0 & r = 1 \text{ to } 2 \\ \frac{\mathrm{d}}{\mathrm{d}t}\{{}^{E}\boldsymbol{\omega}^{\boldsymbol{L}}_{\boldsymbol{r}}\} \times \boldsymbol{r}^{\boldsymbol{QS1}} & \\ +{}^{E}\boldsymbol{\omega}^{\boldsymbol{L}}_{\boldsymbol{r}} \times \left({}^{L}\boldsymbol{v}^{\boldsymbol{S1}}(r) + {}^{E}\boldsymbol{\omega}^{\boldsymbol{L}} \times \boldsymbol{r}^{\boldsymbol{QS1}}\right) & r = GeAz \\ {}^{E}\boldsymbol{\omega}^{\boldsymbol{L}} \times {}^{E}\boldsymbol{v}^{\boldsymbol{S1}}_{\boldsymbol{B1F1}} & r = B1F1 \\ {}^{E}\boldsymbol{\omega}^{\boldsymbol{L}} \times {}^{E}\boldsymbol{v}^{\boldsymbol{S1}}_{\boldsymbol{B1E1}} & r = B1E1 \\ 0 & \text{otherwise} \end{cases} \\
\frac{\mathrm{d}}{\mathrm{d}t}\{{}^{E}\boldsymbol{v}^{\boldsymbol{S1}}_{\boldsymbol{t}}(r)\} &= 0
\end{aligned} \tag{B.53}$$

Equations for $\frac{\mathrm{d}}{\mathrm{d}t}\{{}^{E}\boldsymbol{v}^{\boldsymbol{S1}}_{\boldsymbol{r}}(r)\}$ and $\frac{\mathrm{d}}{\mathrm{d}t}\{{}^{E}\boldsymbol{v}^{\boldsymbol{S1}}_{\boldsymbol{r}}(r)\}$ can be obtained similarly.

B.3 Kinetics of Reduced Order System

Similar to section 3.4, in this section the equations of motion for the reduced order 3-bladed wind turbine will be derived. Here, we do not need to include q_{GeAz} in generalized coordinates and equations of motion can be derived for the 8-DOFs model. Following section 3.4

$$F_r + F_r^* = 0 \quad \text{for } r = 1 \text{ to } 8 \tag{B.54}$$

where, F_r and F_r^* are the generalized active and inertia forces respectively. While the description of the terms remain same the contribution of the generator in *generalized active* and *generalized inertial* forces are neglected. Also, following from the assumptions made, the contribution of internal (elastic) forces in the low speed shaft and yaw spring and damper is neglected. Following similar steps the Kane's equations of motion can be written in matrix form as

$$[\mathbf{M}(\mathbf{q},t)]\,\{\ddot{\mathbf{q}}\} + \{\mathbf{f}(\dot{\mathbf{q}},\mathbf{q},t)\} = 0 \Rightarrow [\mathbf{M}(\mathbf{q},t)]\,\{\ddot{\mathbf{q}}\} = \{-\mathbf{f}(\dot{\mathbf{q}},\mathbf{q},t)\} \tag{B.55}$$

Tower

The distributed mass of the tower and the associated elasticity, damping and aerodynamics brings about generalized inertia and active forces associated with it. Using similar method as used for the derivation of the full order system the elements of the system matrices can be obtained as

$$
\begin{aligned}
[\mathbf{M}(\mathbf{q},t)]\Big|_{T}(k,l) &= \int_0^{TwrHt} \mu^T(h)^{\boldsymbol{E}}\boldsymbol{v}_{\boldsymbol{k}}^{\boldsymbol{T}}(h) \cdot {}^{\boldsymbol{E}}\boldsymbol{v}_{\boldsymbol{l}}^{\boldsymbol{T}}(h)\mathrm{d}h \\
&\quad + YBM.^{\boldsymbol{E}}\boldsymbol{v}_{\boldsymbol{k}}^{\boldsymbol{O}} \cdot {}^{\boldsymbol{E}}\boldsymbol{v}_{\boldsymbol{l}}^{\boldsymbol{O}} && \text{for } k,l = 1 \text{ to } 2 \\
&= 0 && \text{otherwise} \\
\{-\mathbf{f}(\dot{\mathbf{q}},\mathbf{q},t)\}\Big|_{T}(k) &= -\int_0^{TwrHt} \mu^T(h)^{\boldsymbol{E}}\boldsymbol{v}_{\boldsymbol{k}}^{\boldsymbol{T}}(h) \cdot \Big(\sum_{i=1}^{2} \frac{\mathrm{d}}{\mathrm{d}t}\{^{\boldsymbol{E}}\boldsymbol{v}_{\boldsymbol{i}}^{\boldsymbol{T}}(h)\}\dot{q}_i\Big)\mathrm{d}h \\
&\quad - YBM.^{\boldsymbol{E}}\boldsymbol{v}_{\boldsymbol{k}}^{\boldsymbol{O}} \cdot \Big(\sum_{i=1}^{2} \frac{\mathrm{d}}{\mathrm{d}t}\{^{\boldsymbol{E}}\boldsymbol{v}_{\boldsymbol{i}}^{\boldsymbol{O}}\}\dot{q}_i\Big) && \text{for } k = 1 \text{ to } 2 \\
&= 0 && \text{otherwise}
\end{aligned} \tag{B.56}
$$

where, the indices k, l are used to denote the row and column respectively of the matrix. Generalized active forces arise from the elasticity and damping of the flexible members. The generalized elastic forces can be obtained from the potential energy stored in the member as

$$
F_r\Big|_{ElasticT} = \frac{\partial V^T}{\partial q_r} \quad \text{for } r = 1 \text{ to } 8 \tag{B.57}
$$

$$
\{-\mathbf{f}(\dot{\mathbf{q}},\mathbf{q},t)\}\Big|_{T}(k) = \begin{cases} -k_{11}^{TFA} q_{TFA1} & \text{for } k = 1 \\ -k_{11}^{TSS} q_{TSS1} & \text{for } k = 2 \\ 0 & \text{otherwise} \end{cases} \tag{B.58}
$$

where, k_{11}^{TFA} and k_{11}^{TSS} are the generalized stiffness of the tower in the fore-aft and side-to-side directions respectively when gravitational de-stiffening effects are not included

$$
\begin{aligned}
k_{11}^{TFA} &= \int_0^{TwrHt} EI^{TFA}(h)\frac{\mathrm{d}^2\phi_1^{TFA}}{\mathrm{d}h^2}\frac{\mathrm{d}^2\phi_1^{TFA}}{\mathrm{d}h^2}\mathrm{d}h \\
k_{11}^{TSS} &= \int_0^{TwrHt} EI^{TSS}(h)\frac{\mathrm{d}^2\phi_1^{TSS}}{\mathrm{d}h^2}\frac{\mathrm{d}^2\phi_1^{TSS}}{\mathrm{d}h^2}\mathrm{d}h
\end{aligned} \tag{B.59}
$$

Using Rayleigh damping technique where the damping is assumed proportional to the stiffness, the generalized active forces arising from the damping in the member can be obtained as

$$\{-\mathbf{f}(\dot{\mathbf{q}},\mathbf{q},t)\}\Big|_{T}(k) = \begin{cases} -\frac{\zeta_1^{TFA}k_{11}^{TFA}}{\pi f_1^{TFA}}\dot{q}_{TFA1} & \text{for } r=k=1 \\ -\frac{\zeta_1^{TSS}k_{11}^{TSS}}{\pi f_1^{TSS}}\dot{q}_{TSS1} & \text{for } r=k=2 \\ 0 & \text{otherwise} \end{cases} \tag{B.60}$$

where ζ_1^{TFA} and ζ_1^{TSS} represents the structural damping ratio of the tower for the 1^{st} mode in the fore-aft and side-to-side direction respectively. And, f_1^{TFA} and f_1^{TSS} represent the natural frequency of the tower for the 1^{st} mode of the tower in the fore-aft and side-to-side directions respectively without the tower-top mass or gravitational de-stiffening effects.

$$\begin{aligned} f_1^{TFA} &= \frac{1}{2\pi}\sqrt{\frac{k_{11}^{TFA}}{m_{11}^{TFA}}} \\ f_1^{TSS} &= \frac{1}{2\pi}\sqrt{\frac{k_{11}^{TSS}}{m_{11}^{TSS}}} \end{aligned} \tag{B.61}$$

where, m_{11}^{TFA} and m_{11}^{TSS} represents the generalized mass of the tower for 1^{st} mode in fore-aft and side-to-side directions respectively without tower-top mass as follows

$$\begin{aligned} m_{11}^{TFA} &= \int_0^{TwrHt} \mu^T(h)\phi_1^{TFA}(h)\phi_1^{TFA}(h)dh \\ m_{11}^{TSS} &= \int_0^{TwrHt} \mu^T(h)\phi_1^{TSS}(h)\phi_1^{TSS}(h)dh \end{aligned} \tag{B.62}$$

Generalized active force arising from gravity acting on the tower is given by

$$F_r\Big|_{GravT} = \int_0^{TwrHt} {}^{\boldsymbol{E}}\boldsymbol{v}_{\boldsymbol{r}}^{\boldsymbol{T}}(h)\cdot\{-\mu_T(h)g\hat{\boldsymbol{z}}_{\boldsymbol{2}}\}\,\mathrm{d}h - YBM.g.{}^{\boldsymbol{E}}\boldsymbol{v}_{\boldsymbol{r}}^{\boldsymbol{O}}\cdot\hat{\boldsymbol{z}}_{\boldsymbol{2}} \quad \text{for } r=1 \text{ to } 2 \tag{B.63}$$

Thus, the system matrices are

$$\begin{aligned} [\mathbf{M}(\mathbf{q},t)]\Big|_{GravT}(k,l) &= 0 && \forall\ k,l \\ \{-\mathbf{f}(\dot{\mathbf{q}},\mathbf{q},t)\}\Big|_{GravT}(k) &= -\int_0^{TwrHt} {}^{\boldsymbol{E}}\boldsymbol{v}_{\boldsymbol{k}}^{\boldsymbol{T}}(h)\cdot\{\mu_T(h)g\hat{\boldsymbol{z}}_{\boldsymbol{2}}\}\,dh \\ &\quad - YBM.g.{}^{\boldsymbol{E}}\boldsymbol{v}_{\boldsymbol{k}}^{\boldsymbol{O}}\cdot\hat{\boldsymbol{z}}_{\boldsymbol{2}} && \text{for } k=1 \text{ to } 2 \\ &= 0 && \text{otherwise} \end{aligned} \tag{B.64}$$

Generalized active forces due to aerodynamic loads on the tower can be given as

$$F_r\Big|_{AeroT} = \int_0^{TwrHt} \left[{}^{\boldsymbol{E}}\boldsymbol{v}_{\boldsymbol{r}}^{\boldsymbol{T}}(h) \cdot \boldsymbol{F}_{\boldsymbol{AeroT}}^{\boldsymbol{T}}(h) + {}^{\boldsymbol{E}}\boldsymbol{\omega}_{\boldsymbol{r}}^{\boldsymbol{F}}(h) \cdot \boldsymbol{M}_{\boldsymbol{AeroT}}^{\boldsymbol{F}}(h)\right] \mathrm{d}h \quad \text{for } r = 1 \text{ to } 2 \tag{B.65}$$

where, $\boldsymbol{F}_{\boldsymbol{AeroT}}^{\boldsymbol{T}}(h)$ and $\boldsymbol{M}_{\boldsymbol{AeroT}}^{\boldsymbol{F}}(h)$ are aerodynamic forces and moments applied on the tower expressed per unit length. Thus,

$$\begin{aligned}
[\mathbf{M}(\mathbf{q},t)]\Big|_{AeroT}(k,l) &= 0 && \forall\ k,l \\
\{-\mathbf{f}(\dot{\mathbf{q}},\mathbf{q},t)\}\Big|_{GravT}(k) &= \int_0^{TwrHt} \left[{}^{\boldsymbol{E}}\boldsymbol{v}_{\boldsymbol{r}}^{\boldsymbol{T}}(h) \cdot \boldsymbol{F}_{\boldsymbol{AeroT}}^{\boldsymbol{T}}(h)\right. \\
&\quad \left. + {}^{\boldsymbol{E}}\boldsymbol{\omega}_{\boldsymbol{r}}^{\boldsymbol{F}}(h) \cdot \boldsymbol{M}_{\boldsymbol{AeroT}}^{\boldsymbol{F}}(h)\right] \mathrm{d}h && \text{for } k = 1 \text{ to } 2 \\
&= 0 && \text{otherwise}
\end{aligned} \tag{B.66}$$

Nacelle

The rigid lump mass of the nacelle brings about generalized inertia forces and generalized active forces associated with nacelle weight. The generalized inertia forces can be obtained as

$$\begin{aligned}
F_r^*\Big|_N = {}^{\boldsymbol{E}}\boldsymbol{v}_{\boldsymbol{r}}^{\boldsymbol{U}} \cdot &\left[-m^N \left\{\left(\sum_{i=1}^{2} {}^{\boldsymbol{E}}\boldsymbol{v}_{\boldsymbol{i}}^{\boldsymbol{U}} \dot{q}_i\right) + \left(\sum_{i=1}^{2} \frac{\mathrm{d}}{\mathrm{d}t}({}^{\boldsymbol{E}}\boldsymbol{v}_{\boldsymbol{i}}^{\boldsymbol{U}})\dot{q}_i\right)\right\}\right] \\
+ {}^{\boldsymbol{E}}\boldsymbol{\omega}_{\boldsymbol{r}}^{\boldsymbol{N}} &\left[- \bar{\bar{\boldsymbol{I}}}^{\boldsymbol{N}} \cdot \left\{\left(\sum_{i=1}^{2} {}^{\boldsymbol{E}}\boldsymbol{\omega}_{\boldsymbol{i}}^{\boldsymbol{N}} \ddot{q}_i\right) + \left(\sum_{i=1}^{2} \frac{\mathrm{d}}{\mathrm{d}t}({}^{\boldsymbol{E}}\boldsymbol{\omega}_{\boldsymbol{i}}^{\boldsymbol{N}})\dot{q}_i\right)\right\}\right. \\
&\left. - {}^{\boldsymbol{E}}\boldsymbol{\omega}^{\boldsymbol{N}} \times \bar{\bar{\boldsymbol{I}}}^{\boldsymbol{N}} \cdot {}^{\boldsymbol{E}}\boldsymbol{\omega}^{\boldsymbol{N}}\right] \qquad \text{for } r = 1 \text{ to } 8
\end{aligned} \tag{B.67}$$

Thus,

$$
\begin{aligned}
[\mathbf{M}(\mathbf{q},t)]\Big|_N(k,l) &= m^N \, {}^{\boldsymbol{E}}\boldsymbol{v}_{\boldsymbol{k}}^{\boldsymbol{U}} \cdot {}^{\boldsymbol{E}}\boldsymbol{v}_{\boldsymbol{l}}^{\boldsymbol{U}} + {}^{\boldsymbol{E}}\boldsymbol{\omega}_{\boldsymbol{k}}^{\boldsymbol{N}} \cdot \bar{\bar{\boldsymbol{I}}}^{\boldsymbol{N}} \cdot {}^{\boldsymbol{E}}\boldsymbol{\omega}_{\boldsymbol{l}}^{\boldsymbol{N}} \quad && \text{for } k,l = 1 \text{ to } 5 \\
&= 0 && \text{otherwise} \\
\{-\mathbf{f}(\dot{\mathbf{q}},\mathbf{q},t)\}\Big|_N(k) &= -m^N \, {}^{\boldsymbol{E}}\boldsymbol{v}_{\boldsymbol{k}}^{\boldsymbol{U}} \cdot \sum_{i=1}^{2} \frac{\mathrm{d}}{\mathrm{d}t}({}^{\boldsymbol{E}}\boldsymbol{v}_{\boldsymbol{i}}^{\boldsymbol{U}})\dot{q}_i \\
&\quad - {}^{\boldsymbol{E}}\boldsymbol{\omega}_{\boldsymbol{k}}^{\boldsymbol{N}} \cdot \Bigg[- \bar{\bar{\boldsymbol{I}}}^{\boldsymbol{N}} \cdot \Bigg\{ \sum_{i=1}^{2} \frac{\mathrm{d}}{\mathrm{d}t}({}^{\boldsymbol{E}}\boldsymbol{\omega}_{\boldsymbol{i}}^{\boldsymbol{N}})\dot{q}_i \Bigg\} \\
&\quad - {}^{\boldsymbol{E}}\boldsymbol{\omega}^{\boldsymbol{N}} \times \bar{\bar{\boldsymbol{I}}}^{\boldsymbol{N}} \cdot {}^{\boldsymbol{E}}\boldsymbol{\omega}^{\boldsymbol{N}} \Bigg] && \text{for } k = 1 \text{ to } 2 \\
&= 0 && \text{otherwise}
\end{aligned}
\tag{B.68}
$$

The generalized active force brought about by the gravitational force is given as

$$
F_r\Big|_N = {}^{\boldsymbol{E}}\boldsymbol{v}_{\boldsymbol{r}}^{\boldsymbol{U}} \cdot \left(-m^N g \hat{\boldsymbol{z}}_{\boldsymbol{2}}\right) \qquad \text{for } r = 1 \text{ to } 2 \tag{B.69}
$$

Thus, the system matrices are

$$
\begin{aligned}
[\mathbf{M}(\mathbf{q},t)]\Big|_{GravN}(k,l) &= 0 && \forall\ k,l \\
\{-\mathbf{f}(\dot{\mathbf{q}},\mathbf{q},t)\}\Big|_{GravN}(k) &= {}^{\boldsymbol{E}}\boldsymbol{v}_{\boldsymbol{k}}^{\boldsymbol{U}} \cdot \left(-m^N g \hat{\boldsymbol{z}}_{\boldsymbol{2}}\right) \quad && \text{for } k = 1 \text{ to } 2 \\
&= 0 && \text{otherwise}
\end{aligned}
\tag{B.70}
$$

Hub

The rigid lump mass of the hub brings about generalized inertia forces and generalized active forces associated with the hub weight. Generalized inertia forces are given as

$$
\begin{aligned}
F_r^*\Big|_H &= {}^{\boldsymbol{E}}\boldsymbol{v}_{\boldsymbol{r}}^{\boldsymbol{C}} \cdot \Bigg[-m^H \Bigg\{ \Bigg(\sum_{i=1}^{3} {}^{\boldsymbol{E}}\boldsymbol{v}_{\boldsymbol{i}}^{\boldsymbol{C}} \ddot{q}_i \Bigg) + \Bigg(\sum_{i=1}^{3} \frac{\mathrm{d}}{\mathrm{d}t}({}^{\boldsymbol{E}}\boldsymbol{v}_{\boldsymbol{i}}^{\boldsymbol{C}})\dot{q}_i \Bigg) \Bigg\} \Bigg] \\
&\quad + {}^{\boldsymbol{E}}\boldsymbol{\omega}_{\boldsymbol{r}}^{\boldsymbol{H}} \Bigg[- \bar{\bar{\boldsymbol{I}}}^{\boldsymbol{H}} \cdot \Bigg\{ \Bigg(\sum_{i=1}^{3} {}^{\boldsymbol{E}}\boldsymbol{\omega}_{\boldsymbol{i}}^{\boldsymbol{H}} \ddot{q}_i \Bigg) + \Bigg(\sum_{i=1}^{3} \frac{\mathrm{d}}{\mathrm{d}t}({}^{\boldsymbol{E}}\boldsymbol{\omega}_{\boldsymbol{i}}^{\boldsymbol{H}})\dot{q}_i \Bigg) \Bigg\} \\
&\quad - {}^{\boldsymbol{E}}\boldsymbol{\omega}^{\boldsymbol{H}} \times \bar{\bar{\boldsymbol{I}}}^{\boldsymbol{H}} \cdot {}^{\boldsymbol{E}}\boldsymbol{\omega}^{\boldsymbol{H}} \Bigg] \qquad \text{for } r = 1 \text{ to } 2
\end{aligned}
\tag{B.71}
$$

Thus,

$$
\begin{aligned}
[\mathbf{M}(\mathbf{q},t)]\Big|_{H}(k,l) &= m^{N}\,{}^{\boldsymbol{E}}\boldsymbol{v}_{\boldsymbol{k}}^{\boldsymbol{C}} \cdot {}^{\boldsymbol{E}}\boldsymbol{v}_{\boldsymbol{l}}^{\boldsymbol{C}} + {}^{\boldsymbol{E}}\boldsymbol{\omega}_{\boldsymbol{k}}^{\boldsymbol{H}} \cdot \bar{\bar{\boldsymbol{I}}}^{\boldsymbol{H}} \cdot {}^{\boldsymbol{E}}\boldsymbol{\omega}_{\boldsymbol{l}}^{\boldsymbol{H}} && \text{for } k,l = 1 \text{ to } 2 \\
&= 0 && \text{otherwise} \\
\{-\mathbf{f}(\dot{\mathbf{q}},\mathbf{q},t)\}\Big|_{H}(k) &= -m^{H}\,{}^{\boldsymbol{E}}\boldsymbol{v}_{\boldsymbol{k}}^{\boldsymbol{C}} \cdot \sum_{i=1}^{3} \frac{\mathrm{d}}{\mathrm{d}t}({}^{\boldsymbol{E}}\boldsymbol{v}_{\boldsymbol{i}}^{\boldsymbol{C}})\dot{q}_i \\
&\quad - {}^{\boldsymbol{E}}\boldsymbol{\omega}_{\boldsymbol{k}}^{\boldsymbol{H}} \cdot \Bigg[-\bar{\bar{\boldsymbol{I}}}^{\boldsymbol{H}} \cdot \left\{ \sum_{i=1}^{3} \frac{\mathrm{d}}{\mathrm{d}t}({}^{\boldsymbol{E}}\boldsymbol{\omega}_{\boldsymbol{i}}^{\boldsymbol{H}})\dot{q}_i \right\} \\
&\quad - {}^{\boldsymbol{E}}\boldsymbol{\omega}^{\boldsymbol{H}} \times \bar{\bar{\boldsymbol{I}}}^{\boldsymbol{H}} \cdot {}^{\boldsymbol{E}}\boldsymbol{\omega}^{\boldsymbol{H}} \Bigg] && \text{for } k = 1 \text{ to } 2 \\
&= 0 && \text{otherwise}
\end{aligned}
\tag{B.72}
$$

The generalized active force brought about by the gravitational force is given as

$$
F_r\Big|_{H} = {}^{\boldsymbol{E}}\boldsymbol{v}_{\boldsymbol{r}}^{\boldsymbol{C}} \cdot \left(-m^{H} g \hat{\boldsymbol{z}}_{\boldsymbol{2}}\right) \qquad \text{for } r = 1 \text{ to } 2 \tag{B.73}
$$

Thus,

$$
\begin{aligned}
[\mathbf{M}(\mathbf{q},t)]\Big|_{GravH}(k,l) &= 0 && \forall\ k,l \\
\{-\mathbf{f}(\dot{\mathbf{q}},\mathbf{q},t)\}\Big|_{GravH}(k) &= {}^{\boldsymbol{E}}\boldsymbol{v}_{\boldsymbol{k}}^{\boldsymbol{C}} \cdot \left(-m^{H} g \hat{\boldsymbol{z}}_{\boldsymbol{2}}\right) && \text{for } k = 1 \text{ to } 2 \\
&= 0 && \text{otherwise}
\end{aligned}
\tag{B.74}
$$

Blades

The distributed properties of blade 1 brings about generalized inertia forces and generalized active forces associated with blade elasticity, damping, weight and aerodynamic loads. Generalized inertia forces can be given as

$$
F_r^*\Big|_{B1} = -\int_0^{BldLen} \mu^{B1}(r)\,{}^{\boldsymbol{E}}\boldsymbol{v}_{\boldsymbol{r}}^{\boldsymbol{S1}}(r) \cdot \left[\sum_{i=1}^{5} {}^{\boldsymbol{E}}\boldsymbol{v}_{\boldsymbol{i}}^{\boldsymbol{S1}}(r)\ddot{q}_i + \sum_{i=1}^{5} \frac{\mathrm{d}}{\mathrm{d}t}\{{}^{\boldsymbol{E}}\boldsymbol{v}_{\boldsymbol{i}}^{\boldsymbol{S1}}(r)\}\dot{q}_i \right] \mathrm{d}r \qquad \text{for } r = 1 \text{ to } 8 \tag{B.75}
$$

Thus, the elements of the system matrices can be found as

$$
\begin{aligned}
[\mathbf{M}(\mathbf{q},t)]\Big|_{B1}(k,l) &= \int_0^{BldLen} \mu^{B1}(r)\,{}^{\boldsymbol{E}}\boldsymbol{v}_{\boldsymbol{k}}^{\boldsymbol{S1}}(r)\cdot{}^{\boldsymbol{E}}\boldsymbol{v}_{\boldsymbol{l}}^{\boldsymbol{S1}}(r)\mathrm{d}r \quad \text{for } k,l=1 \text{ to } 4\\
&= 0 \quad \text{otherwise}\\
\{-\mathbf{f}(\dot{\mathbf{q}},\mathbf{q},t)\}\Big|_{B1}(k) &= -\int_0^{BldLen} \mu^{B1}(r)\,{}^{\boldsymbol{E}}\boldsymbol{v}_{\boldsymbol{k}}^{\boldsymbol{S1}}(r)\\
&\cdot\Big(\sum_{i=1}^{5}\frac{\mathrm{d}}{\mathrm{d}t}\{{}^{\boldsymbol{E}}\boldsymbol{v}_{\boldsymbol{i}}^{\boldsymbol{S1}}(r)\}\dot{q}_i\Big)\mathrm{d}r \quad \text{for } k=1 \text{ to } 4\\
&= 0 \quad \text{otherwise}
\end{aligned}
\tag{B.76}
$$

The generalized elastic forces can be obtained from the potential energy stored in the member as

$$
F_r\Big|_{ElasticB1} = \frac{\partial V^{B1}}{\partial q_r} \quad \text{for } r=1 \text{ to } 8 \tag{B.77}
$$

$$
\{-\mathbf{f}(\dot{\mathbf{q}},\mathbf{q},t)\}\Big|_{ElasticB1}(k) = \begin{cases} -k_{11}^{B1F}q_{B1F1} & \text{for } k=3\\ -k_{11}^{B1E}q_{B1E1} & \text{for } k=4\\ 0 & \text{otherwise}\end{cases} \tag{B.78}
$$

where, k_{11}^{B1F} and k_{11}^{B1E} are the generalized stiffness of the blade in the local flapwise and edgewise directions respectively when gravitational de-stiffening and centrifugal stiffening effects are not included

$$
\begin{aligned}
k_{11}^{B1F} &= \int_0^{BldLen} EI^{B1F}(r)\left[\frac{\mathrm{d}^2\phi_1^{B1F}(r)}{\mathrm{d}r^2}\right]^2\mathrm{d}r\\
k_{11}^{B1E} &= \int_0^{BldLen} EI^{B1E}(r)\left[\frac{\mathrm{d}^2\phi_1^{B1E}(r)}{\mathrm{d}r^2}\right]^2\mathrm{d}r
\end{aligned}
\tag{B.79}
$$

Using Rayleigh damping technique where the damping is assumed proportional to the stiffness the generalized active forces arising from the damping in the member can be obtained as

$$
\{-\mathbf{f}(\dot{\mathbf{q}},\mathbf{q},t)\}\Big|_{DampB1}(k) = \begin{cases} -\frac{\zeta_1^{B1F}k_{11}^{B1F}}{\pi f_1^{B1F}}\dot{q}_{B1F1} & \text{for } k=3\\ -\frac{\zeta_1^{B1E}k_{11}^{B1E}}{\pi f_1^{B1E}}\dot{q}_{B1E1} & \text{for } k=4\\ 0 & \text{otherwise}\end{cases} \tag{B.80}
$$

where ζ_1^{B1F} and ζ_1^{B1E} represents the structural damping ratio of the blade for the first mode in the flapwise and edgewise directions respectively. And, f_1^{B1F} and f_1^{B1E} represent the natural frequency of the blade for the first mode in the flapwise and edgewise directions respectively without the centrifugal stiffening or gravitational de-stiffening effects.

$$\begin{aligned} f_1^{B1F} &= \frac{1}{2\pi}\sqrt{\frac{k_{11}^{B1F}}{m_{11}^{B1F}}} \\ f_1^{B1E} &= \frac{1}{2\pi}\sqrt{\frac{k_{11}^{B1E}}{m_{11}^{B1E}}} \end{aligned} \tag{B.81}$$

where, m_{11}^{TFA} and m_{11}^{TSS} represents the generalized mass of the blade for first mode in flapwise and edgewise directions respectively as follows

$$\begin{aligned} m_{11}^{B1F} &= \int_0^{BldLen} \mu^{B1}(r)\left[\phi_1^{B1F}(r)\right]^2 \mathrm{d}r \\ m_{11}^{B1E} &= \int_0^{BldLen} \mu^{B1}(r)\left[\phi_1^{B1E}(r)\right]^2 \mathrm{d}r \end{aligned} \tag{B.82}$$

Generalized active force arising from gravity acting on the blade is given by

$$F_r\Big|_{GravB1} = \int_0^{BldLen} {}^{\boldsymbol{E}}\boldsymbol{v}_{\boldsymbol{r}}^{\boldsymbol{S1}}(r)\cdot\{-\mu_{B1}(r)g\hat{\boldsymbol{z}}_{\boldsymbol{2}}\}\,\mathrm{d}r \quad \text{for } r = 1 \text{ to } 8 \tag{B.83}$$

Thus,

$$\begin{aligned} [\mathbf{M}(\mathbf{q},t)]\Big|_{GravB1}(k,l) &= 0 && \forall\, k,l \\ \{-\mathbf{f}(\dot{\mathbf{q}},\mathbf{q},t)\}\Big|_{GravB1}(k) &= -\int_0^{BldLen} {}^{\boldsymbol{E}}\boldsymbol{v}_{\boldsymbol{k}}^{\boldsymbol{S1}}(r)\cdot\{\mu_{B1}(r)g\hat{\boldsymbol{z}}_{\boldsymbol{2}}\}\,dh && \text{for } k = 1 \text{ to } 8 \\ &= 0 && \text{otherwise} \end{aligned} \tag{B.84}$$

Generalized active forces due to aerodynamic loads on the blade can be given as

$$\begin{aligned} F_r\Big|_{AeroB1} = \int_0^{BldLen} &\left[{}^{\boldsymbol{E}}\boldsymbol{v}_{\boldsymbol{r}}^{\boldsymbol{S1}}(r)\boldsymbol{\cdot}\boldsymbol{F}_{\boldsymbol{AeroB1}}^{\boldsymbol{S1}}(r) + {}^{\boldsymbol{E}}\boldsymbol{\omega}_{\boldsymbol{r}}^{\boldsymbol{M1}}(r)\boldsymbol{\cdot}\boldsymbol{M}_{\boldsymbol{AeroB1}}^{\boldsymbol{M1}}(r)\right]\mathrm{d}r \\ &\text{for } r = 1 \text{ to } 8 \end{aligned} \tag{B.85}$$

where, $\boldsymbol{F}_{\boldsymbol{AeroB1}}^{\boldsymbol{S1}}(r)$ and $\boldsymbol{M}_{\boldsymbol{AeroB1}}^{\boldsymbol{M1}}(r)$ are aerodynamic forces and pitching moments applied on the point $S1$ on the blade receptively expressed per unit length. $\boldsymbol{M}_{\boldsymbol{AeroB1}}^{\boldsymbol{M1}}(r)$

can include effect of both direct aerodynamic pitching moments (i.e. C_m) and aerodynamic pitching moments caused by an aerodynamic offset (i.e. moments due to aerodynamic lift and drag acting at a distance away from the center of mass of the blade element along the aerodynamic cord) Thus,

$$\begin{aligned}
[\mathbf{M}(\mathbf{q},t)]\Big|_{AeroB1}(k,l) &= 0 && \forall\ k,l \\
\{-\mathbf{f}(\dot{\mathbf{q}},\mathbf{q},t)\}\Big|_{AeroB1}(k) &= \int_0^{BldLen} \Big[{}^{\boldsymbol{E}}\boldsymbol{v}_{\boldsymbol{r}}^{\boldsymbol{S1}}(r)\cdot \boldsymbol{F}_{\boldsymbol{AeroB1}}^{\boldsymbol{S1}}(r) \\
&\qquad + {}^{\boldsymbol{E}}\boldsymbol{\omega}_{\boldsymbol{r}}^{\boldsymbol{M1}}(r)\cdot \boldsymbol{M}_{\boldsymbol{AeroB1}}^{\boldsymbol{M1}}(r)\Big]\, dr && \text{for } k=1 \text{ to } 8 \\
&= 0 && \text{otherwise}
\end{aligned} \tag{B.86}$$

Similar to blade 1, the distributed properties of blade 2 and blade 3 bring about generalized inertia forces and generalized active forces associated with blade elasticity, blade damping, blade weight, and aerodynamic loads. The equations for $F_r^*\Big|_{B2}$, $F_r^*\Big|_{B3}$, $F_r\Big|_{ElasticB2}$, $F_r\Big|_{ElasticB3}$, $F_r\Big|_{DampB2}$, $F_r\Big|_{DampB3}$, $F_r\Big|_{GravB2}$, $F_r\Big|_{GravB3}$, $F_r\Big|_{AeroB2}$ and $F_r\Big|_{AeroB3}$ can be found similarly.

Equations of Motion & Ad-hoc requirements

The equations of motion obtained from the previous sub section is in the form

$$[\mathbf{M}(\mathbf{q},t)]\,\{\ddot{\mathbf{q}}\} + \{\mathbf{f}(\dot{\mathbf{q}},\mathbf{q},t)\} = 0 \tag{B.87}$$

which can be easily rearranged to be written down in the form in second order form because the equations of motion are vastly simplified by the assumptions made. This form is useful in many types of dynamic analysis and control problem. One particular topic of interest is the effect of centrifugal stiffening of the blades and the gravitational stiffening/softening effect on the blades and the tower. Since, axial deflection was neglected in the formulation, the above effects were not included in the formulation inherently. Ad-hoc provisions are often made in literature to cater for these requirements. Since the tower is much stiffer than the blades and the lateral deflections are as significant, the gravitational stiffening/softening effects are neglected for the tower. Let, the lateral deflection of the blades in out-of-plane and in-plane directions be denoted by u and v respectively. Then, the axial deflection denoted by w can be obtained as

$$
\begin{aligned}
w(r,t) &= \frac{1}{2}\int_0^r \left[\frac{\partial u(r',t)}{\partial r'}\right]^2 \mathrm{d}r' + \frac{1}{2}\int_0^r \left[\frac{\partial v(r',t)}{\partial r'}\right]^2 \mathrm{d}r' \\
&= \frac{1}{2}\int_0^r \left[\frac{\partial \phi_1 B1F(r',t)}{\partial r'}\right]^2 \mathrm{d}r' q_{B1F1}^2 + \frac{1}{2}\int_0^r \left[\frac{\partial \phi_1 B1E(r',t)}{\partial r'}\right]^2 \mathrm{d}r' q_{B1E1}^2
\end{aligned}
\tag{B.88}
$$

Potential energy due to the rotation of the blades

$$
V_{rotation} = \Omega^2 \left[\int_0^{R-R_H} \mu_B(r)(R_H + r) w(r,t)\mathrm{d}r\right] \tag{B.89}
$$

Where, Ω is the constant rotational speed of the wind turbine. Thus, the generalized active force is given as

$$
F_r = \frac{\partial V_{rotation}}{\partial q_r} \tag{B.90}
$$

$$
\begin{aligned}
&\{-\mathbf{f}(\dot{\mathbf{q}},\mathbf{q},t)\}\Big|_{CentrfB1}(k) = \\
&\begin{cases}
-\Omega^2 \left[\int_0^{R-R_H} \mu_B(r)(R_H+r)\int_0^r \left[\frac{\partial \phi_1 B1F(r',t)}{\partial r'}\right]^2 \mathrm{d}r'\mathrm{d}r\right] q_{B1F1} & k=3 \\
-\Omega^2 \left[\int_0^{R-R_H} \mu_B(r)(R_H+r)\int_0^r \left[\frac{\partial \phi_1 B1E(r',t)}{\partial r'}\right]^2 \mathrm{d}r'\mathrm{d}r\right] q_{B1E1} & k=4 \\
0 & \text{otherwise}
\end{cases}
\end{aligned}
\tag{B.91}
$$

Similarly, the potential energy due to gravitational force acting of the blades can be given as

$$
V_{GravB1} = -g\left[\int_0^{R-R_H} \mu_B(r) w(r,t)\mathrm{d}r\right]\cos(q_{GeAz}) \tag{B.92}
$$

Hence, the generalized active forces can be given as

$$
\begin{aligned}
&\{-\mathbf{f}(\dot{\mathbf{q}},\mathbf{q},t)\}\Big|_{GravB1}(k) = \\
&\begin{cases}
-g\cos(q_{GeAz}) \left[\int_0^{R-R_H} \mu_B(r)\int_0^r \left[\frac{\partial \phi_1 B1F(r',t)}{\partial r'}\right]^2 \mathrm{d}r'\mathrm{d}r\right] q_{B1F1} & k=3 \\
-g\cos(q_{GeAz}) \left[\int_0^{R-R_H} \mu_B(r)\int_0^r \left[\frac{\partial \phi_1 B1E(r',t)}{\partial r'}\right]^2 drr'\mathrm{d}r\right] q_{B1E1} & k=4 \\
0 & \text{otherwise}
\end{cases}
\end{aligned}
\tag{B.93}
$$

Once these terms are included in the equations of the motion, the resulting set of equations match completely with those widely available in literature.

Appendix C

Equations of motion of the reduced order model

The linearised equations of motion of the 6 degree of freedom system is described in this section. To derive the equations of motion first it is assumed that the wind turbine is rotating at a constant speed. Hence, the generator speed error is basically zero and it is not a degree of freedom. The equations of motion of the 5 degree of freedom system is then augmented by the generator speed error degree of freedom to obtain the final 6 degree of freedom system. Understandably, the generator speed error degree of freedom is decoupled from the rest of the system. This approach is undertaken since the inclusion of the generator speed error as a degree of freedom introduces non-linearities in the form of cosine and sine terms which cannot be linearised using small angle approximation. We first look at the generator speed error degree of freedom

$$\begin{aligned} \dot{q}_{\varepsilon} &= \delta\Omega = \Omega_0 - q_{GeAz} \\ q_{\varepsilon} &= \int_0^t \dot{q}_{\varepsilon} dt = \int_0^t (\Omega_0 - q_{GeAz}) dt \\ \ddot{q}_{\varepsilon} &= \delta\dot{\Omega} = \ddot{q}_{GeAz} \end{aligned} \tag{C.1}$$

Where, Ω_0 is the rated rated rotor speed of the FOWT. The equation of motion of this degree of freedom assuming only intergal action K_I can be obtained from (Jonkman, 2007) as

$$I_{DT}\ddot{q}_{\varepsilon} + \left(-\frac{P_0}{\Omega_0^2}\right)\dot{q}_{\varepsilon} + \frac{1}{\Omega_0}\left(-\frac{\partial P_0}{\partial \theta}\right) N_{Gear} K_I q_{\varepsilon} = 0 \tag{C.2}$$

Where, $I_{DT} = I_{Rotor} + N_{Gear}^2 I_{Gen}$ is the drive-train inertia cast into the low speed shaft, I_{Rotor} is the inertia of the rotor, I_{Gen} is the inertia of the generator relative to the high speed shaft, N_{Gear} is the gear box ratio. P_0 is the rated mechanical power. As recommended by (Jonkman, 2010) the integral gain K_I is selected such that the frequency of this degree of freedom is 0.2 rad/s. Therefore, the stiffness term can be written as

$$\frac{1}{\Omega_0}\left(-\frac{\partial P_0}{\partial \theta}\right) N_{Gear} K_I = 0.2^2 I_{DT} = k_{\varepsilon\varepsilon} \tag{C.3}$$

The mass, stiffness and damping matrix of the linearised six degree of freedom system are obtained as

$$\mathbf{M} = \begin{bmatrix} m_{PP} & m_{PT} & m_{PB1} & m_{PB2} & m_{PB3} & 0 \\ & m_{TT} & m_{TB1} & m_{TB2} & m_{TB3} & 0 \\ & & m_{BB} & 0 & 0 & 0 \\ & & & m_{BB} & 0 & 0 \\ & sym & & & m_{BB} & 0 \\ & & & & 0 & I_{DT} \end{bmatrix} \tag{C.4}$$

$$\mathbf{C} = \begin{bmatrix} c_{PP} & 0 & 0 & 0 & 0 & 0 \\ & c_{TT} & 0 & 0 & 0 & 0 \\ & & c_{BB} & 0 & 0 & 0 \\ & & & c_{BB} & 0 & 0 \\ & sym & & & c_{BB} & 0 \\ & & & & & \left(-\frac{P_0}{\Omega_0^2}\right) \end{bmatrix} \tag{C.5}$$

$$\mathbf{K} = \begin{bmatrix} k_{PP} & 0 & 0 & 0 & 0 & 0 \\ & k_{TT} & 0 & 0 & 0 & 0 \\ & & k_{BB}^1 & 0 & 0 & 0 \\ & & & k_{BB}^2 & 0 & 0 \\ & sym & & & k_{BB}^3 & 0 \\ & & & & 0 & k_{\varepsilon\varepsilon} \end{bmatrix} \tag{C.6}$$

Where, the rotational inertia of the platform can be given as

$$\begin{aligned} m_{PP} = 12H_t^2 \int_0^L \mu^B(r)\mathrm{d}r + \sum_{i=1}^{3} \Bigg[4H_t \int_0^L r\mu^B(r)\mathrm{d}r \cos(\psi_i) \\ + \int_0^L r^2 \mu^B(r)\mathrm{d}r \cos^2(\psi_i) \Bigg] + H_t^2(m^N + m^H) + I_P + I_P^{AM} \end{aligned} \tag{C.7}$$

The inertial coupling between the platform and tower can be given as

$$m_{PT} = 6H_t \int_0^L \mu^B(r)\mathrm{d}r + \int_0^{H_t} h\mu^T(h)\phi_t(h)\mathrm{d}h \tag{C.8}$$

The inertial coupling between the platform and the blades can be given as

$$m_{PBi} = 2H_t \int_0^L \phi_b(r)\mu^B(r)\mathrm{d}r + \int_0^L r\phi_b(r)\mu^B(r)\mathrm{d}r\cos(\psi_i) \qquad \text{for } i = 1 \text{ to } 3 \tag{C.9}$$

The inertial coupling between the tower and the blades can be given as

$$m_{TB} = \int_0^L \phi_b(r)\mu^B(r)\mathrm{d}r \tag{C.10}$$

The translational inertia term of the tower fore-aft degree of freedom can be given as

$$m_{TT} = 3\int_0^L \mu^B(r)\mathrm{d}r + \int_0^{H_t} \phi_t^2\mu^T(h)\mathrm{d}h + m^N + m^H \tag{C.11}$$

The translational inertia term associated with blade flapwise degree of freedom can be given as

$$m_{BB} = \int_0^L \phi_b(r)^2\mu^B(r)\mathrm{d}r \tag{C.12}$$

Where, H_t is the height of the tower and L is the length of the blades. $\mu^B(r)$ and $\mu^T(h)$ are mass per unit length of the blades and tower respectively. ψ_i is the azimuth angle of the i^{th} blade. I_P is the rotational inertia of the platform and I_P^{AM} is the hydrodynamic added mass coefficient associated with the platform pitch degree of freedom. $\phi_b(r)$ and $\phi_t(h)$ are the normalized fundamental model shapes of the blades and tower in the flapwise and fore-aft directions respectively. c_{PP} is the linear hydrodynamic damping coefficient associated with the platform pitch degree of freedom, c_{TT} and c_{BB} are structural damping coefficient of the tower and the blades respectively. k_{PP} is the summation of hydro-static and linearised mooring lines stiffness associated with the platform pitch degree of freedom. k_{TT} is the elastic stiffness of the tower and $k_{BB}^i = k_{BB}^e + k_{BB}^c + k_{BB}^g\cos(\psi_i)$ is the summation of the elastic stiffness, ,k_{BB}^e, centrifugal stiffness, k_{BB}^c, and, gravitational stiffening/softening, k_{BB}^g, of the i^{th} blade. More details on these terms can be found in (Fitzgerald, Basu, and Nielsen, 2013; Fitzgerald, Sarkar, and Staino, 2018; Sarkar and Chakraborty, 2018).

Bibliography

Achmus, Martin, Yu-Shu Kuo, and Khalid Abdel-Rahman (2009). “Behavior of monopile foundations under cyclic lateral load”. In: *Computers and Geotechnics* 36.5, pp. 725–735.

Anaya-Lara, Olimpo et al. (2018). *Offshore Wind Energy Technology*. Wiley Online Library.

Arapogianni, Athanasia et al. (2013). “Deep Water; The next step for offshore wind energy”. In: *European Wind Energy Association (EWEA)*.

Arrigan, John et al. (2011). “Control of flapwise vibrations in wind turbine blades using semi-active tuned mass dampers”. In: *Structural Control and Health Monitoring* 18.8, pp. 840–851.

Arshad, Muhammad and Brendan C O’Kelly (2016). “Analysis and design of monopile foundations for offshore wind-turbine structures”. In: *Marine Georesources & Geotechnology* 34.6, pp. 503–525.

Azcona, José et al. (2017). “Impact of mooring lines dynamics on the fatigue and ultimate loads of three offshore floating wind turbines computed with IEC 61400-3 guideline”. In: *Wind Energy* 20.5, pp. 797–813.

Basu, Biswajit (2016). “Irrotational two-dimensional free-surface steady water flows over a flat bed with underlying currents”. In: *Nonlinear Analysis: Theory, Methods & Applications* 147, pp. 110–124.

— (2019). “On some properties of velocity field for two dimensional rotational steady water waves”. In: *Nonlinear Analysis* 184, pp. 17–34.

Basu, Biswajit and Satish Nagarajaiah (2008). “A wavelet-based time-varying adaptive LQR algorithm for structural control”. In: *Engineering structures* 30.9, pp. 2470–2477.

— (2010). “Multiscale Wavelet-LQR Controller for Linear Time Varying Systems”. In: *Journal of Engineering Mechanics* 136.9, pp. 1143–1151.

Basu, Biswajit, Andrea Staino, and Malabika Basu (2014). “Role of flexible alternating current transmission systems devices in mitigating grid fault-induced vibration of wind turbines”. In: *Wind energy* 17.7, pp. 1017–1033.

Basu, Biswajit, Zili Zhang, and Søren RK Nielsen (2016). "Damping of edgewise vibration in wind turbine blades by means of circular liquid dampers". In: *Wind Energy* 19.2, pp. 213–226.

Berglind, JJ and Rafael Wisniewski (2014). "Fatigue Estimation Methods Comparison for Wind Turbine Control". In: *arXiv preprint arXiv:1411.3925*.

Berglind, JJ Barradas, Rafael Wisniewski, and Mohsen Soltani (2015). "Fatigue load modeling and control for wind turbines based on hysteresis operators". In: *American Control Conference (ACC), 2015*. IEEE, pp. 3721–3727.

Bossanyi, EA (2003). "Individual blade pitch control for load reduction". In: *Wind energy* 6.2, pp. 119–128.

— (2005). "Further load reductions with individual pitch control". In: *Wind energy* 8.4, pp. 481–485.

Bossanyi, Ervin A, Paul A Fleming, and Alan D Wright (2013). "Validation of individual pitch control by field tests on two-and three-bladed wind turbines". In: *IEEE Transactions on Control Systems Technology* 21.4, pp. 1067–1078.

Brodersen, Mark L, Ann-Sofie Bjørke, and Jan Høgsberg (2017). "Active tuned mass damper for damping of offshore wind turbine vibrations". In: *Wind Energy* 20.5, pp. 783–796.

Buckley, Tadhg et al. (2017). "Mitigating the structural vibrations of wind turbines using tuned liquid column damper considering soil-structure interaction". In: *Renewable Energy*.

Burton, Tony et al. (2011). *Wind energy handbook*. John Wiley & Sons.

Camblong, Haritza et al. (2012). "Control of wind turbines for fatigue loads reduction and contribution to the grid primary frequency regulation". In: *Energy* 48.1, pp. 284–291.

Carlson, Daniel W and Yahya Modarres-Sadeghi (2018). "Vortex-induced vibration of spar platforms for floating offshore wind turbines". In: *Wind Energy* 21.11, pp. 1169–1176.

Carswell, W et al. (2015a). "Foundation damping and the dynamics of offshore wind turbine monopiles". In: *Renewable energy* 80, pp. 724–736.

Carswell, Wystan et al. (2015b). "Soil–structure reliability of offshore wind turbine monopile foundations". In: *Wind energy* 18.3, pp. 483–498.

Caterino, Nicola (2015). "Semi-active control of a wind turbine via magnetorheological dampers". In: *Journal of Sound and Vibration* 345, pp. 1–17.

Caterino, Nicola and Mariacristina Spizzuoco (2017). "Structural Control of a Wind Turbine Accounting for Second Order Effects". In: *IOP Conference Series: Materials Science and Engineering*. Vol. 245. 2. IOP Publishing, p. 022040.

Chen, Bei et al. (2018). “Enhancement of flutter stability in wind turbines with a new type of passive damper of torsional rotation of blades”. In: *Journal of Wind Engineering and Industrial Aerodynamics* 173, pp. 171–179.

Chen, Jianyun et al. (2015). “Semi-active fuzzy control of edgewise vibrations in wind turbine blades under extreme wind”. In: *Journal of Wind Engineering and Industrial Aerodynamics* 147, pp. 251–261.

Chen, Junling and Christos T Georgakis (2013). “Tuned rolling-ball dampers for vibration control in wind turbines”. In: *Journal of Sound and Vibration* 332.21, pp. 5271–5282.

Chen, Lin and Biswajit Basu (2018). “Fatigue load estimation of a spar-type floating offshore wind turbine considering wave-current interactions”. In: *Int J Fatigue* 116, pp. 421–428. DOI: 10.1016/j.ijfatigue.2018.06.002.

— (2019). “Wave-current interaction effects on structural responses of floating offshore wind turbines”. In: *Wind Energy* 22.2, pp. 327–339.

Chen, Lin, Biswajit Basu, and Søren R K Nielsen (2018). “A coupled finite difference mooring dynamics model for floating offshore wind turbine analysis”. In: *Ocean Eng* 162, pp. 304–315. DOI: 10.1016/j.oceaneng.2018.05.001.

Cheon, Jongmin, Soonman Kwon, and Youngkiu Choi (2014). “Design of a pitch controller using disturbance accommodating control for wind turbines under stochastic environments”. In: *Industrial Electronics (ISIE), 2014 IEEE 23rd International Symposium on*. IEEE, pp. 2572–2577.

Colwell, Shane and Biswajit Basu (2009). “Tuned liquid column dampers in offshore wind turbines for structural control”. In: *Engineering Structures* 31.2, pp. 358–368.

Commission, International Electrotechnical et al. (2005). “IEC 61400-1: Wind turbines part 1: Design requirements”. In: *International Electrotechnical Commission*.

Damgaard, Mads, Lars Vabbersgaard Andersen, and Lars Bo Ibsen (2014). “Computationally efficient modelling of dynamic soil–structure interaction of offshore wind turbines on gravity footings”. In: *Renewable Energy* 68, pp. 289–303.

Damgaard, Mads et al. (2015). “A probabilistic analysis of the dynamic response of monopile foundations: Soil variability and its consequences”. In: *Probabilistic Engineering Mechanics* 41, pp. 46–59.

Daubechies, Ingrid (1992). *Ten lectures on wavelets*. Vol. 61. Siam.

De Battista, Hernán, Ricardo J Mantz, and Carlos F Christiansen (2000). “Dynamical sliding mode power control of wind driven induction generators”. In: *IEEE transactions on energy conversion* 15.4, pp. 451–457.

Dinh, Van Nguyen and Biswajit Basu (2013). "Impact of spar-nacelle-blade coupling on the edgewise response of floating offshore wind turbines". In: *Coupled Systems Mechanics* 2.3, pp. 231–253.

— (2015). "Passive control of floating offshore wind turbine nacelle and spar vibrations by multiple tuned mass dampers". In: *Structural Control and Health Monitoring* 22.1, pp. 152–176.

Dinh, Van-Nguyen, Biswajit Basu, and Satish Nagarajaiah (2016). "Semi-active control of vibrations of spar type floating offshore wind turbines". In: *Smart Struct. Syst* 18.4, pp. 683–705.

DNV GL (2015). *DNVGL-SE-0190: Project certification of wind power plants*. `https://rules.dnvgl.com/docs/pdf/DNVGL/SE/2015-12/DNVGL-SE-0190.pdf`. Online; accessed 26 July 2019.

Downing, Stephen D and DF Socie (1982). "Simple rainflow counting algorithms". In: *International journal of fatigue* 4.1, pp. 31–40.

Duan, Fei, Zhiqiang Hu, and Jin Wang (2016). "Investigation of the VIMs of a spar-type FOWT using a model test method". In: *Journal of Renewable and Sustainable Energy* 8.6, p. 063301.

Findeisen, Rolf (2005). *Nonlinear model predictive control: a sampled data feedback perspective.*

Fitzgerald, Breiffni and B Basu (2014). "Cable connected active tuned mass dampers for control of in-plane vibrations of wind turbine blades". In: *Journal of Sound and Vibration* 333.23, pp. 5980–6004.

Fitzgerald, Breiffni and Biswajit Basu (2016). "Structural control of wind turbines with soil structure interaction included". In: *Engineering Structures* 111, pp. 131–151.

Fitzgerald, Breiffni, Biswajit Basu, and Søren RK Nielsen (2013). "Active tuned mass dampers for control of in-plane vibrations of wind turbine blades". In: *Structural Control and Health Monitoring* 20.12, pp. 1377–1396.

Fitzgerald, Breiffni, Saptarshi Sarkar, and Andrea Staino (2018). "Improved reliability of wind turbine towers with active tuned mass dampers (ATMDs)". In: *Journal of Sound and Vibration* 419, pp. 103–122.

Fitzgerald, Breiffni, Andrea Staino, and Biswajit Basu (2019). "Wavelet-based individual blade pitch control for vibration control of wind turbine blades". In: *Structural Control and Health Monitoring* 26.1, e2284.

Fleming, Paul, Jan-Willem Wingerden, and Alan Wright (2012). "Comparing state-space multivariable controls to multi-siso controls for load reduction of drivetrain-coupled modes on wind turbines through field-testing". In: *50th AIAA Aerospace*

Sciences Meeting including the New Horizons Forum and Aerospace Exposition, p. 1152.

Franke, R (1998). “OMUSES-a Tool for the Optimization of MUltistage Systems and HQP-a Solver for Sparse Nonlinear Optimization”. In: *Dept. of Automation and Systems Engineering, Technical University of Ilmenau, Germany.*

Gabbai, RD and H Benaroya (2005). “An overview of modeling and experiments of vortex-induced vibration of circular cylinders”. In: *Journal of Sound and Vibration* 282.3-5, pp. 575–616.

Gao, Richie and Zhiwei Gao (2016). “Pitch control for wind turbine systems using optimization, estimation and compensation”. In: *Renewable Energy* 91, pp. 501–515.

Gobat, J I and M A Grosenbaugh (2006). “Time-domain numerical simulation of ocean cable structures”. In: *Ocean Eng* 33.10, pp. 1373–1400. DOI: 10.1016/j.oceaneng.2005.07.012.

Hall, Matthew (2015). “MoorDynâĂŤUsers Guide”. In: *Department of Mechanical Engineering, University of Maine: Orono, ME, USA*.

Hansen, Martin OL (2015). *Aerodynamics of wind turbines.* Routledge.

Harte, M, B Basu, and Søren RK Nielsen (2012). “Dynamic analysis of wind turbines including soil-structure interaction”. In: *Engineering Structures* 45, pp. 509–518.

Hedges, T S (1981). “Some effects of currents on wave spectra”. In: *Proceedings of the first Indian Conference in Ocean Engineering.* Vol. 1, pp. 30–35.

Hedges, T S, K Anastasiou, and D Gabriel (1985). “Interaction of random waves and currents”. In: *J Waterw Port Coast Ocean Eng* 111.2, pp. 275–288. DOI: 10.1061/(ASCE)0733-950X(1984)110:4(432).

Huang, Chaojun et al. (2010). “Semi-active algorithm for edgewise vibration control in floating wind turbine blades”. In: *Earth and Space 2010: Engineering, Science, Construction, and Operations in Challenging Environments*, pp. 2097–2110.

Huang, Norden E et al. (1972). “Interactions between steady non-uniform currents and gravity waves with applications for current measurements”. In: *Journal of Physical Oceanography* 2.4, pp. 420–431. DOI: 10.1175/1520-0485(1972)002<0420:IBSWUC>2.0.CO;2.

Irani, Mehernosh and Lyle Finn (2004). “Model testing for vortex induced motions of spar platforms”. In: *ASME 2004 23rd International Conference on Offshore Mechanics and Arctic Engineering.* American Society of Mechanical Engineers, pp. 605–610.

Ismail, Nabil M (1984). “Wave-current models for design of marine structures”. In: *J Waterw Port Coast Ocean Eng* 110.4, pp. 432–447. DOI: 10.1061/(ASCE)0733-950X(1984)110:4(432).

Jafarnejadsani, Hamidreza and Jeff Pieper (2015). “Gain-Scheduled ℓ_1-Optimal Control of Variable-Speed-Variable-Pitch Wind Turbines”. In: *IEEE Transactions on Control Systems Technology* 23.1, pp. 372–379.

Jiang, Zhiyu (2018). “The impact of a passive tuned mass damper on offshore single-blade installation”. In: *Journal of Wind Engineering and Industrial Aerodynamics* 176, pp. 65–77.

Jonkman, Bonnie J (2009). *TurbSim user's guide: Version 1.50.* Tech. rep. National Renewable Energy Lab.(NREL), Golden, CO (United States).

Jonkman, Jason Mark (2007). *Dynamics modeling and loads analysis of an offshore floating wind turbine.* University of Colorado at Boulder.

— (2010). *Definition of the Floating System for Phase IV of OC3.* Citeseer.

Jonkman, Jason Mark and Marshall L Buhl Jr (2005). *Fast user's guide-updated august 2005.* Tech. rep. National Renewable Energy Laboratory (NREL), Golden, CO.

Jonkman, Jason Mark et al. (2009). *Definition of a 5-MW reference wind turbine for offshore system development.* National Renewable Energy Laboratory Golden, CO.

Kane, Thomas R and David A Levinson (1985). *Dynamics, theory and applications.* McGraw Hill.

Karimirad, Madjid and Torgeir Moan (2011). “Wave-and wind-induced dynamic response of a spar-type offshore wind turbine”. In: *Journal of waterway, port, coastal, and ocean engineering* 138.1, pp. 9–20.

— (2013). “Stochastic dynamic response analysis of a tension leg spar-type offshore wind turbine”. In: *Wind Energy* 16.6, pp. 953–973.

Kong, Changduk, J Bang, and Y Sugiyama (2005). “Structural investigation of composite wind turbine blade considering various load cases and fatigue life”. In: *Energy* 30.11-12, pp. 2101–2114.

Kong, Changduk et al. (2006). “Investigation of fatigue life for a medium scale composite wind turbine blade”. In: *International Journal of Fatigue* 28.10, pp. 1382–1388.

Kristalny, Maxim, Daria Madjidian, and Torben Knudsen (2013). “On using wind speed preview to reduce wind turbine tower oscillations”. In: *IEEE Transactions on Control Systems Technology* 21.4, pp. 1191–1198.

Lackner, Matthew A (2013). “An investigation of variable power collective pitch control for load mitigation of floating offshore wind turbines”. In: *Wind Energy* 16.4, pp. 519–528.

Lackner, Matthew A and Mario A Rotea (2011a). “Passive structural control of offshore wind turbines”. In: *Wind energy* 14.3, pp. 373–388.

— (2011b). "Structural control of floating wind turbines". In: *Mechatronics* 21.4, pp. 704–719.

Lan, Jianglin, Ron J Patton, and Xiaoyuan Zhu (2018). "Fault-tolerant wind turbine pitch control using adaptive sliding mode estimation". In: *Renewable Energy* 116, pp. 219–231.

Larsen, Torben J and Anders Melchior Hansen (2007). "How 2 HAWC2, the user's manual". In:

Lee, Donghoon, Dewey H Hodges, and Mayuresh J Patil (2002). "Multi-flexible-body Dynamic Analysis of Horizontal Axis Wind Turbines". In: *Wind Energy* 5.4, pp. 281–300.

Lee, Donghoon and DH Hodges (2003). *Multi-flexible-body analysis for applications to wind turbine control design.* School of Aerospace Engineering, Georgia Institute of Technology.

Lee, Sang et al. (2012). "Atmospheric and wake turbulence impacts on wind turbine fatigue loadings". In: *50th AIAA Aerospace Sciences Meeting including the New Horizons Forum and Aerospace Exposition*, p. 540.

Li, Lin, Zhen Gao, and Torgeir Moan (2015). "Joint distribution of environmental condition at five european offshore sites for design of combined wind and wave energy devices". In: *Journal of Offshore Mechanics and Arctic Engineering* 137.3, p. 031901.

Lindelöw, Per Jonas Petter et al. (2008). *Fiber based coherent lidars for remote wind sensing.*

Löfberg, Johan (2004). "YALMIP: A toolbox for modeling and optimization in MATLAB". In: *Proceedings of the CACSD Conference.* Vol. 3. Taipei, Taiwan.

London Array (2016). *Renewable energy record achieved at London Array.* `http://www.londonarray.com/project/renewable-energy-record-achieved-at-london-array/`. Online; accessed 26 July 2019.

Marin, JC et al. (2009). "Study of fatigue damage in wind turbine blades". In: *Engineering failure analysis* 16.2, pp. 656–668.

MATLAB (2018). *version 9.4.0 (R2018a).* Natick, Massachusetts: The MathWorks Inc.

Moriarty, Patrick J and A Craig Hansen (2005). *AeroDyn theory manual.* Tech. rep. National Renewable Energy Lab., Golden, CO (US).

Mosek, ApS (2015). *The MOSEK optimization toolbox for MATLAB manual.*

Mughal, Muhammad Hamid and Li Guojie (2015). "Review of pitch control for variable speed wind turbine". In: *2015 IEEE 12th Intl Conf on Ubiquitous Intelligence and Computing and 2015 IEEE 12th Intl Conf on Autonomic and Trusted Computing* *and 2015 IEEE 15th Intl Conf on Scalable Computing and Communications and Its Associated Workshops (UIC-ATC-ScalCom)*. IEEE, pp. 738–744.

Murtagh, PJ, B Basu, and BM Broderick (2005). “Along-wind response of a wind turbine tower with blade coupling subjected to rotationally sampled wind loading”. In: *Engineering structures* 27.8, pp. 1209–1219.

Murtagh, PJ et al. (2008). “Passive control of wind turbine vibrations including blade/tower interaction and rotationally sampled turbulence”. In: *Wind Energy* 11.4, pp. 305–317.

Nam, Yoonsu, Pham Trung Kien, and Yo-Han La (2013). “Alleviating the tower mechanical load of multi-MW wind turbines with LQR control”. In: *Journal of Power Electronics* 13.6, pp. 1024–1031.

Namik, H and K Stol (2010). “Individual blade pitch control of floating offshore wind turbines”. In: *Wind Energy: An International Journal for Progress and Applications in Wind Power Conversion Technology* 13.1, pp. 74–85.

Namik, H and Karl Stol (2011). “Performance analysis of individual blade pitch control of offshore wind turbines on two floating platforms”. In: *Mechatronics* 21.4, pp. 691–703.

Namik, Hazim and Karl Stol (2014). “Individual blade pitch control of a spar-buoy floating wind turbine”. In: *system* 1.3, p. 6.

Ning, Andrew et al. (2015). “Development and Validation of a New Blade Element Momentum Skewed-Wake Model within AeroDyn”. In: *33rd Wind Energy Symposium*, p. 0215.

Ning, S Andrew (2014). “A simple solution method for the blade element momentum equations with guaranteed convergence”. In: *Wind Energy* 17.9, pp. 1327–1345.

Njiri, Jackson G and Dirk Söffker (2016). “State-of-the-art in wind turbine control: Trends and challenges”. In: *Renewable and Sustainable Energy Reviews* 60, pp. 377–393.

Nocedal, Jorge and Stephen Wright (2006). *Numerical optimization*. Springer Science & Business Media.

Odgaard, Peter Fogh et al. (2016). “On using pareto optimality to tune a linear model predictive controller for wind turbines”. In: *Renewable Energy* 87, pp. 884–891.

Øye, Stig (1996). “FLEX4 simulation of wind turbine dynamics”. In: *Proceedings of the 28th IEA Meeting of Experts Concerning State of the Art of Aeroelastic Codes for Wind Turbine Calculations*, pp. 129–135.

Petrović, Vlaho, Mate Jelavić, and Mato Baotić (2015). “Advanced control algorithms for reduction of wind turbine structural loads”. In: *Renewable Energy* 76, pp. 418–431.

Phillips, O M (1977). *The Dynamics of Upper Ocean.* Cambridge University Press.

Pierson Jr, Willard J and Lionel Moskowitz (1964). "A proposed spectral form for fully developed wind seas based on the similarity theory of SA Kitaigorodskii". In: *Journal of geophysical research* 69.24, pp. 5181–5190.

Raach, Steffen et al. (2014). "Nonlinear model predictive control of floating wind turbines with individual pitch control". In: *2014 American Control Conference.* IEEE, pp. 4434–4439.

Ragan, Patrick and Lance Manuel (2007). "Comparing estimates of wind turbine fatigue loads using time-domain and spectral methods". In: *Wind engineering* 31.2, pp. 83–99.

Ren, Yaxing et al. (2016). "Nonlinear PI control for variable pitch wind turbine". In: *Control Engineering Practice* 50, pp. 84–94.

Sarkar, Saptarshi and Arunasis Chakraborty (2018). "Optimal design of semiactive MR-TLCD for along-wind vibration control of horizontal axis wind turbine tower". In: *Structural Control and Health Monitoring* 25.2.

— (2019). "Development of semi-active vibration control strategy for horizontal axis wind turbine tower using multiple magneto-rheological tuned liquid column dampers". In: *Journal of Sound and Vibration* 457, pp. 15–36.

Sarkar, Saptarshi, Breiffni Fitzgerald, and Biswajit Basu (2018). "Development of a Flexible Multibody Dynamics Wind Turbine Model following Kane's Method". In: *Proceedings of the Civil Engineering Research in Ireland*, pp. 883–888.

Schlipf, David, Dominik Johannes Schlipf, and Martin Kühn (2013). "Nonlinear model predictive control of wind turbines using LIDAR". In: *Wind energy* 16.7, pp. 1107–1129.

Schuler, Simone et al. (2013). "ℓ_1-Optimal Control of Large Wind Turbines". In: *IEEE Transactions on Control Systems Technology* 21.4, pp. 1079–1089.

Shokrieh, Mahmood M and Roham Rafiee (2006). "Simulation of fatigue failure in a full composite wind turbine blade". In: *Composite Structures* 74.3, pp. 332–342.

Silva, M C et al. (2016). "Numerical simulations of wave–current flow in an ocean basin". In: *Appl Ocean Resear* 61, pp. 32–41. DOI: `10.1016/j.apor.2016.10.005`.

Staino, A, B Basu, and Søren RK Nielsen (2012). "Actuator control of edgewise vibrations in wind turbine blades". In: *Journal of Sound and Vibration* 331.6, pp. 1233–1256.

Staino, Andrea and Biswajit Basu (2015). "Emerging trends in vibration control of wind turbines: a focus on a dual control strategy". In: *Phil. Trans. R. Soc. A* 373.2035, p. 20140069.

Stewart, Gordon M and Matthew A Lackner (2014). “The impact of passive tuned mass dampers and wind–wave misalignment on offshore wind turbine loads”. In: *Engineering Structures* 73, pp. 54–61.

Stol, Karl A, Wenxin Zhao, and Alan D Wright (2006). “Individual blade pitch control for the controls advanced research turbine (CART)”. In: *Journal of solar energy engineering* 128.4, pp. 498–505.

Sun, C and V Jahangiri (2018). “Bi-directional vibration control of offshore wind turbines using a 3D pendulum tuned mass damper”. In: *Mechanical Systems and Signal Processing* 105, pp. 338–360.

Sun, Chao (2018). “Mitigation of offshore wind turbine responses under wind and wave loading: Considering soil effects and damage”. In: *Structural Control and Health Monitoring* 25.3.

Sutherland, Herbert J (1999). *On the fatigue analysis of wind turbines*. Tech. rep. Sandia National Labs., Albuquerque, NM (US); Sandia National Labs., Livermore, CA (US).

Tao, Weifeng, Biswajit Basu, and Jie Li (2018). “Reliability analysis of active tendon-controlled wind turbines by a computationally efficient wavelet-based probability density evolution method”. In: *Structural Control and Health Monitoring* 25.3.

Taylor, Michael, Pablo Ralon, and Andrei Ilas (2016). “The power to change: solar and wind cost reduction potential to 2025”. In: *International Renewable Energy Agency (IRENA)*.

Thomas, G P (1981). “Wave-current interactions: an experimental and numerical study. Part 1. Linear waves”. In: *J Fluid Mech* 110, pp. 457–474. DOI: 10.1017/S0022112081000839.

Tjavaras, A A et al. (1998). “The mechanics of highly-extensible cables”. In: *J Sound Vib* 213.4, pp. 709–737. DOI: 10.1006/jsvi.1998.1526.

Tjavaras, Athanassios A. (1996). “The Dynamics of Highly Extensible Cables”. Thesis. Massachusetts Institute of Technology.

Tung, Chi Chao and Norden Eh Huang (1974). “Influence of current on statistical properties of waves”. In: *Journal of Waterways, Harbors & Coast Eng Div* 100.4, pp. 267–278.

Valamanesh, V, AT Myers, and SR Arwade (2015). “Multivariate analysis of extreme metocean conditions for offshore wind turbines”. In: *Structural Safety* 55, pp. 60–69.

Valpy, Bruce et al. (2017). *InnoEnergy - Future renewable energy costs: Offshore wind*. BVG Associates.

Wang, Kai, Torgeir Moan, and Martin OL Hansen (2016). “Stochastic dynamic response analysis of a floating vertical-axis wind turbine with a semi-submersible floater”. In: *Wind Energy* 19.10, pp. 1853–1870.

Waris, Muhammad Bilal and Takeshi Ishihara (2012). "Dynamic response analysis of floating offshore wind turbine with different types of heave plates and mooring systems by using a fully nonlinear model". In: *Coupled systems mechanics* 1.3, pp. 247–268.

Yuan, Yuan and J Tang (2017). "Adaptive pitch control of wind turbine for load mitigation under structural uncertainties". In: *Renewable Energy* 105, pp. 483–494.

Zhang, Mingming, Honglei Yang, and Jianzhong Xu (2017). "Numerical investigation of azimuth dependent smart rotor control on a large-scale offshore wind turbine". In: *Renewable Energy* 105, pp. 248–256.

Zhang, Zili et al. (2014). "Mitigation of edgewise vibrations in wind turbine blades by means of roller dampers". In: *Journal of Sound and Vibration* 333.21, pp. 5283–5298.

Zhang, Zili et al. (2015). "Nonlinear modeling of tuned liquid dampers (TLDs) in rotating wind turbine blades for damping edgewise vibrations". In: *Journal of Fluids and Structures* 59, pp. 252–269.

Zhao, Wenxin and Karl Stol (2007). "Individual blade pitch for active yaw control of a horizontal-axis wind turbine". In: *45th AIAA Aerospace Sciences Meeting and Exhibit*, p. 1022.

Zuo, Haoran, Kaiming Bi, and Hong Hao (2018). "Dynamic analyses of operating offshore wind turbines including soil-structure interaction". In: *Engineering Structures* 157, pp. 42–62.